Cyclic Yielding of Tubular Structures

PhD Thesis

$$(EIv'')'' = q - \rho A\ddot{v}$$

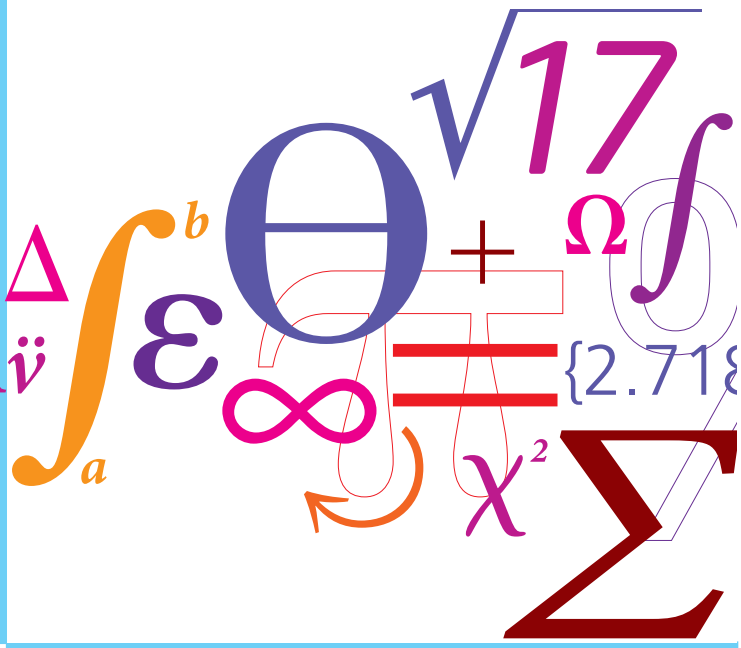

Lasse Tidemann
DCAMM Special Report No. S238
January 2018

DTU Mechanical Engineering
Department of Mechanical Engineering

Cyclic Yielding of Tubular Structures

Lasse Tidemann

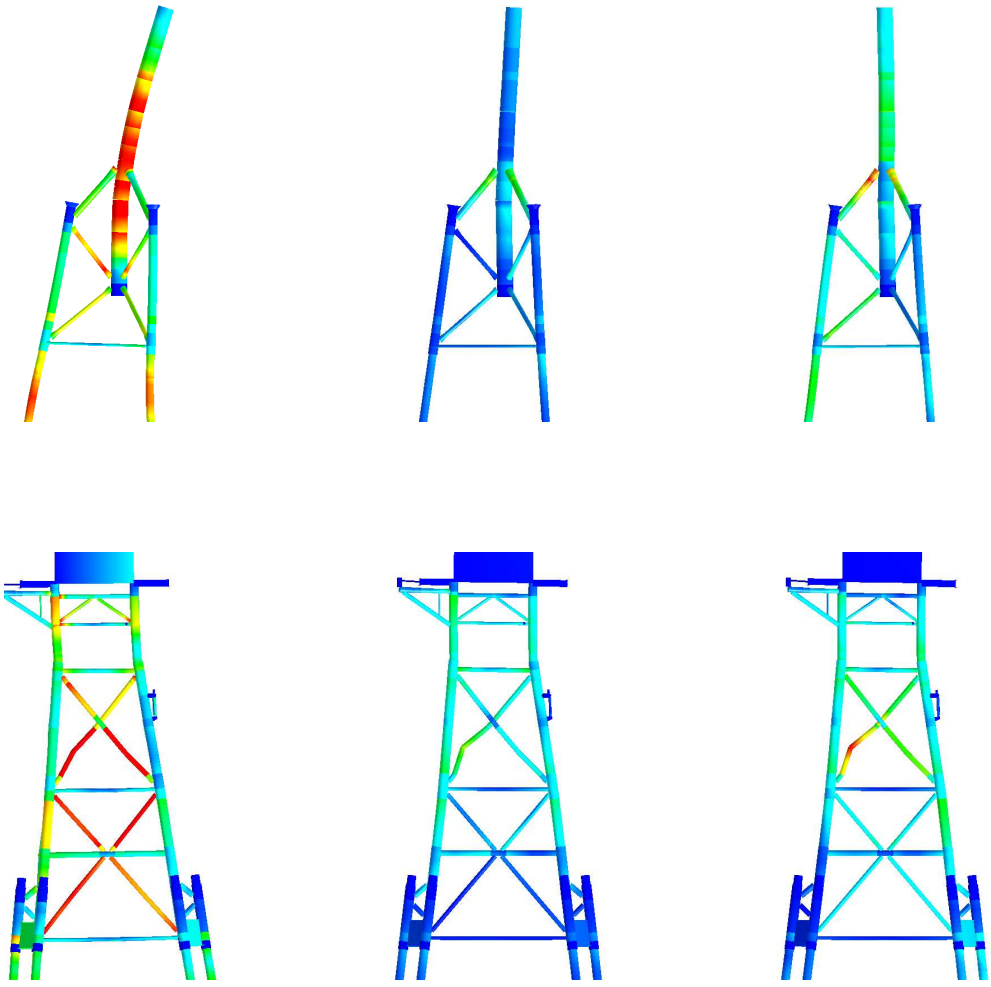

Department of Mechanical Engineering
Section of Solid Mechanics
Technical University of Denmark
January 2018

You can't just turn creativity on like a faucet. You have to be in the right mood.

- Calvin

Section of Solid Mechanics
Department of Mechanical Engineering
Technical University of Denmark
Nils Koppels Alle, Building 404
DK-2800 Kongens Lyngby,
Denmark

Preface

This thesis is submitted in partial fulfilment of the Ph.D. degree from the Technical University of Denmark. The work was done as part of a collaboration between Mærsk Olie og Gas A/S and the Department of Mechanical Engineering at the Technical University of Denmark with the support of Rambøll Oil and Gas. The work has been performed in the period of December 2014 to January 2018 under the supervision of Professor, Dr. Techn. Steen Krenk as main supervisor, Structural Advisor Jesper P. Tychsen as advisor at Mærsk and Lead Specialist John Wægter at Rambøll. I would like to express my deep gratitude towards Steen for taking me under his wings, showing me the beauty and elegance of simple theories. Furthermore I would like to thank Jesper for providing the real-life challenges and practical insights that provide a purpose to the theory. I would also like to thank all my colleagues at Mærsk for their support and always being ready to answer my questions, no matter how stupid they may have been. A big thank you goes towards John for his involvement, providing access to RONJA and creating contact to the right people to help me with the development of the code. Lastly a thank you is due to Rambøll Oil and Gas for letting me peak into and change their code and to Lars Aaes Jakobsen for always picking up the phone, answering my questions and eager discussions on coding.

I would like to thank Professor Stelios Kyriakides at the University of Texas at Austin, for having me for a three month external stay and giving me an experience of the culture of American research groups. I would also like to thank Martin Scales for being a genuinely nice dude, introducing me to all the best of Austin. Go Horns!

Furthermore, I would like to thank my colleagues at the department for a nice time and interesting discussions on everything from sitcoms to benefits and drawbacks of a symmetric formulation of the generalized eigenvalue problem. Finally I owe the deepest of thanks to my family for bearing with me and acting interested after seeing hysteresis curves at each and every family gathering, and to my girlfriend Camilla for maturing me, keeping my spirit high and being my biggest fan. Everything I do, I do it to make you proud.

Kongens Lyngby, January 2018

Lasse Tidemann

Abstract

In an effort to design according to the true behaviour of structures focus is on increasing the accuracy of the individual aspects of the structural models. The present thesis addresses cyclic plasticity models and is organised in five parts; the first four parts focus on different aspects of computational cyclic plasticity models. The fifth part focuses on the effects of using improved cyclic plasticity models. The sum of the parts will support the ability to design according to the true behaviour of a structure.

The first part addresses the development of a cyclic plasticity model. A cyclic plasticity model with parameter evolution is presented based on three potentials; a specific energy defining the constitutive relations, a yield function defining the size and shape of the elastic domain in the form of a yield surface, and a plastic flow potential defining the evolution of the plastic strains. The cyclic plasticity model exhibits kinematic hardening and the translation of the center of the yield surface is limited by a surface similar to the yield surface defining an ultimate capacity. The parameter evolution enables modelling of effects as cyclic hardening/softening.

The second part focuses on developing a generic first-order yield surface format usable for e.g. anisotropic materials and plastic hinges in beam members and joints. The format is defined as a sum of square roots of quadratic terms that individually would represent ellipsoids and the surface is thereby convex. The format will be homogeneous for most yield surfaces of interest resulting in improved algorithmic properties. It is shown to be possible to locally reduce the curvature of the yield surface while still having a single-equation format.

The third part describes how a frame element can include the four most important effects in analysis of tubular structures with cyclic plasticity: an elastic initially imperfect member, elastic local joint flexibility and plastic mechanisms at the member ends and in the joints. The frame element is based on an equilibrium format, splitting element displacements into a set of deformations and a set of rigid body motions. The deformations and thereby the flexibilities are additive. The element has an explicit stiffness matrix that only requires inversion of a matrix of maximum size 4×4. A standard full format element including rigid body motions is obtained by use of the equilibrium conditions.

In the fourth part a robust return algorithm is developed. The return algorithm is based on satisfying the generalized strain evolution equations in the final state in combination with ensuring the final stress state is located on the yield surface. The robustness is increased by making a second order approximation of the generalized stress increment leading to a two-step return algorithm. First a mid-step is made to obtain information and subsequently a full step is made with the information obtained at the mid-step.

In the final part the effects of cyclic plasticity are discussed including the effects of elasto-plastic buckling and plastic deformation for complex structures. The permanent change of the geometry reduces characteristic stiffness and capacities of the structure. The previously developed models have been used to update a recognized computer code making it more robust and increasing the ability to represent the true behaviour of frame structures.

Resumé

Med en ambition om at designe konstruktioner i forhold til deres reelle opførsel fokuseres på at øge præcisionen af de individuelle dele af strukturelle modeller. Denne afhandling behandler cykliske plasticitetsmodeller og er organiseret i fem dele; de første fire fokuserer på forskellige aspekter af beregninger med cykliske plasticitetsmodeller. Den femte fokuserer på effekterne af at bruge en forbedret cyklisk plasticitetsmodel. Summen af de fem dele understøtter udviklingen mod at kunne designe i forhold til en konstruktions reelle opførsel.

Den første del adresserer udviklingen af en cyklisk plasticitetsmodel og en cyklisk plasticitetsmodel med parameterudviking præsenteres. Modellen er baseret på tre potentialer; en specifik indre energi der definerer de konstitutive relationer, en flydefunktion der definerer størrelse og form af det elastiske domæne i form af en flydeflade, samt et plastisk flowpotential der definerer udviklingen af de plastiske tøjninger. Den cykliske plasticitetsmodel udviser kinematisk hærdning og flytningen af flydefladens centrum er begrænset af en flade ensartet med flydefladen, hvilket definerer en ultimativ kapacitet. Parameterudviklingen muliggør modellering af effekter som cyklisk hærdning/relaksation.

Den anden del fokuserer på udviklingen af et generisk førsteordens flydefladeformat, der kan bruges ifm. fx anistrope materialer og plastiske hængsler i bjælker og samlinger. Formatet er pr. definition konvekst, da det er defineret som en sum af kvadratrodsled af kvadratiske former, som individuelt repræsenterer ellipsoider. Formatet vil for de fleste flydeflader af interesse være homogent, hvilket resulterer i forbedrede algoritmiske egenskaber. Det vises hvordan det med formatet er muligt lokalt at reducere krumningen af flydefladen og samtidig beholde et enkeltligningsformat.

Den tredje del beskriver hvordan et rammeelement kan inkludere de fire vigtigste effekter ifm. analyse af tubulære konstruktioner med cyklisk plasticitet: en elastisk bjælke med initielle imperfektioner, elastisk lokal samlingsfleksibilitet og plastiske mekanismer i bjælkeenderne og samlingerne. Rammeelementet er baseret på et ligevægtsformat, der opdeler elementflytnignerne i et sæt deformationer og et sæt fastlegemebevægelser. Deformationerne og dermed fleksibiliteterne er additive. Elementet har en eksplicit stivhedsmatrix, som kun kræver invertering af en matrix med en maksimal størrelse på 4×4. Et element i standardformat inkluderende fastlegemebevægelser opnås ved brug af ligevægtsbetingelser.

I den fjerde del udvikles en robust returalgoritme. Returalgoritmen er baseret på tilfredsstillelse af de generaliserede tøjningsudviklingsligninger i den endelige tilstand. Desuden kræves det at den endelige spændingstilstand er lokaliseret på flydefladen. Robustheden er øget ved at lave en andenordens approksimation af inkrementet i den generaliserede spændingstilstand, hvilket leder til en to-skridts-returalgoritme. Først laves et mellemskridt hvor der hentes information og dernæst laves et fuldt skridt vha. informationen opnået i mellemskridtet.

Til sidst diskuteres effekterne af cyklisk plasticitet inklusiv effekterne af elasto-plastisk buling og plastisk deformation af komplekse konstruktioner. Den permanente ændring af geometrien reducerer karakteristiske stivheder og kapaciteter af konstruktionen. De tidligere udviklede modeller benyttes til at opdatere et anset computerprogram, en opdatering der gør programmet mere robust og øger dets evne til at repræsentere den reelle opførsel af rammekonstruktioner.

Publications

Journal papers

[P1] S. Krenk and L. Tidemann, A compact cyclic plasticity model with parameter evolution, *Mechanics of Materials*, **113**:57–68, 2017.

[P2] L. Tidemann and S. Krenk, Cyclic plastic hinges with degradation effects for frame structures, *Journal of Engineering Mechanics*, **143**(12):04017142-1–15, 2017.

[P3] L. Tidemann and S. Krenk, A robust frame element with cyclic plasticity and local joint effects, *Engineering Structures*, **168**:191–204, 2018.

Conference papers

[C1] L. Tidemann and S. Krenk, Beam element including local member and joint plasticity effects. Proceedings of the 27th (2017) International Ocean and Polar Engineering Conference, pp. 249–256, San Francisco, California, June 25–30, 2017.

[C2] L. Tidemann and S. Krenk, Robust return algorithm for anisotropic plasticity models. Proceedings of the 30th Nordic Seminar on Computational Mechanics, pp. 197–200, Kongens Lyngby, Denmark, October 25–27, 2017.

Additional contributions

[A1] L. Tidemann, Cyclic yielding of tubular structures, Abstract, DCAMM 15th Internal Symposium, Abstract and poster, March 16–18, Horsens, Denmark, 2015.

[A2] S. Krenk and L. Tidemann, A cyclic plasticity model with damage-induced stiffness and yield capacity reduction, Abstract, XIII International Conference on Computational Plasticity - COMPLAS XIII, September 1–3, Barcelona, Spain, 2015.

[A3] L. Tidemann and S. Krenk, Cyclic plastic hinges with degradation of stiffness and strength, Abstract, 13th US National Congress on Computational Mechanics, July 26–30, San Diego, California, 2015.

[A4] L. Tidemann, Beam element with cyclic plasticity effects, Abstract, DCAMM 16th Internal Symposium, March 13–15, Middelfart, Denmark, 2017.

Contents

1. Introduction

Cyclic plastic deformation is an important failure mechanism in severely loaded structures with variable loading history, e.g. pressure vessels, nuclear piping, steel frame structures subjected to earthquakes and offshore tubular structures in large waves. In problems involving monotonic plastic deformation the maximum load is typically the limiting factor, whereas for problems governed by cyclic plastic deformation it is the difference in maximum and minimum load that is the limiting factor. In the case of offshore tubular structures located in areas with gas production, subsidence is a common phenomenon. Subsidence in combination with large waves may lead to so-called wave-in-deck events, where a wave is sufficiently tall to hit the topside of the structure that has a substantially larger wave impact area than the foundation structure. Once the wave passes, the loading is much smaller than the maximum loading. A wave-in-deck event may thus satisfy the two criteria for cyclic plastic deformation: sufficiently large loading to introduce plasticity and a very large difference in maximum and minimum loading. A wave-in-deck event is illustrated in Fig. 1.1.

Figure 1.1. Wave-in-deck event at Ekofisk.[1]

An accurate model representing the structural behaviour in a realistic manner is paramount when analysing cyclic plastic deformation. This is illustrated in the conceptual sketch in Fig. 1.2.

[1]Source: http://www.moisund.com/Eldre%20Arkiv/Arkiv%202007/Ekofisk.htm

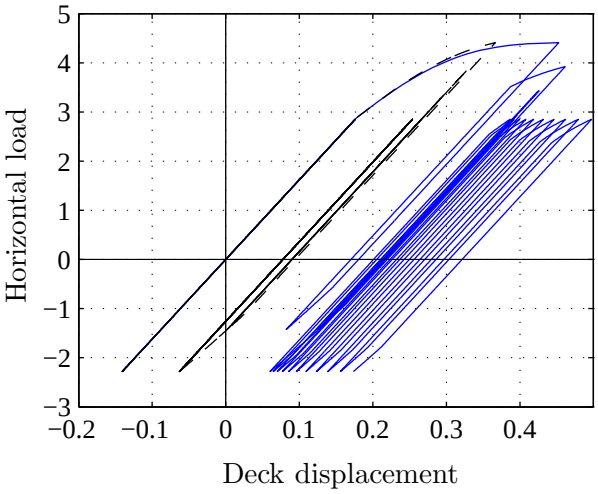

Figure 1.2. Conceptual sketch of prediction of cyclic plastic deformation.

Fig. 1.2 illustrates two simple models subjected to the same load history representing realistic ratios between maximum and minimum loading used in the design of offshore tubular structures. The loading history corresponds to three small waves followed by four large waves and subsequently eight small waves. The two models have the same elastic stiffness, yield capacity and ultimate capacity. The model represented by the solid blue line includes degradation of the yield capacity during plastic deformation, whereas the model represented by the dashed black line has constant capacity. Capacity degradation can originate from global phenomena such as elasto-plastic buckling that permanently changes the geometry of the structure, or from local phenomena as ovalisation or fracture in individual members or joints. The dashed black line indicates that some plastic deformation will be present after the passing of the large waves. After the passing of the large waves the structure will exhibit purely elastic deformation, experiencing so-called elastic shakedown. The blue solid line indicates that the degradation of the yield capacity leads to continued plastic deformation after the passing of the large waves, so-called ratcheting. Fig. 1.2 illustrates the importance of realistic modelling: if elastic shakedown with the given loading is a design requirement, the design is acceptable if the dashed black line represents the actual behaviour and unacceptable if the solid blue line represents the actual behaviour.

To model the behaviour of a full structure it is important to understand the behaviour of the individual structural elements. While it may be easier to develop simple models on a material scale it is computationally inefficient to model full offshore frame structures using solid or shell elements. A representation using beam-column elements is potentially preferable, if the plastic mechanisms can be modelled accurately. An example of a plastic mechanism is illustrated in Fig. 1.3.

The cyclically deformed beam and the corresponding hysteresis curve shown in Fig. 1.3 illustrate the characteristics of cyclic plastic mechanisms in beams; the localized deformation in the form of a plastic hinge and a hysteresis curve characterized by an elastic stiffness, a yield limit and a gradual change of stiffness until an ultimate capacity is reached. In addition, Fig. 1.3 illustrates that ovalisation affects the hysteresis curve by gradually reducing the parameters mentioned. On a material scale the cyclic deformation response has similar characteristics. The yield criteria on a material scale are often simpler

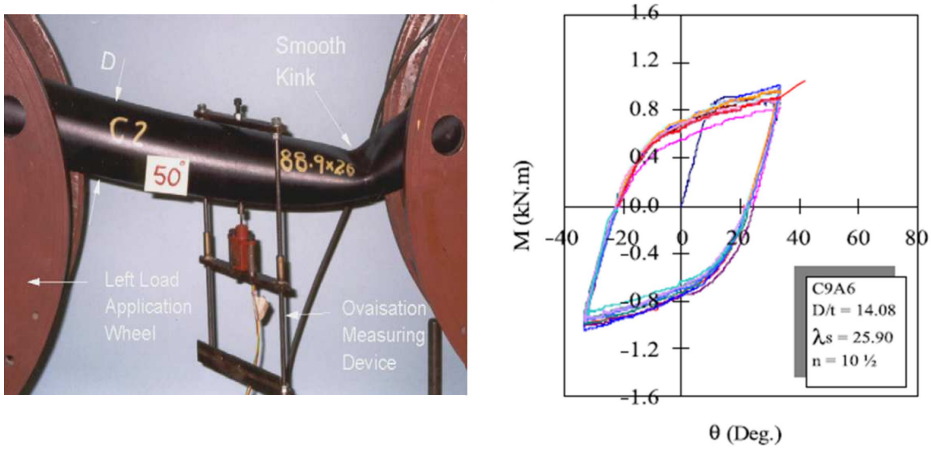

Figure 1.3. Ovalisation of tubular beam, [37].

than the yield criteria for plastic mechanisms in beams and it may be easier to develop a multi-axial cyclic plasticity model on a material scale and subsequently extend it to a generalized formulation usable in beam models. Aside from the cyclic plastic deformation in the members as illustrated in Fig. 1.3, local joint effects are also important phenomena. The effects include local joint flexibility and plastic mechanisms in the joints, illustrated in Fig. 1.4.

Analysing cyclic plasticity in tubular structures effectively requires a representative, accurate and robust formulation of the beam elements used and the ability to make large load/deformation increments. The beam elements must represent the four basic types of mechanisms relevant to the problem: elastic member deformation, plastic hinges at the member ends, joint elastic deformation and joint plastic deformation. As the latter three mechanisms are located at the beam ends they can all be implemented in a single element via an equilibrium formulation. In the case of a plastic hinge at the center of the member experienced in e.g. elasto-plastic buckling, the member is modelled using two elements, introducing the displacements and rotations of the center point as additional degrees of freedom. With an equilibrium formulation a global analysis is made and based on global displacements the local beam element deformations are found along with the corresponding element forces. The element forces are found in a separate return algorithm ensuring that the yield criteria for the different plastic mechanisms are not violated. The yield criteria for the different mechanisms may differ significantly and a generic formulation of a yield

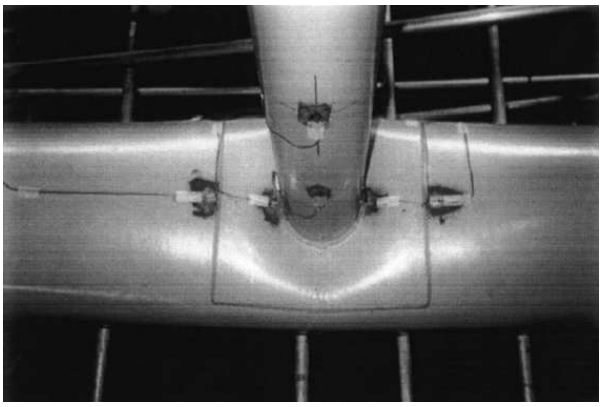

Figure 1.4. Local joint deformation, [44].

criterion is desirable. The use of large increments of deformation puts a strict demand on the robustness of the return algorithm and the different types of plastic mechanisms introduce a need for a very general formulation of the algorithm.

The objective of the present work is to develop a plasticity model with non-linear hardening to represent monotonic and cyclic plasticity accurately. The parameters of the model have a clear link to physical characteristics, enabling an intuitive understanding of the role of the model parameters. The plasticity model is sufficiently general to represent plastic hinges in beams, and a generic yield criterion is introduced to describe these. The plasticity model with a generic yield criterion lays the foundation for an updated formulation of the elasto-plastic frame element presented in [66], where local joint flexibility and plastic mechanisms in joints can be introduced as well. A robust return algorithm is developed to ensure analyses with plastic deformation are computationally efficient. The present thesis combines an introductory summary with three attached journal papers [P1]–[P3] and two conference papers [C1]–[C2]. The summary is organised in six chapters. First the developed plasticity model is presented. The format of the plasticity model is introduced on a material scale as developed in [P1] and generalizations to plastic hinge formulations of the types presented in [P2] and [P3] are discussed. The applicability of the plasticity model is illustrated by comparison with experiments on a material scale. The second chapter introduces the generic yield surface format developed in [P2] and further discussed in [P3]. The generic yield surface is based on the first-order homogeneous representation of ellipsoids guaranteeing convexity and the benefits of the homogeneous property is discussed in relation to plasticity theory. The third chapter summarizes how the plasticity model is included in a frame element as described in [P2] and how elastic and plastic joint effects can be included by utilizing an equilibrium format as described in [P3] and [C1]. The equilibrium format in combination with the local mechanisms ensures an additive flexibility format defining the elasto-plastic stiffness matrix explicitly. The frame element is used to model simple structures and results from [P2] and [C1] are discussed. The fourth chapter summarizes the steps of defining a return algorithm and identifying the algorithmic tangent stiffness as presented in [P2]. The robustness of the numerical procedure is increased by making a second-order approximation of the return step as proposed in [P3] and [C2]. The return algorithm is sufficiently general to be valid for multiple types of plasticity models and element formulations. The fifth chapter presents analyses of tubular offshore structures where comparisons with experimental data was presented in [P2] and effects of using the proposed models and algorithms are highlighted in [P3]. The summary is rounded off with concluding remarks summarising the contributions of the present work and potential further work.

2. Cyclic plasticity model

The basic characteristics of cyclic plastic deformation can be identified by a hysteresis curve of the type illustrated in Fig. 2.1 representing uni-axial cyclic deformation. From A to B the material is in the elastic domain. The elastic domain is limited by a yield surface with a given shape and size. The size of the yield surface is here represented by the uni-axial yield stress σ_y. Within the elastic domain, i.e. for stress states located inside the yield surface, there is an elastic flexibility, here represented by $1/E_\mathrm{e}$. Once the yield surface is reached elasto-plastic deformation takes place from B to C. The elasto-plastic domain is characterised by additional flexibility in comparison with the elastic domain, here represented by $1/H$ in terms of a hardening parameter H. The plastic flexibility increases gradually from $1/H_B$ at B and asymptotically approaches an infinite value at C' corresponding to ideal plasticity. Approaching the state of ideal plasticity corresponds to approaching the maximum stress state, here represented by the ultimate capacity $\sigma_y+\sigma_m$. When the load is reversed the material will deform elastically from C to D and it appears that the reversed loading branch is stretched by a factor of two, i.e. twice the elastic deformation is necessary to once again reach a state of elasto-plastic deformation at D. Here the additional flexibility $1/H_D$ is typically about half the additional flexibility $1/H_B$ at the point of first yield B.

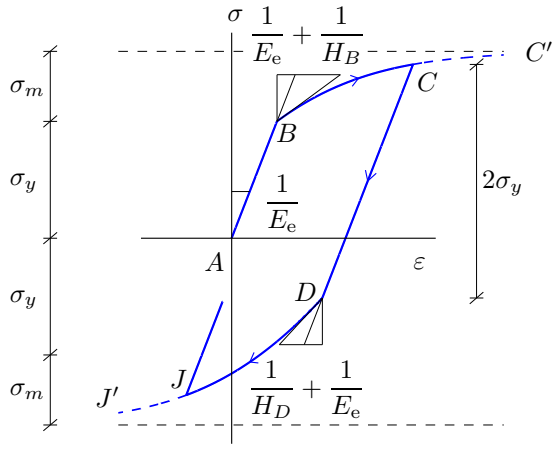

Figure 2.1. Characteristics of uni-axial cyclic plastic deformation.

The apparent stretch of the elastic domain by a factor of two suggests the use of a representation in terms of kinematic hardening, controlling the movement of the yield surface. The kinematic hardening model must represent three basic things: the movement of the yield surface, the shape and size of the yield surface and possible change of characteristics, e.g. evolution of the characteristic stress σ_m as a result of cyclic hardening/softening. The

movement of the yield surface and inclusion of parameter evolution is addressed in the present chapter and [P1], and the modelling of the yield surface is addressed in Chapter 3, [P2] and [P3].

2.1 Plasticity model with parameter evolution

Different approaches have been used to model the characteristics of elasto-plastic deformation including use of kinematic hardening [88, 110], nested yield surfaces [76] and two-surface models [27, 28, 67]. Common to these models is that they are defined with use of external variables that are observable and internal variables that are not observable. The external variables will typically be the generalized elastic strains $\boldsymbol{\gamma}_\mathrm{e}$ being the traditional strain measures $\boldsymbol{\gamma}_\mathrm{e} = [\varepsilon_{11}, \varepsilon_{22}, ...]^T_\mathrm{e}$ on a material scale and the generalized strains and curvatures $\boldsymbol{\gamma}_\mathrm{e} = [\varepsilon, \kappa, ...]^T_\mathrm{e}$ for beams. While the generalized strains $\boldsymbol{\gamma}_\mathrm{e}$ are observable, different sets of strain-like non-observable internal variables can be introduced. The constitutive relations are defined via a specific energy and it may be desirable to decouple some of the internal variables from the external variables as discussed in [62]. The internal variables $\boldsymbol{\gamma}_\mathrm{i}$ are basic model parameters not directly coupled to the observable generalized strains $\boldsymbol{\gamma}_\mathrm{e}$. The internal variables $\boldsymbol{\gamma}_\mathrm{d}$ may be directly coupled to the observable generalized strains $\boldsymbol{\gamma}_\mathrm{e}$ to represent evolution of the model parameters caused by e.g. cyclic hardening/softening, damage etc. A specific energy that allows for such partial coupling is

$$\varphi(\boldsymbol{\gamma}_\mathrm{e}, \boldsymbol{\gamma}_\mathrm{i}, \boldsymbol{\gamma}_\mathrm{d}) \;=\; \varphi_\mathrm{e}(\boldsymbol{\gamma}_\mathrm{e}, \boldsymbol{\gamma}_\mathrm{d}) + \varphi_\mathrm{i}(\boldsymbol{\gamma}_\mathrm{i}, \boldsymbol{\gamma}_\mathrm{d}) + \varphi_\mathrm{d}(\boldsymbol{\gamma}_\mathrm{d})\,. \tag{2.1}$$

To account for e.g. non-linear elasticity or different types of parameter evolution the individual energy terms may have different formulations as discussed in [P1]–[P3]. The constitutive relations are defined by partial derivatives ensuring that the external generalized stresses $\boldsymbol{\tau}_\mathrm{e}$ and the internal stress-like variables $\boldsymbol{\tau}_\mathrm{i}$ and $\boldsymbol{\tau}_\mathrm{d}$ are energy conjugate to the external generalized strains $\boldsymbol{\gamma}_\mathrm{e}$ and the internal strain-like variables $\boldsymbol{\gamma}_\mathrm{i}$ and $\boldsymbol{\gamma}_\mathrm{d}$. The energy conjugate generalized variables take the generic form

$$\boldsymbol{\tau}_\mathrm{e} = \partial_{\boldsymbol{\gamma}_\mathrm{e}}\varphi = \partial_{\boldsymbol{\gamma}_\mathrm{e}}\varphi_\mathrm{e} \tag{2.2}$$

$$\boldsymbol{\tau}_\mathrm{i} \;= \partial_{\boldsymbol{\gamma}_\mathrm{i}}\varphi \;= \partial_{\boldsymbol{\gamma}_\mathrm{i}}\varphi_\mathrm{i} \tag{2.3}$$

$$\boldsymbol{\tau}_\mathrm{d} = \partial_{\boldsymbol{\gamma}_\mathrm{d}}\varphi = \partial_{\boldsymbol{\gamma}_\mathrm{d}}\varphi_\mathrm{e} + \partial_{\boldsymbol{\gamma}_\mathrm{d}}\varphi_\mathrm{i} + \partial_{\boldsymbol{\gamma}_\mathrm{d}}\varphi_\mathrm{d}\,, \tag{2.4}$$

where by convention the partial derivatives $\partial_{\boldsymbol{\gamma}}\varphi$ are in column format. $\boldsymbol{\tau}_\mathrm{e}$ are the observable generalized stresses, i.e. $\boldsymbol{\tau}_\mathrm{e} = [\sigma_{11}, \sigma_{22}, ...]^T$ on a material scale and $\boldsymbol{\tau}_\mathrm{e} = [N, M, ...]^T$ for beams. The internal stress-like variables $\boldsymbol{\tau}_\mathrm{i}$ and $\boldsymbol{\tau}_\mathrm{d}$ can be used to represent various mechanisms. In the present model $\boldsymbol{\tau}_\mathrm{i}$ is used to model kinematic hardening and $\boldsymbol{\tau}_\mathrm{d}$ is used to model parameter evolution. Evolution of the elastic stiffness can be modelled by $\boldsymbol{\gamma}_\mathrm{d}$ via the definition of φ_e, see [P1] and [P3] for a detailed discussion.

The incremental relations needed in a non-linear analysis are found by partial differentiation corresponding to use of 'the chain rule', giving

$$\dot{\tilde{\boldsymbol{\tau}}} \;=\; \begin{bmatrix} \dot{\boldsymbol{\tau}}_\mathrm{e} \\ \dot{\boldsymbol{\tau}}_\mathrm{i} \\ \dot{\boldsymbol{\tau}}_\mathrm{d} \end{bmatrix} \;=\; \begin{bmatrix} \partial^T_{\boldsymbol{\gamma}_\mathrm{e}}\boldsymbol{\tau}_\mathrm{e} & \mathbf{0} & \partial^T_{\boldsymbol{\gamma}_\mathrm{d}}\boldsymbol{\tau}_\mathrm{e} \\ \mathbf{0} & \partial^T_{\boldsymbol{\gamma}_\mathrm{i}}\boldsymbol{\tau}_\mathrm{i} & \partial^T_{\boldsymbol{\gamma}_\mathrm{d}}\boldsymbol{\tau}_\mathrm{i} \\ \left(\partial^T_{\boldsymbol{\gamma}_\mathrm{d}}\boldsymbol{\tau}_\mathrm{e}\right)^T & \left(\partial^T_{\boldsymbol{\gamma}_\mathrm{d}}\boldsymbol{\tau}_\mathrm{i}\right)^T & \partial^T_{\boldsymbol{\gamma}_\mathrm{d}}\boldsymbol{\tau}_\mathrm{d} \end{bmatrix} \begin{bmatrix} \dot{\boldsymbol{\gamma}}_\mathrm{e} \\ \dot{\boldsymbol{\gamma}}_\mathrm{i} \\ \dot{\boldsymbol{\gamma}}_\mathrm{d} \end{bmatrix} \;=\; \mathbf{K}_\mathrm{eid}\dot{\tilde{\boldsymbol{\gamma}}}\,, \tag{2.5}$$

where the notation $\tilde{\boldsymbol{\tau}}$ and $\tilde{\boldsymbol{\gamma}}$ is introduced for compactness. The tangent stiffness matrix $\mathbf{K}_{\mathrm{eid}}$ has three column blocks as illustrated in (2.5), where the first column block denoted $\mathbf{K}_{\mathrm{ec}}$ couples an increment of the elastic generalized strains $\dot{\boldsymbol{\gamma}}_{\mathrm{e}}$ with an increment of all the energy conjugate variables $\dot{\tilde{\boldsymbol{\tau}}}$. Similar relations hold for the two other column blocks denoted $\mathbf{K}_{\mathrm{ic}}$ and $\mathbf{K}_{\mathrm{dc}}$ and the increments $\dot{\boldsymbol{\gamma}}_{\mathrm{i}}$ and $\dot{\boldsymbol{\gamma}}_{\mathrm{d}}$ respectively. The tangent stiffness matrix $\mathbf{K}_{\mathrm{eid}}$ contains the double derivatives of the energy, and as φ_{e} and φ_{i} may both depend on $\boldsymbol{\gamma}_{\mathrm{d}}$ the stiffness may change during loading via proper definition of the two energy terms. The above format thereby includes traditional damage theory [69] in the elasto-plastic constitutive model.

In case of elasto-plastic deformation as illustrated in Fig. 2.1 the observable generalized strains $\boldsymbol{\gamma}_{\mathrm{e}}$ are identified via the observable generalized stresses $\boldsymbol{\tau}_{\mathrm{e}}$ by e.g. the inverse of the constitutive relation (2.2) because parts of the total observable generalized strains are plastic. In contrast the total generalized strains can be observed directly making it desirable to formulate a plasticity model in terms of the total observable generalized strains $\boldsymbol{\gamma}_{\mathrm{t}}$ rather than the elastic part of the observable generalized strains $\boldsymbol{\gamma}_{\mathrm{e}}$. In small deformation theory the strains are additive and it is assumed that the total observable generalized strains $\boldsymbol{\gamma}_{\mathrm{t}}$ are the sum of the elastic observable generalized strains $\boldsymbol{\gamma}_{\mathrm{e}}$ and the plastic observable generalized strains $\boldsymbol{\gamma}_{\mathrm{p}}$

$$\boldsymbol{\gamma}_{\mathrm{t}} \;=\; \boldsymbol{\gamma}_{\mathrm{e}} + \boldsymbol{\gamma}_{\mathrm{p}}\,. \tag{2.6}$$

An extension of the additive format to finite strains is possible by the so-called operator split as discussed by [77, 92, 91, 107], and similar formats may be used in the case of generalized strains. The plastic generalized strains $\boldsymbol{\gamma}_{\mathrm{p}}$ and the strain-like internal variables $\boldsymbol{\gamma}_{\mathrm{i}}$ and $\boldsymbol{\gamma}_{\mathrm{d}}$ must have separate evolution equations. In previous works [3, 18, 15] the strain evolution equations are postulated directly whereas in the present format the evolution equations are obtained by use of a plastic flow potential G. The evolution equations are obtained by maximizing the dissipation rate as described in detail in [P1]. The resulting evolution equations are

$$\begin{bmatrix}\dot{\boldsymbol{\gamma}}_{\mathrm{e}}\\ \dot{\boldsymbol{\gamma}}_{\mathrm{i}}\\ \dot{\boldsymbol{\gamma}}_{\mathrm{d}}\end{bmatrix} \;=\; \begin{bmatrix}\dot{\boldsymbol{\gamma}}_{\mathrm{t}}\\ \mathbf{0}\\ \mathbf{0}\end{bmatrix} - \begin{bmatrix}\partial_{\boldsymbol{\tau}_{\mathrm{e}}} G\\ \partial_{\boldsymbol{\tau}_{\mathrm{i}}} G\\ \partial_{\boldsymbol{\tau}_{\mathrm{d}}} G\end{bmatrix} \dot{\lambda} \;=\; \begin{bmatrix}\dot{\boldsymbol{\gamma}}_{\mathrm{t}}\\ \mathbf{0}\\ \mathbf{0}\end{bmatrix} - \partial_{\tilde{\boldsymbol{\tau}}} G\, \dot{\lambda}\,, \quad \dot{\lambda} \geq 0\,, \tag{2.7}$$

where $\dot{\lambda}$ is the so-called plastic multiplier that originates from the maximization of the dissipation rate. It is noted that the increment in the observable elastic generalized strains $\dot{\boldsymbol{\gamma}}_{\mathrm{e}}$ depends on both the increment in total observable strains $\dot{\boldsymbol{\gamma}}_{\mathrm{t}}$ and the gradient of the plastic flow potential $\partial_{\boldsymbol{\tau}_{\mathrm{e}}} G$. The increments in the internal strain-like variables $\dot{\boldsymbol{\gamma}}_{\mathrm{i}}$ and $\dot{\boldsymbol{\gamma}}_{\mathrm{d}}$ depend solely on the gradient of the flow potential via $\partial_{\boldsymbol{\tau}_{\mathrm{i}}} G$ and $\partial_{\boldsymbol{\tau}_{\mathrm{d}}} G$, respectively, highlighting that they are internal non-observable variables. The direction of the increment of the plastic generalized strains $\dot{\boldsymbol{\gamma}}_{\mathrm{p}}$ is controlled by the gradient of the plastic flow potential $\partial_{\boldsymbol{\tau}_{\mathrm{e}}} G$ and the magnitude is controlled by the plastic multiplier $\dot{\lambda}$.

The plastic multiplier is found by ensuring that the stress state is located on the yield surface during elasto-plastic loading. The yield surface is defined as an isosurface of a yield function F and thus it must have a constant value during elasto-plastic loading, leading to a plastic multiplier

$$\dot{\lambda} \;=\; \frac{(\partial_{\tilde{\boldsymbol{\tau}}} F)^T\, \mathbf{K}_{\mathrm{ec}}}{(\partial_{\tilde{\boldsymbol{\tau}}} F)^T\, \mathbf{K}_{\mathrm{eid}}\, (\partial_{\tilde{\boldsymbol{\tau}}} G)}\, \dot{\boldsymbol{\gamma}}_{\mathrm{t}}\,. \tag{2.8}$$

Here $\mathbf{K}_{\text{ec}}$ is the first block column of $\mathbf{K}_{\text{eid}}$ defined in (2.5). Combining the incremental constitutive equations (2.5) with the generalized strain evolution equation (2.7) and the definition of the plastic multiplier (2.8) gives the incremental elasto-plastic constitutive relation

$$\dot{\tilde{\boldsymbol{\tau}}} \;=\; \Big(\mathbf{K}_{\text{ec}} - \frac{\mathbf{K}_{\text{eid}}\,(\partial_{\tilde{\boldsymbol{\tau}}} G)\,(\partial_{\tilde{\boldsymbol{\tau}}} F)^T\,\mathbf{K}_{\text{ec}}}{(\partial_{\tilde{\boldsymbol{\tau}}} F)^T\,\mathbf{K}_{\text{eid}}\,(\partial_{\tilde{\boldsymbol{\tau}}} G)}\Big)\,\dot{\boldsymbol{\gamma}}_{\text{t}} \;=\; \mathbf{K}^{\text{ep}}_{\text{eid}}\dot{\boldsymbol{\gamma}}_{\text{t}}\,. \tag{2.9}$$

It is noted that the second term is symmetric only when $\varphi_{\text{e}} = \varphi_{\text{e}}(\boldsymbol{\gamma}_{\text{e}})$ is independent of the internal variables, see [P3] and [62] for discussions on coupling between internal and external variables. With the above format a plasticity model with possible non-linear kinematic hardening and parameter evolution is defined by the three potential functions φ, F and G. The specific energy φ defines the constitutive relations in the elastic domain, while the yield function F defines the shape and size of the elastic domain, and the plastic flow potential G defines the generalized strain evolution during elasto-plastic loading.

2.2 Non-linear kinematic hardening

There are various ways of defining the two plastic potentials that characterize the model, namely the yield function F and the plastic flow potential G, to represent non-linear kinematic hardening. On a material scale a kinematic hardening yield function F is

$$F(\tilde{\boldsymbol{\tau}}) \;=\; \|\boldsymbol{\tau}_{\text{e}} - \boldsymbol{\tau}_{\text{i}}\| - \sigma_y\,, \tag{2.10}$$

where $\|\,\|$ is a suitable first-order norm and $F = 0$ defines the yield surface. In the case of steel the norm may be the von Mises first-order homogeneous norm. The von Mises norm was used in [P1] to define the format of the kinematic hardening model and in the following chapter a generic yield function is presented, enabling use of the plasticity model for plastic hinges. The format of the plastic flow potential G has been addressed by several authors [3, 18, 15, 78] and is the key to a representative cyclic plasticity model, as it defines the plastic strain evolution via its gradient according to (2.7).

For von Mises materials Armstrong and Frederick [3] proposed a plastic flow potential where the definition of the gradient $\partial_{\boldsymbol{\tau}_{\text{i}}} G$ led to a gradual decrease in the increment of the internal stress-like variables $\dot{\boldsymbol{\tau}}_{\text{i}}$, ultimately limiting the magnitude of the kinematic hardening. The limit on the kinematic hardening in combination with the yield surface poses a natural bound on the observable generalized stresses $\boldsymbol{\tau}_{\text{e}}$ identifying the ultimate capacity. Chaboche [17] showed that a non-linear modification of the representation of the gradient $\partial_{\boldsymbol{\tau}_{\text{i}}} G$ improved the ability to reproduce the gradual reduction of stiffness. Several authors [18, 16, 78, 24] have proposed different ways of representing the center of the yield surface by a sum of internal stress-like variables $\boldsymbol{\tau}_{\text{i}}$ where the evolution of each term in the sum is similar to the evolution equation proposed by Armstrong and Frederick [3]. The specific form of the format of the gradient $\partial_{\boldsymbol{\tau}_{\text{i}}} G$ was investigated in the case of negligible parameter evolution in [P1] in an effort to reduce the number of model parameters, leading to the uni-axial definition

$$\partial_{\tau_{\text{i}}} G \;=\; -\text{sign}(\tau_{\text{e}} - \tau_{\text{i}}) + \frac{\tau_{\text{i}}}{(1-\alpha)\sigma_m + \alpha|\tau_{\text{i}}|}\,, \quad \alpha < 1\,. \tag{2.11}$$

The first term originates from the uni-axial definition of the yield function where the norm $\|\,\|$ simply becomes the absolute function $|\,|$. The yield function is introduced in

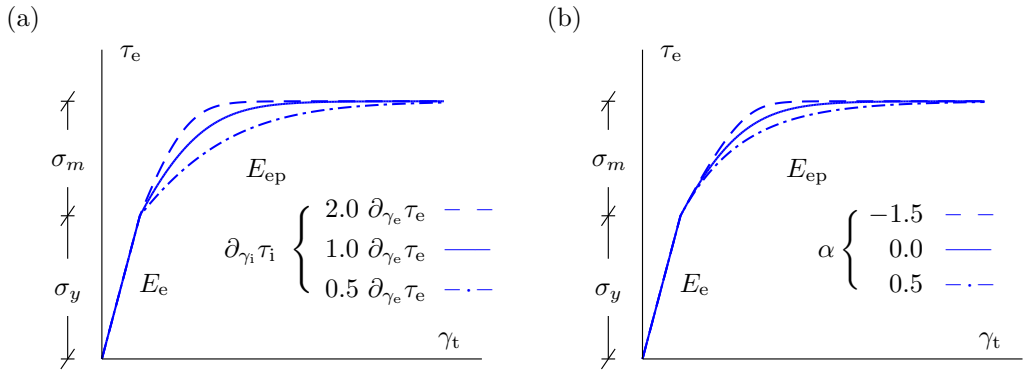

Figure 2.2. Influence of parameters on stress-strain relation: (a) relative internal stiffness $\partial_{\gamma_i}\tau_i = (-)\partial_{\gamma_e}\tau_e$, (b) modification of flow potential G via the shape parameter α.

the plastic flow potential to have an associated formulation for the generalized plastic strain i.e. $\partial_{\boldsymbol{\tau}_e} G = \partial_{\boldsymbol{\tau}_e} F$. It is seen that when $\tau_e - \tau_i = \sigma_y$ the gradient $\partial_{\tau_i} G$ is equal to zero when $\tau_i = \sigma_m$ and according to the strain evolution equation (2.7) the kinematic hardening stops at this state. Note that at this state $\partial_{\tau_e} G \neq 0$ and the plastic strain γ_p will increase continuously. The parameter α is a weighting parameter between ideal-plasticity represented by $\alpha \simeq 1$ and bi-linear hardening represented when $\alpha \ll 0$ and the original Armstrong-Frederick model [3] is recovered when $\alpha = 0$. Typical values of α are in the range of $0.7 - 0.95$ for metals, representing a substantial difference from the Armstrong-Frederick model [P1]. The form of the gradient (2.11) leads to the possibility of modification of the gradual reduction of the stiffness without affecting the ultimate capacity defined by $\sigma_y + \sigma_m$. Fig. 2.2 illustrates the effects of the basic model parameters.

Fig. 2.2 shows that the magnitude of the internal stiffness $\partial_{\gamma_i}\tau_i$ relative to the observable external stiffness $\partial_{\gamma_e}\tau_e$, here represented by E_e, controls the size of the kink once the yield criterion is met. The parameter σ_m represents the capacity in addition to the yield capacity, and in principle the kink and σ_m control the curve between initial yield and ultimate capacity along which the observable elasto-plastic stiffness E_{ep} gradually changes. The ability to control the shape between initial yield and the ultimate capacity is introduced via the parameter α and controlling the shape via a single parameter ultimately reduces the total number of parameters needed to model cyclic plasticity. Furthermore, each model parameter represents a key characteristic of the response by the introduction of the parameter α.

Based on the gradient defined in (2.11) the corresponding plastic flow potential can be found by integration and including parameter evolution it takes the form

$$G(\tilde{\boldsymbol{\tau}}) = F(\tilde{\boldsymbol{\tau}}) + \frac{\sigma_m}{\alpha}\left\{\frac{|\tau_i| - \sigma_m}{\sigma_m} - \frac{1-\alpha}{\alpha}\ln\left[1 + \alpha\left(\frac{|\tau_i| - \sigma_m}{\sigma_m}\right)\right]\right\} + G_d(\boldsymbol{\tau}_d)\,, \qquad (2.12)$$

for uni-axial stress states. When parameter evolution is included the model parameters $\sigma_y = \sigma_y(\boldsymbol{\tau}_d)$, $\sigma_m = \sigma_m(\boldsymbol{\tau}_d)$ and $\alpha = \alpha(\boldsymbol{\tau}_d)$ depend on the stress-like internal variables $\boldsymbol{\tau}_d$. The ultimate capacity is reached when $|\tau_i| = \sigma_m$ and τ_i has the same sign as the relative stress $\tau_e - \tau_i$, and for this value it is noted that $G = 0$ when parameter evolution is neglected. Thereby the formulation of the plastic flow potential (2.12) becomes the plastic equivalent of the yield function F. When the yield function (2.10) equals zero, the elastic capacity is fully utilized and when the plastic flow potential is equal to zero, the ultimate

(plastic) capacity is fully utilized. The plastic flow potential (2.12) can be extended to a multi-axial format and for a von Mises material the absolute value $|\,|$ is simply replaced by the von Mises norm $\|\,\|$ as described in [P1], and $\|\boldsymbol{\tau}_{\mathrm{i}}\| = \sigma_m$ effectively defines a limiting surface for the internal stress-like variables $\boldsymbol{\tau}_{\mathrm{i}}$. For anisotropic materials and plastic hinges in beams there may be different capacities for different generalized stress components and the shape of the hysteresis curves may differ for different uni-axial loadings. This implies that σ_y, σ_m and α may not be representative for all the generalized stress components and a normalized format must be made. In [P2] a normalized format was proposed where each of the internal stress-like variables $\boldsymbol{\tau}_{\mathrm{i}}$ entered the plastic flow potential via a term similar to the one presented in (2.12) creating a sum of such terms. In [P3] the flow potential has the same format as (2.12). The absolute value sign $|\,|$ is replaced by a representative norm $\|\,\|$, and the generalized stresses $\boldsymbol{\tau}_{\mathrm{e}}$ and stress-like internal variables $\boldsymbol{\tau}_{\mathrm{i}}$ appear in normalized form. Representative values of σ_m and α are introduced via a weighting of the values relating to each generalized stress component by use of the norm $\|\,\|$.

2.3 Examples

The potential ability of a model to represent cyclic plasticity can be illustrated with use of simple experiments. Calibration procedures based on direct interpretation of the parameters from the characteristics of the response illustrated in Figs. 2.1 and 2.2 has been developed in [P1] and typical intervals for the model parameters have been estimated. For a more general discussion of material characterisation and general parameter estimation including determination of parameter evolution see e.g. [83]. On a material scale the cyclic plasticity model developed in [P1] has been shown to represent simple experiments accurately without introducing parameter evolution. The model compares well with multiple other common models developed for steels, alloys, viscoplasticity and hot working tool steels [86, 49, 59, 102]. For many materials the first loading branch is less rounded in comparison to the subsequent loading branches. That effect may be modelled by introduction of parameter evolution. Parameter evolution may also effectively be used for representing cyclic hardening or softening materials as illustrated in Fig. 2.3.

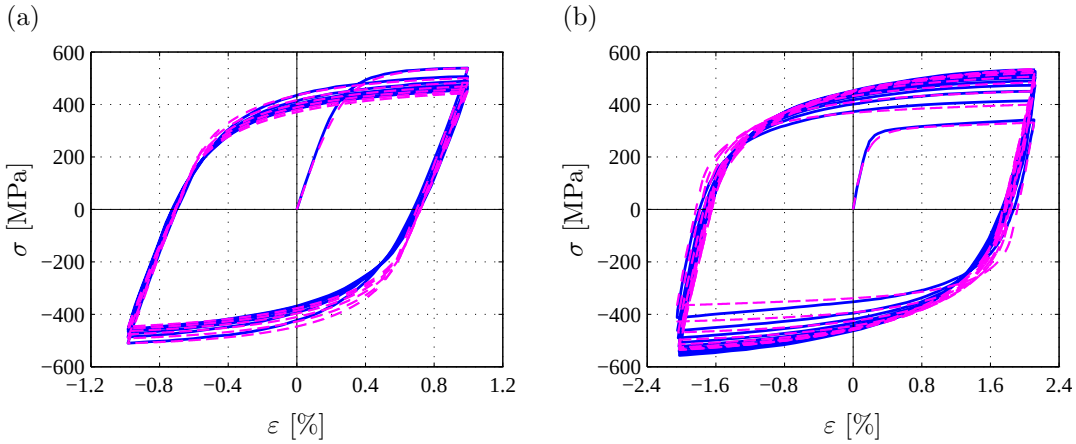

Figure 2.3. (a) Cyclic softening. (b) Cyclic hardening. Experiment, [50] (—). Present model (– –). From [P1].

The parameter evolution format introduced to model the experimental results shown in Fig. 2.3 is of an exponential type similar to the format proposed by [24] for evolution of

Table 2.1. Biaxial ratcheting: Experiment characteristics.

Marker	σ_{11} [MPa]	$\Delta(2\varepsilon_{12})/\sqrt{3}$ [%]	$\Lambda \cdot 10^3$
$\triangledown$	100	0.8	8.84
$\times$	50	1.0	1.37
$\circ$	50	0.8	2.24
$\bullet$	50	0.6	4.10

the yield stress. The exponential format goes asymptotically towards a prescribed relative level for each model parameter. It is observed in Fig. 2.3 that in both the cyclic hardening and softening case the roundedness of the first loading branch of the hysteresis curve differs from the remaining branches. This is accounted for mainly by use of evolution of the shape parameter α, see [P1] for details of the model parameters used. In addition to the evolution of the shape parameter evolution of the elastic stiffness, the internal stiffness, the yield capacity and the capacity in addition to yield was introduced to account for the relevant changes in the response during loading.

For multi-axial loading the cyclic hardening/softening is influenced by non-proportionality of the strain path [13, 97], and for strain-controlled cycling the ratio of one strain component amplitude to another is a dominant factor as well. The phenomenon has been discussed in detail in [6] for bi-axial strain cycling and solutions with memory surfaces were introduced as a possible solution [56]. In bi-axial elasto-plastic loading with one stress component constant and the other cycled either via strain or stress cycling, the strain component conjugate to the constant stress component may gradually increase as a result of the plasticity, so-called ratcheting. For uni-axial loadings ratcheting is experienced as an increase in the mean strain, e.g. when the stress is cycled between constant minimum and maximum levels as illustrated in Fig. 1.2. In [P1] bi-axial ratcheting experiments presented by Ohno and Wang [79] were used to illustrate the capabilities of the developed model. The material was initially brought to a state of constant tension stress σ_{11} with an initial axial strain ε_{11} and subsequently the material was subjected to cyclic shear strain $2\varepsilon_{12}$ varied between states of $\pm\Delta(2\varepsilon_{12})/2$. The cycling resulted in axial strain ratcheting, i.e. gradual increase of the axial strain despite constant axial stress.

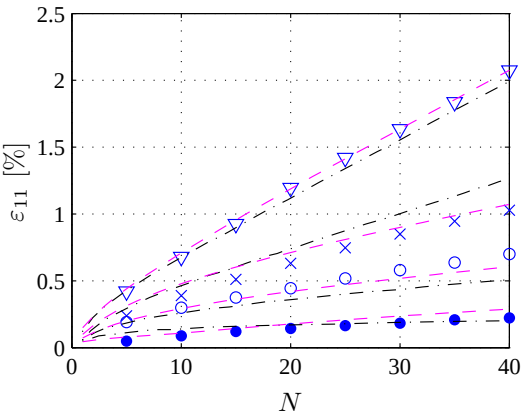

Figure 2.4. Biaxial cycling. Experiment, [96] ($\triangledown$,$\times$,$\circ$,$\bullet$). Model, [79] ($- \cdot -$). Present model ($- -$). From [P1].

The plasticity model was calibrated using an interpolation scheme proposed by Benallal and Marquis [6]. The scheme makes use of the parameter Λ representing the degree of proportionality between the incremental plastic strain and the incremental deviatoric stress. The parameter Λ is thereby a measure of the non-proportionality of the strain path, and Λ is used for interpolation of the model parameters between two experimentally established parameter sets. In theory Λ may take any value between zero and one but for the present experiment a very small interval is sufficient to cover all the tested combinations of axial stress σ_{11} and cycled shear strain $\Delta(2\varepsilon_{12})$. The details of the calibration procedure are found in [P1]. The four bi-axial ratcheting experiments are characterised in Table 2.1 and the results are illustrated in Fig. 2.4, showing a good agreement of the four experiments, of which only two are calibrated.

3. Generic yield surface format

The yield surface and its gradient are key ingredients in the cyclic plasticity model as illustrated in the previous chapter. The yield surface limiting the elastic domain is characterized by a shape and a size. Yield surfaces for materials and plastic hinges in beams may be determined by analytical considerations [98, 75, 22], numerical computations [73] or experimental results [80, 34]. Whether based on analytical considerations or numerical estimates the determined yield surface is an estimate of the actual yield surface. For plastic hinges in beams the underlying assumption when determining the yield surface is often an ideal-plastic behaviour of the material [22] that may not represent the experimental behaviour [80]. An approximate representation of a theoretical yield surface is often sufficient for yield hinges in beams. Yield surfaces may be anisotropic for both plastic hinges in beams [80, 22] and at the material level [5], and may have regions with undefined gradients [73]. A generic and flexible yield surface format capable of representing anisotropic yield surfaces is desirable, especially for plastic hinges in beams where multiple different beam types may be used in a single analysis. A simple elliptic format capable of representing anisotropic yield surfaces at the material level was proposed by Hill [52].

A piecewise linear yield surface can model most yield surfaces for both materials and plastic hinges in beams. However, it introduces multiple checks for violation of the yield criterion and special measures have to be taken when defining the gradient at intersections between planes [65]. Single-equation yield criteria eliminate the need for multiple checks and will often have defined gradients everywhere. The format of a single-equation yield criterion may vary from combinations of polynomial and trigonometric functions [61] to mixed-order polynomials [80], strictly cubic polynomials [72], NURBS-formulations [26] and Fourier series [95]. Most of such formulations have defined gradients everywhere although they may be difficult to determine. Ensuring convexity of the yield surface can be cumbersome, either because of the order of the polynomial or the location of the control points for NURBS-formulations. The difficulty of ensuring convexity can be overcome by use of convex shapes. Bleyer and de Buhan [7, 8] proposed a yield surface format to be used in plastic limit analysis based on a Minkowski sum of the guaranteed convex shape of an ellipsoid. The actual formation of the Minkowski sum may be difficult but the format has proved convenient in relation to the optimization routines in plastic limit analysis. A generic yield surface format for plastic hinges in beams must be sufficiently flexible to model yield surfaces for different cross section types and it must ensure convexity. In addition the type of cyclic plasticity model developed in [P1] and discussed in the previous chapter is based on a first-order yield function. The formulation of a flexible generic yield surface format that is convex by definition is addressed in the present chapter and [P2], [P3] and [C1]. The benefits of having a homogeneous first-order formulation are described in the present chapter and detailed in [P2] and [C1].

3.1 Ellipsoidal concept

For metals first-order single-equation yield surfaces that exploit the convexity of ellipsoids include the von Mises and the Hill yield criteria [75, 52] where a single ellipsoid can represent the yield surface. Similarly the convexity of ellipsoids has been exploited to represent yield surfaces for concrete although not using a first-order formulation [105, 43]. For plastic hinges in beams representation of the yield surface using a single ellipsoid was investigated by [94]. The overall shape of analytically or numerically determined yield surfaces is not well-represented by a single ellipsoid [94], but the possible first-order formulation is desirable. An ellipsoid can be defined in a first-order format via the equation

$$\sqrt{\mathbf{x}'^T \mathbf{A} \mathbf{x}'} = 1\,, \tag{3.1}$$

where $\mathbf{x}'$ is the local coordinate system that may be translated and rotated relative to the global coordinate system $\mathbf{x}$ and $\mathbf{A}$ is a symmetric, positive definite matrix. In relation to yield surfaces the coordinates $\mathbf{x}$ correspond to stress components. The left-hand side of (3.1) defines the relative sizes of the semi-axes and hence the shape of the ellipsoid via the ratios of the eigenvalues of $\mathbf{A}$ and the right-hand side defines the size of the ellipsoid. Inspired by Bleyer and de Buhan [7, 8] a type of sum of ellipsoids may be used to represent multiple types of yield surfaces sufficiently accurate. Instead of forming the Minkowski sum, the sum

$$\sqrt{\mathbf{x}_1'^T \mathbf{A}_1 \mathbf{x}_1'} + \sqrt{\mathbf{x}_2'^T \mathbf{A}_2 \mathbf{x}_2'} + \cdots = 1 \tag{3.2}$$

is formed, where $\mathbf{x}_1'$ and $\mathbf{x}_2'$ may have different locations and orientations relative to the global coordinate system. Each of the terms on the left hand size represents an ellipsoidal shape and the size of each ellipsoid is defined by assigning a proportion of the 1 on the right hand side to the corresponding term. If the sum consists of two terms, the proportion of the 1 assigned to the first term defines the remaining proportion of the 1 assigned to the second term. In the case of three terms, the proportions assigned to the first and second term defines the remaining proportion assigned to the third term and so on when more terms are applied. Once the proportions of the 1 have been assigned any intersection between the resulting ellipsoids will be a point on the surface that is defined by making all the possible combinations of proportion assignments. The resulting surface will not necessarily be an ellipsoid, but it is guaranteed to be convex because each of the ellipsoids are convex. The concept is illustrated in Fig. 3.1.

In Fig. 3.1(a) two ellipsoidal terms with coincident local coordinate systems have been used and they form a symmetric surface. In Fig. 3.1(b) the ellipsoids have different local coordinate systems resulting in a non-symmetric surface. The fact that both symmetric and non-symmetric surfaces can be modelled while the format is still first order with gradients defined everywhere suggests that it is a useful format for representation of yield surfaces.

When the ellipsoids have the same center, the form (3.2) will be homogeneous whereby larger surfaces, generated by replacing the 1 on the right hand side with a larger number, will simply be scaled versions of the original surface. This is a useful property in computational plasticity and it is often utilized in connection with return to von Mises yield surface [33]. As most yield surfaces for plastic mechanisms in tubular structures are symmetric, ellipsoids with coinciding centres are deemed sufficient to represent the yield surfaces of interest with the benefit that the yield surface becomes homogeneous of degree 1. The yield surface of anisotropic materials and plastic hinges in beams are often normalized

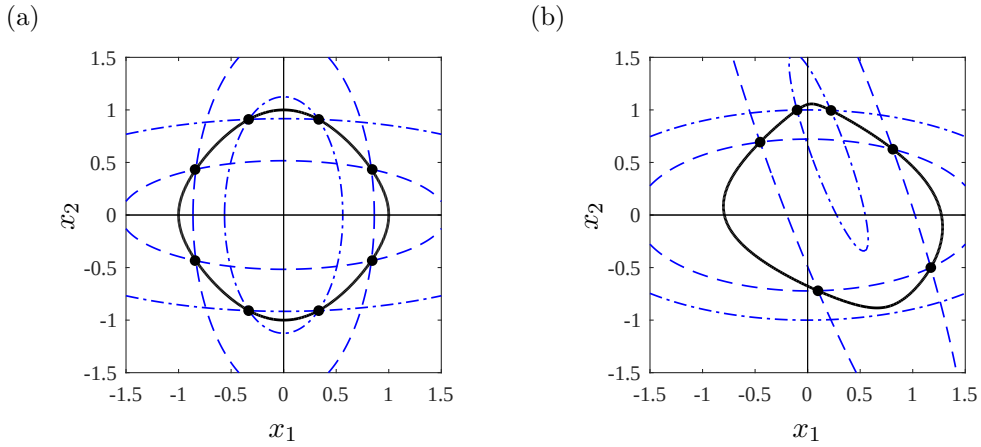

Figure 3.1. Intersections of finite ellipsoids, (– · –) and (– –), are points, (•), on the resulting surface, (—). From [P2].

[52, 5, 94, 7], and a generic normalized kinematic hardening yield surface can be defined by use of the norm

$$\|\bar{\boldsymbol{\tau}}_{\mathrm{e}} - \bar{\boldsymbol{\tau}}_{\mathrm{i}}\| = \sqrt{(\bar{\boldsymbol{\tau}}_{\mathrm{e}} - \bar{\boldsymbol{\tau}}_{\mathrm{i}})^T \mathbf{A}_1 (\bar{\boldsymbol{\tau}}_{\mathrm{e}} - \bar{\boldsymbol{\tau}}_{\mathrm{i}})} + \sqrt{(\bar{\boldsymbol{\tau}}_{\mathrm{e}} - \bar{\boldsymbol{\tau}}_{\mathrm{i}})^T \mathbf{A}_2 (\bar{\boldsymbol{\tau}}_{\mathrm{e}} - \bar{\boldsymbol{\tau}}_{\mathrm{i}})} + \cdots . \tag{3.3}$$

Here $\bar{\boldsymbol{\tau}}_{\mathrm{e}}$ are the normalized generalized stresses and $\bar{\boldsymbol{\tau}}_{\mathrm{i}}$ are the normalized stress-like internal variables. Both are normalized with the current uni-axial yield capacities of each stress component, and hence for a von Mises material all stress components may be normalized by σ_y. The von Mises yield criterion (2.10) is then a special case obtained by multiplication with σ_y.

3.2 Applications

The challenges of the yield surface with a norm in the format of (3.3) is to determine the coefficients in the matrices $\mathbf{A}_1$, $\mathbf{A}_2$, ..., and to decide how many terms are necessary to get a proper representation of the yield surface. For simple yield surfaces a direct process of determining the coefficients is described in detail in [P2]. The process is based on identifying a plane in which only two stress components are non-zero. In the given plane two characteristics of the shape of the yield surface are used to determine the coefficients of $\mathbf{A}_1$, $\mathbf{A}_2$, ..., and hence the shape of the individual ellipsoids. The first characteristic is the shape of the yield surface for stress states where none of the stress components are close to zero. The other characteristic is the shape of the yield surface for stress states where one of the stress components is close to zero. Different possibilities of using optimization methods to determine a representative norm are discussed in [P3]. For most plastic mechanisms related to tubular structures it is sufficient to make use of two terms, where both $\mathbf{A}_1$ and $\mathbf{A}_2$ are diagonal matrices. Fig. 3.2 illustrates how such a format can represent yield surfaces common in tubular structures accurately.

The representation of the yield surfaces in Fig. 3.2 are very accurate and it is practically impossible to distinguish the yield surface representation from the theoretical yield surface when observing the contour lines. While the representations are very accurate they have the downside of regions with very large curvature. In Fig. 3.2(a) the regions are concentrated in the areas with $m_y = m_z \simeq 0$ and $n = \pm 1$ and in Fig. 3.2(b) around the curve of the surface where $n \simeq 0$. However, with the present format the gradient is defined in these regions in contrast to the theoretical yield surfaces.

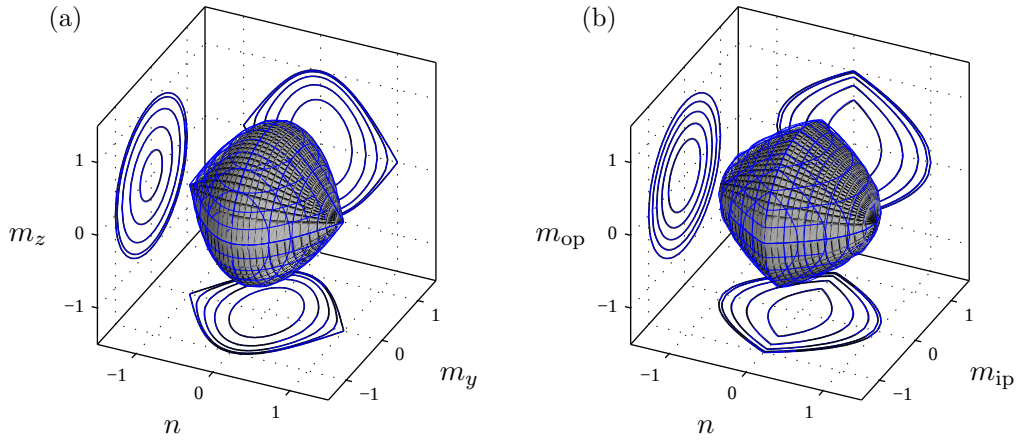

Figure 3.2. Theoretical yield surface for (a) tubular steel beam and (b) tubular joint (MSL surface) and representations, (—). Contour lines are plotted in various planes.

Because the yield surfaces for plastic mechanisms in frame elements typically are (best) estimates of the true yield surface, small local modifications of the shape of the yield surface can be made without compromising the accuracy of the model. Modifications to the theoretical yield surface have been made to increase the accuracy of models for anisotropic materials [11, 74]. The modification was made by a simple weighting of different yield surfaces, and an extension to local modifications using the present format is discussed in [P3]. Small local modifications may both increase the accuracy of the model as well as improve the algorithmic properties, e.g. by reduction of the curvature in certain regions. Reducing the curvature in certain regions generally decreases the sensitivity of the elasto-plastic stiffness with respect to the stress state creating a more robust model. Furthermore it eases return to the yield surface as discussed in [66], [P2] and [P3]. In return to the yield surface the gradients of outer surfaces are typically used [66, 33], and the first-order homogeneous property of the von Mises yield surface therefore eases the return. The yield surface format is first-order homogeneous as well and outer surfaces are always scaled versions of the original yield surface in contrast to outer surfaces for typical theoretical yield surfaces. The scalability is illustrated in Fig. 3.3. The yield surface representation in Fig. 3.3 has a small local rounding that hardly affects the overall shape of the yield surface. It is observed that the gradients of the outer surfaces are much more similar to the gradients of the yield surface for the present format in comparison with the theoretical format.

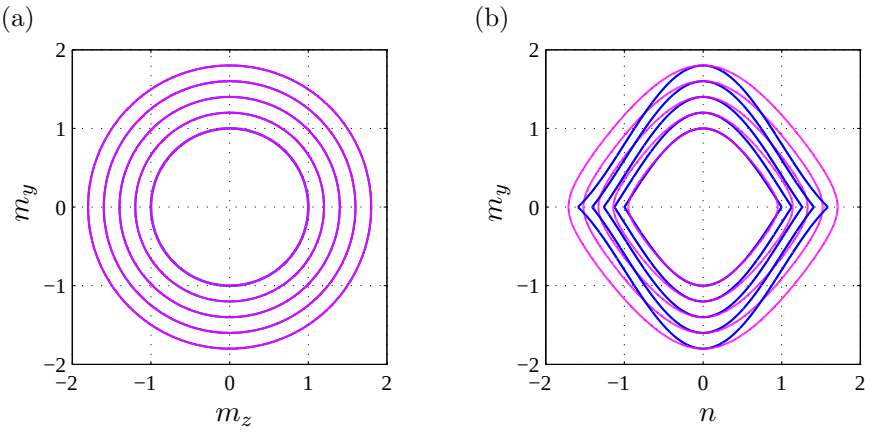

Figure 3.3. Outer surfaces for theoretical yield surface for a tubular steel beam, (—), and for a rounded representation, (—).

4. Frame element with cyclic plastic hinges and joint effects

For tubular frame structures it is important to be able to model plastic mechanisms in the members as well as in the local tubular joints [9]. The additional elastic local joint flexibility and the effect of the normal force in imperfect members must be modelled as well [23, 53, 29, 30]. The plastic mechanisms in the members can be modelled including spread of plasticity over the cross section and over the length of the beam using a so-called fibre model, where the cross sections of the beam are discretized by uni-axial fibres [58]. Alternatively the plastic mechanisms can be modelled as local effects located at the ends of the member in the form of plastic hinges [66]. It has been found that the predicted angle between the plastic strain components are similar for the two analysis types [36] and the plastic hinge approach demands less computations [1]. The plastic mechanisms in both members [39] and local joints [81] have been thoroughly investigated experimentally and joints are typically characterised with the use of parametric equations [68]. The hysteresis curves of plastic mechanisms in both members and joints have characteristics similar to those presented in Chapter 2 suggesting that the plasticity model is applicable to plastic mechanisms in beams as well. A frame element capable of modelling tubular frame structures must include four phenomena: an imperfect elastic member with effects of the normal force, plastic mechanisms in the member at each end, additional elastic flexibility at the local joints, and plastic mechanisms in the local joints. The inclusion of the different mechanisms in a single element is addressed in the present chapter and in [P2], [P3] and [C1]. The formulation of a representative plasticity model and yield surface format was addressed in Chapter 2 and Chapter 3 respectively and discussed in detail in [P1]–[P3] and [C1].

4.1 Equilibrium format

The inclusion of plastic hinges in members is typically modelled with use of an equilibrium format where the flexibilities become additive [100, 99, 66] but other approaches including static condensation have also been applied [71, 89, 32, 2]. A comparison of different approaches [1] found that the equilibrium format has a very high accuracy compared to the low order of modelling. The equilibrium format lends itself easily to a co-rotational formulation as it splits the displacement of an element into a set of deformations and a set of rigid body translations and rotations [66, 62]. The deformations of the individual element mechanisms are assumed small and become additive, even when the structure experiences large deformations. The additive format enables direct use of the plasticity model presented in Chapter 2. The equilibrium format is discussed in [P2], [P3] and [C1]

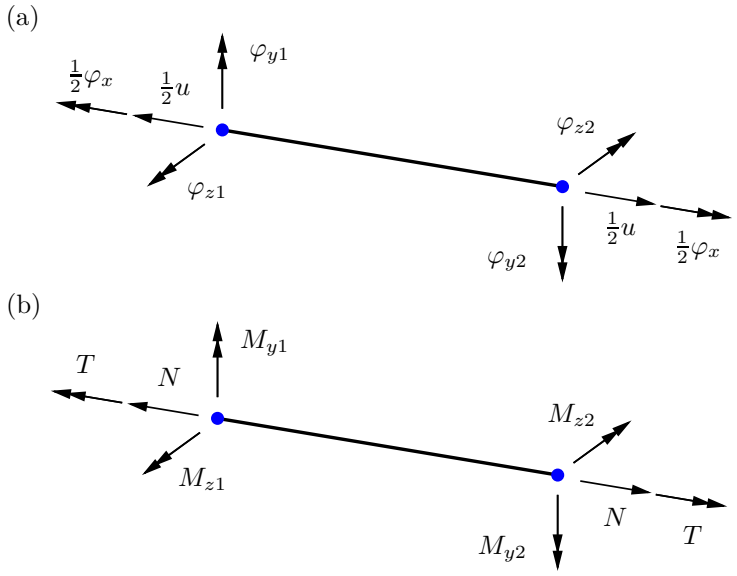

Figure 4.1. Equilibrium format of beam element. (a) Element deformations, (b) section forces. From [P3].

is defined via the generalized strains and stresses

$$\boldsymbol{\gamma}_{\mathrm{t}} = [u, \varphi_x, \varphi_{z1}, \varphi_{z2}, \varphi_{y1}, \varphi_{y2}]_{\mathrm{t}}^T , \tag{4.1}$$

$$\boldsymbol{\tau}_{\mathrm{e}} = [N, T, M_{z1}, M_{z2}, M_{y1}, M_{y2}]^T , \tag{4.2}$$

that represent the deformations and section forces respectively as illustrated in Fig. 4.1. The subscript 't' indicates that the element deformations illustrated in Fig. 4.1 are the total deformations including all mechanism deformations while the subscript 'e' indicates that the section forces are energy conjugate to the elastic deformations. The elastic local joint deformations are often included by use of special elements [101, 57, 48, 4] or by introduction of a separate node and use of static condensation. The need for special elements and static condensation can be eliminated by introduction of the local mechanisms at the end of the elastic member as illustrated in Fig. 4.2. The total deformations $\boldsymbol{\gamma}_{\mathrm{t}}$ then consist of the elastic and the plastic member deformations $\boldsymbol{\gamma}_{\mathrm{e}}^{\mathrm{M}}$ and $\boldsymbol{\gamma}_{\mathrm{p}}^{\mathrm{M}}$, and the elastic and plastic local joint deformations $\boldsymbol{\gamma}_{\mathrm{e}}^{\mathrm{J}}$ and $\boldsymbol{\gamma}_{\mathrm{p}}^{\mathrm{J}}$.

At the material level plasticity models are typically defined with a single plastic mechanism [15, 102, 49], while the present element has four possible plastic mechanism; one for each member end and one for each local joint connection. The presence of multiple plastic mechanisms imposes a need to extend the evolution equations (2.7) and the constitutive format (2.9). To do so the four plastic flow potentials and the four yield functions are arranged in the vectors

$$\mathbf{g} = [G_1(\tilde{\boldsymbol{\tau}}), \ldots, G_4(\tilde{\boldsymbol{\tau}})]^T, \quad \mathbf{f}_y = [F_1(\tilde{\boldsymbol{\tau}}), \ldots, F_4(\tilde{\boldsymbol{\tau}})]^T. \tag{4.3}$$

In the plasticity model presented in Chapter 2 the stress-like internal variables $\boldsymbol{\tau}_{\mathrm{i}}$ represented the center of the yield surface of the plastic mechanism. For elements with multiple plastic mechanisms there are typically more stress-like internal variables $\boldsymbol{\tau}_{\mathrm{i}}$ than observable generalized stresses $\boldsymbol{\tau}_{\mathrm{e}}$ to ensure the mechanisms are independent. Subsets of the stress-like internal variables are therefore related to each plastic mechanism to ensure they are

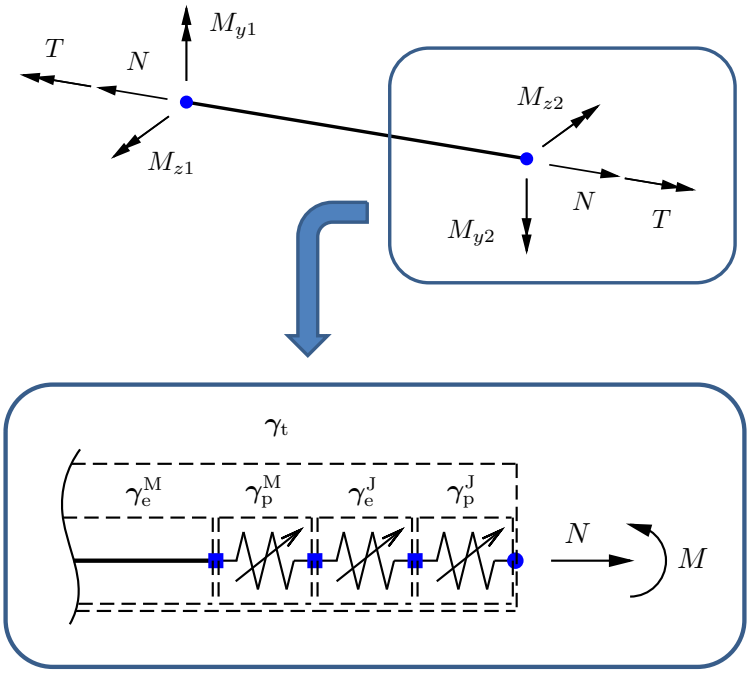

Figure 4.2. Frame element with non-linear elastic and plastic mechanisms. From [P3].

independent of each other. The subsequent steps of deriving the elasto-plastic stiffness matrix including all four plastic mechanisms are explained in detail in [P2]. Conceptually the steps are the same as those needed for determining the elasto-plastic stiffness with a single plastic mechanism but because of the multiple mechanisms the gradients of the four individual plastic flow potentials and yield functions are needed simultaneously. The vector gradients $\partial_{\tilde{\boldsymbol{\tau}}}^T G$ and $\partial_{\tilde{\boldsymbol{\tau}}}^T F$ become matrices $\partial_{\tilde{\boldsymbol{\tau}}}^T \mathbf{g}$ and $\partial_{\tilde{\boldsymbol{\tau}}}^T \mathbf{f}_y$ and the hardening is no longer described by a scalar H but by the matrix

$$\mathbf{H} \;=\; (\partial_{\tilde{\boldsymbol{\tau}}}^T \mathbf{f}_y)\mathbf{K}_{\mathrm{eid}}(\partial_{\tilde{\boldsymbol{\tau}}}^T \mathbf{g})^T \,, \tag{4.4}$$

where $\mathbf{K}_{\mathrm{eid}}$ is the tangent stiffness matrix defined in (2.5). $\mathbf{K}_{\mathrm{ec}}$ is the column block of the stiffness matrix $\mathbf{K}_{\mathrm{eid}}$ coupling increments in $\tilde{\boldsymbol{\tau}}$ with an elastic generalized strain increment $\dot{\boldsymbol{\gamma}}_{\mathrm{e}}$ as described in Chapter 2. The hardening matrix is symmetric when parameter evolution of the elastic stiffness is neglected. The hardening matrix provides the coupling between the different plastic mechanisms created by the common generalized stresses $\boldsymbol{\tau}_{\mathrm{e}}$. The size of the hardening matrix depends on the number of active plastic mechanisms. When all four plastic mechanisms are active the size of $\mathbf{H}$ is 4×4, and for most load combinations it will be smaller, as not all plastic mechanisms will be active simultaneously. In the limit when only one plastic mechanism is active it reduces to a scalar. Because of the relatively small size it is most often possible to invert the hardening matrix analytically. The hardening matrix is used to determine the four plastic multipliers that describe the magnitude of the plastic deformations originating from each plastic mechanism. The incremental constitutive equations for the element take the form

$$\dot{\tilde{\boldsymbol{\tau}}} \;=\; \left[\mathbf{K}_{\mathrm{ec}} - \mathbf{K}_{\mathrm{eid}}(\partial_{\tilde{\boldsymbol{\tau}}}^T \mathbf{g})^T \mathbf{H}^{-1}(\partial_{\tilde{\boldsymbol{\tau}}}^T \mathbf{f}_y)\mathbf{K}_{\mathrm{ec}}\right]\dot{\boldsymbol{\gamma}}_{\mathrm{t}} \,. \tag{4.5}$$

The incremental constitutive format (4.5) provides a clear link with the single-mechanism plasticity formulation (2.9) and holds for general multiple plastic mechanism models, not only the present element formulation.

4.2 Full format implementation

In the global equilibrium iterations of finite element calculations only the part of the stiffness matrix relating to the increment in the observable generalized stresses $\dot{\boldsymbol{\tau}}_\mathrm{e}$ is needed. In the case of elastic deformation it is simply $\partial^T_{\boldsymbol{\gamma}_\mathrm{e}} \boldsymbol{\tau}_\mathrm{e}$ and for elasto-plastic deformation it can be extracted from (4.5) as

$$\mathbf{K}_\mathrm{ep} \;=\; \partial^T_{\boldsymbol{\gamma}_\mathrm{e}} \boldsymbol{\tau}_\mathrm{e} - \mathbf{K}^T_\mathrm{ec} (\partial^T_{\tilde{\boldsymbol{\tau}}} \mathbf{g})^T \mathbf{H}^{-1} (\partial^T_{\tilde{\boldsymbol{\tau}}} \mathbf{f}_y) \mathbf{K}_\mathrm{ec} \,. \tag{4.6}$$

The elasto-plastic tangent stiffness matrix $\mathbf{K}_\mathrm{ep}$ relates an increment in the total observable generalized stresses $\dot{\boldsymbol{\gamma}}_\mathrm{t}$ to an increment in the observable generalized stresses $\dot{\boldsymbol{\tau}}_\mathrm{e}$. With the present equilibrium format the elastic stiffness matrix $\partial^T_{\boldsymbol{\gamma}_\mathrm{e}} \boldsymbol{\tau}_\mathrm{e}$ accounting for both elastic local joint flexibility and the effect of the normal force in imperfect members is defined via the additive flexibilities. While the elastic local joint flexibility matrix is typically readily available via parametric equations [42, 21, 12, 46, 47, 45], the flexibility matrix of an imperfect member is typically found by inversion of the stiffness matrix. The inversion of the stiffness matrix is only possible because of equilibrium format; in a traditional full format that includes the rigid body translations and rotations the stiffness matrix cannot be inverted. A stiffness matrix of an imperfect elastic member in the form of a parabola or a sine shape has been proposed by [20, 19] when the shear flexibility can be neglected. A stiffness matrix was derived for a parabolic shaped shear flexible elastic member in an explicit format in [66]. Determining the resulting elastic stiffness via additive flexibilities is described in detail in [P3] with the result

$$\partial^T_{\boldsymbol{\gamma}_\mathrm{e}} \boldsymbol{\tau}_\mathrm{e} \;=\; \mathbf{K}_\mathrm{e} \;=\; \left((\mathbf{K}^\mathrm{M}_\mathrm{e})^{-1} + (\mathbf{K}^\mathrm{J}_\mathrm{e})^{-1} \right)^{-1} , \tag{4.7}$$

where $(\mathbf{K}^\mathrm{M}_\mathrm{e})^{-1}$ is the member tangent flexibility and $(\mathbf{K}^\mathrm{J}_\mathrm{e})^{-1}$ is the local joint tangent flexibility. The corresponding energy potential φ_e can be defined subsequently if needed. The derivation in [P3] includes a short algorithm for determining the correct distribution of deformations for a given total elastic deformation. While the elastic stiffness $\partial^T_{\boldsymbol{\gamma}_\mathrm{e}} \boldsymbol{\tau}_\mathrm{e} = \mathbf{K}_\mathrm{e}$ may be non-linear e.g. due to the effect of the normal force, bowing etc. it is most convenient to have a constant internal stiffness $\partial^T_{\boldsymbol{\gamma}_\mathrm{i}} \boldsymbol{\tau}_\mathrm{i}$ when parameter evolution is neglected. A constant internal stiffness separates the non-linearity in the evolution of the stress-like internal variables $\boldsymbol{\tau}_\mathrm{i}$ to the gradient of the plastic flow potential. A constant internal stiffness can be obtained by defining a quadratic energy of the form

$$\varphi_\mathrm{i}(\boldsymbol{\gamma}_\mathrm{i}, \boldsymbol{\gamma}_\mathrm{d}) \;=\; \tfrac{1}{2} \boldsymbol{\gamma}_\mathrm{i}^T \, \mathbf{K}_\mathrm{i}(\boldsymbol{\gamma}_\mathrm{d}) \, \boldsymbol{\gamma}_\mathrm{i} \,, \tag{4.8}$$

and by double differentiation it determines the internal stiffness as $\partial^T_{\boldsymbol{\gamma}_\mathrm{i}} \boldsymbol{\tau}_\mathrm{i} = \mathbf{K}_\mathrm{i}(\boldsymbol{\gamma}_\mathrm{d})$. The internal stiffness matrix implemented is diagonal ensuring that any coupling of the individual terms in $\boldsymbol{\tau}_\mathrm{i}$ originates solely from the gradient of the plastic flow potential.

The equilibrium format of the beam element shown in Fig. 4.1 refers to the deformations only, and does not initially include rigid body motions. As described in [66], [P2], [P3] and [C1] the rigid body motions are added by transformation to a traditional full format element with 12 degrees of freedom in the form of three translational and three rotational degrees of freedom at each end of the beam. The equilibrium format is extended to the full format by use of the equilibrium conditions as the element nodal forces $\mathbf{q}$ can be expressed in terms of the element section forces $\boldsymbol{\tau}_\mathrm{e}$ from the equilibrium format. The element nodal forces are found by the equilibrium relations

$$\mathbf{q} \;=\; \begin{bmatrix} \mathbf{q}_1 \\ \mathbf{q}_2 \end{bmatrix} \;=\; \begin{bmatrix} \mathbf{S}_1 \\ \mathbf{S}_2 \end{bmatrix} \boldsymbol{\tau}_\mathrm{e} \;=\; \mathbf{S} \, \boldsymbol{\tau}_\mathrm{e} \,, \tag{4.9}$$

where $\mathbf{q}$ contains the element nodal forces and $\mathbf{q}_1$ and $\mathbf{q}_2$ are the nodal forces at node 1 and node 2 respectively. The matrix $\mathbf{S}$ is defined from the equilibrium conditions and may include effects of axial shortening, bowing etc. [66]. The tangent stiffness matrix of the full format is derived by requiring the virtual work to be the same for the equilibrium format and the full format establishing a relation similar to (4.9) where the increment of the deformations $\dot{\boldsymbol{\gamma}}_\mathrm{t}$ are defined in terms of the increment of the nodal displacements $\dot{\mathbf{u}}$. The increment of the relation (4.9) generates the incremental relation

$$\dot{\mathbf{q}} = \left(\mathbf{S}\mathbf{K}_\mathrm{ep}\mathbf{S}^T + \mathbf{K}_\mathrm{g}\right)\dot{\mathbf{u}}\,, \tag{4.10}$$

where the elasto-plastic tangent stiffness matrix $\mathbf{K}_\mathrm{ep}$ is replaced by the elastic tangent stiffness matrix $\mathbf{K}_\mathrm{e}$ when no plastic mechanisms are active. The second term $\mathbf{K}_\mathrm{g}$ is a geometric stiffness matrix originating from the increment in the transformation matrix $\mathbf{S}$ and it contributes to the symmetry of the formulation [66, 62].

4.3 Examples

For simple structures, e.g. cantilevered beams, the response may be dominated by degradation effects for the individual members as a result of cyclic plasticity [31]. For more complex structures the degradation effects will typically be dominated by the cyclic deformation of the full structure rather than that of the individual members [108]. In [P2] bending of cantilevered I-beams was modelled taking into account degradation effects from local plastic buckling in an approximate but representative way. The effects of local buckling phenomena were identified and represented via the parameter evolution format. Instead of using the exponential format described in Chapter 2 a modified format of the parameter evolution was introduced. The format represents a relative modification of a given parameter with a modification curve in the shape of a hyperbola rather than an exponential curve. The format allows choice of the final value and the stretch of the hyperbola, i.e. how fast the final value is reached. A cantilevered IPE300 beam was cyclically bent via displacement control of the free end. The results are illustrated in Fig. 4.3.

Fig. 4.3 illustrates the ability of the frame element to model the complex response of the slender IPE300 beam that is evidently dominated by the degradation effects caused primarily by local buckling. The local plastic buckling influences all the model characteristics, namely the elastic stiffness, the yield capacity, the additional flexibility at yield, the ultimate capacity and the curvature of the hysteresis curve. The first effect is clearly observed as the elastic part of the hysteresis curve becomes less steep and the second effect is observed as the part of the hysteresis curve that is linear-elastic is reduced. The additional flexibility at yield is seen to increase and the ultimate capacity is seen to decrease along with the curvature of the hysteresis curve. The main difference between the model and the experiment is observed in the last few cycles, where torsional buckling was observed experimentally - a mechanism not included in the model and hence not well-represented.

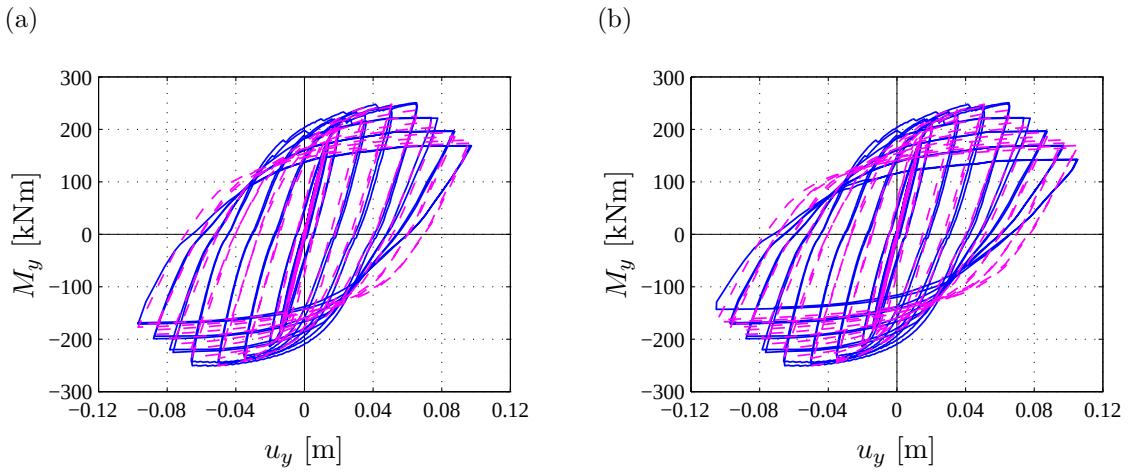

Figure 4.3. Cyclic bending of cantilevered IPE 300 beam: Experiment, [31] (—). Present model (– –). (a) First 38 cycles. (b) All 40 cycles. From [P2].

For cantilevered beams the joint plastic mechanisms are often negligible whereas they are important in other simple structures, e.g. tubular X-joints subjected to out-of-plane bending [104]. An analysis of a tubular X-joint is included in [C1] and it is found that the effect of the local joint plastic mechanism is non-negligible as plastic deformation is observed at load levels far below the load causing plastic deformation in the member. Degradation effects are negligible and therefore not included in the model. The X-joint and the response is illustrated in Fig. 4.4. For details of the geometry see [C1].

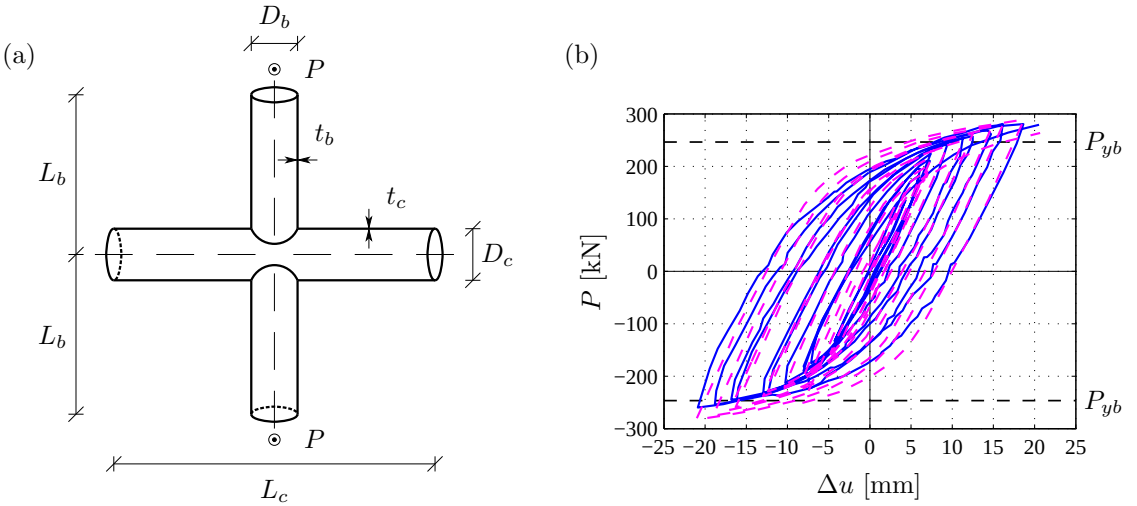

Figure 4.4. X-joint: (a) Geometry. (b) Experiment, [104] (—). Present model (– –). From [C1].

The cyclic deformation of the X-joint is well-represented by the model as illustrated in Fig. 4.4. At the load level P_{yb} plastic mechanisms form in the members of the connecting braces. It is clear that both local joint plasticity and member plasticity is present at the same time and that a frame element used for analysis of tubular structures must be able to represent this.

5. Robust return algorithm

The constitutive relations presented in Chapters 2 and 4 are defined in a differential format and need to be integrated to obtain the finite increments needed in computations. In general the elasto-plastic tangent stiffness matrix $\mathbf{K}_{\text{ep}}$ is not constant as it depends on the gradients of the yield surface and the plastic flow potential and thereby on the generalized stress state. The non-constant tangent stiffness matrix implies that explicit integration of the constitutive equations will lead to drift away from the yield surface unless special measures are taken [111, 33, 62]. As an alternative to explicit integration various implicit methods exist, typically based on satisfying a set of evolution equations, e.g. the generalized strain evolution equations, at a certain point [111, 33, 62]. Implicit methods are often called return algorithms because they typically involve an initial elastic estimate of the final stress state that is located outside the yield surface. Satisfying the set of evolution equations will lead to a generalized stress state located on the yield surface and the generalized stress state will thereby be 'returned' to the yield surface. The return algorithm should be as robust and efficient as possible and for specific problems, e.g. plane stress at the material level, very specific return algorithms with simple results may be derived [93]. At the material level transformation to invariant space is also applied to increase the effectiveness [82], even for materials with non-smooth yield surfaces [25]. For coupled elasto-plasticity and damage models separate algorithms have also been developed [51]. The present type of problem involves multiple plastic mechanisms that may have different yield surfaces and different elasto-plastic behaviour. In addition, the plastic mechanisms may not always be active at the same time, making it difficult to formulate a highly specified return algorithm that increases the efficiency. Instead it is important to have a robust return algorithm that is independent of the yield surface and plasticity model of each individual mechanism. The algorithm should work in the same way independent of how many plastic mechanisms are active at the same time. The development of a robust return algorithm is addressed in the present chapter, and derived in [P3] and [C2].

5.1 Satisfying the strain evolution equation

In order to develop a general and robust return algorithm that works with multiple plastic mechanisms, the set of generalized strain evolution equations is the chosen starting point for deriving the algorithm [62]. In a differential format with a single plastic mechanism the set of generalized strain evolution equations has the form (2.7). In a finite increment setting a $\dot{}$ is replaced by a Δ to indicate a finite increment. With multiple plastic mechanisms the finite increment version of the generalized strain evolution equations take the form

$$\Delta\tilde{\boldsymbol{\gamma}} = \begin{bmatrix} \Delta\boldsymbol{\gamma}_{\text{t}} \\ \mathbf{0} \\ \mathbf{0} \end{bmatrix} - \sum_j \partial_{\tilde{\boldsymbol{\tau}}} G_j \, \Delta\lambda_j = \begin{bmatrix} \Delta\boldsymbol{\gamma}_{\text{t}} \\ \mathbf{0} \\ \mathbf{0} \end{bmatrix} - \left(\partial_{\tilde{\boldsymbol{\tau}}}^T \mathbf{g}\right)^T \Delta\boldsymbol{\lambda} \,. \tag{5.1}$$

In the differential setting the equation must be satisfied at all times, whereas the finite increment format (5.1) does not initially specify what values of the gradients $\partial_{\tilde{\boldsymbol{\tau}}}^T \mathbf{g}$ and the plastic multipliers $\Delta\boldsymbol{\lambda}$ are to be used. An explicit algorithm is obtained if the initial values are used and a fully implicit algorithm is obtained if the final values are used. In general a representative set of gradients and plastic multipliers must be used and different possibilities exist, including weighting of the values at the initial and final states, values found at mid-points etc. [93, 111, 33]. With multiple possible plastic mechanisms there is no guarantee that the mechanisms become active at the same time. The generalized strain evolution equations (5.1) are only meaningful for active plastic mechanisms and use of anything but the values of the gradients and the plastic multipliers in the final state will impose a need for finding the state at which a mechanism becomes active. The generalized strain evolution equations are therefore required to be satisfied in the final state. It is worth noting that for offshore tubular structures an important contribution to the increment in the total observable generalized strains $\Delta\boldsymbol{\gamma}_{\mathrm{t}}$ comes from the local distributed load. Waves, wind and current loads are the main contributors to the global load and act distributed over the elements. In the equilibrium format local distributed loads can be handled consistently even for beams with non-homogeneous cross sections [64].

The finite increment form of the generalized strain evolution equations (5.1) is generally not satisfied with the initial estimates of the gradients of the flow potentials and the plastic multipliers, and a residual is formed

$$\mathbf{r}_{\tilde{\gamma}} = \begin{bmatrix} \Delta\boldsymbol{\gamma}_{\mathrm{t}} \\ \mathbf{0} \\ \mathbf{0} \end{bmatrix} - \Delta\tilde{\boldsymbol{\gamma}} - \left(\partial_{\tilde{\boldsymbol{\tau}}}^T \mathbf{g}\right)^T \Delta\boldsymbol{\lambda}\,. \tag{5.2}$$

Traditional return algorithms are derived by making a first-order Taylor expansion of the residual $\mathbf{r}_{\tilde{\gamma}}$ and setting it equal to zero [62]. The Taylor expansion can be formulated in terms of the sub-increment $\delta\tilde{\boldsymbol{\tau}}$ by inversion of the constitutive relations (2.5). Note, that for beams the inversion of the constitutive relations are only possible in an equilibrium format where the rigid body motions are removed. While the Taylor expansion provides equations to solve for the sub-increment $\delta\tilde{\boldsymbol{\tau}}$ additional equations are needed to determine the sub-increment $\delta\boldsymbol{\lambda}$. Ensuring that the final generalized stress state is located on the yield surface corresponding to $\mathbf{f}_y = \mathbf{0}$ provides the remaining equations making the equation system solvable. A traditional return algorithm is defined by the first-order equation system

$$\begin{bmatrix} \left(\mathbf{K}_{\mathrm{eid}}^A\right)^{-1} & \left(\partial_{\tilde{\boldsymbol{\tau}}}^T \mathbf{g}\right)^T \\ \partial_{\tilde{\boldsymbol{\tau}}}^T \mathbf{f}_y & \mathbf{0} \end{bmatrix} \begin{bmatrix} \delta\tilde{\boldsymbol{\tau}} \\ \delta\boldsymbol{\lambda} \end{bmatrix} = \begin{bmatrix} \mathbf{r}_{\tilde{\gamma}} \\ -\mathbf{f}_y \end{bmatrix}, \tag{5.3}$$

defining the sub-increments $\delta\tilde{\boldsymbol{\tau}}$ and $\delta\boldsymbol{\lambda}$ that update the state in each iteration. The algorithmic tangent stiffness $\mathbf{K}_{\mathrm{eid}}^A$ is a generalized version of the standard algorithmic tangent stiffness [93] accounting for changes in the gradient of the plastic flow potential $\partial_{\tilde{\boldsymbol{\tau}}} G_j$ of the different plastic mechanisms. The equation system (5.3) can in principle be solved directly but a sequential solution is desirable as limitations on $\delta\boldsymbol{\lambda}$ can be enforced to ensure that all the plastic multipliers $\Delta\boldsymbol{\lambda}$ are non-negative. The sequential solution is obtained by isolating the generalized stress increment $\delta\tilde{\boldsymbol{\tau}}$ in the first row of equations and substituting the result into the second row whereby $\delta\boldsymbol{\lambda}$ is found. The generalized stress increment $\delta\tilde{\boldsymbol{\tau}}$ is then found by substituting $\delta\boldsymbol{\lambda}$ into the solution of the first row of equations.

5.2 Increasing the robustness

The initial gradient of the individual plastic mechanism $\partial_{\tilde{\boldsymbol{\tau}}} G_j$ may not be representative of the final state, leading to lack of convergence in traditional return algorithms. The misrepresentation of the gradient originates primarily from two things: the anisotropic form of the yield surface discussed in Chapter 3 and the gradual change of the hardening parameters, gradually changing the gradient relating to $\boldsymbol{\tau}_{\mathrm{i}}$. Thus, return algorithms used in relation to analysis of cyclic plasticity in tubular structures need to be extra robust. The robustness of different return algorithms has been increased by use of e.g. sub-stepping techniques [70], bisection methods [55], multi-stage returns [10] and relaxation techniques [54]. A second-order correction of the Taylor expansion (5.3) resulting in a two-step return algorithm has shown to increase the robustness significantly in [P3] and [C2]. The second order correction is obtained determining the sub-increment $\delta\boldsymbol{\tau}$ from (5.3). Because (5.3) is a first order approximation the sub-increment $\delta\tilde{\boldsymbol{\tau}} = \delta\tilde{\boldsymbol{\tau}}(\xi) = \delta\tilde{\boldsymbol{\tau}}(\xi\mathbf{r}_{\tilde{\gamma}}, \xi\mathbf{f}_y)$ is a linear function of ξ. The coefficients in the function $\delta\tilde{\boldsymbol{\tau}}(\xi\mathbf{r}_{\tilde{\gamma}}, \xi\mathbf{f}_y)$ depend on the initial values of the gradients $\partial_{\tilde{\boldsymbol{\tau}}}\mathbf{f}_y$ and $\partial_{\tilde{\boldsymbol{\tau}}}\mathbf{g}$ and the algorithmic tangent stiffness matrix $\mathbf{K}^A_{\mathrm{eid}}$. However, $\partial_{\tilde{\boldsymbol{\tau}}}\mathbf{f}_y$, $\partial_{\tilde{\boldsymbol{\tau}}}\mathbf{g}$ and $\mathbf{K}^A_{\mathrm{eid}}$ are all non-linear, and assuming they depend on ξ rather than being constant, makes the sub-increment $\delta\tilde{\boldsymbol{\tau}}(\xi\mathbf{r}_{\tilde{\gamma}}, \xi\mathbf{f}_y)$ a non-linear function of ξ. If $\xi = 0$ then $\delta\tilde{\boldsymbol{\tau}} = \mathbf{0}$ and a second order approximation becomes

$$\delta\tilde{\boldsymbol{\tau}}(\xi) \;=\; \xi\frac{\partial(\delta\tilde{\boldsymbol{\tau}})}{\partial\xi}\Big|_{\xi=0} + \tfrac{1}{2}\xi^2\frac{\partial^2(\delta\tilde{\boldsymbol{\tau}})}{\partial\xi^2}\Big|_{\xi=0}. \tag{5.4}$$

The second order approximation (5.4) is the key to the increased robustness found in [P3] and [C2]. The method of determining the first and second order derivatives is explained in detail in [P3] and [C2] and resembles methods used for higher-order time integration of non-linear dynamic problems [63]. If only the first order term is included the format (5.3) is retained. The second order correction needs more information than what is readily available at the initial estimate of the final state and makes use of mid-step to obtain information. A consistent second order step is made from the initial estimate of the final state by setting up the equation system (5.3) using the gradients $\partial^T_{\tilde{\boldsymbol{\tau}}}\mathbf{f}_y$ and $\partial_{\tilde{\boldsymbol{\tau}}}\mathbf{g}$ and the algorithmic tangent stiffness matrix $\mathbf{K}^A_{\mathrm{eid}}$ determined at the mid-step and solving it sequentially. The use of the mid-step values of gradients and stiffness resembles the format used for explicit stress integration proposed by Zienkiewicz [111]. The return algorithm can be used with any type of plasticity model defined by a specific energy, a yield function and a plastic flow potential. In case of the plasticity model presented in Chapter 2 special limitations are put on $\delta\boldsymbol{\tau}_{\mathrm{i}}$ to ensure consistency of the gradient calculation, see [P3] for details.

5.3 Examples

The difference between the two-step return algorithm with increased robustness and the standard single-step return algorithm is illustrated in Fig. 5.1

Fig. 5.1 illustrates return to the yield surface for a single active plastic mechanism with ideal plastic behaviour using the two-step return algorithm as well as a traditional single-step return algorithm. The plastic mechanism is formulated in terms of the normalized normal force $n = N/N^y$ and the normalized bending moment $m = M/M^y$ where N^y and M^y are the yield capacities. From the initial state $\bar{\boldsymbol{\tau}}^0_{\mathrm{e}}$ a mid-step to the state $\bar{\boldsymbol{\tau}}^{1/2}_{\mathrm{e}}$ is made

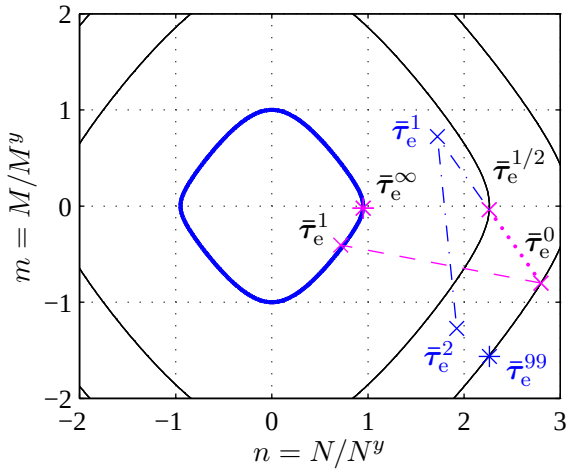

Figure 5.1. Comparison between single step return (blue) and the proposed return algorithm (magenta). From [P3].

and the relevant information is obtained at this state. With the information from the mid-step a full step from the initial state $\bar{\boldsymbol{\tau}}_e^0$ to the state $\bar{\boldsymbol{\tau}}_e^1$ is made. It is seen that the state $\bar{\boldsymbol{\tau}}_e^1$ is fairly close to the final converged state $\bar{\boldsymbol{\tau}}_e^{\infty}$. The direction of return is changed dramatically with the updated gradients and algorithmic tangent stiffness resulting in a better correction $\delta\bar{\boldsymbol{\tau}}_e$. With a traditional single-step return algorithm the steps marked in blue are taken and it is observed that the state determined in the second iteration $\bar{\boldsymbol{\tau}}_e^2$ is about as far away from the yield surface as the initial state $\bar{\boldsymbol{\tau}}_e^0$. In the present case a traditional single-step return algorithm does not converge and after 99 iterations the state $\bar{\boldsymbol{\tau}}_e^{99}$ is reached - a state located at the same isosurface as the initial state.

Applying the two-step return algorithm to a more complex problem highlights the robustness of the algorithm. A tubular steel beam initially unloaded is subjected to deformation corresponding to an elastically estimated stress state of $n = 14$ and $m = -4$ at one end and $n = 14$ and $m = 0$ at the other end. The plastic mechanisms are modelled in two different ways: as ideal plastic and with non-linear kinematic hardening.

Fig. 5.2(a) and (b) illustrates the return in case of ideal plasticity. In the final state both mechanisms are active. It is observed that the first estimate of the final stress state is located fairly close to the converged state, however two iterations later it is located far away. At the end of the second iteration the mechanism shown in Fig. 5.2(a) is inactive because the stress state is located inside the yield surface and the plastic multiplier for the mechanism is zero. The mechanism shown in Fig. 5.2(b) is active although the stress state is located inside the yield surface, because the plastic multiplier of the mechanism is positive. At the end of the third iteration the stress state is located far away from the yield surface of the mechanism shown in Fig. 5.2(a) and the mechanism is active again. The stress state is located far away from the final state because the mechanism was initially inactive in the iteration step, resulting in a poor prediction of the increment. After the third iteration the algorithm converges towards fast towards in a few iterations. A single-step return algorithm does not convergence in the present case. It may seem advantageous to use traditional a single-step return algorithm once the state is 'sufficiently close' to the yield surface, in an effort to reduce the amount of computations. However, Fig. 5.2(a) illustrates that it is difficult to quantify a measure of what would be 'sufficiently close'.

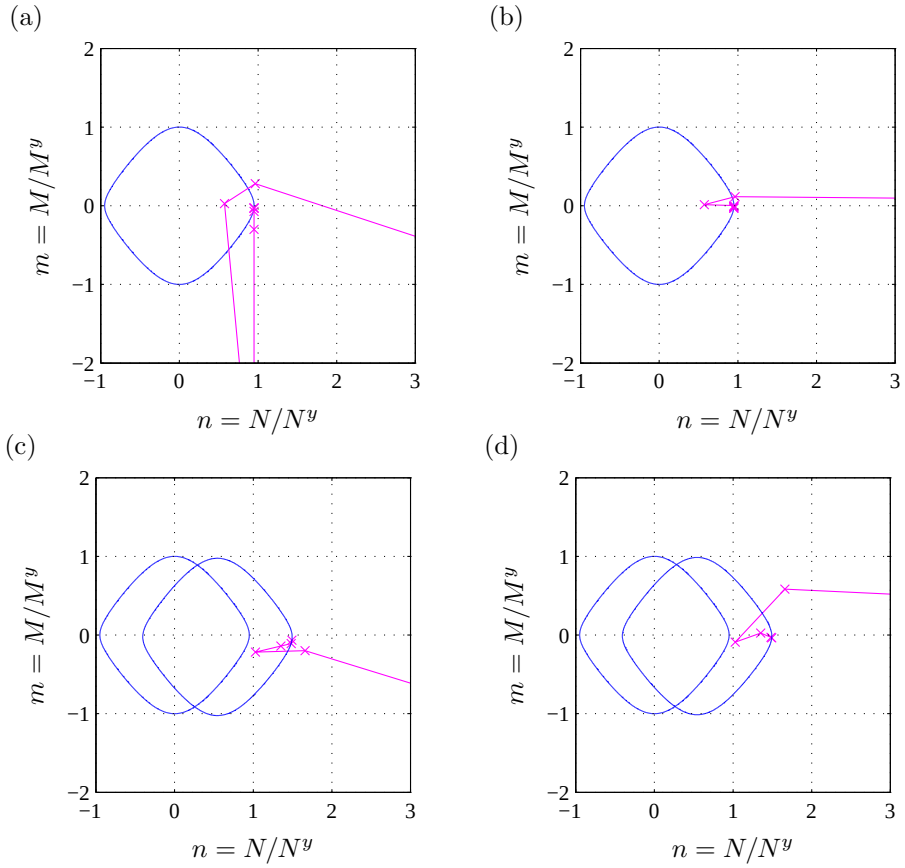

Figure 5.2. Return for ideal plasticity (top) and non-linear kinematic hardening plasticity (bottom). Left: Mechanism 1. Right: Mechanism 2. From [C2].

In Fig. 5.2(c) and (d) the non-linear kinematic hardening case is illustrated and it is observed that the algorithm converges faster. Despite the fact that return is often easier for hardening plastic mechanisms, a traditional single-step return algorithm does not converge in this case either. It is found that the ease of return with the two-step algorithm depends on the shape parameter of the hysteresis curve α, justifying the need for a general formulation of the return algorithm even for the specialized use in connection with frame elements.

6. Effects of cyclic plasticity in tubular structures

The effects of cyclic plasticity in tubular structures have been investigated extensively in experimental work ranging from pure bending of simple members [41, 39, 37, 38] to axial loading of beam-columns where buckling is a substantial part of the problem [40, 87, 109] to cyclic loading of tubular joints [44, 103, 106, 104, 90, 60]. In the case of cyclic bending the hysteresis loops are typically symmetric about the mean deformation and have a shape similar to what is illustrated in Figs. 1.3 and 2.1. For axial loading the hysteresis loops are symmetric only if the deformations are sufficiently small for column buckling not to occur as illustrated in Fig. 6.1(a). When column buckling occurs the geometric non-linearity becomes dominant typically introducing limit points where the column will experience elasto-plastic buckling typically forming a plastic hinge at mid-span. The effect of the elasto-plastic buckling is evident when the load is reversed as the column will gradually straighten creating a stiffening effect as illustrated in Fig. 6.1(a). The transverse displacement will mainly be in one direction as illustrated in Fig. 6.1(b) and the shape of the response curve changes with increased cycling. If the cycling is increased local degradation effects as local buckling, ovalisation and fracture will have an impact on the response as well [109].

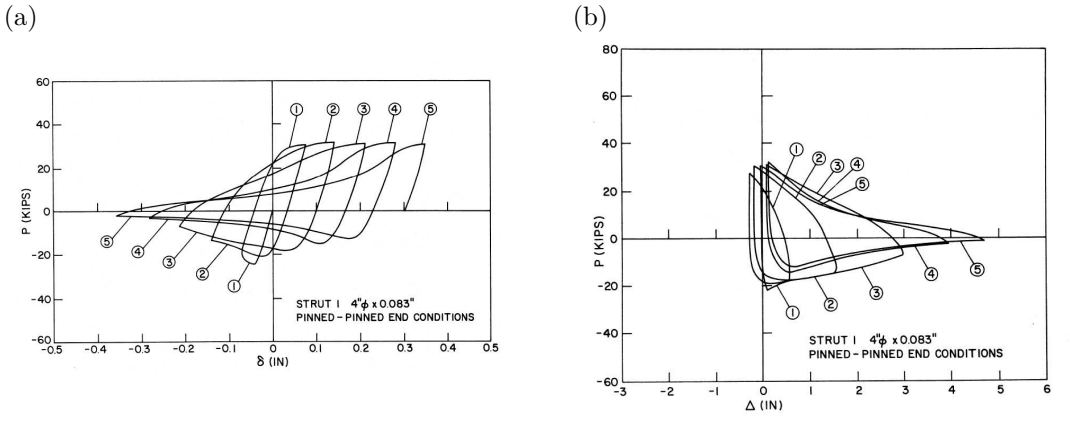

Figure 6.1. Elasto-plastic buckling of simple supported beam-column. (a) Axial displacement vs. axial load. (b) Transverse displacement vs. axial load, [109].

In simple members the permanent change of geometry is mainly a degradation mechanism when buckling is present, whereas for more complex structures the permanent change of geometry from plastic deformation without buckling may act as degradation mechanisms as well. The complex response of a full structure is often a combination of plastic deformation and elasto-plastic buckling [85, 84, 108] that for redundant structures leads to

load shedding. Load shedding may lead to cyclic plasticity in the individual elements even without unloading of the global structure i.e. for monotonic global loading. The ability of the developed frame element in combination with the cyclic plasticity model to model the behaviour of real structures in a representative way is addressed in the present chapter and discussed in detail in [P2] and [P3].

6.1 Verification of model

Zayas et al. [108] tested a 1:6 scale model of an offshore tubular structure representative of structures located in the Gulf of Mexico. The plane frame structure shown in Fig. 6.2 is used to verify the ability of the model to represent the response of an experimentally tested structure. For details of the geometry see [P2]. Zayas et al. [108] tested a plane frame in order to simplify the production and the number of activated mechanisms. The frame is loaded only by a horizontal compressive point load P at the upper right corner.

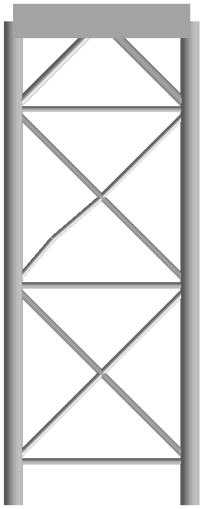

Figure 6.2. Plane offshore frame structure geometry. From [P2].

From monotonic pushover analysis of similar structures [66] it is known that failure typically occurs in the compression braces of the upper X-brace and the lower part of the compression brace is modelled with an initial imperfection. Different ways of representing the member imperfection effect was investigated by D'Aniello et al. [29, 30] for simple column elements as well as for full structures subjected to earthquakes. In the analysis made in [P2] the imperfection is modelled by an offset of the center of the compression brace. The offset is fairly large compared to standard imperfections, see [P2]. Both the effects of local joint flexibility and initial curvature imperfection of the individual members are neglected in the model and including these effects may reduce the representative offset to a value closer to standard values.

The response of the structure in the form of the $(P-\Delta u)$ curves for the top right corner is illustrated in Fig. 6.3 where each figure contains five cycles. Fig. 6.3 illustrates that the simple model without local degradation mechanisms and local joint effects represents the behaviour of the experimentally tested structure rather well. In the first five cycles, shown in Fig. 6.3(a), the shapes of the hysteresis loops as well as the characteristic load levels are very similar. In the following five cycles, shown in Fig. 6.3(b), the correspondence between

the experimental and the modelled results are very similar as well and the response is dominated by plastic deformation. In the final five cycles, shown in Fig. 6.3(c), the discrepancy between the experimental and the modelled results becomes larger but the shape of most of the hysteresis loops are still well-represented just as the characteristic load levels. Note, how the model is able to capture the degradation of the response in the form of reduced yield and ultimate capacity of the structure as a whole in Fig. 6.3(c). The degradation is a result of the permanent plastic deformation changing the geometry and thereby the way the load is carried through the structure down to the supports.

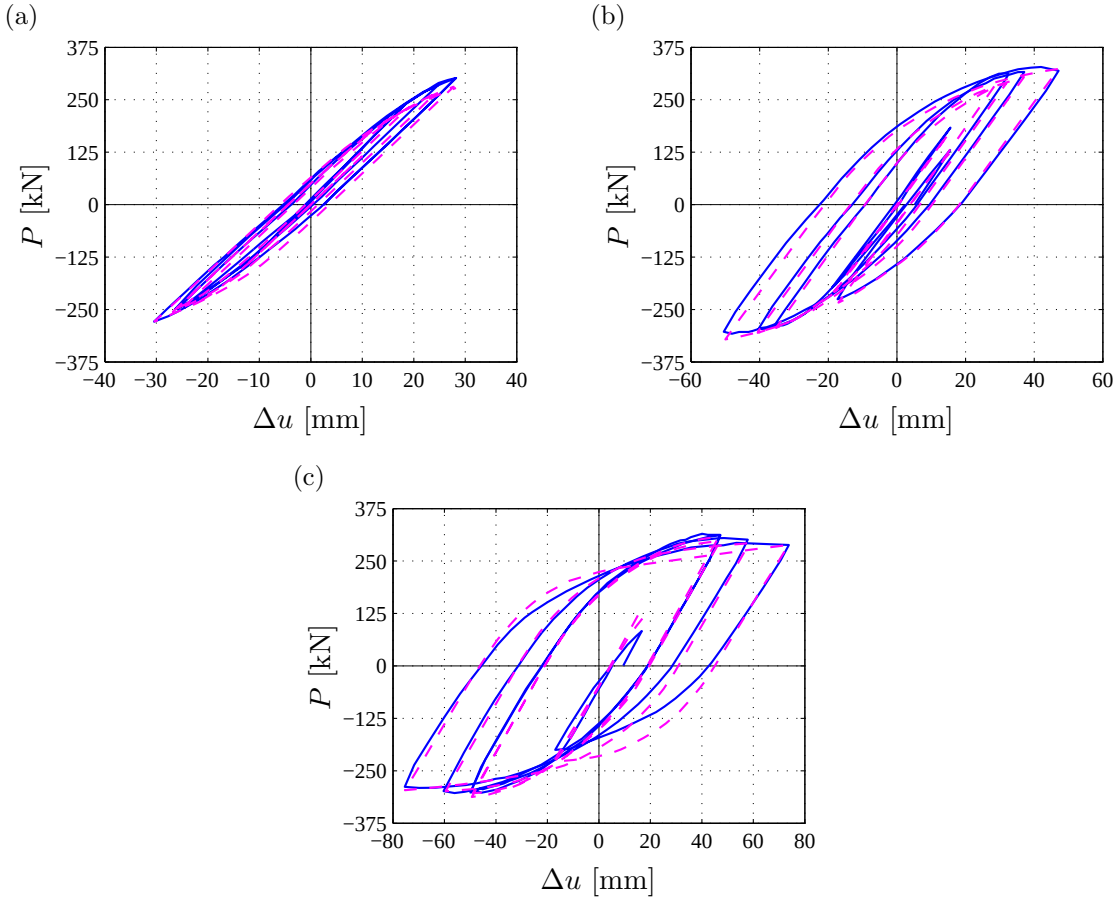

Figure 6.3. Plane offshore frame: Experiment, [108] (—). Present model (– –). (a) Cycle 1–5, (b) Cycle 6–10, (c) Cycle 11–15. From [P2].

6.2 Typical North Sea structures

The computer code RONJA (Rambøll Offshore Non-linear Jacket Analysis) is currently used by several engineering companies including Maersk Oil and Rambøll to analyse existing and to-be-built offshore structures. The computer code can include piles supported by soil, weight of topsides and connected bridges, wave impact areas of appurtenances, distributed loading from waves, current and buoyancy, etc. RONJA is based on an equilibrium format frame element with initial imperfections and two possible plastic hinges with linear hardening including a slight rounding by accounting for the length of the plastic hinge [66]. The code uses linear plastic hardening, and therefore a fairly low hardening has to be used to avoid predicting section forces larger than the capacity of the members and

joints. Elastic local joint flexibility is included by use of static condensation. A benchmark study [9] classified RONJA as one of the best computer codes for collapse analysis of offshore structures. The main improvement point was to increase the hardening after initial yielding, a natural consequence of the intended low hardening. With the plasticity model presented in Chapter 2 the need for an initial low hardening vanishes as there is a defined ultimate capacity that limits the section forces. Because the code is based on equilibrium format frame elements the models and algorithms presented in the previous chapters can be implemented fairly easily and realistic structural models can be analysed.

Two typical structures, representative of the structures located in the North Sea, are analysed and discussed in [P3]. One represents monopile structures with little structural redundancy and the other represents jacket structures with typically fairly large structural redundancy. The loading applied to the structures are according to Ultiguide [35]. The horizontal loading history starts by applying a scaled version of a wave with a recurrence period of 10.000 years, followed by complete unloading of the structure. Subsequently, a wave with a recurrence period of 100 years is applied in the opposite direction of the first wave, followed by complete unloading. Finally, a wave with a recurrence period of 100 years is applied in the same direction as the first wave. The joint capacities are determined based on the ISO 19902 standard [14] with a rounded version of the yield surface illustrated in Fig. 3.2(b). The elastic local joint flexibility is modelled according to [12]. The structures are located at water depths of 47.9 meters and 45.0 meters, respectively. The waves with a recurrence period of 10.000 years have a height of 27.7 meters, while the smaller waves with a recurrence period of 100 years have a wave height of 21.9 meters. Both structures are analysed using the original RONJA code as well as the code updated with the models presented in the previous chapters.

Monopile structure

The monopile structure is illustrated in Fig. 6.4. The monopile structure has very little redundancy and very few tubular joints are present. The horizontal loading is applied in the plane shown in Fig. 6.4, with the largest wave coming from the left.

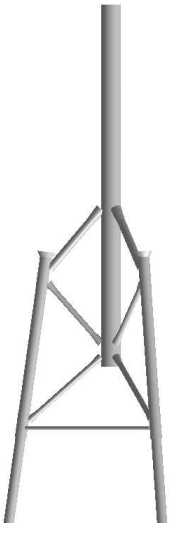

Figure 6.4. Geometry of monopile structure. From [P3].

The response history is shown in Fig. 6.5 where Fig. 6.5(a) represents the models being loaded to similar load levels and Fig. 6.5(b) represents similar deformation levels using the updated and the original RONJA code respectively. The results of the updated code are represented by the solid blue line and those of the original code are represented by the dashed black line. The load has been normalized with the horizontal load of a wave with a 10.000 year recurrence period $P_{10.000\mathrm{y}} = 14.5\,\mathrm{MN}$.

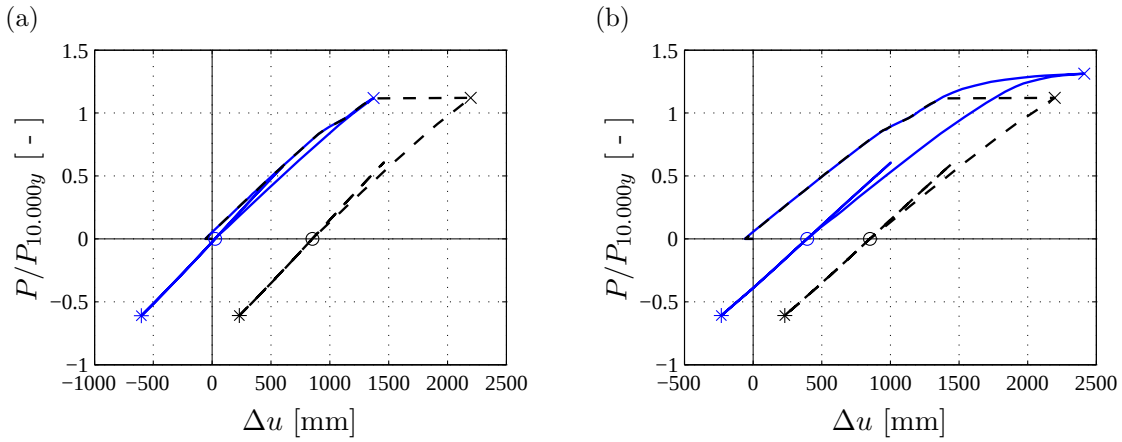

Figure 6.5. Extreme response of monopile structure. Total horizontal load vs. top displacement. (a) Load control. (b) Displacement control. Original code (– –), updated code (—). From [P3].

Fig. 6.5 illustrates that the elastic part of the response is the same for the two codes as expected, because the only difference between the codes in the elastic regime is the method of including the elastic local joint flexibility. The first plastic mechanism that activates is in the single brace at the intersection with the main column, and subsequently the plastic mechanisms in the two other braces at the intersection with the main column activate. The low hardening used in the original code implies that once a plastic mechanism activates in the main column it is essentially free to rotate illustrated in Fig. 6.5 by the almost horizontal response curve. The original code predicts a limit point almost coincident with the activation of the first plastic mechanism. The updated code includes substantial hardening and load reversal at the limit point of the original code corresponds to almost no plastic deformation, illustrated in Fig. 6.5(a). To have a similar deformation level the load must be increased substantially as illustrated in Fig. 6.5(b). Comparing Fig. 6.5(a) and (b) it is noted that elastic unloading is predicted by the original code and the updated code in the case of similar load levels (Fig. 6.5(a)). For the updated code the unloading is initially plastic for similar deformation levels and subsequently elastic. The reason for this is that the bending moment in the main column is so large that the bending capacity of the local joint plastic mechanism in the connecting tension brace is virtually zero. The mechanism is active until the bending moment in the main column is decreased sufficiently, whereby the bending capacity of the joint plastic mechanisms in the brace is increased. The deformed structure is illustrated in Fig. 6.6 for the three load levels indicated in Fig. 6.5. The displacements are scaled by a factor of 5.

Fig. 6.6(a)–(c) illustrate the structure at the state of maximum load (×). The critical plastic mechanisms can be observed and comparing the deformed structure at the same load levels indicates that the original code predicts much larger deformations than the updated code. When comparing the original code with the updated code at similar deformation levels it is clear that plasticity is more widespread in the main column with

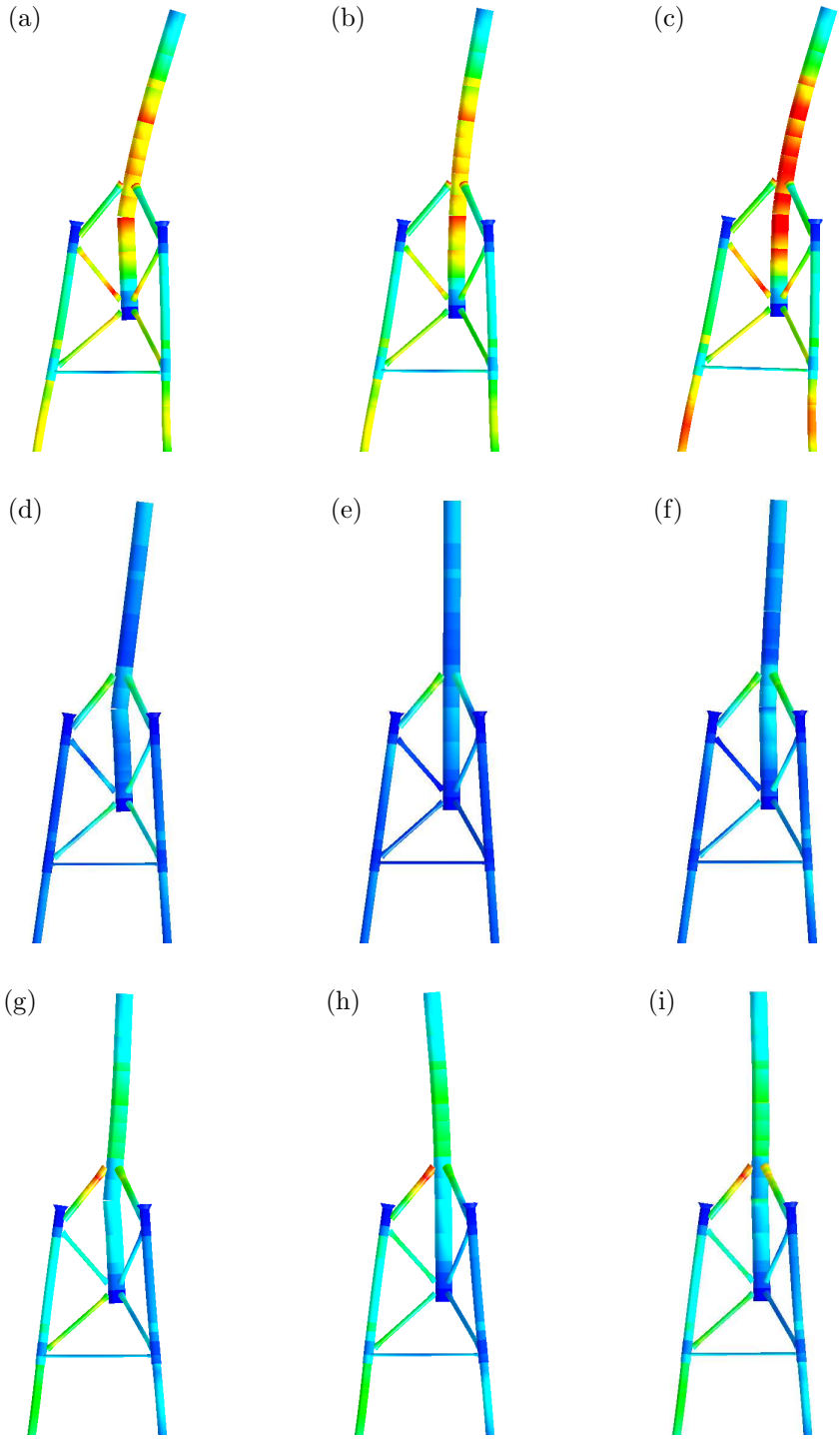

Figure 6.6. Deformation of monopile structure. Top: State $\times$. Center: State $\circ$. Bottom: State $*$. Left: Original code. Middle: Updated code with load control. Right: Updated code with displacement control. From [P3].

the present model. Fig. 6.6(d)–(f) show the deformed structure at the unloaded state ($\circ$) where it is clear that the updated code predicts almost no permanent deformation when loaded to the ultimate capacity of the original code. Fig. 6.6(g)–(i) illustrate the structure

loaded by maximum load in the opposite direction (∗) and it is seen that the most severely loaded section is in the original tension brace (now in compression) that almost becomes plastic. The structure experiences elastic shakedown in all three analysed cases.

Jacket structure

The jacket type structure is illustrated in Fig. 6.7. The jacket structure has a high degree of redundancy and many tubular joints. Typical failure mechanisms are expected to be elasto-plastic buckling of the compression braces, most likely occurring in the top X-brace initially [66]. The horizontal loading is applied in the plane shown in Fig. 6.9, with the largest wave coming from the right.

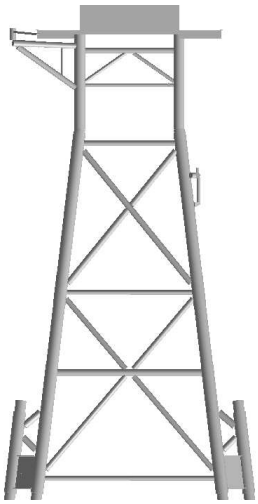

Figure 6.7. Geometry of jacket structure. From [P3].

The response history is shown in Fig. 6.8 where Fig. 6.8(a) represents an analysis in which the two codes have been used to apply similar load levels and Fig. 6.8(b) represents an analysis in which similar deformation levels are reached. The updated code is represented by the solid blue line and the original code is represented by the dashed black line. The horizontal load is normalized with the load of a wave with a 10.000 year recurrence period $P_{10.000\mathrm{y}} = 36.1\,\mathrm{MN}$.

Similar to Fig. 6.5 the response in Fig. 6.8 illustrates that the elastic response is the same independent of the code used. The initial plastic mechanism is elasto-plastic buckling of the compression braces in the upper X-braces and because of the redundancy of the structure both codes predict some hardening behaviour in contrast to the monopile analysis. For the original code with linear hardening the buckling of the compression braces leads to a redistribution of load in the braces as they buckle sufficiently to carry the load by bending rather than as axial load. With the updated code the buckling is observable but the braces keep on carrying the load primarily as axial force because of the substantial hardening of the hinges. Carrying the load by bending significantly reduces the stiffness of the structure as illustrated in Fig. 6.8(a). Fig. 6.8(b) shows the response of the structure loaded to similar deformation levels using the two different codes and the shape of the two response curves are similar except for the more pronounced hardening in the case of the updated code. In both cases plastic unloading is observed caused by the redistribution of the loading when some elements unload elastically and thereby shed the load to other

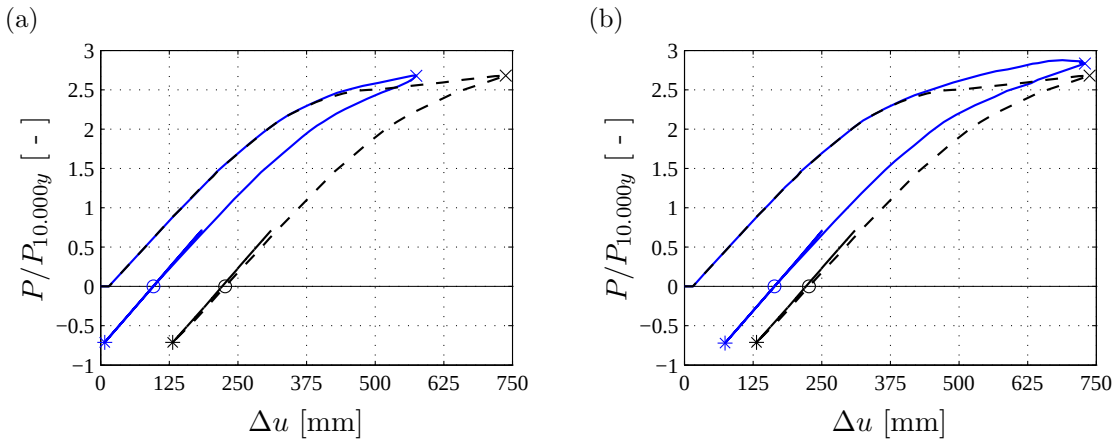

Figure 6.8. Extreme response of jacket structure. Total horizontal load vs. top displacement. (a) Load control. (b) Displacement control. Original code (– –), updated code (—). From [P3].

members. The structure unloads elastically at a load level of approximately 2 for both models. The deformed jacket structure is illustrated in Fig. 6.9 for the three different load levels with displacements scaled by a factor of 5.

Similar to Fig. 6.6 the left column of Fig. 6.9 represents the response of structure modelled using the original code. The middle and right columns represent the updated code with the structure subjected to similar load and deformations levels as with the original code respectively. In the top row representing the maximum load ($\times$) the redistribution of the load is illustrated and it is seen that there is a clear difference in the load redistribution because of the difference in the behaviour of the buckled compression braces. The updated code predicts far less loading in the jacket legs and a larger distribution to the lower X-brace instead. In Fig. 6.9(d)–(f) the deformed structure at zero horizontal load ($\circ$) is shown and the permanent deformation at the buckled braces and the permanent deformation is far greater for the original code. In Fig. 6.9(g)–(i) the deformed structure at maximum load in the opposite direction ($*$) is illustrated. It is seen that plastic mechanisms develop in the buckled braces with the original code essentially straightening the braces creating a stiffer response of the structure. When the structure is modelled with the updated code and subjected to a similar deformation level the buckled braces are loaded most heavily as well slightly straightening the braces. The deformation is still less than that predicted with the original model.

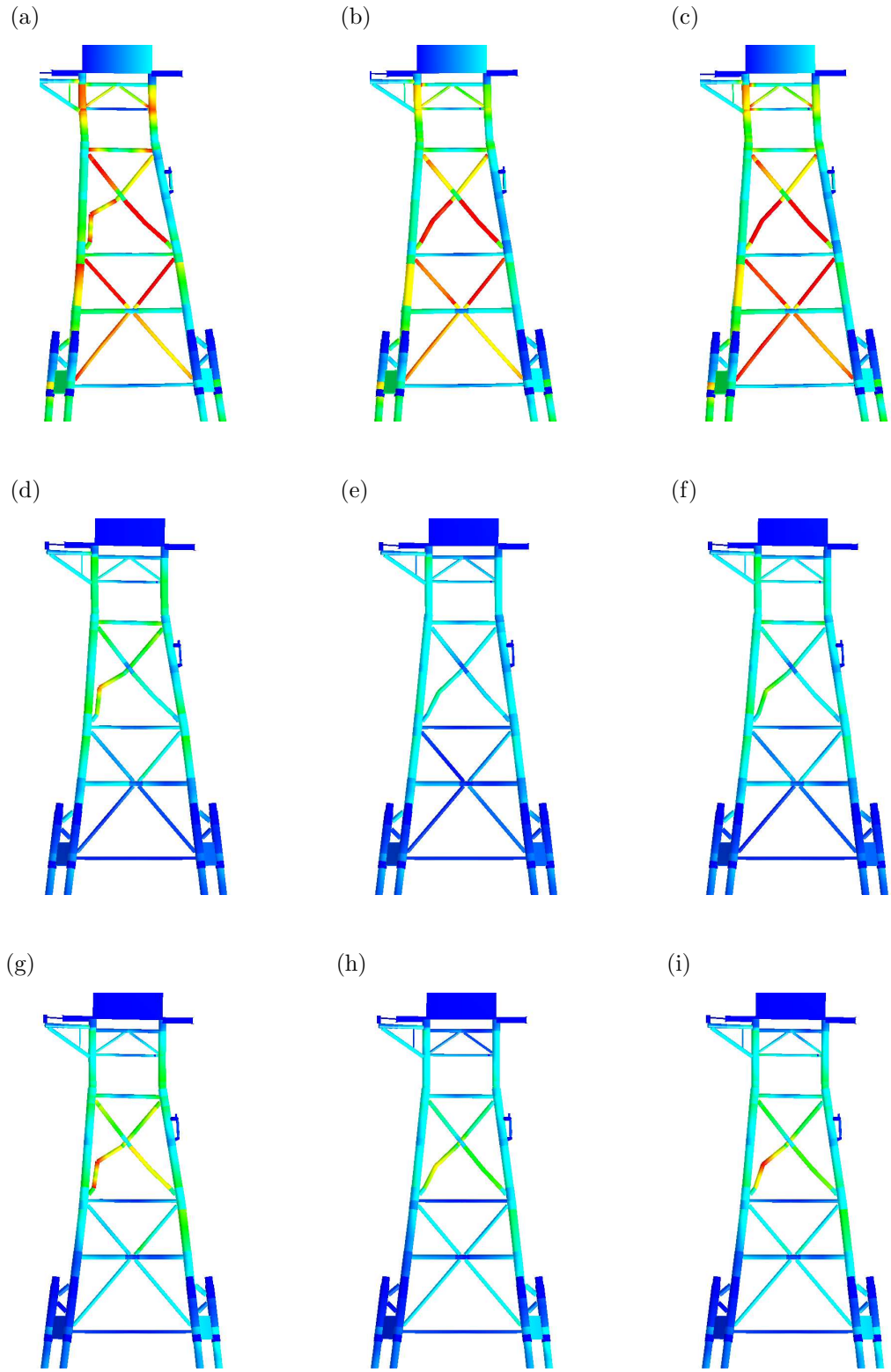

Figure 6.9. Deformation of jacket structure. Top: State $\times$. Center: State $\circ$. Bottom: State $*$. Left: Original code. Middle: Updated code with load control. Right: Updated code with displacement control. From [P3].

6.3 Effects of updated code

The updated code is more robust than the original code. The robustness is increased partly because the elastic local joint flexibility is included in the equilibrium format instead of being introduced via static condensation and partly because of the improved return algorithm. In the analysis of the jacket structure with the original RONJA code a restart of the iteration step has to be made 46 times in need of applying a smaller load step. The restarts are necessary because of lack of convergence in either the static condensation of the elastic local joint flexibility or in the return algorithm. With the updated code no restarts are necessary enabling the use of larger load steps and faster and more robust computations. The benchmark study [9] rated RONJA among the best structural codes because of its ability to predict the sequence of failure mechanisms, e.g. elasto-plastic buckling of X-braces followed by plastic deformation in local joints. The main improvement point of increasing the hardening to a more representative level is inherently solved with the updated plasticity model. A more representative hardening will lead to an increased accuracy of predicting the ultimate capacity of the structure. The updated code does not only improve the ability to represent cyclic plasticity, the improved representation of the hardening behaviour also improves the ability to represent monotonic plasticity. In total the updated code is expected to represent a more realistic prediction of elasto-plastic behaviour of tubular structures. The expected increase in correspondence between model and reality may benefit both safety and undesirably large conservatism in the design of tubular structures as discussed in the introduction.

7. Conclusions

The main purpose of the present thesis is to develop a cyclic plasticity model that accurately represents non-linear hardening behaviour in materials and plastic hinges in beam members and joints. The plasticity model is implemented in a frame element including the four most important effects in analysis of tubular structures: an elastic initially imperfect beam member, plastic mechanisms at the member ends, elastic local joint flexibility and plastic mechanisms in the joints. The implementation makes use of a generic yield surface format and a return algorithm with increased robustness. The frame element implementation enhances the abilities of a recognized structural computer code, making it more robust and more representative in analysis of severely loaded frame structures.

A plasticity model with parameter evolution was presented in [P1]. The plasticity model makes use of external and internal variables. The external variables represent the observable stresses and strains, while the internal variables represent mechanisms in the model. Three potentials define the model: a specific energy defining the constitutive relations, a yield surface describing the shape and size of the elastic domain, and a plastic flow potential defining the evolution of the plastic strain and the internal variables. The model enables a coupling between traditional plasticity theory and damage theory. By definition of the three potentials a cyclic plasticity model at the material level is developed in [P1] and extended to representation of plastic mechanisms in beam members and joints in [P2], [P3] and [C1]. The yield surface has a movable center, with the movement controlled by the internal variables. The movement is analogous to extending a hardening spring, ultimately limiting the movement of the yield surface. The cyclic plasticity model has five basic model parameters, each representing a characteristic of the hysteresis curve. Because of the clear relation between model parameters, the effects of cyclic hardening/softening, fracture, local buckling etc. are representable via evolution of the model parameters as demonstrated [P1] and [P2]. The applicability of the model is illustrated in [P1] by calibration against and subsequent comparison with numerous experimental data for different materials and loadings.

The cyclic plasticity model is made applicable to plastic mechanisms in beams and joints by introduction of a generic yield surface format proposed in [P2]. The versatility of the format is further discussed in [P3] and [C1]. The yield surface format is defined by a function that is homogeneous of degree one for most plastic mechanisms in tubular structures. The homogeneous format ensures that the gradients of outer surfaces are similar to the gradients of the yield surface, easing return to the yield surface in return algorithms. By definition the yield surface format is convex and in addition it is flexible, enabling the representation of different types of yield surfaces. In [P2], [P3] and [C1] the flexibility of the format is illustrated by application to multiple different yield surfaces. With the format local modifications of the yield surface are possible, improving the algorithmic properties of the plasticity model.

In order to effectively model tubular structures a frame element with plastic hinges in the beam member is developed in [P2] and extended to include plastic mechanisms in joints in [C1] and additionally elastic local joint flexibility in [P3]. The frame element is formulated in an equilibrium format, separating the displacements of the element into a set of deformations and a set of rigid body motions. The equilibrium format makes the deformations and thereby the flexibilities additive, enabling a direct representation of the plastic deformations and elastic local joint deformation in the total deformation measure of the element. The additive deformations enable the use of the developed cyclic plasticity model. The additive flexibilities result in an explicitly defined stiffness matrix even with multiple active plastic mechanisms. The equilibrium format is extended to a standard full format element by use of the equilibrium conditions and the format is very suitable for a co-rotational formulation [66]. The ability of the frame element to represent simple structures accurately is illustrated in [P2] and [C1]. Currently there is no experimental or theoretical quantification of the parameter evolution of tubular beams and joints. To increase the knowledge about the impact of phenomena as ovalisation, fracture, local buckling etc. experimental work is required. A potential non-costly method would be detailed finite element models using the implementation of a representative cyclic plasticity model.

The implementation of the frame element developed in [P2], [P3] and [C1] requires the development of a return algorithm. To ensure convergence of the algorithm even with large load steps, a robust return algorithm is developed in [C2] and [P3]. Special measures to increase the robustness in relation to the specific cyclic plasticity model used are discussed in [P3]. The return algorithm is based on satisfying the finite increment version of the generalized strain evolution equations in the final state. The use of the final state removes the need for obtaining information at intermediate points of the load step, a requirement that may be cumbersome with multiple active plastic mechanisms. The derivation of the return algorithm includes identification of the consistent algorithmic tangent stiffness matrix, enabling a second order convergence rate of the equilibrium iterations. The return algorithm is enhanced by a second-order correction of the stress increment resulting in a two-step procedure. The two-step procedure uses information obtained at a mid-step to improve the accuracy of the return direction. The second order correction highly increases the robustness in comparison with traditional single-step return algorithms. While the return algorithm exhibits increased robustness, the time integration methods used in dynamic analysis have not been investigated in the present work. Standard Newmark time integration schemes are inherently incapable of preserving energy for non-linear problems [62]. The robustness may be increased in dynamic analysis by use of an improved time integration scheme.

The effects of cyclic plasticity in materials are illustrated in [P1] while the effects of cyclic plasticity in structures are demonstrated in [P2] and [C1]. The developed models and algorithms are used to update the structural computer code RONJA used by several engineering companies. The differences between the orginal and the updated code are highlighted by analysis of representative North Sea structures in [P3]. A good agreement between experimental observations for complex structures and the developed models is found as discussed in [P2]. The update of the code RONJA increases the robustness and improves the representation of monotonic as well as cyclic plasticity in structures. The cyclic plasticity model improves the representation of the response in the areas with room for improvement as highlighted in the benchmark study [9]. It may be useful to carry out a detailed study of a series of built and to-be-built offshore tubular platforms to investigate the safety of current platforms and identify the degree of conservatism in current design standards.

References

[1] B. N. Alemdar and D. W. White. Displacement, flexibility, and mixed beam-column finite element formulations for distributed plasticity analysis. *Journal of Structural Engineering*, **131**:1812–1819, 2005.

[2] F. Armero and D. Ehrlich. Numerical modeling of softening hinges in thin Euler-Bernoulli beams. *Computers and Structures*, **84**:641–656, 2006.

[3] P. J. Armstrong and C. O. Frederick. A mathematical representation of the multiaxial Bauschinger effect. Technical Report Report RD/B/N731, CEGB, Central Electricity Generating Board, Berkeley, UK, 1966. (Reprinted in Materials at High Temperatures, **24**, 1–26, 2007).

[4] B. Asgarian, P. Alanjari, and V. Aghaeidoost. Three-dimensional joint flexibility element for modeling of tubular offshore connections. *Journal of Marine Science and Technology*, **20**:629–639, 2015.

[5] F. Barlat, J. M. Ferreira Duarte, J. J. Gracio, A. B. Lopes, and E. F. Rauch. Plastic flow for non-monotnoic loading conditions of an aluminum alloy sheet sample. *International Journal of Plasticity*, **19**:1215–1244, 2003.

[6] A. Benallal and D. Marquis. Constitutive equations for nonproportional cyclic elasto-viscoplasticity. *Journal of Engineering Materials and Technology ASME*, **109**:326–336, 1987.

[7] J. Bleyer and P. de Buhan. A greedy algorithm for yield surface approximation. *Comptes Rendus Mecanique*, **341**:605–615, 2013.

[8] J. Bleyer and P. de Buhan. Yield surface approximation for lower and upper bound yield design of 3D composite frame structures. *Computers and Structures*, **129**:86–98, 2013.

[9] H. M. Bolt. Benchmark conclusions. Technical Report C636\32\084R, BOMEL Engineering Consultants, Berkshire, UK, 1999.

[10] R. M. Brannon and S. Leelavanichkul. A multi-stage return algorithm for solving the classical damage component of constitutive models for rocks, ceramics and other rock-like media. *International Journal of Fracture*, **163**:133–149, 2010.

[11] F. Bron and J. Besson. A yield function for anisotropic materials: Application to aluminum alloys. *International Journal of Plasticity*, **20**:937–963, 2004.

[12] J. Buitrago, B. E. Healy, and T. Y. Chang. Local joint flexibility of tubular joints. In S. K. Chakrabarti, editor, *Proceedings of the 12th International Conference on Offshore Mechanics and Arctic Engineering*. The American Society of Mechanical Engineers, Offshore Mechanics and Arctic Engineering Division, Glasgow, Scotland, June 20–24, 1993.

[13] S. Calloch and D. Marquis. Triaxial tension-compression tests for multiaxial cyclic plasticity. *International Journal of Plasticity*, **15**:521–549, 1999.

[14] CEN. *EN ISO 19902 - Petroleum and natural gas industries - Fixed steel offshore structures*. European Committee for Standardization, Brussels, Belgium, 2007.

[15] J. L. Chaboche. Time-independent constitutive theories for cyclic plasticity. *International Journal of Plasticity*, **2**:149–188, 1986.

[16] J. L. Chaboche. On some modifications of kinematic hardening to improve the description of ratchetting effects. *International Journal of Plasticity*, **7**:661–678, 1991.

[17] J. L. Chaboche. Modeling of ratchetting: evaluation of various approaches. *European Journal of Mechanics and Solids*, **13**:501–518, 1994.

[18] J. L. Chaboche and G. Rousselier. On the plastic and viscoplastic constitutive equations – Part 1: Rules developed with internal variable concept. *Journal of Pressure Vessel Technology*, **105**:153–158, 1983.

[19] S.-L. Chan and J.-X. Gu. Exact tangent stiffness for imperfect beam-column members. *Journal of Structural Engineering*, **126**:1094–1102, 2000.

[20] S.-L. Chan and Z. H. Zhou. Second-order elastic analysis of frames using single imperfect element per member. *Journal of Structural Engineering*, **121**:939–945, 1995.

[21] B. Chen, Y. Hu, and M. Tan. Local joint flexibility of tubular joints of offshore structures. *Marine Structures*, **3**:177–197, 1990.

[22] W.-F. Chen and T. Atsuta. *Theory of Beam-Columns*. J. Ross Publishing, Fort Lauderdale, USA, 2008.

[23] W.-F. Chen and E. M. Lui. Effects of joint flexibility on the behavior of steel frames. *Computers and Structures*, **26**:719–732, 1987.

[24] B. K. Chun, J. T. Jinn, and J. K. Lee. Modeling the Bauschinger effect for sheet metals, Part I: Theory. *International Journal of Plasticity*, **18**:571–595, 2002.

[25] J. Clausen, L. Damkilde, and L. Andersen. An efficient return algorithm for non-associated plasticity with linear yield criteria in principal stress space. *Computers and Structures*, **85**:1795–1807, 2007.

[26] W. M. Coombs, O. A. Petit, and Y. G. Motlagh. NURBS plasticity: yield surface representation and implicit stress integration for isotropic inelasticity. *Computer Methods in Applied Mechanics and Engineering*, **304**:342–358, 2016.

[27] Y. F. Dafalias and E. P. Popov. A model of nonlinearly hardening materials for complex loading. *Acta Mechanica*, **21**:173–192, 1975.

[28] Y. F. Dafalias and E. P. Popov. Plastic internal variables formalism of cyclic plasticity. *Journal of Applied Mechanics - Transactions of the ASME.*, **43**:645–651, 1976.

[29] M. D'Aniello, G. La Manna Ambrosino, F. Portioli, and R. Landolfo. Modelling aspects of the seismic response of steel concentric braced frames. *Steel and Composite Structures, An International Journal*, **15**:539–566, 2013.

[30] M. D'Aniello, G. La Manna Ambrosino, F. Portioli, and R. Landolfo. The influence of out-of-straightness imperfection in Physical-Theory models of bracing members on seismic performance assessment of concentric braced structures. *The Structural Design of Tall and Special Buildings*, **24**:176–197, 2015.

[31] M. D'Aniello, R. Landolfo, V. Piluso, and G. Rizzano. Ultimate behavior of steel beams under non-uniform bending. *Journal of Constructional Steel Research*, **78**:144–158, 2012.

[32] A. Davaran and N. E. Far. An inelastic model for low cycle fatigue prediction in steel braces. *Journal of Constructional Steel Research*, **65**:523–530, 2009.

[33] E. A. de Souza Neto, D. Perić, and D. R. J. Owen. *Computational Methods for Plasticity*. Wiley, Chichester, UK, 2008.

[34] A. F. Dier and M. Lalani. JIP - Assessment criteria, reliability, and reserve strength of tubular joints (Phase II). Technical Report C20400R014, MSL Engineering Limited, Ascot, UK, 2000.

[35] DNV, SINTEF, and BOMEL. *Ultiguide - Best practice guidelines for use of nonlinear analysis methods in documentation of ultimate limit states of jacket type offshore structures*. Det Norske Veritas, Høvik, Norway, 1999.

[36] S. El-Tawil and G. G. Deierlein. Stress-resultant plasticity for frame structures. *Journal of Engineering Mechanics*, **124**:1360–1370, 1998.

[37] M. Elchalakani. Plastic mechanism analyses of circular tubular members under cyclic loading. *Thin-Walled Structures*, **45**:1044–1057, 2007.

[38] M. Elchalakani and X. L. Zhao. Concrete-filled cold-formed circular steel tubes subjected to variable amplitude cyclic pure bending. *Engineering Structures*, **30**:287–299, 2008.

[39] M. Elchalakani, X. L. Zhao, and R. Grzbeita. Variable amplitude cyclic pure bending tests to determine fully ductile section slenderness limits for cold-formed CHS. *Engineering Structures*, **28**:1223–1235, 2006.

[40] M. Elchalakani, X. L. Zhao, and R. Grzbieta. Tests of cold-formed circular tubular braces under cyclic axial loading. *Journal of Structural Engineering*, **129**:507–514, 2003.

[41] M. Elchalakani, X. L. Zhao, and R. Grzbieta. Concrete-filled steel circular tubes subjected to constant amplitude cyclic pure bending. *Engineering Structures*, **26**:2125–2135, 2004.

[42] H. Fessler, P. B. Mockford, and J. J. Webster. Parametric equations for the flexibility matrices of multi-brace tubular joints in offshore structures. *Proceedings of the Institution of Civil Engineers*, **81**:675–696, 1986.

[43] P. Folino, G. Etse, and A. Will. Performance dependent failure criterion for normal- and high-strength concretes. *Journal of Engineering Mechanics, ASCE*, **135**:1393–1409, 2009.

[44] T. C. Fung, T. K. Chan, and C. K. Soh. Ultimate capacity of doubler plate-reinforced tubular joints. *Journal of Structural Engineering*, **125**:891–899, 1999.

[45] F. Gao and B. Hu. Local joint flexibility of completely overlapped tubular joints under out-of-plane bending. *Journal of Constructional Steel Research*, **115**:121–130, 2015.

[46] F. Gao, B. Hu, and H. P. Zhu. Parametric equations to predict LJF of completely overlapped tubular joints under lap brace axial loading. *Journal of Constructional Steel Research*, **89**:284–292, 2013.

[47] F. Gao, B. Hu, and H. P. Zhu. Local joint flexibility of completely overlapped tubular joints under in-plane bending. *Journal of Constructional Steel Research*, **99**:1–9, 2014.

[48] A. A. Golafshani, M. Kia, and P. Alanjari. Local joint flexibility element for offshore plateforms structures. *Marine Structures*, **33**:56–70, 2013.

[49] S. Guo, G. Z. Kang, and J. Zhang. A cyclic visco-plastic constitutive model for time-dependent ratchetting of particle-reinforced metal matrix composites. *International Journal of Plasticity*, **40**:101–125, 2013.

[50] T. Hassan and S. Kyriakides. Ratcheting in cyclic plasticity, Part I: Uniaxial behavior. *International Journal of Plasticity*, **8**:91–116, 1992.

[51] T. Heinze and B. Galvan. Novel numerical strategy for solving strongly coupled elastoplastic damage models with explicit return algorithms: Applications to geomaterials. *International Journal of Solids and Structures*, **80**:64–72, 2016.

[52] R. Hill. A theory of the yielding and plastic flow of anisotropic metals. *Proceedings of The Royal Society of London Series A - Mathematical and Physical Sciences*, **193**:281–297, 1948.

[53] W. M. G. Ho and S.-L. Chan. Semibifurcation and bifurcation analysis of flexibly connected steel frames. *Journal of Structural Engineering*, **117**:939–945, 1991.

[54] M. A. Homel and R. M. Brannon. Relaxing the multi-stage nested return algorithm for curved yield surfaces and nonlinear hardening laws. *International Journal of Fracture*, **194**:51–57, 2015.

[55] M. A. Homel, J. E. Guilkey, and R. M. Brannon. Numerical solution for plasticity models using consistency bisection and a transformed-space closest-point return: a nongradient solution method. *Computational Mechanics*, **56**:565–584, 2015.

[56] O. S. Hopperstad, M. Langseth, and S. Remseth. Cyclic stress-strain behaviour of alloy AA6060 T4, Part II: Biaxial experiments and modelling. *International Journal of Plasticity*, **11**:741–762, 1995.

[57] Y. Hu, B. Chen, and J. Ma. An equivalent element representing local flexibility of tubular joints in structural analysis of offshore platforms. *Computers and Structures*, **47**:957–969, 1993.

[58] X.-M. Jiang, H. Chen, and J. Y. R. Liew. Spread-of-plasticity analysis of three-dimensional steel frames. *Journal of Constructional Steel Research*, **58**:193–212, 2002.

[59] G. Z. Kang, N. Ohno, and A. Nebu. Constitutive modeling of strain range dependent cyclic hardening. *International Journal of Plasticity*, **19**:1801–1819, 2003.

[60] J. K. Kim, S. S. Kim, M. J. Lee, and J. G. Yang. Vierendeel joints in the circular hollow sections of high strength steel subjected to brace moment and chord compressive loadings. *International Journal of Steel Structures*, **12**:579–587, 2012.

[61] S. Kitipornchai, K. Zhu, Y. Xiang, and F. G. A. Al-Bermani. Single-equation yield surfaces for monosymmetric and asymmetric sections. *Engineering Structures*, **13**:366–370, 1991.

[62] S. Krenk. *Non-Linear Modeling and Analysis of Solids and Structures*. Cambridge University Press, Cambridge, UK, 2009.

[63] S. Krenk. Global format for energy-momentum based time integration in nonlinear dynamics. *International Journal of Numerical Methods*, **100**:458–476, 2014.

[64] S. Krenk and P. Couturier. Equilibrium-based nonhomogeneous anisotropic beam element. *AIAA Journal*, **55**:2773–2782, 2017.

[65] S. Krenk, S. Vissing, and C. Vissing-Jørgensen. A finite step updating method for elastoplastic analysis of frames. *Journal of Engineering Mechanics*, **119**:2478–2495, 1993.

[66] S. Krenk, C. Vissing-Jørgensen, and L. Thesbjerg. Efficient collapse analysis techniques for framed structures. *Computers & Structures*, **72**:481–496, 1999.

[67] R. D. Krieg. A practical two surface plasticity theory. *Journal of Applied Mechanics*, **42**:641—646, 1975.

[68] Y. Kurobane. Static behaviour and earthquake resistant design of welded tubular structures. In K. Jármai and J. Farkas, editors, *Mechanics and Design of Tubular Structures. International Centre for Mechanical Sciences (Courses and Lectures)*, volume **394**, pages 53–116. Springer, Vienna, 1998.

[69] J. Lemaitre. Coupled elasto-plasticity and damage constitutive equations. *Computer Methods in Applied Mechanics and Engineering*, **51**:31–49, 1985.

[70] T. Li and R. Crouch. A C_2 plasticity model for structural concrete. *Computers and Structures*, **88**:1322–1332, 2010.

[71] J. Y. R. Liew and L. K. Tang. Advanced plastic hinge analysis for the design of tubular space frames. *Engineering Structures*, **22**:769–783, 2000.

[72] L.-W. Liu and H.-K. Hong. A description of three-dimensional yield surfaces by cubic polynomials. *Journal of Engineering Mechanics*, **143**, 2017.

[73] Y. Liu, L. Xu, and D. E. Grierson. Combined MVP failure criterion for steel cross-sections. *Journal of Constructional Steel Research*, **65**:116–124, 2009.

[74] M. Martinez, A. Pépin, and P. Sicsic. Ovality prediction of reeled seamless and seam welded pipes. In J. Chung, editor, *The Proceedings of the 27th (2017) International Ocean and Polar Engineering Conference*. International Society of Offshore and Polar Engineering, ISOPE, San Francisco, California, 2017.

[75] R. V. Mises. Mechanik der festen Körper im plastich deformablen Zustand. *Nachrichten von der Gesellschaft der Wissenschaften zu Göttingen, Mathematisch-Physikalische Klasse*, **1**:582–592, 1913.

[76] Z. Mroz. On the description of anisotropic workhardening. *Journal of the Mechanics and Physics of Solids*, **15**:163–175, 1967.

[77] P. M. Naghdi and J. A. Trapp. Restrictions on constitutive equations of finitely deformed elastic-plastic materials. *Quarterly Journal of Mechanics and Applied Mathematics*, **28**:25–46, 1978.

[78] N. Ohno and J.-D. Wang. Kinematic hardening rules with critical state of dynamic recovery, Part I: Formulation and basic features for ratchetting behavior. *International Journal of Plasticity*, **9**:375–390, 1993.

[79] N. Ohno and J.-D. Wang. Kinematic hardening rules with critical state of dynamic recovery, Part II: Application to experiments of ratchetting behavior. *International Journal of Plasticity*, **9**:391–403, 1993.

[80] J. G. Orbison, W. McGuire, and J. F. Abel. Yield surface applications in nonlinear steel frame analysis. *Computer Methods in Applied Mechanics and Engineering*, **33**:557–573, 1982.

[81] J. C. Paul, Y. Makino, and Y. Kurobane. Ultimate resistance of unstiffened multiplanar tubular TT- and KK-joints. *Journal of Structural Engineering*, **120**:2853–2870, 1994.

[82] Q. Peng and M. X. Chen. An efficient return mapping algorithm for general isotropic elastoplasticity in principal space. *Computers and Structures*, **92–93**:173–184, 2012.

[83] M. S. Pham, S. R. Holdsworth, K. G. F. Janssens, and E. Mazza. Cyclic deformation response of AISI 316L at room temperature: Mechanical behaviur, microstructural evolution, physically-based evolutionary constitutive modelling. *International Journal of Plasticity*, **47**:143–164, 2013.

[84] E. P. Popov, S. A. Mahin, and R. W. Clough. Inelastic response of tubular steel offshore towers. *Journal of Structural Engineering*, **111**:2240–2258, 1985.

[85] E. P. Popov, S. A. Mahin, and V. A. Zayas. Inelastic cyclic behavior of tubular braced frames. *Journal of the Structural Division, ASCE.*, **106**:2375–2390, 1980.

[86] E. P. Popov and H. Petersson. Cyclic metal plasticity: Experiments and theory. *Journal of the Engineering Mechanics Division, ASCE.*, **114**:1371–1388, 1978.

[87] E. P. Popov, V. A. Zayas, and S. A. Mahin. Cyclic inelastic buckling of thin tubular columns. *Journal of the Structural Division, ASCE.*, **105**:2261–2277, 1979.

[88] W. Prager. A new method of analyzing stresses and strains in work-hardening plastic solids. *Journal of Applied Mechanics*, **23**:493–496, 1956.

[89] P. F. N. Rodrigues and B. P. Jacob. Collapse analysis of steel jacket structures for offshore oil exploitation. *Journal of Constructional Steel Research*, **61**:1147–1171, 2005.

[90] Y. B. Shao, S. T. Lie, S. P. Chiew, and Y. Q. Cai. Hysteretic performance of circular hollow section tubular joints with collar-plate reinforcement. *Journal of Constructional Steel Research*, **67**:1936–1947, 2011.

[91] J. C. Simo. A framework for finite strain elastoplasticity based on maximum plastic dissipation and the multiplicative decomposition: Part I. Continuum formulation. *Computer Methods in Applied Mechanics and Engineering*, **66**:199–219, 1988.

[92] J. C. Simo and M. Ortiz. A unified approach to finite deformation elastoplastic analysis based on the use of hyperelastic constitutive equations. *Computer Methods in Applied Mechanics and Engineering*, **49**:221–245, 1985.

[93] J. C. Simo and R. L. Taylor. A return mapping algorithm for plane stress elastoplasticity. *International Journal for Numerical Methods in Engineering*, **22**:649–670, 1986.

[94] M.-A. A. Skordeli and C. D. Bisbos. Limit and shakedown analysis of 3D steel frames via approximate ellipsoidal yield surfaces. *Engineering Structures*, **32**:1556–1567, 2010.

[95] S. C. Soare and A. A. Benzerga. On the modeling of asymmetric yield functions. *International Journal of Solids and Structures*, **80**:486–500, 2016.

[96] E. Tanaka, S. Murakami, M. Mizuno, H. Yamada, and K. Iwata. Inelastic behavior of modified 9Cr-1Mo steel and its unified constitutive model. In *Proceedings of the 6th International Conference on Mechanical Behaviour of Materials, Vol. 3*, pages 781–786. Pergamon Press, Oxford, 1991.

[97] V. Tarigopula, O. Hopperstad, M. Langseth, and A. H. Clausen. Elastic-plastic behaviour of dual-phase, high-strength steel under strain-path changes. *European Journal of Mechanics and Solids*, **27**:764–782, 2008.

[98] H. Tresca. Mémoire sur l'écoulement des corps solides soumis à de fortes pressions. *Comptes Rendus de l'Académie des Sciences*, **59**:754–758, 1864.

[99] Y. Ueda, T. Akamatsu, and Y. Ohmi. Elastic-plastic analysis of framed structures using the matrix method (in Japanese). *Journal of the Society of Naval Architects of Japan*, **126**:253–262, 1969.

[100] Y. Ueda, M. Matsuishi, T. Yamakawa, and Y. Akamatsu. Elastic-plastic analysis of framed structures using the matrix method (in Japanese). *Journal of the Society of Naval Architects of Japan*, **124**:183–191, 1968.

[101] Y. Ueda, S. M. H. Rashed, and K. Nakacho. An improved joint model and equations for flexibility of tubular joints. *Journal of Offshore Mechanics and Arctic Engineering*, **112**:157–168, 1990.

[102] V. Velay, G. Bernhart, and L. Penazzi. Cyclic behavior modeling of a tempered martensitic hot work tool steel. *International Journal of Plasticity*, **22**:459–496, 2006.

[103] W. Wang and Y. Y. Chen. Hysteretic behaviour of tubular joints under cyclic loading. *Journal of Constructional Steel Research*, **63**:1384–1395, 2007.

[104] W. Wang, Y. Y. Chen, X. Meng, and R. T. Leon. Behavior of thick-walled CHS X-joints under cyclic out-of-plane bending. *Journal of Constructional Steel Research*, **66**:826–834, 2010.

[105] K. J. Willam and E. P. Warnke. Constitutive model for the triaxial behaviour of concrete. *Proceedings of International Association of Bridge and Structural Engineering*, **19**, Sec. III:1–30, 1974.

[106] Y. Yin, Q. H. Han, L. J. Bai, H. D. Yang, and S. P. Wang. Experimental study on hysteretic behaviour of tubular N-joints. *Journal of Constructional Steel Research*, **65**:326–334, 2009.

[107] F. Yoshida and T. Uemori. A model of large-strain cyclic plasticity describing the Bauschinger effect and workhardening stagnation. *International Journal of Plasticity*, **18**:661–686, 2002.

[108] V. A. Zayas, S. A. Mahin, and E. P. Popov. Cyclic inelastic behavior of steel offshore structures. Technical Report Report UCB/EERC-80/27, EERC, Earthquake Engineering Research Center, Berkeley, CA, 1980.

[109] V. A. Zayas, S. A. Mahin, and E. P. Popov. Cyclic inelastic buckling of tubular steel braces. Technical Report Report UCB/EERC-80/16, EERC, Earthquake Engineering Research Center, Berkeley, CA, 1980.

[110] H. Ziegler. A modification of Prager's hardening rule. *Quarterly of Applied Mathematics*, **17**:55–65, 1959.

[111] O. C. Zienkiewicz, R. L. Taylor, and J. Z. Zhu. *The Finite Element Method*. Elsevier Butterworth–Heinemann, Oxford, 6 edition, 2005.

P1

A compact cyclic plasticity model with parameter evolution

S. Krenk & L. Tidemann

Mechanics of Materials,
Vol. **113**:57–68, 2017.

Mechanics of Materials 113 (2017) 57–68

Contents lists available at ScienceDirect

Mechanics of Materials

journal homepage: www.elsevier.com/locate/mechmat

Research paper

A compact cyclic plasticity model with parameter evolution

S. Krenk[a,*], L. Tidemann[a,b]

[a] Department of Mechanical Engineering, Technical University of Denmark, DK-2800 Kongens Lyngby, Denmark
[b] Mærsk Olie og Gas A/S, DK-6700 Esbjerg, Denmark

ARTICLE INFO

Article history:
Received 17 March 2017
Revised 18 July 2017
Available online 21 July 2017

Keywords:
Cyclic plasticity
Kinematic hardening
Material degradation
Model parameter evolution

ABSTRACT

The paper presents a compact model for cyclic plasticity based on energy in terms of external and internal variables, and plastic yielding described by kinematic hardening and a flow potential with an additive term controlling the nonlinear cyclic hardening. The model is basically described by five parameters: external and internal stiffness, a yield stress and a limiting ultimate stress, and finally a parameter controlling the gradual development of plastic deformation. Calibration against numerous experimental results indicates that typically larger plastic strains develop than predicted by the Armstrong–Frederick model, contained as a special case of the present model for a particular choice of the shape parameter. In contrast to previous work, where shaping the stress-strain loops is derived from multiple internal stress states, this effect is here represented by a single parameter, and it is demonstrated that this simple formulation enables very accurate representation of experimental results. An extension of the theory to account for model parameter evolution effects, e.g. in the form of changing yield level, is included in the form of extended evolution equations for the model parameters. Finally, it is demonstrated that the model in combination with a simple parameter interpolation scheme enables representation of ratcheting effects.

1. Introduction

A central feature of cyclic plasticity is the representation of the Bauschinger effect, in which the original elasto-plastic stress strain relation is stretched upon stress reversal, leading to nested loops, Masing (1927). Typically, full stress reversal leads to approximate doubling of the elastic stress range, suggesting representation in terms of a translating yield surface in the form of kinematic hardening, Prager (1956) and Ziegler (1959). The classic hardening rules do not lend themselves easily to the stretching of the stress-strain curve in the reversed yielding. This problem was resolved by Mroz (1967) by introducing a set of nested yield surfaces, each controlled by linear kinematic hardening. For circular/cylindrical yield surfaces this model is simple in principle, but it leads to a rather large number of parameters to keep track of all yield surfaces. For proportional loading the model leads to stretched and nested loops, and there is a close analogy to the method of 'rainflow counting' used in fatigue life evaluation for irregular load histories.

An alternative to the multi-surface model is the two surface concept developed by Dafalias and Popov (1975, 1976) and Krieg (1975). In this concept the inner surface acts as a yield surface, while the relation to the bounding surface controls the hardening via translation of the yield surface. The hardening is derived using the relation between the current stress state on the yield surface and an equivalent point, characterized by a common direction of the normal on the bounding surface. When using a common homogeneous function for describing the yield surface as well as the bounding surface the intermediate steps can be eliminated, see e.g. Ottosen and Ristinmaa (2005). However, the model retains two variables, describing distances in stress space and varying in a discontinuous fashion.

A shift of focus from yield and bounding surfaces to a reference stress state within the yield surface was central in the model proposed by Armstrong and Frederick (1966). The key characteristic of the Armstrong–Frederick formulation based on the von Mises yield surface is the assumption of kinematic hardening, in which the center of the yield surface $\boldsymbol{\alpha}$ evolves according to a relation of the form

$$\dot{\boldsymbol{\alpha}} = c\left(\dot{\boldsymbol{\varepsilon}}_p - \frac{\dot{\varepsilon}^*_p}{\alpha_*}\boldsymbol{\alpha}\right), \tag{1}$$

* Corresponding author.
E-mail address: sk@mek.dtu.dk (S. Krenk).

http://dx.doi.org/10.1016/j.mechmat.2017.07.012
0167-6636/

where c is a characteristic parameter, $\dot{\boldsymbol{\varepsilon}}_p$ is the plastic strain rate, and the asterisk symbol indicates a normalized scalar form of the corresponding symbol. As the value of the center stress $\boldsymbol{\alpha}$ increases the rate of increase diminishes, eventually leading to asymptotic approach of the center stress $\boldsymbol{\alpha}$ to a limiting surface generated by the format of the model. A central point is that the bound in this model is on the internal stress state $\boldsymbol{\alpha}$, and not a tangent condition on the yield surface, thereby avoiding the construction of rules for the relative motion of two surfaces. This theory has been extended to several internal stress states, Chaboche and Rousselier (1983), and presented in terms of internal energy and flow potential by Chaboche (1986), and the thermodynamic consistency of multi-mechanism models was investigated by Wolff and Taleb (2008). Multi-surface, two-surface and Armstrong–Frederick models have been discussed in the extensive review by Chaboche (2008), also including visco-plastic models. An attractive feature of the Armstrong–Frederick type of model is the possibility of a fairly free selection of yield surfaces to account e.g. for anisotropy, Chun et al. (2002) or yield hinges in structural members, Tidemann and Krenk (2017).

One of the challenges of cyclic plasticity theories is the phenomenon of ratcheting, in which a non-zero mean stress leads to continuously increasing mean strain upon superposition of a cyclic stress component. The mean and cyclic components may be of the same type, e.g. uniaxial tension, or different components, e.g. axial and circumferential stresses in a tube. The modeling problem was considered by Ohno and Wang (1993a, 1993b), who found that the lack of closure of the cycles in the original model by Armstrong and Frederick (1966) leads to excessive accumulated ratcheting strain. They proposed a modified model consisting of several internal stress states $\boldsymbol{\alpha}_j$, each bounded to a constant surface. This leads to a modification of the form of the basic Armstrong–Frederick evolution relation (1), changing the last term to a projection of the plastic strain rate tensor onto the tangent plane of the corresponding surface. It was subsequently demonstrated by Chaboche (1994), that the improved representation of ratcheting is mainly due to the non-linear representation of the second term in the evolution Eq. (1) following from the use of multiple intervals, rather than from the projection property. Thus, a suitable non-linear form of the second term may be a key to an improved theory, as demonstrated in the present paper. An extensive series of experiments on ratcheting of metals were reported in Hassan and Kyriakides (1992), and Hassan et al. (1992). It was found that in order to model the ratcheting behavior the two-surface model of Dafalias and Popov (1975, 1976) needed a modification relating motion of the bounding surface to the development of plastic mean strain, while the model of Armstrong and Frederick (1966) needed a modification of the second term in (1) to a non-linear form. Alternatively, the performance of the Ohno-Wang model for ratcheting can be improved by supplementing the original kinematic hardening by combined kinematic-isotropic hardening, controlled by a balance parameter in each of the stress ranges, as proposed by Abdel-Karim (2010). An extensive overview of much of the previous work on cyclic plasticity was presented by Xiao et al. (2012), placing the theories within a general thermodynamic framework.

It is a common feature of cyclic behavior of metals that properties typically characterized by model parameters, such as elastic stiffness and yield stress, may change during the process. These effects may be included in a manner similar to traditional damage theory, see e.g. Lemaitre (1985) where both isotropic and kinematic hardening were introduced in the plasticity model and the evolution of the elastic stiffness was represented by continuous internal variables and coupled to the plastic evolution laws. As an alternative to the coupling between internal variables controlling model parameter evolution and plastic deformation, evolution of the model parameters can be introduced via a separate mechanism and a separate criterion, a so-called 2M2C model, where a damage strain is introduced similar to the plastic strain and has a separate evolution law, see e.g. Ibrahimbegovic et al. (2008). A detailed discussion of the relation between model parameters in relation to material characteristics was given by Pham et al. (2013), presenting relations integrating to an exponential development in terms of accumulated plastic strain.

In multi-axial deformation the cyclic hardening/softening will be highly influenced by non-proportionality of the strain path as discussed by Calloch and Marquis (1999) and Tarigopula et al. (2008). In multi-axial strain-controlled cycling the ratio of the amplitude of one strain component to the amplitude of another strain component, the so-called strain range ratio, has a large influence on the cyclic hardening/softening. In the case of bi-axial strain cycling with combined axial and shear cycling the phenomenon has been discussed by Benallal and Marquis (1987). The effect of non-proportionality may be accounted for in various ways e.g. a strain-path memory surface as discussed by Hopperstad et al. (1995).

The present paper develops a simple compact elasto-plastic model of Armstrong–Frederick type, in which the second term in the evolution equation for the center of the instantaneous yield surface is generalized to non-linear form by use of a single parameter that controls the development of the plastic strain. This non-linear form replaces the need for multiple additive internal stress states $\boldsymbol{\alpha}_j$. The result is a simple model with 5-parameters: yield stress and ultimate stress; external and internal elastic stiffness; and a non-dimensional parameter characterizing the development of the plastic strain. These can be read fairly directly off a typical experimental stress-strain curve. Each of the parameters can be given a development by an evolution equation relating model parameters with internal parameters. A basic form of the plasticity model is developed in Section 2 from an internal energy potential, a yield function and a flow potential. The model characteristics are illustrated in Section 3 and the extension to include a non-linear representation of the gradual development of plasticity is introduced. The theory is extended to its full format including parameter evolution in Section 4, where internal parameters are introduced to permit gradual changes of the yield stress, the ultimate stress, and the elastic and the elasto-plastic stiffness. The ability of the model to represent uniaxial cyclic experimental results is presented in Section 5 for constant model parameters and the representation of cyclic hardening/softening by parameter evolution in Section 6. Finally, the ability to represent ratcheting strain development by a parameter interpolation based on the load cycle characteristics is demonstrated in Section 7.

2. Simple cyclic plasticity model

In this section the basic theory of Armstrong–Frederick type cyclic elasto-plasticity is developed based on the concept of external and internal strains and their conjugate stresses. This 'minimum' cyclic plasticity model is then generalized to account for a more detailed description of the development of yielding in Section 3 and of parameter evolution effects in Section 4.

2.1. External and internal variables

The elastic properties are represented by a specific internal energy, given by the function $\varphi(\boldsymbol{\varepsilon}_e, \boldsymbol{\varepsilon}_i)$, where $\boldsymbol{\varepsilon}_e$ is the elastic strain, while $\boldsymbol{\varepsilon}_i$ is a set of internal strain parameters, that represent development of the internal state of the material. For a linear elastic material with a corresponding representation of the internal strain parameters the internal energy function is a quadratic form in the strain components:

$$\varphi(\boldsymbol{\varepsilon}_e, \boldsymbol{\varepsilon}_i) = \tfrac{1}{2}\boldsymbol{\varepsilon}_e^T \mathbb{C}_e \boldsymbol{\varepsilon}_e + \tfrac{1}{2}\boldsymbol{\varepsilon}_i^T \mathbb{C}_i \boldsymbol{\varepsilon}_i. \tag{2}$$

Here and in the following a notation is used that permits interpretation of stresses, strains and stiffness properties either as symmetric tensors or the equivalent 'vector–matrix' format. $\mathbb{C}_e$ is the symmetric elastic stiffness matrix, and $\mathbb{C}_i$ is an analogous symmetric internal stiffness matrix. The superscript T denotes transposition, securing consistency of the 'vector-matrix' notation.

The external observable stress $\boldsymbol{\sigma}$ corresponding to the elastic strain $\boldsymbol{\varepsilon}_e$ and an internal stress $\boldsymbol{\sigma}_i$ corresponding to the internal strain $\boldsymbol{\varepsilon}_i$ are obtained from the internal energy function via the derivatives

$$\boldsymbol{\sigma} \;= \partial_{\boldsymbol{\varepsilon}_e}\varphi \;= \mathbb{C}_e\,\boldsymbol{\varepsilon}_e\,, \tag{3}$$

$$\boldsymbol{\sigma}_i = \partial_{\boldsymbol{\varepsilon}_i}\varphi = \mathbb{C}_i\,\boldsymbol{\varepsilon}_i\,. \tag{4}$$

By convention the partial derivatives are in column format. The first of the relations reproduces the classic linear Hooke's law, while the second gives a similar linear relation between the internal stresses $\boldsymbol{\sigma}_i$ and the internal strains $\boldsymbol{\varepsilon}_i$.

2.2. Yield surface

The yield function $F(\boldsymbol{\sigma},\,\boldsymbol{\sigma}_i)$ defines the yield surface bounding the elastic stress region,

$$F(\boldsymbol{\sigma},\boldsymbol{\sigma}_i) \;\le\; 0\,. \tag{5}$$

In the present model the yield function is of the form $F(\boldsymbol{\sigma}-\boldsymbol{\sigma}_i)$. This implies that the surface translates in stress space as prescribed by the internal stress $\boldsymbol{\sigma}_i$. The yield surface is given by

$$F(\boldsymbol{\sigma},\boldsymbol{\sigma}_i) \;=\; \|\boldsymbol{\sigma}-\boldsymbol{\sigma}_i\| \;-\; \sigma_y, \tag{6}$$

where the symbol $\|\;\|$ denotes a norm of the multi-component stress state, and σ_y is the initial yield stress. In the following the norm will be taken as the von Mises equivalent stress $\sigma_e = \|\boldsymbol{\sigma}\|$, defined in terms of the deviatoric stress $\boldsymbol{\sigma}' = \boldsymbol{\sigma} - \frac{1}{3}\mathrm{trace}(\boldsymbol{\sigma})$ by $\sigma_e^2 = \frac{3}{2}\sigma'_{\alpha\beta}\sigma'_{\alpha\beta}$.

2.3. Plastic flow

The plastic deformation is associated with the rate of energy dissipation, evaluated as the difference between the rate of energy supplied through the total strain rate $\dot{\boldsymbol{\varepsilon}}$ and the time derivative of the internal energy $\dot{\varphi}$,

$$\mathcal{D} \;=\; \boldsymbol{\sigma}^T\dot{\boldsymbol{\varepsilon}} \;-\; \dot{\varphi}(\boldsymbol{\sigma},\boldsymbol{\sigma}_i) \;=\; \boldsymbol{\sigma}^T\big(\dot{\boldsymbol{\varepsilon}}-\dot{\boldsymbol{\varepsilon}}_e\big) \;-\; \boldsymbol{\sigma}_i^T\dot{\boldsymbol{\varepsilon}}_i \;\ge\; 0\,, \tag{7}$$

where the time derivative of the internal energy potential has been expressed by use of (3) and (4). This relation identifies the second factor in the first term as the plastic strain rate

$$\dot{\boldsymbol{\varepsilon}}_p \;=\; \dot{\boldsymbol{\varepsilon}} \;-\; \dot{\boldsymbol{\varepsilon}}_e\,, \tag{8}$$

corresponding to additive elastic and plastic strain rates.

The relations that govern the strain rates are defined by introducing a plastic flow potential $G(\boldsymbol{\sigma},\,\boldsymbol{\sigma}_i)$, and assuming that the rate of dissipation $\mathcal{D}$ is maximized on an equipotential surface for given strain rates $\dot{\boldsymbol{\varepsilon}}_p, \dot{\boldsymbol{\varepsilon}}_i$. According to this principle the strain rates are proportional to the normal to the equipotential surface at the point $\boldsymbol{\sigma},\,\boldsymbol{\sigma}_i$, corresponding to

$$\begin{aligned}\dot{\boldsymbol{\varepsilon}} &= \dot{\boldsymbol{\varepsilon}}_e \;+\; \dot{\lambda}\,\partial_{\boldsymbol{\sigma}}G,\\ \mathbf{0} &= \dot{\boldsymbol{\varepsilon}}_i \;+\; \dot{\lambda}\,\partial_{\boldsymbol{\sigma}_i}G.\end{aligned} \tag{9}$$

The common multiplier $\dot{\lambda}$ is determined by the consistency condition, securing that the stress state $\boldsymbol{\sigma}$ remains on the yield surface.

The flow potential contains the internal stress $\boldsymbol{\sigma}_i$ and its mathematical form is essential for controlling the motion of the yield surface in connection with cyclic plasticity. A simple plastic flow potential corresponding to the yield surface $F(\boldsymbol{\sigma},\,\boldsymbol{\sigma}_i)$ in (6) can be expressed in the form

$$G(\boldsymbol{\sigma},\boldsymbol{\sigma}_i) \;=\; F(\boldsymbol{\sigma},\boldsymbol{\sigma}_i) \;+\; \frac{1}{2\sigma_m}\big(\|\boldsymbol{\sigma}_i\|^2-\sigma_m^2\big), \tag{10}$$

where σ_m is a model parameter of dimension stress. The term σ_m^2 is included to make the limiting value of $G(\boldsymbol{\sigma},\,\boldsymbol{\sigma}_i)$ equal to zero in analogy to the yield function, i.e. $F(\boldsymbol{\sigma},\boldsymbol{\sigma}_i)=0$ corresponds to maximum elastic capacity and $G(\boldsymbol{\sigma},\boldsymbol{\sigma}_i)=0$ corresponds to maximum plastic capacity. It is an important feature of the flow potential format (10) that the yield function is of degree one in the stresses, while the additional hardening term is of higher degree in the internal stress $\boldsymbol{\sigma}_i$ - here two. This particular feature implies that increasing value of $\|\boldsymbol{\sigma}_i\|$ leads to faster growth of the second term, eventually stopping further increase at $\|\boldsymbol{\sigma}_i\|=\sigma_m$. This feature is discussed in detail in Section 3 together with a simple generalization of the hardening term.

Much of the present theory is retained for more general yield surfaces, if these are represented by a homogeneous function of degree one, thereby covering the cases of anisotropy via a modified von Mises yield surface, and yield hinges e.g. in structural members when using a yield surface format in the form of a sum of square roots of quadratic forms, Tidemann and Krenk (2017).

2.4. Elasto-plastic evolution equations

During elasto-plastic loading the stress $\boldsymbol{\sigma}$ remains on the yield surface, and thus the yield condition $F(\boldsymbol{\sigma},\boldsymbol{\sigma}_i)=0$ is identically satisfied during this time. The plastic multiplier is found by time differentiation of the yield function, followed by substitution of the stress rates $\dot{\boldsymbol{\sigma}}$ and $\dot{\boldsymbol{\sigma}}_i$ in terms of the equivalent strain rates $\dot{\boldsymbol{\varepsilon}}_e$ and $\dot{\boldsymbol{\varepsilon}}_i$ via (3) and (4). Finally, the strain rates are expressed by the flow rule (9), whereby the plastic multiplier is obtained as

$$\dot{\lambda} \;=\; \boldsymbol{\Gamma}^T\dot{\boldsymbol{\varepsilon}} \tag{11}$$

in terms of the one-dimensional array

$$\boldsymbol{\Gamma} \;=\; \frac{\mathbb{C}_e\,(\partial_{\boldsymbol{\sigma}}F)}{(\partial_{\boldsymbol{\sigma}}F)^T\,\mathbb{C}_e\,(\partial_{\boldsymbol{\sigma}}G) \;+\; (\partial_{\boldsymbol{\sigma}_i}F)^T\,\mathbb{C}_i\,(\partial_{\boldsymbol{\sigma}_i}G)}\,. \tag{12}$$

Plastic loading is based on the condition that the plastic multiplier $\dot{\lambda}$ calculated from this expression is positive. If this is not the case, the corresponding increment is elastic corresponding to $\dot{\lambda}=0$.

The stress rate and internal stress rate now follow directly from the evolution Eqs. (9) by multiplication with $\mathbb{C}_e$ and $\mathbb{C}_i$, respectively,

$$\begin{aligned}\dot{\boldsymbol{\sigma}} &= \big[\mathbb{C}_e \;-\; \mathbb{C}_e\,(\partial_{\boldsymbol{\sigma}}G)\,\boldsymbol{\Gamma}^T\big]\dot{\boldsymbol{\varepsilon}},\\ \dot{\boldsymbol{\sigma}}_i &= \qquad -\; \mathbb{C}_i\,(\partial_{\boldsymbol{\sigma}_i}G)\,\boldsymbol{\Gamma}^T\dot{\boldsymbol{\varepsilon}}.\end{aligned} \tag{13}$$

These equations describe the evolution of stresses in response to an imposed strain history. The elastic part of the response follows by simply omitting the terms containing $\boldsymbol{\Gamma}$.

2.5. Relation to the Armstrong–Frederick model

The model of Armstrong and Frederick (1966) was developed for a von Mises material with kinematic hardening, governed by the evolution Eq. (1). It is of interest to compare this with the evolution equation for the internal stress $\boldsymbol{\sigma}_i$ in the basic form of the model developed above. When defining the stress norm by the equivalent stress, $\|\boldsymbol{\sigma}\|^2=\sigma_e^2=\frac{3}{2}\boldsymbol{\sigma}'^T\boldsymbol{\sigma}'$, the plastic strain rate follows from (9 a) in the form

$$\dot{\boldsymbol{\varepsilon}}_p \;=\; \dot{\lambda}\,\partial_{\boldsymbol{\sigma}}G \;=\; \dot{\lambda}\,\frac{3}{2}\,\frac{\boldsymbol{\sigma}'-\boldsymbol{\sigma}'_i}{\|\boldsymbol{\sigma}'-\boldsymbol{\sigma}'_i\|}. \tag{14}$$

The corresponding scalar equivalent plastic strain rate is defined by $\dot{\varepsilon}_p^* = (\frac{2}{3}\dot{\boldsymbol{\varepsilon}}_p^T\dot{\boldsymbol{\varepsilon}}_p)^{1/2} = \dot{\lambda}$, and thus the plastic multiplier is defined

by the equivalent plastic strain rate in the present case of the von Mises stress surface defined via the equivalent stress $\sigma_e = \sigma_y$.

The evolution of the internal stress $\boldsymbol{\sigma}_i$ then follows from (9 b) by multiplication with the internal stiffness tensor $\mathbb{C}_i$ as

$$\dot{\boldsymbol{\sigma}}_i = -\mathbb{C}_i \dot{\lambda}\, \partial_{\boldsymbol{\sigma}_i} G = \mathbb{C}_i \Big(\dot{\lambda}\, \partial_{\boldsymbol{\sigma}} G - \frac{\dot{\lambda}}{2\sigma_m} \partial_{\boldsymbol{\sigma}_i} \|\boldsymbol{\sigma}_i\|^2 \Big). \tag{15}$$

In this relation the first term is recognized as the plastic strain rate from (14), while the second term is evaluated by differentiation of the stress norm and identification of the plastic multiplier with the equivalent plastic strain rate. Hereby the evolution equation takes the form

$$\dot{\boldsymbol{\sigma}}_i = \mathbb{C}_i \Big(\dot{\boldsymbol{\varepsilon}}_p - \frac{3}{2} \frac{\dot{\varepsilon}^*_p}{\sigma_m} \boldsymbol{\sigma}'_i \Big). \tag{16}$$

The plastic strain rate $\dot{\boldsymbol{\varepsilon}}_p$ is deviatoric by (14), and for isotropic internal stiffness $\mathbb{C}_i$ the first factor degenerates to scalar stiffness, whereby the Armstrong–Frederick evolution format (1) is recovered from the basic form of the present model. It is seen that the effect of the internal stress term in the evolution equation is easily modified by changing the second term in the definition of the flow potential as discussed in the following section.

3. Model characteristics and enhanced flow potential

In this section the cyclic elasto-plastic model developed above is specialized to uniaxial format and the basic features and their relation to the model parameters are identified. The specific features of the transition from elastic to mainly plastic behavior is then used to develop a compact but more general representation of the flow potential, containing one additional parameter.

3.1. Uniaxial relations

In the uniaxial model the internal energy is given in terms of the strain ε_e and the internal strain ε_i as

$$\varphi(\varepsilon_e, \varepsilon_i) = \tfrac{1}{2} \varepsilon_e^T E_e\, \varepsilon_e + \tfrac{1}{2} \varepsilon_i^T E_i\, \varepsilon_i. \tag{17}$$

This expression contains two material parameters: the elastic modulus E_e and the internal elastic modulus E_i. The uniaxial yield function takes the form

$$F(\sigma, \sigma_i) = |\sigma - \sigma_i| - \sigma_y, \tag{18}$$

where $||$ denotes the absolute value, and σ_y is the uniaxial yield stress. Finally, the corresponding uniaxial flow potential is

$$G(\sigma, \sigma_i) = F(\sigma, \sigma_i) + \frac{1}{2\sigma_m} \big(|\sigma_i|^2 - \sigma_m^2 \big). \tag{19}$$

The stress parameter σ_m represents a hardening limit as demonstrated below.

In total the model contains four parameters E_e, E_i, σ_y and σ_m. Of these the two first relate directly to the stiffness, while the two latter describe characteristic stress levels. This direct interpretation is illustrated below, and turns out to establish a fairly direct correspondence between each parameter and a characteristic feature of the stress-strain curve.

3.2. Uniaxial evolution equations

The evolution equations of the model follow from evaluation of the derivatives of the yield function $F(\sigma, \sigma_i)$ and the flow potential $G(\sigma, \sigma_i)$ with respect to the stress σ and internal stress σ_i. The evolution equations contain the factor Γ from (12) consisting of two terms. The first term, describing the elastic contribution, is

$$(\partial_\sigma F)^T \mathbb{C}_e\, (\partial_\sigma G) = E_e. \tag{20}$$

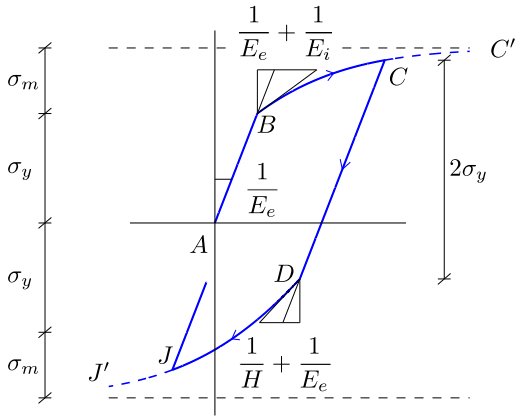

Fig. 1. Stress-strain curve of simple model with simple translation term.

Each of the derivatives with respect to the stress σ contain the factor $\text{sign}(\sigma - \sigma_i) = \partial_\sigma |\sigma - \sigma_i|$ describing the direction of the loading process, but as this factor appears twice the effect cancels, and the factor does not appear explicitly in this term. The second term in the denominator, involving the internal variables, defines the plastic hardening modulus

$$H = (\partial_{\sigma_i} F)^T \mathbb{C}_i\, (\partial_{\sigma_i} G) = E_i \Big[1 - \text{sign}(\sigma - \sigma_i) \frac{\sigma_i}{\sigma_m} \Big]. \tag{21}$$

Here the contribution E_i is similar to (20), while the second contribution combines the sign-function from the derivative of F with the normalized internal stress σ_i/σ_m from the derivative of G.

Evolution equations for both the stress σ and the internal stress σ_i follow from substitution of the uniaxial expressions (20) and (21) into the two general evolution Eqs. (13),

$$\dot{\sigma} = \dot{\sigma}_i = \frac{\dot{\varepsilon}}{1/E_e + 1/H}. \tag{22}$$

A direct interpretation of the hardening modulus H is obtained by writing the stress relation in the form

$$\dot{\varepsilon} = \frac{\dot{\sigma}}{E_e} + \frac{\dot{\sigma}}{H} = \dot{\varepsilon}_e + \dot{\varepsilon}_p. \tag{23}$$

This relation clearly defines $1/H$ as an additional plastic flexibility. It follows immediately that the elastic case is described by an infinite value of H.

The role of $1/H$ as an additional plastic flexibility makes a further analysis of the expression (21) important for identification of the role of the individual model parameters. In Fig. 1 the first part AB of the initial loading curve with $\sigma < \sigma_y$ is elastic with stiffness modulus E_e. When entering the plastic regime for the first time at $\sigma = \sigma_y$ the stiffness changes. At this point the internal stress σ_i is still at its initial value $\sigma_i = 0$, and thus $H = E_i$ at B. With increasing straining the internal stress σ_i increases until $H = 0$, which is reached in the limit $\sigma_i = \sigma_m$. Thus, the monotonic ultimate stress limit is defined by

$$\sigma_u = \sigma_m + \sigma_y. \tag{24}$$

This defines the model parameter σ_m as the stress by which the ultimate stress σ_u exceeds the initial yield stress σ_y.

In the figure unloading is initiated at C, leading to an elastic part CD with stress range $2\sigma_y$ and flexibility $1/E_e$. At D elasto-plastic behavior starts, and the flexibility increases to $1/E_e + 1/H$. The internal stress σ_i, representing the center of the yield surface, does not change during the elastic unloading along CD. The expression (21) can therefore be used to express the sum of the hardening modulus at C and at D as

$$H_D + H_C = 2E_i. \tag{25}$$

Along BC the hardening modulus has decreased from E_i towards the asymptotic value zero. If the plastic straining is large compared to the elastic yield strain σ_y/E_e, then $H_C \ll E_i$ and thus $H_D \simeq 2E_i$. This corresponds to the plastic strain developing at about half the rate at D as compared to the initial plastic straining at B. This generates the often observed cyclic elasto-plastic behavior, that the first loading branch of the stress-strain curve appears as stretched by a factor of two in the following cyclic branches. This behavior is illustrated by the examples in Section 5.

3.3. Enhanced flow potential

The theory developed above constitutes a minimal, but quite versatile, cyclic plasticity model – essentially the Armstrong–Frederick theory, when using the von Mises yield surface. There are only four model parameters: the elastic stiffness E_e, the internal stiffness E_i and the yield and ultimate stress levels σ_y and $\sigma_u = \sigma_y + \sigma_m$. The model represents the principal features of cyclic plasticity well. However, the transition from onset of plastic straining e.g. at the points B or D in Fig. 1 to fully developed plasticity at C' or J' is described by only two parameters: the initial slope, defined by the elasto-plastic flexibility $1/E_e + 1/H$, and the ultimate asymptotic stress limit $\pm\sigma_u$. The transition is governed by the plastic hardening modulus H, given by (21). It consists of a constant E_i, defining the flexibility at initiation of plastic deformation, minus a term that is linear in the internal stress σ_i. As illustrated in the examples in Section 5 an improved quantitative representation of experimental results for steel can be obtained, if the linear term is modified to exhibit a slower than linear increase with respect to σ_i.

In the modified model the gradient of the flow potential with respect to the internal stress is expressed in the form

$$\partial_{\sigma_i} G = -\operatorname{sign}(\sigma - \sigma_i) + \frac{\sigma_i}{(1-\alpha)\sigma_m + \alpha|\sigma_i|}, \qquad \alpha < 1. \tag{26}$$

In the limit $\alpha = 0$ the previous basic model is recovered, while the upper limit $\alpha < 1$ is necessary to retain the last term as an increasing function of σ_i. The flow potential $G(\sigma, \sigma_i)$ follows from integration of (26), whereby

$$G = F + \frac{1}{\alpha}\left\{ |\sigma_i| - \sigma_m - \frac{1-\alpha}{\alpha}\sigma_m \ln\left(1 + \alpha\frac{|\sigma_i| - \sigma_m}{\sigma_m}\right)\right\}, \alpha < 1. \tag{27}$$

It is seen that $G \to 0$ when approaching the ultimate stress limit, where $|\sigma_i| \to \sigma_m$. Furthermore, it is easily verified by expansion of the logarithm that the original flow potential (19) is recovered in the limit $\alpha = 0$.

The hardening modulus follows as

$$H = (\partial_{\sigma_i} F)\,\mathbb{C}_i\,(\partial_{\sigma_i} G) = E_i\left[1 - \operatorname{sign}(\sigma - \sigma_i)\frac{\sigma_i}{(1-\alpha)\sigma_m + \alpha|\sigma_i|}\right]. \tag{28}$$

The ultimate stress limit σ_u corresponds to $H = 0$. The particular parametrization used in the generalized form (28) leads to the same role of the parameter σ_m in the relation (24) giving the ultimate stress for σ_u as the sum of the yield stress σ_y and the stress σ_m. With a parametrization that retains the role of σ_m in defining the ultimate stress level, the role of the non-dimensional parameter α is simply to modify the transition curve between initiation of plastic straining and fully developed plasticity as illustrated in Fig. 2. It is seen that a negative value of the parameter α delays the development of plastic strain, concentrating the curve more into the corner formed by the intersection of the constant hardening part of the stress-strain curve and the curve marking the ultimate stress level. However, as illustrated by the experimental data in Section 5 typical values of α for steel are positive, with $\alpha \simeq 0.8$ as fairly representative and shown in Fig. 2.

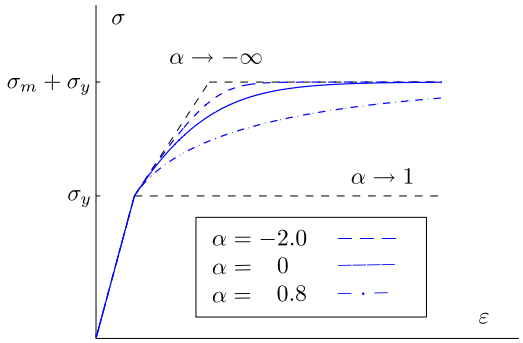

Fig. 2. Influence of parameter α on stress-strain curve.

4. Full model with parameter evolution

In this section the full multi-dimensional plasticity model is developed and supplemented by a systematic framework for parameter evolution. The characteristics and increased flexibility of the enhanced flow potential (27) are easily extended to multi-dimensional formats by replacing the absolute values $|\sigma - \sigma_i|$ and $|\sigma_i|$ by the norms $\|\boldsymbol{\sigma} - \boldsymbol{\sigma}_i\|$ and $\|\boldsymbol{\sigma}_i\|$. The derivatives will not be the sign-function but normalized vectors analogous to a multi-dimensional sign-function.

In uniaxial as well as multi-axial cyclic plasticity it is often found, e.g. Hassan and Kyriakides (1992) and Chun et al. (2002), that cyclic plasticity leads to hardening or softening in the form of an increase or decrease of the apparent ultimate stress $\sigma_u = \sigma_y + \sigma_m$. In analogy with the change of the characteristic internal stress state $\boldsymbol{\sigma}_i$ the ultimate stress was represented by Chun et al. (2002) in terms of the accumulated equivalent plastic strain ε_p as

$$\sigma_u = \sigma_u^0 + K\left(1 - \mathrm{e}^{-N\varepsilon_p}\right). \tag{29}$$

In this formula σ_u^0 is the initial value of the ultimate stress, and the asymptotic value after large plastic straining then is $\sigma_u^\infty = \sigma_u^0 + K$. A direct formulation in terms of (29) would introduce the accumulated plastic strain ε_p as an independent variable of the theory. A more universal form in terms of an evolution equation for σ_u is obtained by differentiation of the relation (29) with respect to time, leading to

$$\dot{\sigma}_u = \dot{\lambda} N(\sigma_u^\infty - \sigma_u), \tag{30}$$

where σ_u is the current value of the ultimate stress, and the relation $\dot{\lambda} = \dot{\varepsilon}_p$ has been used. The evolution Eq. (30) has the same format as that of the internal variable $\boldsymbol{\varepsilon}_i$ in (9 b), illustrating that evolution of the parameters of the model can be treated in a similar way as the internal variables. An extension of the plasticity model developed above to full multidimensional form including evolution of the model parameters is outlined in the following.

4.1. Theory with model parameter evolution

Evolution of the model parameters can be included in a manner similar to traditional damage theory. It is done by introducing an extra set of internal variables in the energy formulation in the form of strain-like evolution parameters $\boldsymbol{\xi}$. To permit evolution of the stiffness the stiffness matrices are considered as functions of $\boldsymbol{\xi}$, and a separate term is added to the internal energy,

$$\varphi(\boldsymbol{\varepsilon}_e, \boldsymbol{\varepsilon}_i, \boldsymbol{\xi}) = \tfrac{1}{2}\boldsymbol{\varepsilon}_e^T\mathbb{C}_e(\boldsymbol{\xi})\boldsymbol{\varepsilon}_e + \tfrac{1}{2}\boldsymbol{\varepsilon}_i^T\mathbb{C}_i(\boldsymbol{\xi})\boldsymbol{\varepsilon}_i + \varphi_d(\boldsymbol{\xi}), \tag{31}$$

where $\varphi_d(\boldsymbol{\xi})$ is a function to be specified to get an appropriate evolution of the model parameters. The energy-conjugate stress and stress-like parameters are defined by

$$\boldsymbol{\sigma} = \partial_{\boldsymbol{\varepsilon}_e}\varphi = \mathbb{C}_e(\boldsymbol{\xi})\boldsymbol{\varepsilon}_e, \tag{32}$$

$$\boldsymbol{\sigma}_i = \partial_{\boldsymbol{\varepsilon}_i}\varphi = \mathbb{C}_i(\boldsymbol{\xi})\boldsymbol{\varepsilon}_i\,, \tag{33}$$

$$\boldsymbol{\eta} = \partial_{\boldsymbol{\xi}}\varphi, \tag{34}$$

where $\boldsymbol{\eta}$ are stress-like evolution parameters, conjugate to $\boldsymbol{\xi}$.

It is assumed that evolution of the model parameters only occurs during plastic loading, and thus the model parameter evolution criterion coincides with the yield surface. Evolution of the yield surface is introduced in the yield function via the yield stress in the form

$$F(\boldsymbol{\sigma}, \boldsymbol{\sigma}_i, \boldsymbol{\eta}) = \|\boldsymbol{\sigma} - \boldsymbol{\sigma}_i\| - \sigma_y(\boldsymbol{\eta}). \tag{35}$$

This formulation enables evolution of the yield stress in a form similar to traditional isotropic hardening/softening.

The evolution of the model parameters is governed by the plastic flow potential, which has to be modified as well. It is desirable to enable evolution of all five model parameters – E_e, E_i representing stiffness, σ_y, σ_m representing stress levels, and α representing the gradual development of plastic straining. The flow potential including evolution of the model parameters is defined as

$$G = F + \frac{1}{\alpha}\left\{\|\boldsymbol{\sigma}_i\| - \sigma_m - \frac{1-\alpha}{\alpha}\,\sigma_m \ln\!\left(1 + \alpha\,\frac{\|\boldsymbol{\sigma}_i\| - \sigma_m}{\sigma_m}\right)\right\} + G_{ei}(\boldsymbol{\eta}), \tag{36}$$

where $\sigma_y = \sigma_y(\boldsymbol{\eta})$, $\sigma_m = \sigma_m(\boldsymbol{\eta})$ and $\alpha = \alpha(\boldsymbol{\eta})$. The term $G_{ei}(\boldsymbol{\eta})$ is introduced to enable evolution parameters related to the stiffness parameters to be separated from the remaining evolution parameters.

The evolution equations relating the evolution of stress and stress-like parameters to a strain increment are determined following the same procedure as in Section 2. They are conveniently expressed with two system stiffness matrices, that include stiffness related to elastic strains and strain-like evolution parameters, and stiffness related to elastic strains, internal strains and strain-like evolution parameters, respectively. These total stiffness matrices are defined as

$$\mathbb{C}_{ed}^T = \begin{bmatrix}\mathbb{C}_e(\boldsymbol{\xi}) & \mathbf{0} & \partial_{\boldsymbol{\xi}}^T\boldsymbol{\sigma}\end{bmatrix}, \tag{37}$$

$$\mathbb{C}_{eid} = \begin{bmatrix}\mathbb{C}_e(\boldsymbol{\xi}) & \mathbf{0} & \partial_{\boldsymbol{\xi}}^T\boldsymbol{\sigma} \\ \mathbf{0} & \mathbb{C}_i(\boldsymbol{\xi}) & \partial_{\boldsymbol{\xi}}^T\boldsymbol{\sigma}_i \\ (\partial_{\boldsymbol{\xi}}^T\boldsymbol{\sigma})^T & (\partial_{\boldsymbol{\xi}}^T\boldsymbol{\sigma}_i)^T & \partial_{\boldsymbol{\xi}}^T\boldsymbol{\eta}\end{bmatrix}. \tag{38}$$

Furthermore the total gradients of the yield surface and the plastic flow potential $\boldsymbol{\partial}F$ and $\boldsymbol{\partial}G$ are defined as

$$\boldsymbol{\partial}F = [\,\partial_{\boldsymbol{\sigma}}^T F\,,\ \partial_{\boldsymbol{\sigma}_i}^T F\,,\ \partial_{\boldsymbol{\eta}}^T F\,]^T, \tag{39}$$

$$\boldsymbol{\partial}G = [\,\partial_{\boldsymbol{\sigma}}^T G\,,\ \partial_{\boldsymbol{\sigma}_i}^T G\,,\ \partial_{\boldsymbol{\eta}}^T G\,]^T. \tag{40}$$

The plastic multiplier is given in terms of these quantities as

$$\dot\lambda = \frac{(\boldsymbol{\partial}F)^T\,\mathbb{C}_{ed}}{(\boldsymbol{\partial}F)^T\,\mathbb{C}_{eid}\,(\boldsymbol{\partial}G)}\,\dot{\boldsymbol{\varepsilon}}\,, \tag{41}$$

and the increment of the different stress and stress-like parameters then follows as

$$\begin{bmatrix}\dot{\boldsymbol{\sigma}} \\ \dot{\boldsymbol{\sigma}}_i \\ \dot{\boldsymbol{\eta}}\end{bmatrix} = \left(\mathbb{C}_{ed} - \frac{\mathbb{C}_{eid}\,(\boldsymbol{\partial}G)\,(\boldsymbol{\partial}F)^T\,\mathbb{C}_{ed}}{(\boldsymbol{\partial}F)^T\,\mathbb{C}_{eid}\,(\boldsymbol{\partial}G)}\right)\dot{\boldsymbol{\varepsilon}}\,. \tag{42}$$

It is noted that if evolution of the model parameters is not introduced in the evolution equations, the general relation (42) reduces to the classic plasticity format (13).

4.2. Model parameter evolution

Model parameter evolution has been incorporated into the theory via a scaling factor on the stiffness matrices $\mathbb{C}_e$ and $\mathbb{C}_i$, and on the parameters σ_y, σ_m and α. In relation to the present theory the five primary variables are $\boldsymbol{\xi} = [\xi_e, \xi_i, \xi_{\sigma_y}, \xi_{\sigma_m}, \xi_\alpha]^T$ with energy conjugates $\boldsymbol{\eta} = [\eta_e, \eta_i, \eta_{\sigma_y}, \eta_{\sigma_m}, \eta_\alpha]^T$. In the present formulation the effects of these evolution parameters are considered independent, and they are introduced into the theory in a form that generalizes the exponential format described by (29) and (30).

The three parameters η_{σ_y}, η_{σ_m} and η_α are introduced as scaling factors of the form

$$\sigma_y = \eta_{\sigma_y}\sigma_y^0, \qquad \sigma_m = \eta_{\sigma_m}\sigma_m^0, \qquad \alpha = \eta_\alpha\alpha^0, \tag{43}$$

where the superscript 0 refers to the initial value. The format of the model for each of the scaling factors η_{σ_y}, η_{σ_m} and η_α are identical, and will be described by the generic symbol η without subscript. The scaling factor η is energy conjugate to the internal variable ξ, with a relation here taken in the following exponential form

$$\eta = \frac{\partial\varphi}{\partial\xi} = \eta^\infty - (\eta^\infty - \eta^0)\mathrm{e}^{-\xi/\xi^*}. \tag{44}$$

The parameters η^0 and η^∞ denote the initial value of the scaling factor and its limiting value after infinite plastic deformation. The parameter ξ^* describes the scaling of the evolution process. It follows from integration that this relation is obtained when a term

$$\varphi_d(\xi) = \eta^\infty\xi + (\eta^\infty - \eta^0)\xi^*\mathrm{e}^{-\xi/\xi^*} \tag{45}$$

is added to the internal potential for each of the three parameters σ_y, σ_m and α. The internal parameter ξ only develops during yielding and evolves similar to the flow rule (9 b), whereby

$$\dot\eta = \frac{\partial\eta}{\partial\xi}\dot\xi = -\frac{\partial\eta}{\partial\xi}\,\frac{\partial G}{\partial\eta}\dot\lambda\,. \tag{46}$$

When evaluating the derivative $\partial\eta/\partial\xi$ from the exponential relation (44) the evolution equation for the scaling factor η takes the form

$$\dot\eta = -\dot\lambda\,\frac{\eta^\infty - \eta}{\xi^*}\,\frac{\partial G}{\partial\eta}\,. \tag{47}$$

For the yield stress $\partial G/\partial\eta = -\sigma_y^0$, and the scaling factor η_{σ_y} becomes an exponential function of λ, representing the accumulated plastic strain. For the scaling parameters η_{σ_m} and η_α the derivative of the potential G is non-trivial and the evolution of these parameters thereby less direct. In the actual numerical implementation the scaling factors η_{σ_y}, η_{σ_m} and η_α follow from the evolution Eq. (42).

In the case of stiffness evolution the parameters ξ_e and ξ_i modify the magnitude of the corresponding stiffness matrices $\mathbb{C}_e$ and $\mathbb{C}_i$ directly as

$$\mathbb{C}_e = \tilde\eta_e(\xi_e)\mathbb{C}_e^0 = \left[\tilde\eta_e^\infty - (\tilde\eta_e^\infty - \tilde\eta_e^0)\mathrm{e}^{-\xi_e/\xi_e^*}\right]\mathbb{C}_e^0 \tag{48}$$

with a similar relation for $\mathbb{C}_i(\xi_i)$. In these expressions $\tilde\eta_e$ and $\tilde\eta_i$ are scaling parameters, but not conjugate to the parameters ξ_e and ξ_i. The evolution of the scaling factors $\tilde\eta_e$ and $\tilde\eta_i$ follow evolution relations similar to (46), e.g.

$$\dot{\tilde\eta}_e = \frac{\partial\tilde\eta_e}{\partial\xi_e}\dot\xi_e = -\frac{\partial\tilde\eta_e}{\partial\xi_e}\,\frac{\partial G}{\partial\eta_e}\dot\lambda\,. \tag{49}$$

The derivative $\partial G/\partial\eta_e$ makes use of the conjugate variable η_e. A simple choice is therefore to introduce the stiffness evolution via the extra term

$$G_{ei}(\eta_e, \eta_i) = -\eta_e - \eta_i \tag{50}$$

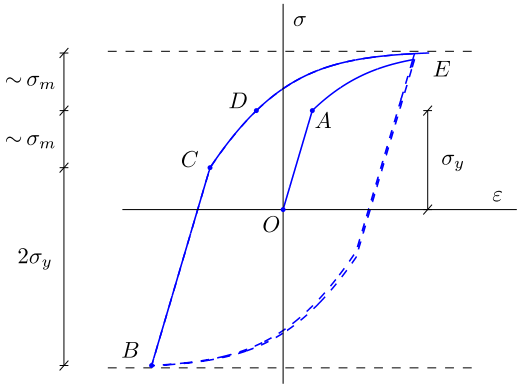

Fig. 3. Conceptual calibration procedure.

in the flow potential (36), thereby reducing the G-derivatives in (49) to $\partial G/\partial\eta_e = \partial G/\partial\eta_i = -1$. The evolution Eq. (42) give the increments of the conjugate variables η_e and η_i, and it is a simple matter to recalculate the current values to corresponding values of the scaling factors $\tilde{\eta}_e$ and $\tilde{\eta}_i$ and the associated internal variables ξ_e and ξ_i.

Here, the parameter evolution has been based on the exponential format (44) and (48), and as illustrated in the following examples this fits experimental data quite well. However, the procedure used here to introduce the basic evolution format can also be modified to represent the evolution via power functions or rational functions of the internal variables $\boldsymbol{\xi}$.

5. Characteristics of the uniaxial model

In this section the uniaxial characteristics of the present model for elasto-plasticity without parameter evolution are identified, and the performance of the model on a number of published cyclic tests from literature is illustrated together with results from alternative models used for representation of these test results.

5.1. Calibration

It is often useful to evaluate the backbone curve of a cyclic loading history when calibrating cyclic plasticity models. The backbone curve can typically be used for the initial estimation of model parameters and the calibration can be finalized with use of the full cyclic response. In the present case all the model parameters can be observed fairly directly from the backbone curve. The conceptual backbone curve of the model is highlighted as a part of the full response in Fig. 3.

In Fig. 3 the point O is the initial stress free state, A corresponds to the first state of yielding, B is the initial stress state at reloading, C is the point where plastic loading starts again, D is the point where the center of the yield surface passes Origo, corresponding to a stress state of $\sigma = \sigma_y$, and E is the point where loading ends. The stress-strain relationship is linear-elastic from B to C with a change in stress between these two states of $2\sigma_y$. From the point C to the point D the stress-strain relation is almost linear, corresponding to constant hardening when σ_i approaches Origo. This linear relation is almost independent of α. From the point D to the point E the stress-strain relationship is non-linear with a clear dependence on α. This type of backbone curve with a linear-elastic, a nearly constant hardening and a non-linear hardening part is observed for many materials.

A direct calibration procedure is described in Table 1. It has been used for different test specimens, described in the following examples, to show the characteristics of the model. The calibrated

Table 1
Calibration procedure.

1. Determine	E_e	by	$E_e = (\sigma_C - \sigma_B)/(\varepsilon_C - \varepsilon_B)$.
2. Determine	σ_y	by	$\sigma_y = (\sigma_C - \sigma_B)/2$.
3. Determine	E_i	by	secant stiffness at CD and E_e
		or	tangent stiffness at C or D and E_e.
4. Determine	σ_m	by	$\sigma_m \simeq \lvert\sigma_B\rvert - \sigma_y$
		or	$\sigma_m \simeq \lvert\sigma_E\rvert - \sigma_y$
		or	$\sigma_m \simeq (\sigma_E - \sigma_B)/2 - \sigma_y$.
5. Determine	α	by	the shape of the curve DE.

Table 2
Model parameters.

Figure	E_e [GPa]	E_i/E_e	σ_y [MPa]	σ_m/σ_y	α
4, 5	195	1.3	190	1.92	0.88
6	200	1.5	150	2.30	0.94
7(a)	65	3.2	150	1.67	0.82
7(b)	90	2.0	150	1.33	0.68
8	220	4.0	40	8.25	0.95
9	170	2.0	360	1.72	0.82

model parameters are shown in Table 2. It is seen that the parameter α lies in the interval 0.68–0.95, with a typical value of 0.80. As seen from Fig. 2 this corresponds to faster development of plastic strain than in the Armstrong–Frederick model.

5.2. Symmetric cycling

The calibration procedure described above is used for different test samples with symmetric cycling, Shi et al. (2012). Two different scenarios of strain-controlled symmetric cycling are considered; in the first case the mean strain is zero and the strain amplitude is initially 1% and then increases by 0.5% for each cycle. In the second case the mean strain is 1% and the amplitude is initially 0.5% and increases 0.5% for each cycle. The test results are shown in Fig. 4 together with the results from the present model with parameters given in Table 2. It is observed that except for the first cycle, the shape of the hysteresis loops as well as the stress levels are predicted accurately by the model. The zero mean strain cycling is predicted slightly more accurately than the non-zero mean strain cycling. This relates to the symmetric format of the model; the zero mean strain cycling is perfectly symmetric whereas the non-zero mean strain cycling is not perfectly symmetric with respect to the strain. A more accurate representation of the first cycle can be obtained by introducing an appropriate evolution function that only affects the first part of the plastic straining, using the framework described in Section 4.

Fig. 4 also shows results from the model proposed by Shi et al. (2012) based on a combination of a peak based model and a backbone curve divided into two separate parts, an elastic part and a hardening part. The hardening part is approximated by curve fitting and the separation point between the elastic and the plastic part is given by the strain. It is observed from Fig. 4 that despite the simplicity of the present model, it gives a more accurate representation of the experimental data.

5.3. Non-symmetric cycling

The present model can also represent non-symmetric cycling fairly accurately as illustrated by the strain-controlled experiment shown in Fig. 5. The strain is cycled between a positive maximum strain which is initially 1% increasing by 0.5% for each cycle, and a negative minimum strain of -1%.

With the exception of the first few cycles the shapes of the hysteresis loops as well as the stress levels are predicted quite accurately. As previously noted, the representation of the first cycle can

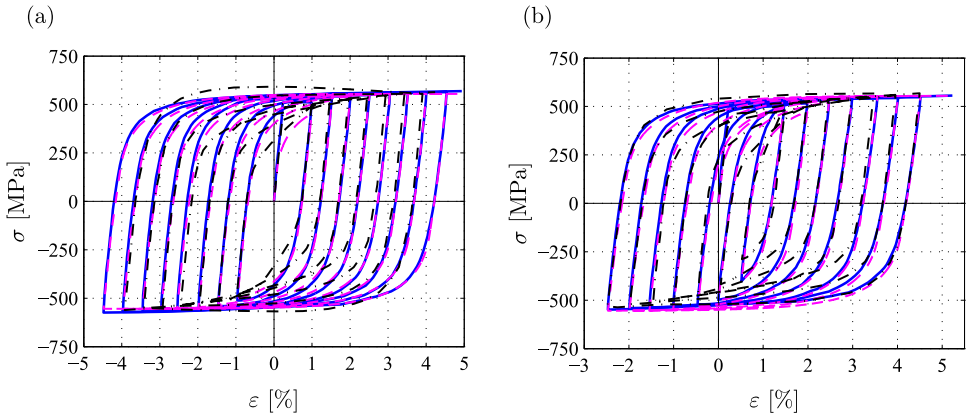

Fig. 4. Symmetric cycling: Shi et al. (2012) experiment (——), model (– · –). Present model (— —).

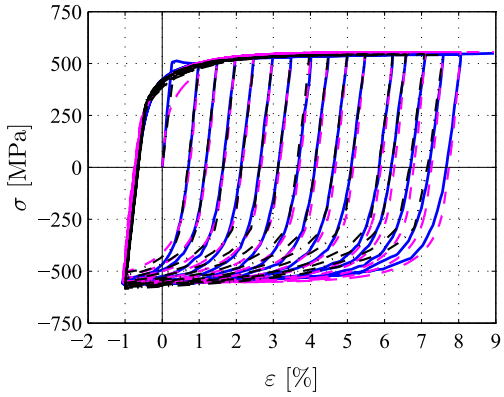

Fig. 5. Non-symmetric cycling: Shi et al. (2012) experiment (——), model (– · –). Present model (— —).

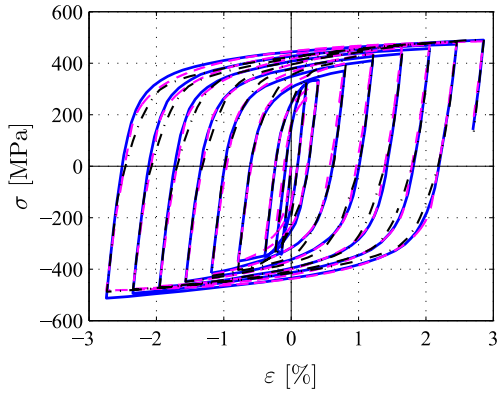

Fig. 6. Popov and Petersson (1978) experiment (——), model (– · –). Present model (— —).

be improved by use of an appropriate evolution of the model parameters.

5.4. Comparison with other models

Popov and Petersson (1978) investigated cyclic plasticity in thin tubular specimens experimentally and used a multi-surface type material model. This was combined with different hardening parameters with formulations based on the plastic strain. The experimental results along with the model proposed by Popov and Petersson (1978) and the present model are shown in Fig. 6. It is seen that the present model reproduces both the stress levels and the shape of the hysteresis loops quite well.

Several models have been based on the model proposed by Armstrong and Frederick (1966) and the subsequent modifications made by Chaboche (1989) and Ohno and Wang (1993a, 1993b). One focus area has been visco-plastic models, and recently Guo et al. (2013) developed a model for particle-reinforced metal matrix composites and alloys. In this model the matrix material and the particle reinforcement have individual material parameters and the resulting material parameters of the alloy are found via a combination depending on the volume fraction of the particle reinforcement. The present model can also be used for such a type of problems if calibrated properly. Fig. 7 shows experimental stabilized response together with theoretical results from Guo et al. (2013) as well as results from the present model, calibrated separately for the two tests with parameters given in Table 2 for matrix material alone and for a composite with 14% reinforcement particles. The ability to capture the shape of the stress-strain curves is notable, and the parameters from Table 2 may be related to the representation of mixture properties.

A visco-plastic model with focus on cyclic hardening/softening was developed by Kang et al. (2003), based on Ohno and Wang (1993a, 1993b). This model typically requires a fairly large number of parameters, and it is of interest to compare its representation of individual cycles with that of the present model, with the five parameters shown in Table 2. Fig. 8 shows a comparison between experimental data, the model proposed by Kang et al. (2003), and the present calibrated model. It is observed that both models are rather accurate in representing the shape and the stress levels of the hysteresis loop, but the present model with only five model parameters.

There are also other types of models, e.g. the so-called 2M1C models (2 Mechanisms, 1 Criterion) models. Such a model has been proposed by Velay et al. (2006) in relation to hot working tool steel. An example of a comparison between the 2M1C model and the present model is shown in Fig. 9 for a case in which the viscous effect on the plastic response is negligible. Both models are predicting the shape of the hysteresis loop and the stress levels rather well, the present being the more accurate.

6. Cyclic hardening/softening by parameter evolution

This section presents three examples illustrating parameter evolution. The initial model parameters are shown in Table 3 which is comparable to Table 2. The initial value of the scaling parameters is $\eta^0 = 1$ and the parameters defining the evolution of the initial parameters are shown in Table 4.

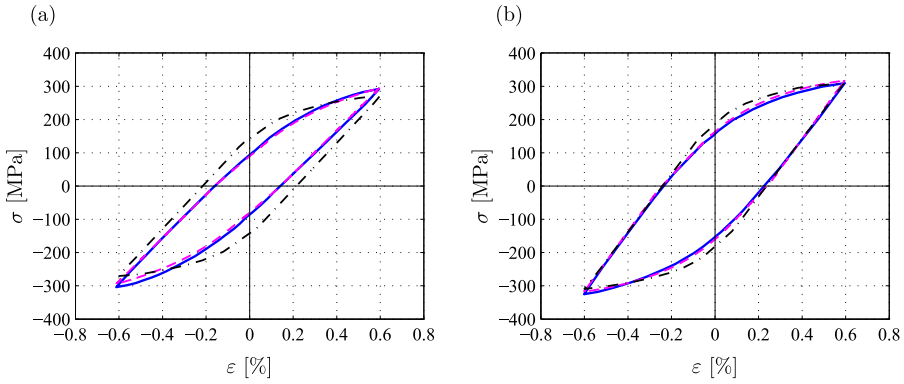

Fig. 7. Guo et al. (2013) experiment (——), model (– · –). Present model (— —). (a) Matrix, (b) alloy.

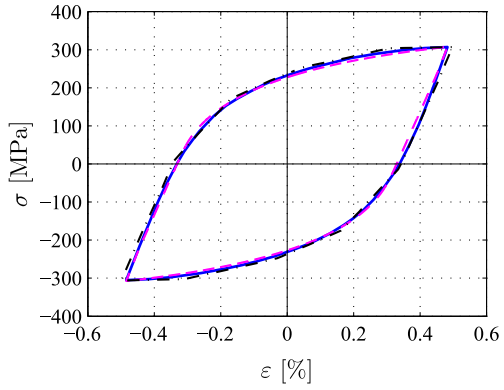

Fig. 8. Kang et al. (2003) experiment (——), model (– · –). Present model (— —).

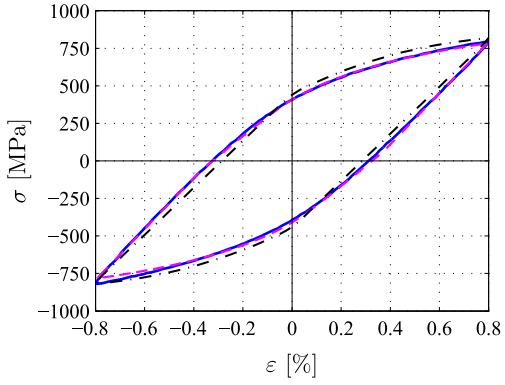

Fig. 9. Velay et al. (2006) experiment (——), model (– · –). Present model (— —).

Table 3
Model initial parameters.

Figure	E_e^0 [GPa]	E_i^0/E_e^0	σ_y^0 [MPa]	σ_m^0/σ_y^0	α^0
10	187	4.5	200	1.75	0.08
11	185	2.5	100	2.10	0.10
12(b)	200	3.5	140	0.68	0.45

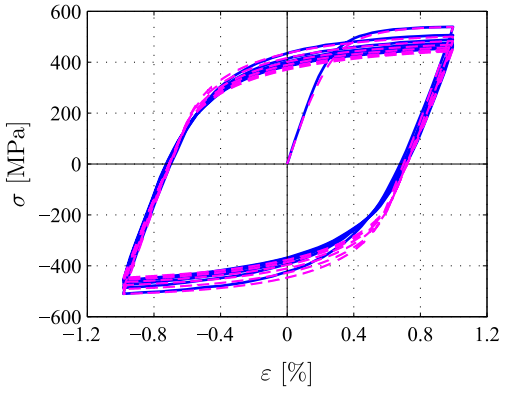

Fig. 10. Degradation: Hassan and Kyriakides (1992) experiment (——). Present model (— —).

6.1. Softening and hardening for constant amplitude strain cycling

A case of cyclic softening, i.e. degradation, is observed for carbon steel CS1020 as reported by Hassan and Kyriakides (1992). With a set of relatively simple evolution functions the uniaxial behaviour can be represented rather accurately with the present model as illustrated in Fig. 10. The experiment is strain controlled and the test specimen is cycled between 1% and -1% strain.

It is observed in Fig. 10 that the combined evolution mechanisms reproduce the shape of the hysteresis loops, the characteristic stress levels and the change in shape from the first loading branch to the remaining loading branches. There is a small discrepancy between the experimental results and the modelled results in the lower right corner, but overall the modelled and the experimental results are very similar.

The theory including model parameter evolution described in Section 4 can also be used to model cyclic hardening. Hassan and Kyriakides (1992) showed results of stainless steel with an initial significant cyclic hardening. In the experiments the hardening is primarily of the ultimate capacity, while the yield limit remains fairly constant. This corresponds to increasing σ_m with asymptotic stabilisation ($\eta^\infty_{\sigma_m} = 2.62$) and relatively slow change of σ_y ($\xi^*_{\sigma_y} \gg \xi^*_{\sigma_m}$). The experimental results are shown in Fig. 11 together

Table 4
Model evolution parameters.

Figure	ξ_e^* [–]	ξ_i^* [–]	$\xi^*_{\sigma_y}$ [MPa]	$\xi^*_{\sigma_m}$ [MPa]	ξ^*_α [kPa]	$\tilde{\eta}_e^\infty$	$\tilde{\eta}_i^\infty$	$\eta^\infty_{\sigma_y}$	$\eta^\infty_{\sigma_m}$	η^∞_α
10	2.0	0.7	20	-	2.0	0.0	0.0	0.55	1	11.75
11	9.0	1.0	100	50	1.8	0.0	0.4	0.00	2.62	9.20
12(b)	7.0	0.9	10	10	1.0	0.0	0.0	0.64	4.42	1.98

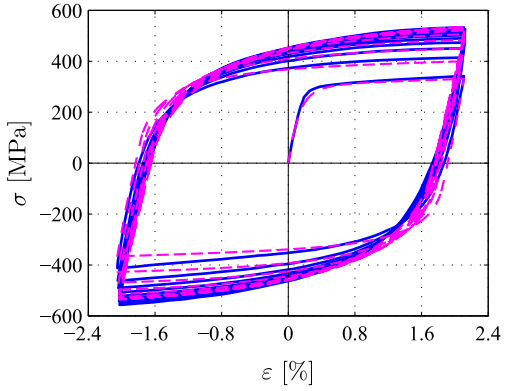

Fig. 11. Degradation: Hassan and Kyriakides (1992) experiment (——). Present model (– –).

Table 5
Biaxial ratcheting: Model initial parameters.

E_e [GPa]	μ_e [GPa]	E_i/E_e	μ_i/μ_e	σ_y^0 [MPa]	σ_m^0/σ_y^0	α^0
162	60.9	2.8	74.5	180	1.72	0.08

with the modelled results. The experiment is strain controlled, and cycled between 2.0% and -2.0% strain.

As shown in Fig. 11 the present model is fairly accurate for this type of behaviour as well. Each hysteresis cycle is represented rather accurately and the characteristic stress levels are also well represented by the model.

6.2. Hardening for increasing strain cycles

Similarly Kang et al. (2003) made experiments on cyclic hardening materials with a strain controlled experiment. The cycling was symmetric about zero mean strain, but with increasing amplitude starting at 0.18% and increasing with 0.30% for each cycle. The experimental results along with the results modelled by Kang et al. (2003) are shown in Fig. 12(a) whereas the experimental results together with results from the present model are shown in Fig. 12(b).

It is observed in Fig. 12 that the present model performs quite well - now with a total of 15 model parameters, five for the initial elasto-plastic model and 10 for the parameter evolution. The present model reproduces the hysteresis loops and the characteristic stress levels quite well, even with the very simple parameter evolution functions.

7. Biaxial ratcheting

To illustrate the capability to model multi-axial loading and ratcheting, experiments presented by Ohno and Wang (1993b) are modelled. In three experiments a specimen is loaded to a constant tension stress state σ giving an initial axial strain ε, and subsequently the shear strain γ is cyclically varied between $\pm\Delta\gamma/2$ resulting in axial strain ratcheting. In the biaxial stress state the elastic and the internal stiffness matrices take the form

$$\mathbb{C}_e = \begin{bmatrix} E_e & 0 \\ 0 & \mu_e \end{bmatrix}, \quad \mathbb{C}_i = \begin{bmatrix} E_i & 0 \\ 0 & \mu_i \end{bmatrix} \tag{51}$$

where E_e is the elastic Young's modulus and μ_e is the elastic shear modulus, whereas E_i and μ_i are the corresponding internal stiffness parameters. The initial model parameters are listed in Table 5. While the ratio E_i/E_e is similar to previous examples these hold no equivalent of the present ratio μ_i/μ_e.

Table 6
Biaxial ratcheting: Experiment characteristics.

Marker	σ [MPa]	$\Delta\gamma/\sqrt{3}$ [%]	$\Lambda \cdot 10^3$
▽	100	0.8	8.84
×	50	1.0	1.37
○	50	0.8	2.24
•	50	0.6	4.10

Table 7
Biaxial ratcheting: Model evolution parameters.

η_α^∞	ξ_α^* [kPa]	$\eta_{\sigma_m}^\infty$	$\frac{\eta_{\sigma_m}^\infty - 1}{\xi_{\sigma_m}^*}$ [GPa^{-1}]
10.6	2.5	1.43 (▽) 2.10 (×)	86.4

In the experiments there is no direct cycling of the axial stress, but rather an indirect effect due to the interaction with the cycling of the shear stain. The combined effect of the different levels of prestress, strain range and degrees of non-proportionality can be represented via a change in the single parameter σ_m as given by an interpolation scheme introduced by Benallal and Marquis (1987),

$$\eta_{\sigma_m}^\infty(\Lambda) = \Lambda\,\eta_{\sigma_m}^\infty(1) + (1-\Lambda)\,\eta_{\sigma_m}^\infty(0), \quad \Lambda = 1 - \cos^2\theta, \tag{52}$$

where θ is the angle between the incremental plastic strain $d\boldsymbol{\varepsilon}^p$ and the incremental deviatoric stress $d\boldsymbol{\sigma}'$, formally considered as vectors. In practice the interpolation does not cover the interval $0 \le \Lambda \le 1$, but typically a much smaller interval between two experiments is used as the basis of the interpolation. The stress and the strain range values used in the experiments are given in Table 6, together with estimated values of the parameter Λ. The value of Λ as well as the parameter $\eta_{\sigma_m}^\infty(\Lambda)$ in these two cases are used as basis, and the interpolated value of $\eta_{\sigma_m}^\infty$ is then obtained by estimating a representative value of Λ for each of the remaining experiments. In the experiments the parameter σ_m increases whereby $\eta_{\sigma_m}^\infty > 0$. It turns out that the corresponding attenuation parameter $\xi_{\sigma_m}^*$ can be assumed proportional to the relative increase of σ_m whereby the ratio $(\eta_{\sigma_m}^\infty - 1)/\xi_{\sigma_m}^*$ is a constant, that is determined from the uniaxial hysteresis curve. The resulting evolution parameters are listed in Table 7. The experiments marked with ▽ and × in Table 6 were used as basis for determining the values at the end of the interpolation interval. The remaining values of $\eta_{\sigma_m}^\infty$ are then obtained by the interpolation procedure. It is noted that only the parameter σ_m^∞ has been subjected to interpolation to account for different values of Λ. In practical cases with unknown stress states at different times and different points in a structure an initial analysis may be performed to determine a representative value for Λ for the given loading condition and subsequently the analysis may be performed with values determined from the interpolation scheme.

The uniaxial stress-strain behaviour is shown in Fig. 13 with all four model parameter combinations and they all show good correspondence with the experimental behaviour and are indistinguishable from one another in the uniaxial single-cycle.

The biaxial ratcheting effect is shown in Fig. 14 where the accumulated axial strain is plotted against the number of shear strain cycles. The modelled results agree well with the experimental results as illustrated in Fig. 14. There is a slight offset between the modelled results and the experimental results when $\sigma = 50$ MPa and $\Delta\gamma/\sqrt{3} = 1.0\,\%$ in the cycles 10–15, but the difference is almost negligible.

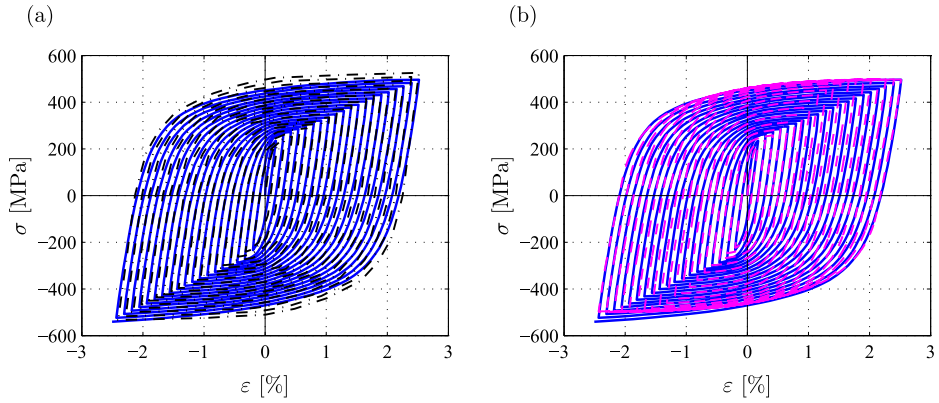

Fig. 12. Cyclic hardening: (a) Kang et al. (2003) experiment (——), model (– · –). (b) Kang et al. (2003) experiment (——). Present model (— —).

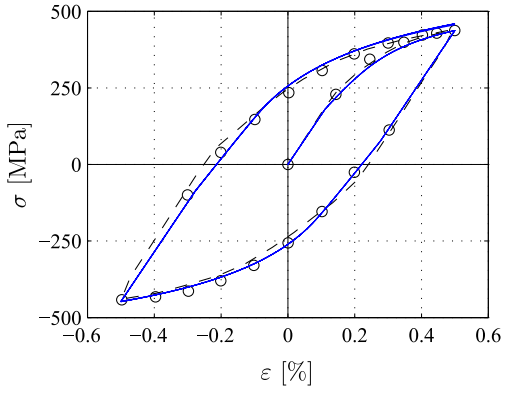

Fig. 13. Uniaxial cycling. Tanaka et al. (1991) experiment (○). Ohno and Wang (1993b) model (– –). Present model (——).

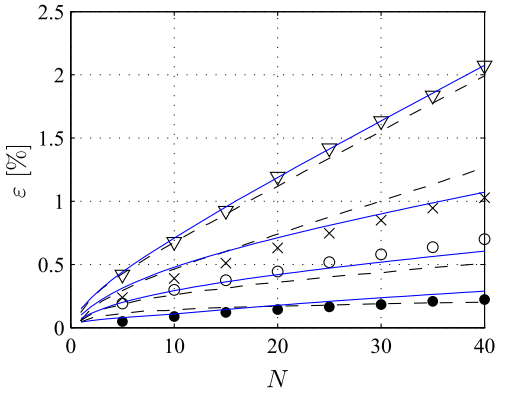

Fig. 14. Biaxial cycling. Tanaka et al. (1991) experiment (▽, ×, ○, •). Ohno and Wang (1993b) model (– –). Present model (——).

8. Conclusions

A simple five-parameter model has been developed for cyclic plasticity. The model parameters are the external and internal stiffness, the yield stress and a stress range parameter σ_m representing the difference between ultimate stress and the yield stress, and finally a non-dimensional shape parameter α describing the development of plastic strain. Each of the five parameters describe a fairly well defined independent feature of the stress strain relation, and thus the parameters can be estimated initially as independent, and subjected to subsequent minor adjustment, if necessary. In the present format the shape parameter α, replaces the often used representation of the internal stress $\boldsymbol{\sigma}_i$ as a sum of stress states, each with their own parameters. The present single parameter modification permits an accurate representation of the cyclic stress-strain loops, and the parameter α exhibits a fairly modest variation for the experimental data analyzed. It also accounts for the experimental observation that the developed plastic strains are larger than predicted by the classic Armstrong–Frederick model, contained in the present model as the special case $\alpha = 0$.

The five-parameter plasticity formulation has been extended by including possible evolution of the model parameters in a format similar to traditional damage-theory. The format contains the plastic multiplier, and evolution of the model parameters can therefore be included by a fairly direct extension of the plasticity format. The ability of this formulation to describe cyclic hardening and softening has been demonstrated by comparison with fairly extensive uniaxial experimental data. The model has also been used for two-dimensional ratcheting, representing the effect of the range magnitude and component ratio via a parameter interpolation scheme involving only the stress range parameter σ_m.

In the literature various forms of the Armstrong–Frederick plasticity model have been recast into visco-plastic form by replacing the plastic strain rate term in the evolution equation of the internal stresses $\boldsymbol{\sigma}_i$ with an expression in terms of current stress. As this transformation does not influence the format of the second term, the present format of this term can be retained in a visco-plastic formulation of the model. However, this aspect has not been included in the present paper.

Acknowledgements

This paper is part of a project sponsored jointly by Innovation Fund Denmark, Maersk Oil A/S and the Technical University of Denmark.

References

Abdel-Karim, M., 2010. An extension for the ohno–wang kinematic hardening rules to incorporate isotropic hardening. Int. J. Press. Vessels Pip. 87, 170–176.
Armstrong, P.J., Frederick, C.O., 1966. A mathematical representation of the multiaxial Bauschinger effect. Technical Report. CEGB, Central Electricity Generating Board, Berkeley, UK. (Reprinted in Materials at High Temperatures, 24, 1–26, 2007).
Benallal, A., Marquis, D., 1987. Constitutive equations for nonproportional cyclic elasto-viscoplasticity. J. Eng. Mat. Technol. ASME 109, 326–336.
Calloch, S., Marquis, D., 1999. Triaxial tension-compression tests for multiaxial cyclic plasticity. Int. J. Plast. 15, 521–549.
Chaboche, J.L., 1986. Time-independent constitutive theories for cyclic plasticity. Int. J. Plast. 2, 149–188.
Chaboche, J.L., 1989. Constitutive equations for cyclic plasticity and cyclic viscoplasticity. Int. J. Plast. 5, 247–302.
Chaboche, J.L., 1994. Modeling of ratchetting: evaluation of various approaches. Eur. J. Mech. Solids 13, 501–518.
Chaboche, J.L., 2008. A review of some plasticity and viscoplasticity constitutive theories. Int. J. Plast. 24, 1642–1693.

Chaboche, J.L., Rousselier, G., 1983. On the plastic and viscoplastic constitutive equations – part 1: rules developed with internal variable concept. J. Press. Vessel Technol. 105, 153–158.
Chun, B.K., Jinn, J.T., Lee, J.K., 2002. Modeling the Bauschinger effect for sheet metals, part I: theory. Int. J. Plast. 18, 571–595.
Dafalias, Y.F., Popov, E.P., 1975. A model of nonlinearly hardening materials for complex loading. Acta Mech. 21, 173–192.
Dafalias, Y.F., Popov, E.P., 1976. Plastic internal variables formalism of cyclic plasticity. J Appl Mech. 43, 645–651.
Guo, S., Kang, G.Z., Zhang, J., 2013. A cyclic visco-plastic constitutive model for time-dependent ratchetting of particle-reinforced metal matrix composites. Int. J. Plast. 40, 101–125.
Hassan, T., Corona, E., Kyriakides, S., 1992. Ratcheting in cyclic plasticity, part II: multiaxial behavior. Int. J. Plast. 8, 117–146.
Hassan, T., Kyriakides, S., 1992. Ratcheting in cyclic plasticity, part I: uniaxial behavior. Int. J. Plast. 8, 91–116.
Hopperstad, O.S., Langseth, M., Remseth, S., 1995. Cyclic stress-strain behaviour of alloy AA6060 T4, part II: biaxial experiments and modelling. Int. J. Plast. 11, 741–762.
Ibrahimbegovic, A., Jehel, P., Davenne, L., 2008. Coupled damage-plasticity constitutive model and direct stress interpolation. Comput Mech 42, 1–11.
Kang, G.Z., Ohno, N., Nebu, A., 2003. Constitutive modeling of strain range dependent cyclic hardening. Int. J. Plast. 19, 1801–1819.
Krieg, R.D., 1975. A practical two surface plasticity theory. J. Appl. Mech. 42, 641–646.
Lemaitre, J., 1985. Coupled elasto-plasticity and damage constitutive equations. Comput Methods Appl Mech Eng 51, 31–49.
Masing, G., 1927. Wissenschaftliche Veröffentlichungen aus dem Siemens-Konzern. Band III..
Mroz, Z., 1967. On the description of anisotropic workhardening. J. Mech. Phys. Solids 15, 163–175.
Ohno, N., Wang, J.-D., 1993. Kinematic hardening rules with critical state of dynamic recovery, part I: formulation and basic features for ratchetting behavior. Int. J. Plast. 9, 375–390.
Ohno, N., Wang, J.-D., 1993. Kinematic hardening rules with critical state of dynamic recovery, part II: application to experiments of ratchetting behavior. Int. J. Plast. 9, 391–403.
Ottosen, N.S., Ristinmaa, M., 2005. The mechanics of constitutive modeling. Elsevier, Amsterdam, The Netherlands.
Pham, M.S., Holdsworth, S.R., Janssens, K.G.F., Mazza, E., 2013. Cyclic deformation response of AISI 316l at room temperature: mechanical behavior, microstructural evolution, physically-based evolutionary constitutive modelling. Int. J. Plast. 47, 143–164.
Popov, E.P., Petersson, H., 1978. Cyclic metal plasticity: experiments and theory. J. Engineering Mechanics Division, ASCE. 114, EM6, 1371–1388.
Prager, W., 1956. A new method of analyzing stresses and strains in work-hardening plastic solids. J Appl Mech 23, 493–496.
Shi, G., Wang, M., Bai, Y., Wang, F., Shi, Y., Wang, Y., 2012. Experimental and modeling study of high-strength structural steel under cyclic loading. Eng. Struct. 37, 1–13.
Tanaka, E., Murakami, S., Mizuno, M., Yamada, H., Iwata, K., 1991. Inelastic behavior of modified 9Cr-1Mo steel and its unified constitutive model. In: Proceedings of the 6th International Conference on Mechanical Behaviour of Materials, Vol. 3. Pergamon Press, Oxford.
Tarigopula, V., Hopperstad, O., Langseth, M., Clausen, A.H., 2008. Elastic-plastic behaviour of dual-phase, high-strength steel under strain-path changes. Euro. J. Mech. Solids 27, 764–782.
Tidemann, L., Krenk, S., 2017. Cyclic plastic hinges with degradation effects for frame structures. J. Eng. Mech.. (accepted for publication)
Velay, V., Bernhart, G., Penazzi, L., 2006. Cyclic behavior modeling of a tempered martensitic hot work tool steel. Int. J. Plast. 22, 459–496.
Wolff, M., Taleb, L., 2008. Consistency for two multi-mechanism models in isothermal plasticity. Int. J. Plast. 24, 2059–2083.
Xiao, Y., Chen, J., Cao, J., 2012. A generalized thermodynamic approach for modeling nonlinear hardening behaviors. Int. J. Plast. 38, 102–122.
Ziegler, H., 1959. A modification of Prager's hardening rule. Q. Appl. Math. 17, 55–65.

P2

Cyclic plastic hinges with degradation effects for frame structures

L. Tidemann & S. Krenk

Journal of Engineering Mechanics,
Vol. **143**(12):04017142-1–15, 2017.

Cyclic Plastic Hinges with Degradation Effects for Frame Structures

Lasse Tidemann[1] and Steen Krenk[2]

Abstract: A model of cyclic plastic hinges in frame structures including degradation effects for stiffness and strength is developed. The model is formulated via potentials in terms of section forces. It consists of a yield surface, described in a generic format permitting representation of general convex shapes including corners, and a set of evolution equations based on an internal energy potential and a plastic flow potential. The form of these potentials is specified by five parameters for each generalized stress-strain component describing yield level, ultimate stress capacity, elastic and elastoplastic stiffnesses, and a shape parameter. The model permits gradual changes in stiffness and strength parameters via damage-based degradation. The degradation effects are introduced in the energy and flow potentials and result in additional evolution equations for the corresponding strength and stiffness parameters. The cyclic plastic hinges are introduced into a six-component equilibrium-based beam element, using additive element and hinge flexibilities. When converted to stiffness format the plastic hinges are incorporated into the element stiffness matrix. The cyclic plastic hinge model is implemented in a computer program and used for analysis of some simple structures, illustrating the characteristic features of the cyclic response and the accuracy of the proposed model.
DOI: 10.1061/(ASCE)EM.1943-7889.0001358.

Author keywords: Cyclic plasticity; Plastic hinges; Frame structures; Damage effects.

Introduction

The concept of plastic hinges has been widely used for ultimate load carrying capacity analysis with focus on monotonically varying loads (Powell and Chen 1986; Liew et al. 1993; Attalla et al. 1994; Krenk et al. 1999), but also to a more limited extent for analysis with cyclic plasticity as, e.g., earthquake response analysis, taking into account some kind of degradation effect (Inglessis et al. 1999; Kaewkulchai and Williamson 2004). The theory of plastic hinges was introduced in the late 1960s for both monotonic loading (Ueda et al. 1968) and cyclic loading with large displacements (Ueda et al. 1969). The theory of elastic tangent stiffness matrix for large displacement and small deformation was derived by Oran (1973) with the use of an equilibrium format of the beam. The theory of concentrated yield hinges in beams was further extended to a general plastic node method (Ueda and Yao 1982) with extensions to, e.g., plate elements. Other works on plastic hinge theory for beams include analysis of the effect of geometric nonlinearity (Liew et al. 2000), spread of plasticity (Jiang et al. 2002), and plastic behavior during fire (Iu and Chan 2004).

One of the early works on cyclic plasticity with degradation in relation to structures (Baber and Wen 1981) focused on random vibrations but emphasized the importance of degradation mechanisms and the identification of these in the mathematical model as well as the separation of the individual mechanisms in the model. Later works (Ibarra et al. 2005; Lignos and Krawinkler 2011; Kamaris et al. 2013) adopted the concept of separation of the mechanisms by modeling each section force component separately with predefined hysteresis and backbone curves and describing relevant model parameters statistically. Degradation mechanisms have also been introduced into beam elements via the flexibility format, in which plasticity and degradation have been combined using specified degradation functions (Inglessis et al. 1999; Cipollina et al. 1995).

The degradation mechanisms typically include degradation of elastic stiffness, elastoplastic stiffness, the yield capacity of the different section force components, and the ultimate capacity of the section force components. The effects were experimentally observed in reinforced concrete structures (Lu et al. 1999; Masi et al. 2013), where a substantial part of the degradation originates from cracking in the concrete, and in steel structures (Popov et al. 1980; Mamaghani and Kajikawa 1998; Elchalakani et al. 2003; Elchalakani 2007), where the degradation mechanisms typically include fracture and local buckling.

Key ingredients in plasticity theories are the yield surface and the gradient of the flow potential, which may be obtained for beam cross sections using analytical expressions (Chen and Atsuta 2008) or numerical estimates (Liu et al. 2009). However, for most practical purposes it is of interest to use an approximate representation of the yield surface and the flow potential, because most analytical yield surfaces describing beam cross sections are based on ideal plasticity and have corners with undefined gradients (Chen and Atsuta 2008). A multilinear approximation of experimental yield surfaces also introduces corners, and certain measures have to be taken to overcome the problem with undefined gradients at the corners (e.g., Krenk et al. 1993). Furthermore, a multilinear representation leads to multiple algorithmic checks for violation of the yield constraint, a complication that may be circumvented by approximating the yield surface using a single-equation approximation (e.g., Kitipornchai et al. 1991). To overcome problems with undefined gradients at corners in a multilinear approximation, Orbison et al. (1982) proposed a single-equation representation

[1]Industrial Ph.D. Student, Dept. of Mechanical Engineering, Technical Univ. of Denmark, DK-2800 Kongens Lyngby, Denmark (corresponding author). ORCID: https://orcid.org/0000-0003-4004-2072. E-mail: lastid@mek.dtu.dk

[2]Professor, Dept. of Mechanical Engineering, Technical Univ. of Denmark, DK-2800 Kongens Lyngby, Denmark.

Note. This manuscript was submitted on January 12, 2017; approved on May 25, 2017; published online on October 13, 2017. Discussion period open until March 13, 2018; separate discussions must be submitted for individual papers. This paper is part of the ***Journal of Engineering Mechanics***, © ASCE, ISSN 0733-9399.

of the yield function as a sum of even powers of the generalized stress components for I-beams. However, it was quite difficult to guarantee convexity of yield surfaces of this format. In contrast, convexity is ensured when using ellipsoids for approximation of the yield surface, and an early proposal (Willam and Warnke 1974) for the use of an elliptical approximation of yield surfaces has been fairly widely adopted, e.g., by Folino et al. (2009). However, the determination of the necessary gradients may be elaborate and the format has limited flexibility with regard to general geometric shapes.

In order to increase the flexibility of the representation, various methods known from isogeometric analysis have been proposed during recent years. Coombs et al. (2016) suggested a nonuniform rational B-spline (NURBS)–based approach that can in principle accurately approximate any yield surface, provided the control points can be chosen appropriately. Hardening may be introduced via movement of the control points, providing an option of modifying the shape of the yield surface locally during hardening. Depending on the number of control points, however, it may be cumbersome, and special care has to be taken to ensure convexity of the surface. Bleyer and de Buhan (2013a, b) suggested an alternative quite simple and flexible generic surface format using a Minkowski sum of ellipsoids ensuring convexity. The format has a high accuracy but the actual formation of the Minkowski sum and derivation of the gradients may be difficult.

This paper develops a cyclic plasticity formulation for plastic hinges in beam elements. First, the basic evolution equations for cyclic plasticity with optional degradation of stiffness and strength are developed, generalizing the stress-based von Mises theory presented by Krenk and Tidemann (2017) to a format in terms of normalized section forces. Then a novel generic yield surface format, based on the sum of square roots of quadratic forms, is introduced. This yield surface format plays a key role in representing realistic convex yield surfaces for beam cross sections, and includes the option of smoothing sharp corners of the surface. The cyclic plasticity model is then implemented in the form of plastic hinges into a beam element via the flexibility format from Krenk et al. (1999), including the derivation of the consistent algorithmic tangent stiffness matrix. Finally, examples illustrate the characteristic properties of the cyclic response and the accuracy of the proposed model.

Plastic Hinge Model

A plastic hinge in a beam is a local deformation mechanism located at a cross section of the beam in which local elongation and angle discontinuities are considered as generalized plastic strains corresponding to generalized stresses defined in terms of the local section forces. For beams, the generalized stresses governing the behavior of plastic hinges will typically be the normal force and two bending moments (Fig. 1). Other section forces may also be included but are typically of minor influence.

Thus the generalized stresses and strains used are defined as

$$\boldsymbol{\tau} = [N, M_y, M_z, \ldots]^T, \qquad \boldsymbol{\gamma} = [\varepsilon_x, \kappa_y, \kappa_z, \ldots]^T \tag{1}$$

These generalized stresses and strains are used to define a cyclic plasticity model, following the procedure developed by Krenk and Tidemann (2017). The first step is to introduce an internal energy function consisting of a sum of three contributions: a quadratic function of the generalized elastic strains $\boldsymbol{\gamma}_\mathrm{e}$, a quadratic function of a corresponding set of generalized internal strains $\boldsymbol{\gamma}_\mathrm{i}$, and an additive function of a set of generalized strains $\boldsymbol{\xi}$ representing damage. The internal energy hereby takes the form

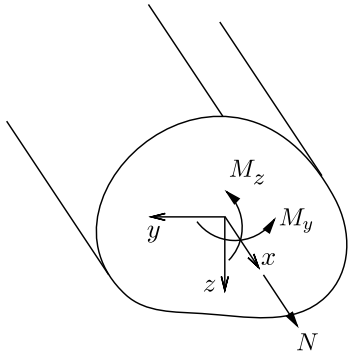

Fig. 1. Beam cross section with section forces as generalized stresses

$$\varphi(\boldsymbol{\gamma}_\mathrm{e}, \boldsymbol{\gamma}_\mathrm{i}, \boldsymbol{\xi}) = \frac{1}{2}\boldsymbol{\gamma}_\mathrm{e}^T \mathbb{D}_\mathrm{e}(\boldsymbol{\xi})\boldsymbol{\gamma}_\mathrm{e} + \frac{1}{2}\boldsymbol{\gamma}_\mathrm{i}^T \mathbb{D}_\mathrm{i}(\boldsymbol{\xi})\boldsymbol{\gamma}_\mathrm{i} + \varphi_\mathrm{d}(\boldsymbol{\xi}) \tag{2}$$

The matrices $\mathbb{D}_\mathrm{e}(\boldsymbol{\xi})$ and $\mathbb{D}_\mathrm{i}(\boldsymbol{\xi})$ representing the contributions from the elastic and the internal strains may depend on the damage parameters $\boldsymbol{\xi}$, thereby permitting changes in stiffness due to degradation. The energy conjugate generalized stresses are found via differentiation of the energy potential as

$$\boldsymbol{\tau} = \partial_{\boldsymbol{\gamma}_\mathrm{e}}\varphi = \mathbb{D}_\mathrm{e}(\boldsymbol{\xi})\boldsymbol{\gamma}_\mathrm{e} \tag{3}$$

$$\boldsymbol{\tau}_\mathrm{i} = \partial_{\boldsymbol{\gamma}_\mathrm{i}}\varphi = \mathbb{D}_\mathrm{i}(\boldsymbol{\xi})\boldsymbol{\gamma}_\mathrm{i} \tag{4}$$

$$\boldsymbol{\eta} = \partial_{\boldsymbol{\xi}}\varphi \tag{5}$$

It is observed that the generalized stresses $\boldsymbol{\tau}$ and the generalized internal stresses $\boldsymbol{\tau}_\mathrm{i}$ defined via Eqs. (3) and (4), respectively, have a Hooke's law–type relation to their energy conjugate generalized strains.

Normalized Yield Surface and Flow Potential

In plasticity models such as the one presented here, based on generalized stresses representing different quantities like forces and moments, plasticity parameters such as yield and ultimate stress levels may be different and also may develop differently during plastic loading. This suggests the use of the normalized section forces $[n, m_y, m_z, \ldots] = [N/N^y, M_y/M_y^y, M_z/M_z^y, \ldots]$ in the formulation of the yield surface and the flow potential. This corresponds to using normalized generalized stresses $\tilde{\boldsymbol{\tau}}$ and normalized internal stresses $\tilde{\boldsymbol{\tau}}_\mathrm{i}$ defined by

$$\tilde{\boldsymbol{\tau}}(\boldsymbol{\eta}) = \mathbb{B}_y^{-1}\boldsymbol{\tau}, \qquad \tilde{\boldsymbol{\tau}}_\mathrm{i}(\boldsymbol{\eta}) = \mathbb{B}_y^{-1}\boldsymbol{\tau}_\mathrm{i} \tag{6}$$

where the normalization coefficients are arranged in the diagonal matrix

$$\mathbb{B}_y(\boldsymbol{\eta}) = \begin{bmatrix} N^y(\boldsymbol{\eta}) & & & \\ & M_y^y(\boldsymbol{\eta}) & & \\ & & M_z^y(\boldsymbol{\eta}) & \\ & & & \ddots \end{bmatrix} \tag{7}$$

It is convenient to choose the normalization coefficients as the current yield level for the corresponding single component load.

The yield surface bounds the elastic generalized stress states. In cyclic plasticity the yield surface moves in stress space, and the simplest format consists of a translation of the yield surface described by the generalized internal stresses $\boldsymbol{\tau}_\mathrm{i}$, the so-called

kinematic hardening. This is conveniently represented by the generic yield function format

$$F(\boldsymbol{\tau}, \boldsymbol{\tau}_{\mathrm{i}}, \boldsymbol{\eta}) = \|\tilde{\boldsymbol{\tau}}(\boldsymbol{\eta}) - \tilde{\boldsymbol{\tau}}_{\mathrm{i}}(\boldsymbol{\eta})\| - 1 \tag{8}$$

where $\|\cdot\|$ = suitable norm of the normalized generalized stresses; and $\tilde{\boldsymbol{\tau}}_{\mathrm{i}}(\boldsymbol{\eta})$ = current center of the normalized yield function. It is well known from von Mises plasticity that a particularly simple formulation is obtained when the yield condition is expressed via the equivalent stress σ_{e}, which is a homogeneous form of degree one in the stress components. This concept is extended to a more general yield function of degree one in the "Generic Yield Surface" section.

The flow potential controls the direction of the increments of the generalized plastic strains and the strain-like damage parameters. The basic form of the flow potential is constructed in a way similar to the flow potential in the stress-based model of Krenk and Tidemann (2017), in which a quadratic term of the normalized internal generalized stresses $\tilde{\boldsymbol{\tau}}_{\mathrm{i}}$ is added to the yield function along with an unspecified function of the stress-like damage parameters, $\boldsymbol{\eta}$, giving the flow potential

$$G(\boldsymbol{\tau}, \boldsymbol{\tau}_{\mathrm{i}}, \boldsymbol{\eta}) = F(\boldsymbol{\tau}, \boldsymbol{\tau}_{\mathrm{i}}, \boldsymbol{\eta}) + \frac{1}{2}\tilde{\boldsymbol{\tau}}_{\mathrm{i}}^T \mathbb{B}_{\beta}^{-1} \tilde{\boldsymbol{\tau}}_{\mathrm{i}} + G_{\mathrm{d}}(\boldsymbol{\eta}) \tag{9}$$

where $\tilde{\boldsymbol{\tau}}_{\mathrm{i}} = \tilde{\boldsymbol{\tau}}_{\mathrm{i}}(\boldsymbol{\eta})$ and the coefficient matrix $\mathbb{B}_{\beta}$ is defined as

$$\mathbb{B}_{\beta}(\boldsymbol{\eta}) = \begin{bmatrix} \beta_N(\boldsymbol{\eta}) & & & \\ & \beta_{M_y}(\boldsymbol{\eta}) & & \\ & & \beta_{M_z}(\boldsymbol{\eta}) & \\ & & & \ddots \end{bmatrix} \tag{10}$$

In the yielding process, the yield surface moves as described by the normalized center stress $\tilde{\boldsymbol{\tau}}_{\mathrm{i}}$. The first term in the flow potential Eq. (9) is of degree one, whereas the second term is of degree two. Hereby the parameters in the array $\boldsymbol{\beta} = [\beta_N, \beta_{M_y}, \beta_{M_z}, \ldots]^T$ determine the limits on the normalized center stress components $\tilde{\boldsymbol{\tau}}_{\mathrm{i}}$, thereby defining the ultimate stress capacity. In the von Mises stress-based model (Krenk and Tidemann 2017), the ratio between ultimate and initial yield level is given by a single parameter corresponding to $1 + \beta$, whereas in the present model the additional capacity is defined individually for each generalized stress component.

Generalized Stress Evolution Matrix

The evolution equations for external stresses, internal stresses and damage parameters are derived from the assumption of maximum dissipation rate. The dissipation rate is expressed as the rate of externally supplied energy $\boldsymbol{\tau}\dot{\boldsymbol{\gamma}}$ minus the change in the internal energy represented by $\dot{\varphi}$

$$\dot{\mathcal{D}} = \boldsymbol{\tau}\dot{\boldsymbol{\gamma}} - \dot{\varphi}(\boldsymbol{\gamma}_{\mathrm{e}}, \boldsymbol{\gamma}_{\mathrm{i}}, \boldsymbol{\xi}) \geq 0 \tag{11}$$

It is assumed that the observable generalized strain $\boldsymbol{\gamma}$ is the sum of the generalized elastic strain $\boldsymbol{\gamma}_{\mathrm{e}}$ and the generalized plastic strain $\boldsymbol{\gamma}_{\mathrm{p}}$. The evolution equations for the generalized stresses and damage parameters are derived by maximizing the dissipation rate, under the constraint that the material can be described by the flow potential, $G(\boldsymbol{\tau}, \boldsymbol{\tau}_{\mathrm{i}}, \boldsymbol{\eta})$, and the consistency condition $\dot{F}(\boldsymbol{\tau}, \boldsymbol{\tau}_{\mathrm{i}}, \boldsymbol{\eta}) = 0$.

The first step is to express the time increments of the generalized stress and stress-like damage variables given by Eqs. (3)–(5) in the compact form

$$\begin{bmatrix} \dot{\boldsymbol{\tau}} \\ \dot{\boldsymbol{\tau}}_{\mathrm{i}} \\ \dot{\boldsymbol{\eta}} \end{bmatrix} = \mathbb{D}_{\mathrm{eid}} \begin{bmatrix} \dot{\boldsymbol{\gamma}}_{\mathrm{e}} \\ \dot{\boldsymbol{\gamma}}_{\mathrm{i}} \\ \dot{\boldsymbol{\xi}} \end{bmatrix} \tag{12}$$

where the combined external-internal-damage evolution matrix is introduced as

$$\mathbb{D}_{\mathrm{eid}}(\boldsymbol{\xi}) = \begin{bmatrix} \mathbb{D}_{\mathrm{e}}(\boldsymbol{\xi}) & \mathbf{0} & \partial_{\boldsymbol{\xi}}^T \boldsymbol{\tau} \\ \mathbf{0} & \mathbb{D}_{\mathrm{i}}(\boldsymbol{\xi}) & \partial_{\boldsymbol{\xi}}^T \boldsymbol{\tau}_{\mathrm{i}} \\ (\partial_{\boldsymbol{\xi}}^T \boldsymbol{\tau})^T & (\partial_{\boldsymbol{\xi}}^T \boldsymbol{\tau}_{\mathrm{i}})^T & \partial_{\boldsymbol{\xi}}^T \boldsymbol{\eta} \end{bmatrix} \tag{13}$$

The evolution equations for the generalized strain, internal strain and the strain-like damage parameters follow from the maximum dissipation condition Eq. (11) in the form

$$\begin{bmatrix} \dot{\boldsymbol{\gamma}} \\ \mathbf{0} \\ \mathbf{0} \end{bmatrix} = \begin{bmatrix} \dot{\boldsymbol{\gamma}}_{\mathrm{e}} \\ \dot{\boldsymbol{\gamma}}_{\mathrm{i}} \\ \dot{\boldsymbol{\xi}} \end{bmatrix} + \dot{\lambda} \boldsymbol{\partial} G^T \tag{14}$$

where the flow potential gradient is defined as

$$\boldsymbol{\partial} G = [\partial_{\boldsymbol{\tau}}^T G, \partial_{\boldsymbol{\tau}_{\mathrm{i}}}^T G, \partial_{\boldsymbol{\eta}}^T G]^T \tag{15}$$

During plastic flow the stress remains on the yield surface, leading to the consistency condition

$$\dot{F} = \boldsymbol{\partial} F^T \begin{bmatrix} \dot{\boldsymbol{\tau}} \\ \dot{\boldsymbol{\tau}}_{\mathrm{i}} \\ \dot{\boldsymbol{\eta}} \end{bmatrix} = 0 \tag{16}$$

in terms of the yield function gradient

$$\boldsymbol{\partial} F = [\partial_{\boldsymbol{\tau}}^T F, \partial_{\boldsymbol{\tau}_{\mathrm{i}}}^T F, \partial_{\boldsymbol{\eta}}^T F]^T \tag{17}$$

Substitution of the generalized stress rate vector from Eq. (12) and use of the evolution Eq. (14) gives an equation for the multiplier $\dot{\lambda}$, from which

$$\dot{\lambda} = \frac{\boldsymbol{\partial} F^T \mathbb{D}_{\mathrm{ed}} \dot{\boldsymbol{\gamma}}}{\boldsymbol{\partial} F^T \mathbb{D}_{\mathrm{eid}} \boldsymbol{\partial} G} \tag{18}$$

where the block matrix $\mathbb{D}_{\mathrm{ed}}$ is the first column of the block matrix $\mathbb{D}_{\mathrm{eid}}$

$$\mathbb{D}_{\mathrm{ed}}(\boldsymbol{\xi}) = [\mathbb{D}_{\mathrm{e}}(\boldsymbol{\xi}), \mathbf{0}, \partial_{\boldsymbol{\xi}}^T \boldsymbol{\tau}]^T \tag{19}$$

The final evolution equation for the generalized stresses and the stress-like damage parameters then follow from Eq. (12) by substitution of the generalized strain parameters from Eq. (14) and the multiplier from Eq. (18)

$$\begin{bmatrix} \dot{\boldsymbol{\tau}} \\ \dot{\boldsymbol{\tau}}_{\mathrm{i}} \\ \dot{\boldsymbol{\eta}} \end{bmatrix} = \left[\mathbb{D}_{\mathrm{ed}} - \frac{\mathbb{D}_{\mathrm{eid}}(\boldsymbol{\partial} G)(\boldsymbol{\partial} F)^T \mathbb{D}_{\mathrm{ed}}}{(\boldsymbol{\partial} F)^T \mathbb{D}_{\mathrm{eid}}(\boldsymbol{\partial} G)} \right] \dot{\boldsymbol{\gamma}} \tag{20}$$

From Eq. (20), the elastoplastic stiffness is identified as

$$\mathbb{D}_{\mathrm{eid}}^{\mathrm{ep}} = \mathbb{D}_{\mathrm{ed}} - \frac{\mathbb{D}_{\mathrm{eid}}(\boldsymbol{\partial} G)(\boldsymbol{\partial} F)^T \mathbb{D}_{\mathrm{ed}}}{(\boldsymbol{\partial} F)^T \mathbb{D}_{\mathrm{eid}}(\boldsymbol{\partial} G)} \tag{21}$$

where the subscript eid indicates that the elastoplastic stiffness matrix relates to the generalized external, internal, and damage stresses; and the superscript ep indicates the elastoplastic stiffness

matrix. With this formulation, $\mathbb{D}_e$ describes the elastic stiffness, $\mathbb{D}_i$ describes the tangent stiffness at initial yield, and the β-parameters describe the relative value of the ultimate capacity of the respective generalized stress components.

Plastic Straining and Enhanced Flow Potential

The elastic stiffness is described by the stiffness matrix $\mathbb{D}_e$. At initial yield, additive plastic strains appear, and if disregarding possible damage effects in this particular context, the initial elastoplastic stress-strain relation follows from Eq. (20) in the form

$$\dot{\boldsymbol{\tau}} = \mathbb{D}_e\dot{\boldsymbol{\gamma}} - \mathbb{D}_e(\partial_{\boldsymbol{\tau}}G)\frac{(\partial_{\boldsymbol{\tau}}^T F)\mathbb{D}_e\dot{\boldsymbol{\gamma}}}{(\partial_{\boldsymbol{\tau}}^T F)\mathbb{D}_e(\partial_{\boldsymbol{\tau}}G) + (\partial_{\boldsymbol{\tau}_i}^T F)\mathbb{D}_i(\partial_{\boldsymbol{\tau}_i}G)} \tag{22}$$

In general, the elastic and the plastic strain rates may have different directions. However, if the directions are assumed to be identical, amounting to proportionality between the strain rate and the stress gradient of the flow potential, $\dot{\boldsymbol{\gamma}} \propto \partial_{\boldsymbol{\tau}}G$, the stress-strain evolution relation Eq. (22) can be expressed in the form

$$\dot{\boldsymbol{\tau}} = \frac{\mathbb{D}_e\dot{\boldsymbol{\gamma}}}{1 + \frac{(\partial_{\boldsymbol{\tau}}^T F)\mathbb{D}_e(\partial_{\boldsymbol{\tau}}G)}{(\partial_{\boldsymbol{\tau}_i}^T F)\mathbb{D}_i(\partial_{\boldsymbol{\tau}_i}G)}} \tag{23}$$

In this formula, the second term in the denominator represents the relative increase in flexibility due to the additional plastic strain. This term depends on the ratio of the internal stiffness $\mathbb{D}_i$ to the external stiffness $\mathbb{D}_e$. Fig. 2(a) illustrates the effect of the relative magnitude of the internal stiffness at 2.0, 1.0, and 0.5. For a large value of the relative internal stiffness, the kink in the stress-strain curve at beginning yield becomes small, and vice versa.

Although the initial inclination of the stress-strain relation at initial yield is governed by the relative magnitude of the internal stiffness parameters, the subsequent development of plastic strain, and thereby the generalized stress-strain relation, between initial yield and the ultimate capacity is governed by the gradient of the internal stress term in the flow potential. With the flow potential of the basic form indicated in Eq. (9), the gradient with respect to the (normalized) internal stress components is given by the partial derivatives

$$\partial_{\tilde{\tau}_j^i}G = \partial_{\tilde{\tau}_j^i}F + \frac{\tilde{\tau}_j^i}{\beta_j} \tag{24}$$

This form leads to a development of the plastic strain determined by the yield and ultimate stress levels and the initial slope at first yield. As demonstrated by Krenk and Tidemann (2017) for the von Mises stress-based model, it is possible to enhance the flow potential, making it possible to control the development of plastic strain between the point of initial yield and ultimate stress level. In the present context the hysteresis curves for the individual generalized stress components may be different, and thus must be defined by parameters each associated with a specific generalized stress component. A quite flexible format is obtained by replacing the denominator β_j by a weighted average of the parameter β_j and the current absolute value of the corresponding normalized internal stress component $\tilde{\tau}_j^i$. Hereby the components of the flow potential gradient take the form

$$\partial_{\tilde{\tau}_j^i}G = \partial_{\tilde{\tau}_j^i}F + \frac{\tilde{\tau}_j^i}{(1-\alpha_j)\beta_j + \alpha_j|\tilde{\tau}_j^i|} \tag{25}$$

where α_j = weight parameter for component j. This formulation enables different α parameters for each generalized stress component. The rational function in Eq. (25) can be expressed as a constant plus the reciprocal of a linear function of $|\tilde{\tau}_j^i|$, and integration of the gradient components defined in Eq. (25) then leads to the following form of the flow potential:

$$G(\boldsymbol{\tau}, \boldsymbol{\tau}_i, \boldsymbol{\eta}) = F(\boldsymbol{\tau}, \boldsymbol{\tau}_i, \boldsymbol{\eta}) + G_d(\boldsymbol{\eta}) + \sum_j \frac{1}{\alpha_j}\left\{|\tilde{\tau}_j^i| - \frac{1-\alpha_j}{\alpha_j}\beta_j \ln\left(1 + \frac{\alpha_j}{1-\alpha_j}\frac{|\tilde{\tau}_j^i|}{\beta_j}\right)\right\} \tag{26}$$

where $\alpha_j = \alpha_j(\boldsymbol{\eta})$, $\beta_j = \beta_j(\boldsymbol{\eta})$, and $\tilde{\tau}_j^i = \tilde{\tau}_j^i(\boldsymbol{\eta})$. The basic potential from Eq. (9) corresponds to the limit $\alpha_j = 0$, whereas in accordance with Krenk and Tidemann (2017), more representative values for von Mises plasticity were found to be in the order of $\alpha_j = 0.7$–0.9. Fig. 2(b) illustrates the effect of the shape parameter α_j with stress-strain curves for $\alpha_j = -1.5$, 0.0, and 0.5. Appropriate combinations of the parameter(s) α_j and the relative magnitude of the internal stiffness gives a very versatile representation of the shape of the elastic-plastic stress-strain curve with only two parameters per generalized stress component. The representation of the cyclic behavior is illustrated and discussed in connection with specific examples subsequently.

Generic Yield Surface

The gradients of the yield surface and the flow potential are of central importance because they determine the basic properties of the elastoplastic evolution matrix Eq. (20), as well as the algorithmic

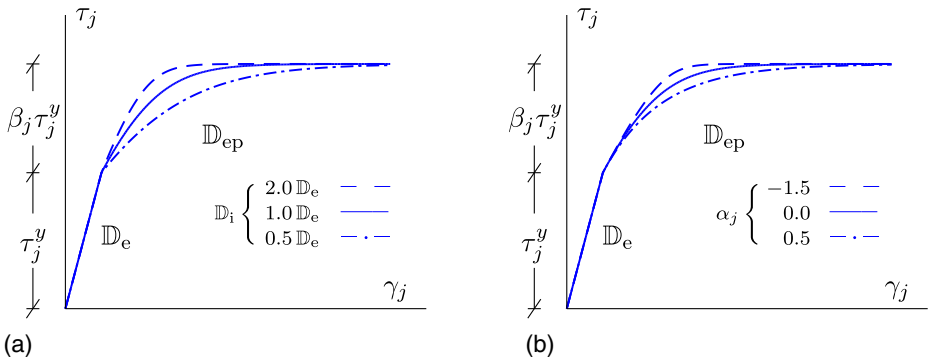

Fig. 2. Influence of parameters on stress-strain relation: (a) relative internal stiffness $\mathbb{D}_i \propto \mathbb{D}_e$; (b) modification of flow potential G via the shape parameter α_j

properties used in return algorithms in the numerical computations. In the case of materials that can be represented by the von Mises yield criterion, the gradients are well defined over the entire yield surface, whereas that may not be the case for yield surfaces representing beam cross sections, because these may typically have corners. This problem can be overcome in various ways, e.g., with use of a locally modified yield function for tubular beam cross sections (Krenk et al. 1999). However, most techniques of that type require individual extensions for different types of cross sections and hence a study of a proper extension of the yield function is necessary for each type of cross section. Additionally, return algorithms and consistent tangent operators have to be derived for each individual yield surface, an undesirable feature in a space frame program where multiple different beam cross sections may be needed. In order to circumvent the corner problem and the need for a library of different yield function formats, a generic yield surface representation is proposed in the following.

Simple Approach

The simplest form of a guaranteed convex representation, excluding the degenerate case of straight lines or planes, is an ellipsoid (in two dimensions, an ellipse, but the term ellipsoid will be used to refer to the general n-dimensional version here). Skordeli and Bisbos (2010) suggested the use of approximating yield surfaces for frame structures in the form of a single ellipsoid. However, this approximation is not very flexible, and degenerates to a sphere when expressed in terms of the normalized generalized stresses. There are two logical possibilities for a next step in the line of simple suggestions: make use of a super ellipsoid, where the exponent is larger than 2; or make use of the convexity guaranteed by the mathematical representation of an ellipsoid and add several of these together, leading to a convex surface. The latter approach is more general and is chosen here.

A single ellipsoid can be represented as a homogeneous form of degree one

$$\sqrt{\mathbf{x}'^T\mathbf{A}\mathbf{x}'} = 1 \tag{27}$$

when $\mathbf{A}$ = symmetric, positive definite matrix; and $\mathbf{x}'$ = local coordinates of the ellipsoid, which may be translated and rotated relative to the global coordinate system, $\mathbf{x}$. The homogeneous form of degree one is desirable because the von Mises yield function with equivalent stress σ_e is homogeneous of degree one, suggesting that an ellipsoidal representation in the form of Eq. (27) qualitatively has the same properties as the von Mises yield surface. An addition of terms of the type in Eq. (27) with different matrices $\mathbf{A}_1, \mathbf{A}_2, \ldots$ does not reduce to an ellipsoid, even if the centers are the same, and thus a format represented as a sum of terms of the type in Eq. (27) offers the possibility of representing more general shapes. The suggested format is therefore

$$\sqrt{\mathbf{x}_1'^T\mathbf{A}_1\mathbf{x}_1'} + \sqrt{\mathbf{x}_1'^T\mathbf{A}_2\mathbf{x}_2'} + \cdots = 1 \tag{28}$$

which is guaranteed convex because of the convexity of each of the terms, where Eq. (27) represents a single ellipsoid and the sum in Eq. (28) represents a combination of ellipsoids. The ratio of the axes of an ellipsoid is given by the matrix $\mathbf{A}$, whereas the finite size of the ellipsoid is given by the right-hand side in Eq. (27). Because the combination of ellipsoidal terms in Eq. (28) does not identify the finite size of the individual terms, an infinity of combinations of finite-sized ellipsoids exists. Assigning each ellipsoid a finite size, i.e., setting each ellipsoidal term equal to a value less than 1, the intersection of the individual ellipsoids—being points in two dimensions and curves in three dimensions—will be points on the resulting surface described by Eq. (28). Fig. 3 illustrates the concept in a format with two ellipsoidal terms, where different combinations of finite-sized ellipsoids result in a convex but nonellipsoidal surface.

Fig. 3 illustrates that the suggested format can approximate both symmetric surfaces [Fig. 3(a)] and nonsymmetric surfaces [Fig. 3(b)]. Symmetric yield surfaces are typical for symmetric beam cross sections, whereas nonsymmetric yield surfaces are typical for nonsymmetrical beam cross sections or beams of materials with different yield strengths in tension and compression, such as concrete. Furthermore, Fig. 3 shows that there is a high degree of flexibility in the approximation despite using only two terms. Including more than two terms will naturally lead to a higher degree of flexibility, but also to a higher degree of complexity when determining the ratios of the semiprincipal axes of the ellipsoids and the rotation of each ellipsoid. Because of the high degree of flexibility, the ensured convexity, and the elimination of corners (the gradient of each ellipsoidal term is defined everywhere), the following generic yield surface format is suggested:

$$F(\boldsymbol{\tau}, \boldsymbol{\tau}_i, \boldsymbol{\eta}) = \sqrt{\bar{\boldsymbol{\tau}}_1^T\mathbf{A}_1\bar{\boldsymbol{\tau}}_1} + \sqrt{\bar{\boldsymbol{\tau}}_2^T\mathbf{A}_2\bar{\boldsymbol{\tau}}_2} + \cdots - 1 \tag{29}$$

where $\mathbf{A}_k$ = positive definite, symmetric matrix for $k = 1, 2, \ldots$; and

$$\bar{\boldsymbol{\tau}}_k(\boldsymbol{\eta}) = \tilde{\boldsymbol{\tau}}(\boldsymbol{\eta}) - \tilde{\boldsymbol{\tau}}_i(\boldsymbol{\eta}) - \hat{\boldsymbol{\tau}}_k \tag{30}$$

where $\hat{\boldsymbol{\tau}}_k$ = constant offset in the normalized stress space. The number of terms and the inclusion of the offset are both options to

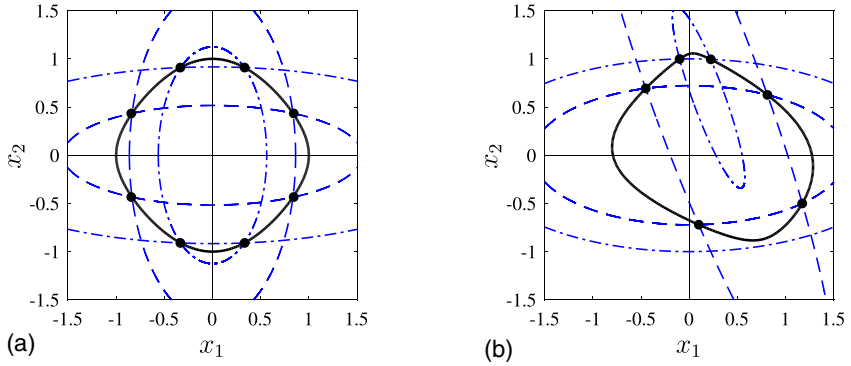

(– · –) and (– –): Finite ellipsoids. (•): Intersections. (—): Resulting surface.

Fig. 3. Intersections of finite ellipsoids are points on the resulting surface

increase the accuracy of the representation. However, for most symmetric beam cross sections, two or three terms are sufficient, where the matrices $\mathbf{A}_k$ are diagonal matrices and $\hat{\boldsymbol{\tau}}_k = \mathbf{0}$, i.e., the ellipsoids are centered at origo and are not rotated. For reinforced concrete cross sections, however, it typically is advantageous to include an offset that is the same for all terms and that only offsets the yield surface on the axis of the normal force.

Choosing Parameters for Simple Yield Surfaces

Yield surfaces for typical steel beam cross sections are symmetric and centered around origo with contour lines in the $(n, m_y, 0)$, $(n, 0, m_z)$, and $(0, m_y, m_z)$ planes resembling shapes that are interpolations between a rhombus and a circle. Such shapes can be represented rather accurately with the suggested format using two ellipsoidal terms with diagonal matrices, $\mathbf{A}_1$ and $\mathbf{A}_2$, and with zero offsets, $\hat{\boldsymbol{\tau}}_1 = \hat{\boldsymbol{\tau}}_2 = \mathbf{0}$. Generating a proper representation of a simple, symmetric yield surface with the format of Eq. (29) is most often eased by prescribing the matrix $\mathbf{A}_1$ and defining $\mathbf{A}_2$ by the intersection of the yield surface and with the n-axis, m_y-axis, and m_z-axis denoted by n^0, m_y^0, and m_z^0, respectively. The diagonal matrix $\mathbf{A}_2$ is defined via the constraints

$$\sqrt{A_{1,1}^1} + \sqrt{A_{1,1}^2} = \frac{1}{|n^0|}, \qquad \sqrt{A_{2,2}^1} + \sqrt{A_{2,2}^2} = \frac{1}{|m_y^0|},$$
$$\sqrt{A_{3,3}^1} + \sqrt{A_{3,3}^2} = \frac{1}{|m_z^0|} \tag{31}$$

Typically, $n^0 = m_y^0 = m_z^0 = 1$ in order to permit full yield capacity of each section force, but values may be subject to change in order to change geometric properties of the yield surface representation.

The shape of the yield surface is governed by the ratios of $A_{1,1}^1, A_{1,1}^2, \ldots$, leading to a fairly simple method of choosing the values of $\mathbf{A}_1$. In the $(n, m_y, 0)$, $(n, 0, m_z)$, and $(0, m_y, m_z)$ planes, the shape is governed by two types of ratios with different effects: ratios of type $A_{1,1}^k/A_{2,2}^k$ and ratios of type $A_{1,1}^1/A_{1,1}^2$. The first ratio type is most important, because it controls whether the shape between the intersections of the yield surface and the axes is more rhombic or more circular. If the ratio is close to 1:1, the shape will be circular, whereas a ratio very different from one will be rhombic. The second type of ratio controls how rounded the yield surface is close to the intersections with the axes. In the $(n, m_y, 0)$ plane the shape around the intersection with the m_y-axis will be rounded compared with the shape around the intersection with the n-axis when $A_{1,1}^1/A_{1,1}^2 \gg A_{2,2}^1/A_{2,2}^2$, and vice versa when $A_{1,1}^1/A_{2,2}^1 > 1$, i.e., for a very rhombic shape of the yield surface, there will be a corner at the intersection with the n-axis when $A_{1,1}^1/A_{1,1}^2 \gg A_{2,2}^1/A_{2,2}^2$. With this knowledge it is fairly easy to choose the parameters $\mathbf{A}_1$, n^0, m_y^0, and m_z^0 to get a proper representation of a simple, symmetric yield surface. For nonsymmetric yield surfaces the process of choosing the number of terms to include in Eq. (29) may be more difficult and could potentially combine with optimization routines as in Bleyer and de Buhan (2013b).

Tubular Beam Yield Surface

In order to illustrate the suggested method, a tubular steel cross section was investigated. The yield function for the axial stress component of the tubular cross section is

$$F(n, m_y, m_z) = \sqrt{m_y^2 + m_z^2} - \cos\left(\frac{\pi}{2} n\right) \tag{32}$$

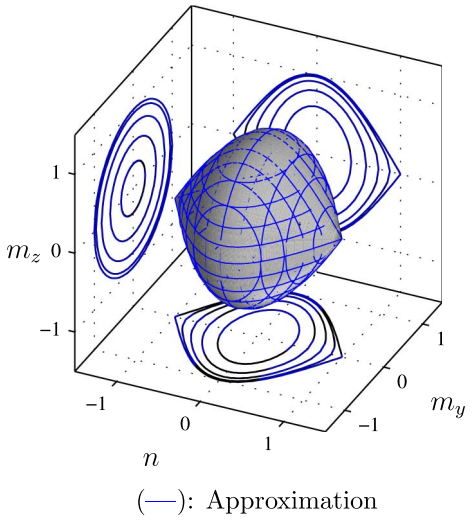

Fig. 4. Theoretical yield surface for tubular steel beam and approximation; contour lines are plotted in various planes

At yield, the function equals zero, which defines the yield surface. The yield surface is symmetric and fairly simple (Fig. 4), and thus it is assumed that it can be accurately approximated using Eq. (29) with two terms, diagonal matrices, and without offsets, i.e., $\hat{\boldsymbol{\tau}}_1 = \hat{\boldsymbol{\tau}}_2 = \mathbf{0}$, based on the above discussion. The constraints of Eq. (31) are applied, effectively reducing the problem to the determination of the three diagonal terms in $\mathbf{A}_1$, using the normalization $|n^0| = |m_y^0| = |m_z^0| = 1$. Because the yield surface Eq. (32) in the $(0, m_y, m_z)$ plane is a circle, it is chosen that $A_{2,2}^1 = A_{3,3}^1$, which gives a perfect circular representation. In the two remaining planes, the yield surface Eq. (32) is very rhombic and with a sharp corner at the intersection with the n-axis, suggesting that $A_{1,1}^1/A_{2,2}^1 \neq 1$, $A_{1,1}^2/A_{2,2}^2 \neq 1$, and $A_{1,1}^1/A_{1,1}^2 \gg A_{2,2}^1/A_{2,2}^2$ to get a good representation of Eq. (32) with the format of Eq. (29). Therefore $\mathbf{A}_1$ is chosen to have the diagonal terms $A_{1,1}^1 = 1 - 2 \times 10^{-5}$ and $A_{2,2}^1 = A_{3,3}^1 = 0.16$, and $\mathbf{A}_2$ given by the constraints of Eq. (31) has the diagonal terms $A_{1,1}^2 = 1 \times 10^{-10}$ and $A_{2,2}^2 = A_{3,3}^2 = 0.36$, whereby $A_{1,1}^1/A_{2,2}^1 = 6.25 \gg 1$, $A_{1,1}^2/A_{2,2}^2 = 2.8 \times 10^{-10} \ll 1$, and $A_{1,1}^1/A_{1,1}^2 = 10^{10}$ which is far bigger than $A_{2,2}^1/A_{2,2}^2 = 0.44$. Fig. 4 shows the resulting approximation.

The approximation is nearly indistinguishable from the original analytically determined surface (Fig. 4). However, there are slight differences because the approximation is a smooth surface with a unique gradient everywhere, whereas the theoretical surface has singularities at the points $(n, m_y, m_z) = (\pm 1, 0, 0)$. Thus for this particular yield surface it is quite easy to determine an accurate representation of the yield surface within the proposed generic yield surface format Eq. (29).

Exterior Surfaces

One issue that arises with the very accurate approximation is that even though the gradient is defined where the theoretical yield surface has corners, the yield surface and the exterior surfaces still have a very large curvature in that region. The exterior surfaces are used for the return to the yield surface, and especially for large load steps the return may be difficult in regions with high curvature. Because of the mathematical formulation of the yield surface Eq. (29), the exterior surfaces will simply be scaled versions of the yield surface, whereby the curvature of the exterior surfaces will be similar to that of the yield surface. Hence it may be advantageous to

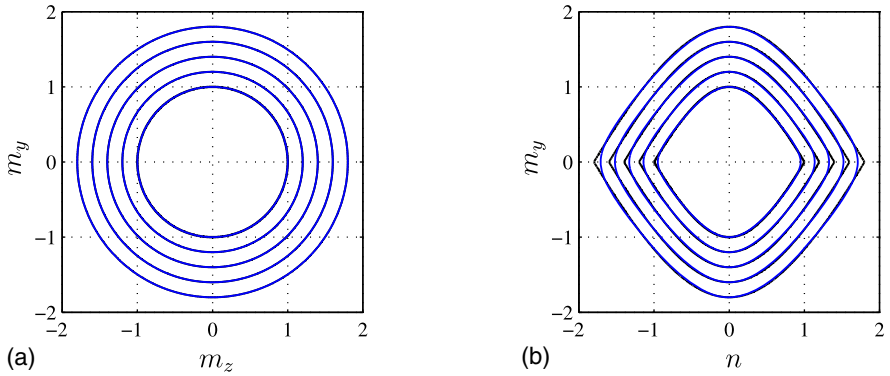

Fig. 5. Outer surfaces for accurate approximation and for rounded approximation

adjust the local curvature to facilitate the ensuing iterations. Fig. 5 shows an example of how this is achieved, in which the parameters are $|n^0| = 0.95$, $|m_y^0| = |m_z^0| = 1$, $A_{1,1}^1 = 0.865$, $A_{2,2}^1 = A_{3,3}^1 = 0.0961$, and $\mathbf{A}_2$ = diagonal matrix given by the constraints of Eq. (31). The parameters are chosen such that the shape of the yield surface in the $(n, m_y, 0)$ and $(n, 0, m_z)$ planes is still rather rhombic, suggesting $A_{1,1}^1/A_{2,2}^1 \neq 1$ and $A_{1,1}^2/A_{2,2}^2 \neq 1$, but the shape at the intersection with the n-axis should be more rounded than in the accurate representation but still somewhat resembling corners, suggesting $A_{1,1}^1/A_{1,1}^2 \gg A_{2,2}^1/A_{2,2}^2$ but with a smaller factor compared to the accurate representation.

Fig. 5 shows that although the slight change in the parameters does not change the representation of the analytical yield surface much, the curvature is reduced dramatically in the critical regions, thereby improving the iteration convergence rate. The fact that the generic yield surface is guaranteed convex without singularities, has gradients that are easy to determine, has a high degree of flexibility and accuracy, and can create exterior surfaces with relatively low curvature indicates that it is a suitable generic method to model yield surfaces for beam cross sections.

Beam Model with Degrading Plastic Hinges

In principle, the plastic hinge model presented in the previous sections can be implemented for any type of element where the generalized strains can be assumed to be the sum of elastic and plastic generalized strains. Many frame structures have loads leading to maximum load at joints or at specific cross sections in the spans, and it is therefore of interest to use the theory for representing plastic deformation in the form of local yield hinges. This section demonstrates how the present cyclic plasticity model can be implemented in the form of a plastic hinge that is incorporated into the formulation of the element, leading to an explicit elastoplastic tangent stiffness matrix including degradation effects. This beam element can then be used in a corotating element formulation for large displacements, if needed. The formulation is an extension of that presented by Krenk et al. (1999) to include the internal variable and damage features of the present plasticity model.

The beam element is formulated in terms of six equilibrium states and the conjugate states of deformation. It is assumed that the plastic deformation is concentrated at the nodes at the ends of the element in the form of yield hinges. With the choice of deformation measures for a beam shown in Fig. 6, the generalized elastic strains and the conjugate generalized stresses within the beam element between the plastic hinges are defined as

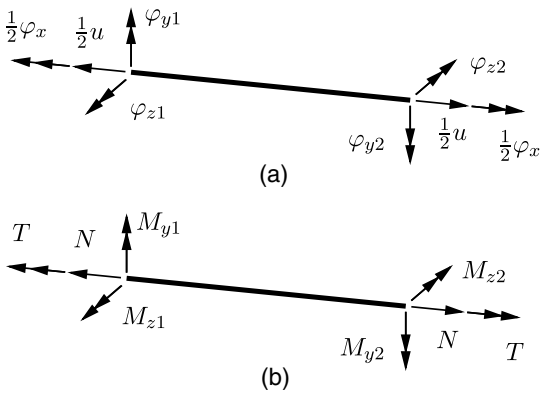

Fig. 6. Equilibrium format of beam element: (a) element deformations; (b) section forces

$$\tilde{\mathbf{u}}_e = [u, \varphi_x, \varphi_{z1}, \varphi_{z2}, \varphi_{y1}, \varphi_{y2}]^T \tag{33}$$

$$\tilde{\mathbf{q}}_e = [N, T, M_{z1}, M_{z2}, M_{y1}, M_{y2}]^T \tag{34}$$

where the tilde indicates reference to the six-component element equilibrium format. For the equilibrium beam element, the generalized strains are the axial deformation and the rotations about the different axes, rather than the axial strain and the curvatures about the different axes, in order to be conjugate to the section forces defined in Eq. (34). In the equilibrium element, the normal force and torsion moment are of equal magnitude but opposite at the two ends of the beam, and the shear forces follow from the bending moments by equilibrium.

Elastoplastic Tangent Stiffness

In the derivation of the elastoplastic tangent stiffness it is necessary to have a relation between the elastic and the plastic deformations, which is particularly simple for small deformation theories. For a beam, the assumption of small deformations, which can be combined with large displacements via, e.g., the corotational formulation, implies that the total deformations, $\tilde{\mathbf{u}}_t$, can be split additively into elastic deformation $\tilde{\mathbf{u}}_e$ and plastic deformation $\tilde{\mathbf{u}}_p$

$$\tilde{\mathbf{u}}_t = \tilde{\mathbf{u}}_e + \tilde{\mathbf{u}}_p \tag{35}$$

The internal energy of the beam element is analogous to the general format of the internal energy [Eq. (2)], with the only difference

being the notation introduced to indicate the relation to a beam element

$$\Phi(\tilde{\mathbf{u}}_e, \tilde{\mathbf{u}}_i, \tilde{\mathbf{u}}_d) = \frac{1}{2}\tilde{\mathbf{u}}_e^T \mathbf{K}_e(\tilde{\mathbf{u}}_d)\tilde{\mathbf{u}}_e + \frac{1}{2}\tilde{\mathbf{u}}_i^T \mathbf{K}_i(\tilde{\mathbf{u}}_d)\tilde{\mathbf{u}}_i + \Phi_d(\tilde{\mathbf{u}}_d) \quad (36)$$

Whereas the original energy definition Eq. (2) was given per length, the present energy applies to the full beam element. The energy is denoted Φ rather than φ, and the stiffness matrices are denoted $\mathbf{K}_e$ and $\mathbf{K}_i$ rather than $\mathbb{D}_e$ and $\mathbb{D}_i$, respectively. The energy conjugate section forces are found via differentiation as

$$\tilde{\mathbf{q}}_e = \partial_{\tilde{\mathbf{u}}_e}\Phi = \mathbf{K}_e(\tilde{\mathbf{u}}_d)\tilde{\mathbf{u}}_e \quad (37)$$

$$\tilde{\mathbf{q}}_i = \partial_{\tilde{\mathbf{u}}_i}\Phi = \mathbf{K}_i(\tilde{\mathbf{u}}_d)\tilde{\mathbf{u}}_i \quad (38)$$

$$\tilde{\mathbf{q}}_d = \partial_{\tilde{\mathbf{u}}_d}\Phi \quad (39)$$

The remaining steps of determining the elastoplastic tangent stiffness matrix accounting for degradation follow the steps of Eqs. (8)–(21) using the generic yield surface described previously. In order to retain a compact notation, the section forces $\tilde{\mathbf{q}}_e$, the internal section forces $\tilde{\mathbf{q}}_i$, and the section force-like damage parameters, $\tilde{\mathbf{q}}_d$, are arranged in a common vector $\tilde{\mathbf{q}}$ that has the energy conjugate vector $\tilde{\mathbf{u}}$

$$\tilde{\mathbf{q}}^T = [\tilde{\mathbf{q}}_e^T, \tilde{\mathbf{q}}_i^T, \tilde{\mathbf{q}}_d^T], \qquad \tilde{\mathbf{u}}^T = [\tilde{\mathbf{u}}_e^T, \tilde{\mathbf{u}}_i^T, \tilde{\mathbf{u}}_d^T] \quad (40)$$

which are defined to ease the notation, especially when deriving the return algorithm.

When developing a beam element with plastic hinges at both ends, these must be combined and plasticity may occur at each end of the beam, whereby the maximization of the dissipation rate [Eq. (11)] will involve two constraints, namely the plastic flow potential at each end. The consistency condition for the yield surface at each end will provide the other constraints, making it possible to derive the elastoplastic tangent stiffness. The plastic flow potentials and the yield functions are arranged in the vector format

$$\mathbf{g}(\tilde{\mathbf{q}}) = [G_1(\tilde{\mathbf{q}}), G_2(\tilde{\mathbf{q}})]^T, \qquad \mathbf{f}_y(\tilde{\mathbf{q}}) = [F_1(\tilde{\mathbf{q}}), F_2(\tilde{\mathbf{q}})]^T \quad (41)$$

With the use of the gradient of the plastic flow potential, the increment in the total deformations, $d\tilde{\mathbf{u}}_t$, internal deformations, $d\tilde{\mathbf{u}}_i$ and deformation-like damage parameters, $d\tilde{\mathbf{u}}_d$, can be expressed as

$$\begin{bmatrix} d\tilde{\mathbf{u}}_t \\ \mathbf{0} \\ \mathbf{0} \end{bmatrix} = d\tilde{\mathbf{u}} + (\partial_{\tilde{\mathbf{q}}}^T \mathbf{g})^T d\boldsymbol{\lambda}, \qquad d\boldsymbol{\lambda} = \begin{bmatrix} d\lambda_1 \\ d\lambda_2 \end{bmatrix} \quad (42)$$

where $d\boldsymbol{\lambda}$ = vector containing the two plastic multipliers, which are determined using the consistency condition at each end. The solution of the consistency condition is found in a compact form with use of the combined external, internal, and damage stiffness matrices

$$\mathbf{K}_{ed} = [\mathbf{K}_e(\tilde{\mathbf{u}}_d), \mathbf{0}, \partial_{\tilde{\mathbf{u}}_d}^T \tilde{\mathbf{q}}_e]^T \quad (43)$$

$$\mathbf{K}_{eid} = \begin{bmatrix} \mathbf{K}_e(\tilde{\mathbf{u}}_d) & \mathbf{0} & \partial_{\tilde{\mathbf{u}}_d}^T \tilde{\mathbf{q}}_e \\ \mathbf{0} & \mathbf{K}_i(\tilde{\mathbf{u}}_d) & \partial_{\tilde{\mathbf{u}}_d}^T \tilde{\mathbf{q}}_i \\ (\partial_{\tilde{\mathbf{u}}_d}^T \tilde{\mathbf{q}}_e)^T & (\partial_{\tilde{\mathbf{u}}_d}^T \tilde{\mathbf{q}}_i)^T & \partial_{\tilde{\mathbf{u}}_d}^T \tilde{\mathbf{q}}_d \end{bmatrix} \quad (44)$$

where $\mathbf{K}_{ed}$ is analogous to $\mathbb{D}_{ed}$ and $\mathbf{K}_{eid}$ is analogous to $\mathbb{D}_{eid}$. The coupled evolution equations for the section forces $\tilde{\mathbf{q}}_e$, the internal section forces $\tilde{\mathbf{q}}_i$, and the section force–like damage parameters $\tilde{\mathbf{q}}_d$ can compactly be described by

$$d\tilde{\mathbf{q}} = \mathbf{K}_{eid} d\tilde{\mathbf{u}} \quad (45)$$

which is essential in formulating a return algorithm as well as in solving the consistency conditions.

The solution of the consistency conditions gives the plastic multipliers

$$d\boldsymbol{\lambda} = \left[\left(\partial_{\tilde{\mathbf{q}}}^T \mathbf{f}_y\right)\mathbf{K}_{eid}\left(\partial_{\tilde{\mathbf{q}}}^T \mathbf{g}\right)^T\right]^{-1}(\partial_{\tilde{\mathbf{q}}}^T \mathbf{f}_y)\mathbf{K}_{ed} d\tilde{\mathbf{u}}_t \quad (46)$$

where $d\lambda_j \geq 0$; and the two equations reduce to one if the generalized stress state is only located on one of the two yield surfaces. The matrix product to be inverted is a 2×2 matrix in the case of yield at both nodes and reduces to a scalar in the case of yield at only one node. The increment in the section forces $d\tilde{\mathbf{q}}_e$, the internal section forces $d\tilde{\mathbf{q}}_i$, and the section force-like damage parameters, $d\tilde{\mathbf{q}}_d$ are expressed as

$$\begin{aligned} d\tilde{\mathbf{q}} &= [d\tilde{\mathbf{q}}_e^T, d\tilde{\mathbf{q}}_i^T, d\tilde{\mathbf{q}}_d^T]^T \\ &= [\mathbf{K}_{ed} - \mathbf{K}_{eid}(\partial_{\tilde{\mathbf{q}}}^T \mathbf{g})^T[(\partial_{\tilde{\mathbf{q}}}^T \mathbf{f}_y)\mathbf{K}_{eid}(\partial_{\tilde{\mathbf{q}}}^T \mathbf{g})^T]^{-1}(\partial_{\tilde{\mathbf{q}}}^T \mathbf{f}_y)\mathbf{K}_{ed}]d\tilde{\mathbf{u}}_t \end{aligned} \quad (47)$$

The tangent stiffness matrix relating only to the increment in the section forces, which is needed in the equilibrium iterations in a finite element code, is identified as

$$\mathbf{K}_{ep} = \mathbf{K}_e - \mathbf{K}_{ed}^T(\partial_{\tilde{\mathbf{q}}}^T \mathbf{g})^T[(\partial_{\tilde{\mathbf{q}}}^T \mathbf{f}_y)\mathbf{K}_{eid}(\partial_{\tilde{\mathbf{q}}}^T \mathbf{g})^T]^{-1}(\partial_{\tilde{\mathbf{q}}}^T \mathbf{f}_y)\mathbf{K}_{ed} \quad (48)$$

In the case without degradation of the elastic stiffness, the matrix $\mathbf{K}_{ed}$ reduces to $[\mathbf{K}_e, \mathbf{0}]^T$ and the elastoplastic tangent stiffness is only affected by degradation in the hardening term, i.e., the matrix $[(\partial_{\tilde{\mathbf{q}}}^T \mathbf{f}_y)\mathbf{K}_{eid}(\partial_{\tilde{\mathbf{q}}}^T \mathbf{g})^T]^{-1}$.

Full-Format Beam Element

The 6×6 equilibrium format of the beam is not sufficient for an implementation in a finite element program because all rigid-body displacements are absent. In order to be able to implement it in a finite element code, the equilibrium beam element needs to be embedded in a general 12×12 three-dimensional beam element (Fig. 7), with the classical sign convention of the element displacements and the energy conjugate element forces.

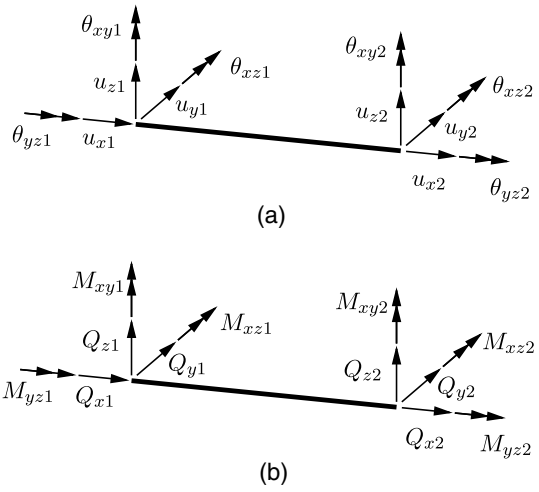

Fig. 7. Full format of beam element: (a) element displacements; (b) element forces

Just as the deformations and section forces of the equilibrium element in Fig. 6 are arranged in the vectors $\tilde{\mathbf{u}}_t$ and $\tilde{\mathbf{q}}_e$, the element displacements and forces of the full-format beam element in Fig. 7 are sorted in the vectors

$$\mathbf{u}^T = [\mathbf{u}_1^T, \mathbf{u}_2^T], \qquad \mathbf{u}_j = [u_x, u_y, u_z, \theta_{yz}, \theta_{xz}, \theta_{xy}]_j^T \tag{49}$$

$$\mathbf{q}^T = [\mathbf{q}_1^T, \mathbf{q}_2^T], \qquad \mathbf{q}_j = [Q_x, Q_y, Q_z, M_{yz}, M_{xz}, M_{xy}]_j^T \tag{50}$$

In order for the two elements to be equivalent, the corresponding generalized strains and stresses of the two formulations must satisfy the incremental virtual work relation

$$\mathbf{q}^T d\mathbf{u} = \tilde{\mathbf{q}}_e^T d\tilde{\mathbf{u}}_t \tag{51}$$

providing a link between the two formulations. From the equilibrium conditions of the beam, the element forces $\mathbf{q}$ can be expressed in terms of the equilibrium section forces $\tilde{\mathbf{q}}_e$ via a transformation matrix $\mathbf{T}$

$$\mathbf{q} = \begin{bmatrix} \mathbf{q}_1 \\ \mathbf{q}_2 \end{bmatrix} = \begin{bmatrix} \mathbf{T}_1 \\ \mathbf{T}_2 \end{bmatrix} \tilde{\mathbf{q}}_e = \mathbf{T}\tilde{\mathbf{q}}_e \tag{52}$$

With this relation it is realized that the total deformations $\tilde{\mathbf{u}}_t$ of the equilibrium format can be expressed via the nodal displacements $\mathbf{u}$ and the transformation matrix $\mathbf{T}$, using the work increment Eq. (51)

$$d\tilde{\mathbf{u}}_t = \mathbf{T}^T d\mathbf{u} \tag{53}$$

With the use of Eqs. (52) and (53) it is possible to derive the elastoplastic tangent stiffness matrix for a beam element with 12 degrees of freedom (Fig. 7). An increment in the element forces, $d\mathbf{q}$, can be expressed as

$$d\mathbf{q} = \mathbf{T}d\tilde{\mathbf{q}}_e + d\mathbf{T}\ \tilde{\mathbf{q}}_e = \mathbf{T}\mathbf{K}_{ep}\mathbf{T}^T d\mathbf{u} + d\mathbf{T}\ \tilde{\mathbf{q}}_e \tag{54}$$

The last term $d\mathbf{T}\ \tilde{\mathbf{q}}_e$ relates to the geometric effects of rotation and length change of the element. Although the second effect is small, it contributes to the symmetry of the element stiffness matrix. The second term may be rearranged into the form of an additional stiffness matrix $\mathbf{K}_r$ (e.g., Krenk et al. 1999; Krenk 2009)

$$d\mathbf{q} = (\mathbf{T}\mathbf{K}_{ep}\mathbf{T}^T + \mathbf{K}_r)d\mathbf{u} \tag{55}$$

which has a form suitable for a finite element implementation, because it relates increments in the element forces directly to increments in the element displacements.

Return Algorithm

In a finite-element setting, the use of the elastic or the elastoplastic tangent stiffness matrix Eq. (48) will often lead to a violation of the yield criterion in the predicted state for finite load/deformation increments. In order to enable the use of larger increments, a return algorithm is developed which returns the predicted section force state to the yield surface, taking into account kinematic hardening as well as the degradation mechanisms. The return algorithm is developed with the use of a Newton-Raphson solution scheme for the deformation evolution Eq. (42), using finite increments giving the residual

$$\mathbf{r}_{\tilde{\mathbf{u}}} = \begin{bmatrix} \Delta\tilde{\mathbf{u}}_t \\ \mathbf{0} \\ \mathbf{0} \end{bmatrix} - \Delta\tilde{\mathbf{u}} - (\partial_{\tilde{\mathbf{q}}}^T \mathbf{g})^T \Delta\boldsymbol{\lambda}, \qquad \Delta\boldsymbol{\lambda} = \begin{bmatrix} \Delta\lambda_1 \\ \Delta\lambda_2 \end{bmatrix} \tag{56}$$

The variation of the residual is needed in the Newton-Raphson solution procedure and because the yield function and the flow potential is defined via $\tilde{\mathbf{q}}$ it is desirable to formulate the return algorithm in terms of the subincrement of the section forces, $\delta\tilde{\mathbf{q}}$, rather than the subincrement of the deformations, $\delta\tilde{\mathbf{u}}$. However, the variation of the residual Eq. (56) is initially expressed via the subincrements $\delta\tilde{\mathbf{u}}$, $\delta\tilde{\mathbf{q}}$, and $\delta\boldsymbol{\lambda}$

$$\delta\mathbf{r}_{\tilde{\mathbf{u}}} = -\delta\tilde{\mathbf{u}} - \partial_{\tilde{\mathbf{q}}}^T[(\partial_{\tilde{\mathbf{q}}}^T \mathbf{g})^T \Delta\boldsymbol{\lambda}]\delta\tilde{\mathbf{q}} - (\partial_{\tilde{\mathbf{q}}}^T \mathbf{g})^T \delta\boldsymbol{\lambda} \tag{57}$$

because $\delta\tilde{\mathbf{u}}$ is rather conveniently expressed by $\delta\tilde{\mathbf{q}}$ via the variation of the evolution equation of $\tilde{\mathbf{q}}$, Eq. (45), yielding

$$\delta\tilde{\mathbf{q}} = [\mathbf{K}_{eid} + \partial_{\tilde{\mathbf{u}}}^T(\mathbf{K}_{eid}\Delta\tilde{\mathbf{u}})]\delta\tilde{\mathbf{u}} \tag{58}$$

In the Newton-Raphson scheme the increments $\Delta\tilde{\mathbf{u}}$ and $\Delta\boldsymbol{\lambda}$ are considered constants in each iteration and hence they are only placed inside the derivatives in Eqs. (57) and (58) to give the correct dimension of vectors. Combining Eqs. (56)–(58) with the consistency condition that the yield functions must be equal to zero, the following equation system defining the return algorithm is found:

$$\begin{bmatrix} (\mathbf{K}_{eid}^A)^{-1} & (\partial_{\tilde{\mathbf{q}}}^T \mathbf{g})^T \\ \partial_{\tilde{\mathbf{q}}}^T \mathbf{f}_y & \mathbf{0} \end{bmatrix} \begin{bmatrix} \delta\tilde{\mathbf{q}} \\ \delta\boldsymbol{\lambda} \end{bmatrix} = \begin{bmatrix} \mathbf{r}_{\tilde{\mathbf{u}}} \\ -\mathbf{f}_y \end{bmatrix} \tag{59}$$

where the algorithmic stiffness matrix is defined via its inverse

$$(\mathbf{K}_{eid}^A)^{-1} = [\mathbf{K}_{eid} + \partial_{\tilde{\mathbf{u}}}^T(\mathbf{K}_{eid}\Delta\tilde{\mathbf{u}})]^{-1} + \partial_{\tilde{\mathbf{q}}}^T[(\partial_{\tilde{\mathbf{q}}}^T \mathbf{g})^T \Delta\boldsymbol{\lambda}] \tag{60}$$

The two derivatives needed in the algorithmic stiffness matrix are obtained as

$$\partial_{\tilde{\mathbf{q}}}^T[(\partial_{\tilde{\mathbf{q}}}^T \mathbf{g})^T \Delta\boldsymbol{\lambda}] = \frac{\partial^2 G_1}{\partial\tilde{\mathbf{q}}\partial\tilde{\mathbf{q}}^T}\Delta\lambda_1 + \frac{\partial^2 G_2}{\partial\tilde{\mathbf{q}}\partial\tilde{\mathbf{q}}^T}\Delta\lambda_2 \tag{61}$$

and

$$\partial_{\tilde{\mathbf{u}}}^T(\mathbf{K}_{eid}\Delta\tilde{\mathbf{u}}) = \begin{bmatrix} \dfrac{\partial^2(\tilde{\mathbf{q}}_d^T\Delta\tilde{\mathbf{u}}_d)}{\partial\tilde{\mathbf{u}}_e\partial\tilde{\mathbf{u}}_e^T} & \mathbf{0} & \dfrac{\partial^2(\tilde{\mathbf{q}}_e^T\Delta\tilde{\mathbf{u}}_e + \tilde{\mathbf{q}}_d^T\Delta\tilde{\mathbf{u}}_d)}{\partial\tilde{\mathbf{u}}_d\partial\tilde{\mathbf{u}}_e^T} \\ & \dfrac{\partial^2(\tilde{\mathbf{q}}_d^T\Delta\tilde{\mathbf{u}}_d)}{\partial\tilde{\mathbf{u}}_i\partial\tilde{\mathbf{u}}_i^T} & \dfrac{\partial^2(\tilde{\mathbf{q}}_i^T\Delta\tilde{\mathbf{u}}_i + \tilde{\mathbf{q}}_d^T\Delta\tilde{\mathbf{u}}_d)}{\partial\tilde{\mathbf{u}}_d\partial\tilde{\mathbf{u}}_i^T} \\ \text{symm.} & & \dfrac{\partial^2(\tilde{\mathbf{q}}_e^T\Delta\tilde{\mathbf{u}}_e + \tilde{\mathbf{q}}_i^T\Delta\tilde{\mathbf{u}}_i + \tilde{\mathbf{q}}_d^T\Delta\tilde{\mathbf{u}}_d)}{\partial\tilde{\mathbf{u}}_d\partial\tilde{\mathbf{u}}_d^T} \end{bmatrix} \tag{62}$$

where $\partial_{\tilde{\mathbf{u}}}^T(\mathbf{K}_{eid}\Delta\tilde{\mathbf{u}})$ is composed of three diagonal blocks, which themselves are symmetric matrices, as well as two off-diagonal blocks which are not symmetric. Because of the differentiation procedure, however, the full matrix $\partial_{\tilde{\mathbf{u}}}^T(\mathbf{K}_{eid}\Delta\tilde{\mathbf{u}})$ is symmetric, because the off-diagonal blocks are transposed on the other side of the diagonal blocks.

Because both $\mathbf{K}_{eid}$ and $\partial_{\tilde{\mathbf{u}}}^T(\mathbf{K}_{eid}\Delta\tilde{\mathbf{u}})$ have a structure with three symmetric diagonal blocks and two off-diagonal nonsymmetric blocks, it is possible to invert the first term, $[\mathbf{K}_{eid} + \partial_{\tilde{\mathbf{u}}}^T(\mathbf{K}_{eid}\Delta\tilde{\mathbf{u}})]^{-1}$, of the inverse algorithmic stiffness matrix in a simple way because the sum $\mathbf{K}_{eid} + \partial_{\tilde{\mathbf{u}}}^T(\mathbf{K}_{eid}\Delta\tilde{\mathbf{u}})$ has a block structure similar to $\mathbf{K}_{eid}$ and $\partial_{\tilde{\mathbf{u}}}^T(\mathbf{K}_{eid}\Delta\tilde{\mathbf{u}})$. The inverse $[\mathbf{K}_{eid} + \partial_{\tilde{\mathbf{u}}}^T(\mathbf{K}_{eid}\Delta\tilde{\mathbf{u}})]^{-1}$ can be determined using only the inverse of the two first diagonal blocks of the sum and the inverse of the difference between the third diagonal block of the sum and the matrix

products of the off-diagonal blocks of the sum and the inverse of the corresponding diagonal block of the sum. The remaining part of inverting the first term of the inverse algorithmic stiffness matrix will then be simple matrix multiplication. The algorithmic stiffness matrix can therefore be determined by numerical inversion of one matrix, the size of which depends on the number of internal variables, $\tilde{\mathbf{u}}_{\mathrm{i}}$, and damage variables, $\tilde{\mathbf{u}}_{\mathrm{d}}$, used in the element, along with inversion of three smaller matrices and a series of matrix multiplications. The two first block diagonal terms in the sum $\mathbf{K}_{\mathrm{eid}} + \partial^T_{\tilde{\mathbf{u}}}(\mathbf{K}_{\mathrm{eid}}\Delta\tilde{\mathbf{u}})$ are most likely possible to invert analytically because they involve the elastic and internal stiffness matrices, which themselves tend to be block diagonal. Furthermore, the algorithmic stiffness matrix is symmetric.

Using the algorithmic stiffness matrix Eq. (60) makes it possible to solve the equation system Eq. (59) in a relatively compact form without having to solve the full system numerically. Initially, the force subincrement $\delta\tilde{\mathbf{q}}$ is solved for in the first row of equations in Eq. (59), and subsequently substituted into the second row, making it possible to solve for $\delta\boldsymbol{\lambda}$, giving the relations

$$\delta\boldsymbol{\lambda} = [(\partial^T_{\tilde{\mathbf{q}}}\mathbf{f}_y)\mathbf{K}^A_{\mathrm{eid}}(\partial^T_{\tilde{\mathbf{q}}}\mathbf{g})^T]^{-1}((\partial^T_{\tilde{\mathbf{q}}}\mathbf{f}_y)\mathbf{K}^A_{\mathrm{eid}}\mathbf{r}_{\tilde{\mathbf{u}}} + \mathbf{f}_y) \tag{63}$$

$$\delta\tilde{\mathbf{q}} = \mathbf{K}^A_{\mathrm{eid}}(\mathbf{r}_{\tilde{\mathbf{u}}} - (\partial^T_{\tilde{\mathbf{q}}}\mathbf{g})^T\delta\boldsymbol{\lambda}) \tag{64}$$

The return algorithm described by Eq. (56) and Eqs. (60)–(64) is shown as pseudo-code in the following computational procedure.

Algorithm. Computational Procedure: Return Algorithm

1. Calculate elastic increment in forces, $\Delta\tilde{\mathbf{q}}^0 = \mathbf{K}_{\mathrm{ed}}\Delta\tilde{\mathbf{u}}_t$.
2. Calculate value of yield functions, $\mathbf{f}^k_y$, using $\tilde{\mathbf{q}} = \tilde{\mathbf{q}}^0 + \Delta\tilde{\mathbf{q}}^k$. If $F^0_1 \le 0$ and $F^0_2 \le 0$, accept $\tilde{\mathbf{q}} = \tilde{\mathbf{q}}^0 + \Delta\tilde{\mathbf{q}}^0$ and exit.
3. Calculate $\Delta\boldsymbol{\lambda}^0$ using Eq. (46) and $\Delta\tilde{\mathbf{u}}_t$ or update $\Delta\boldsymbol{\lambda}^k = \Delta\boldsymbol{\lambda}^{k-1} + \delta\boldsymbol{\lambda}^{k-1}$.
4. Determine $\partial^T_{\tilde{\mathbf{q}}}\mathbf{g}$, $\partial^T_{\tilde{\mathbf{q}}}\mathbf{f}_y$, and $\mathbf{r}^k_{\tilde{\mathbf{u}}}$ using $\tilde{\mathbf{q}} = \tilde{\mathbf{q}}^0 + \Delta\tilde{\mathbf{q}}^k$. If $\|\mathbf{r}^k_{\tilde{\mathbf{u}}}\| < \epsilon_{\mathrm{tol}}$, accept $\tilde{\mathbf{q}} = \tilde{\mathbf{q}}^0 + \Delta\tilde{\mathbf{q}}^k$ and exit.
5. Calculate $\mathbf{K}^A_{\mathrm{eid}}$ by Eq. (60) and determine $\delta\boldsymbol{\lambda}^k$ by Eq. (63).
6. Determine subincrements $\delta\tilde{\mathbf{q}}^k$ and $\delta\tilde{\mathbf{u}}^k$ by Eqs. (64) and (58).
7. Update $\Delta\tilde{\mathbf{q}}^{k+1} = \Delta\tilde{\mathbf{q}}^k + \delta\tilde{\mathbf{q}}^k$ and $\Delta\tilde{\mathbf{u}}^{k+1} = \Delta\tilde{\mathbf{u}}^k + \delta\tilde{\mathbf{u}}^k$ and go to 2 using $k = k + 1$.

The return algorithm is based on a fixed deformation increment for each element, $\Delta\tilde{\mathbf{u}}_{\mathrm{t}}$, which is obtained via a displacement increment found in a global finite-element analysis and is subsequently transformed into a deformation increment for each element via Eq. (53). Additionally, the section forces prior to the deformation increment $\tilde{\mathbf{q}}^0$ are known. Initially, an elastic prediction step of $\Delta\tilde{\mathbf{q}}$ is made, and if the new stress state is located on or inside the yield surface, the elastic prediction step is accepted because an elastic change has taken place, because of the convexity of the yield surface. Subsequently, the increment in the plastic multipliers $\Delta\boldsymbol{\lambda}^0$ is calculated, based on the finite increment in deformations $\Delta\tilde{\mathbf{u}}_{\mathrm{t}}$, followed by determination of the gradients of the plastic flow potential and the yield surface, $\partial^T_{\tilde{\mathbf{q}}}\mathbf{g}$ and $\partial^T_{\tilde{\mathbf{q}}}\mathbf{f}_y$, respectively, along with the current value of the residual $\mathbf{r}^k_{\tilde{\mathbf{u}}}$ based on the predicted final value of $\tilde{\mathbf{q}}$. If the residual is sufficiently small, the iteration procedure is ended; otherwise, the algorithmic stiffness matrix $\mathbf{K}^A_{\mathrm{eid}}$ is recalculated via Eq. (60) and the subincrement in the plastic multipliers is calculated, $\delta\boldsymbol{\lambda}^k$. There are limitations on the values $\delta\boldsymbol{\lambda}^k$, because $\Delta\lambda_j \ge 0$ for $j = 1, 2$. The subincrements $\delta\tilde{\mathbf{q}}^k$ and $\delta\tilde{\mathbf{u}}^k$ are determined via Eqs. (64) and (58), respectively, whereby the increments $\Delta\tilde{\mathbf{q}}^k$ and $\Delta\tilde{\mathbf{u}}^k$ can be updated and the iteration procedure repeated until convergence.

Simple Damage Formulation

A very simple damage formulation is implemented in the beam element to illustrate the concept of degradation. The damage functions used for the different parameters are chosen because of the ability to model increase as well as decrease of a parameter with a prescribed asymptotic saturation level at which a final value of the parameter is reached, and because of their simple format. In total, nine different damage variables are introduced, one relating to the elastic stiffness and two each relating to the inelastic stiffness, the yield capacity, the β_j values, and the α_j values, respectively. The deformation-like damage parameters are arranged in the vector

$$\tilde{\mathbf{u}}_{\mathrm{d}} = [\tilde{u}^{\mathrm{e}}_{\mathrm{d}}, \tilde{u}^{\mathrm{i},1}_{\mathrm{d}}, \tilde{u}^{\mathrm{i},2}_{\mathrm{d}}, \tilde{u}^{y,1}_{\mathrm{d}}, \tilde{u}^{y,2}_{\mathrm{d}}, \tilde{u}^{\beta,1}_{\mathrm{d}}, \tilde{u}^{\beta,2}_{\mathrm{d}}, \tilde{u}^{\alpha,1}_{\mathrm{d}}, \tilde{u}^{\alpha,2}_{\mathrm{d}}]^T \tag{65}$$

where the superscript indicates the parameter type and node number to which the damage variable relates. The elastic stiffness is degraded via the function

$$\mathbf{K}_{\mathrm{e}}(\tilde{\mathbf{u}}_{\mathrm{d}}) = \frac{1 + \eta_{\mathrm{e}}\tilde{u}^{\mathrm{e}}_{\mathrm{d}}/\tilde{u}^{\mathrm{e}}_{\mathrm{d},0}}{1 + \tilde{u}^{\mathrm{e}}_{\mathrm{d}}/\tilde{u}^{\mathrm{e}}_{\mathrm{d},0}}\mathbf{K}^0_{\mathrm{e}} \tag{66}$$

where $\mathbf{K}^0_{\mathrm{e}}$ = elastic stiffness matrix without damage; η_{e} = saturation level; and $\tilde{u}^{\mathrm{e}}_{\mathrm{d},0}$ = factor accounting for how fast the saturation level is reached. Similarly, the stiffness matrix relating to the deformation-like internal parameters is degraded via the function

$$\mathbf{K}_{\mathrm{i}}(\tilde{\mathbf{u}}_{\mathrm{d}}) = \begin{bmatrix} \mathbf{K}^1_{\mathrm{i}}(\tilde{\mathbf{u}}_{\mathrm{d}}) & \mathbf{0} \\ \mathbf{0} & \mathbf{K}^2_{\mathrm{i}}(\tilde{\mathbf{u}}_{\mathrm{d}}) \end{bmatrix},$$
$$\mathbf{K}^j_{\mathrm{i}}(\tilde{\mathbf{u}}_{\mathrm{d}}) = \frac{1 + \eta_{\mathrm{i},j}\tilde{u}^{\mathrm{i},j}_{\mathrm{d}}/\tilde{u}^{\mathrm{i},j}_{\mathrm{d},0}}{1 + \tilde{u}^{\mathrm{i},j}_{\mathrm{d}}/\tilde{u}^{\mathrm{i},j}_{\mathrm{d},0}}\mathbf{K}^0_{\mathrm{i},j} \tag{67}$$

where $\mathbf{K}^j_{\mathrm{i}}$ = part of the internal stiffness matrix relating to node j with the corresponding undamaged internal stiffness matrix $\mathbf{K}^0_{\mathrm{i},j}$. The remaining material parameters are functions of the section force-like damage parameters $\tilde{\mathbf{q}}_{\mathrm{d}}$, and each of these is defined as

$$\tilde{q}^k_{\mathrm{d}} = \frac{1 + \eta_{k,j}\tilde{u}^{k,j}_{\mathrm{d}}/\tilde{u}^{k,j}_{\mathrm{d},0}}{1 + \tilde{u}^{k,j}_{\mathrm{d}}/\tilde{u}^{k,j}_{\mathrm{d},0}} \tag{68}$$

where the index k may be y, β, or α. The relation between the material parameters and the section force-like damage parameters is defined as

$$\mathbb{B}_{y,j}(\tilde{\mathbf{q}}_{\mathrm{d}}) = \tilde{q}^{y,j}_{\mathrm{d}}\mathbb{B}^0_{y,j}, \qquad \boldsymbol{\beta}_j(\tilde{\mathbf{q}}_{\mathrm{d}}) = \tilde{q}^{\beta,j}_{\mathrm{d}}\boldsymbol{\beta}^0_j, \qquad \boldsymbol{\alpha}_j(\tilde{\mathbf{q}}_{\mathrm{d}}) = \tilde{q}^{\alpha,j}_{\mathrm{d}}\boldsymbol{\alpha}^0_j \tag{69}$$

where $\mathbb{B}^0_{y,j}$ = undamaged yield capacity matrix for node j; $\boldsymbol{\beta}^0_j$ = array of undamaged β-values for node j; and $\boldsymbol{\alpha}^0_j$ = array of undamaged α values for node j. The damage functions described above are used in the following examples.

Examples

The equilibrium based element including plastic hinges using the generic yield surface was implemented in a *MATLAB* toolbox, CycPlasFrame. The toolbox has linear geometry and does not at the present stage include the stiffness contribution from normal forces, making it unsuitable for frame structures dominated by buckling

failure but highly suitable for frame structures dominated by plastic deformation.

Cantilevered I-Beams

Estimates of the model parameters can be found by the use of experimental results, and most easily with displacement-controlled experiments of cantilevered beams. Displacement-controlled bending of a cantilevered beam activates only one hinge, eliminating the coupling between hinges and subsequently simplifying the calibration procedure. D'Aniello et al. (2012) tested cantilevered I-beams with various cross sections subjected to cyclic displacement controlled bending and observed a significant degradation of the parameters, primarily because of local buckling. In the test, a cantilever of length $L = 1.875$ m was subjected to 12 symmetric cycles with approximate tip displacement 2×10^{-3} L followed by six symmetric cycles of approximate tip displacement 3.5×10^{-3} L, four symmetric cycles of approximate tip displacement 5×10^{-3} L, and sets of two symmetric cycles in which the tip displacement increased by approximately 10^{-2} L per set until failure. Test results for an IPE 300 cross section and a HEB 240 cross section were used for calibration of the present model. The IPE 300 and HEB 240 have approximately the same slenderness of the flanges but the web of the IPE 300 is substantially more slender than the web of the HEB 240, suggesting that local buckling and thereby degradation will occur earlier in the bending of the IPE 300 than the HEB 240. Table 1 presents the model parameters for the nondegraded system.

Aside from being more slender, the IPE 300 also has a smaller elastic stiffness and a smaller yield capacity than the HEB 240 profile. Table 2 shows the model parameters relating to degradation of stiffness. The higher slenderness of the IPE 300 profile compared with the HEB 240 profile is apparent in the degradation parameters in Table 2 because $u^{e}_{d,0}$ and $u^{i,1}_{d,0}$ are significantly lower for the IPE 300 profile, indicating that the degradation process develops at a faster rate. The increments in the deformation-like damage parameters u^{e}_{d} and $u^{i,1}_{d}$ are proportional to $d\lambda_1$ and thus have the dimension of energy and relate to the dissipated energy. This suggests that the reference values $u^{e}_{d,0}$ and $u^{i,1}_{d,0}$ may be scaled with the size of a characteristic hysteresis loop for cross sections of similar type. Table 3 shows the model parameters for degradation of the capacity parameters and α. Similar to Table 2, the reference energy levels, $u^{y,1}_{d,0}$, $u^{\beta,1}_{d,0}$, and $u^{\alpha,1}_{d,0}$ are lower for the IPE 300 profile compared with the HEB 240 profile.

Fig. 8 plots both the experimental and the modeled results of the tip displacement and reaction moment of the IPE 300. Fig. 8(a) shows the first 38 cycles to illustrate that the accuracy of the model is fairly high for most of the response despite the very simple damage functions used. Fig. 8(b) includes the remaining two cycles, which are not modeled very accurately compared with the previous cycles. In the experiment, torsional buckling took place after the local plastic buckling (D'Aniello et al. 2012), which led to failure of the beam, and it is expected that this mechanism was the cause of the nonsmooth change in the response in the last two cycles compared with the initial ~38 cycles.

Fig. 9 shows the response of the HEB 240 profile. Fig. 9(a) models the first 38 cycles almost perfectly, with very little difference between the experimental and modelled result. In the first 38 cycles very little degradation takes place, suggesting that the model without degradation is sufficiently accurate. In Fig. 9(b), after an additional nine cycles, during which a significant amount of degradation occurred, the modeled response still represents the experimental response with good accuracy despite the simple damage functions used. Figs. 9(c and d) show that when the degradation process progresses further, the modeled response is not as accurate as for the first cycles. Torsional buckling also occurred in the final stages of the experimental testing of the HEB 240 profile (D'Aniello et al. 2012), which might explain the discrepancy

Table 1. Initial Model Parameters

Cross section	$(EI_y)_e$ (MNm^2)	$\frac{(EI_y)_i}{(EI_y)_e}$	M^y_y (kNm)	β_{M_y}	α_{M_y}
IPE 300	15.9	4.5	175.8	0.20	0.80
HEB 240	21.4	2.0	295.1	0.03	0.80

Table 2. Model Parameters for Stiffness Degradation

Cross section	$u^{e}_{d,0}$ (kJ)	η_e	$u^{i,1}_{d,0}$ (kJ)	$\eta_{i,1}$
IPE 300	60	0.2	28	0.3
HEB 240	400	0.2	70	0.4

Table 3. Model Parameters for Capacity Degradation

Cross section	$u^{y,1}_{d,0}$ (kJ)	$\eta_{y,1}$	$u^{\beta,1}_{d,0}$ (kJ)	$\eta_{\beta,1}$	$u^{\alpha,1}_{d,0}$ (kJ)	$\eta_{\alpha,1}$
IPE 300	70	0.3	0.30	7.8	−70	1.10
HEB 240	700	0.2	0.80	95	−100	1.06

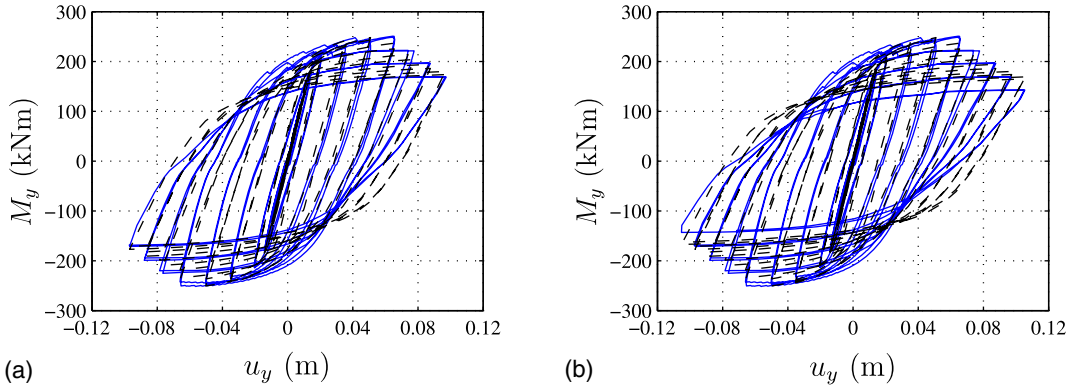

(—): Experiment, (D'Aniello et al. 2012). (– –): Present model.

Fig. 8. Cyclic bending of cantilevered IPE 300 beam: (a) first 38 cycles; (b) all 40 cycles

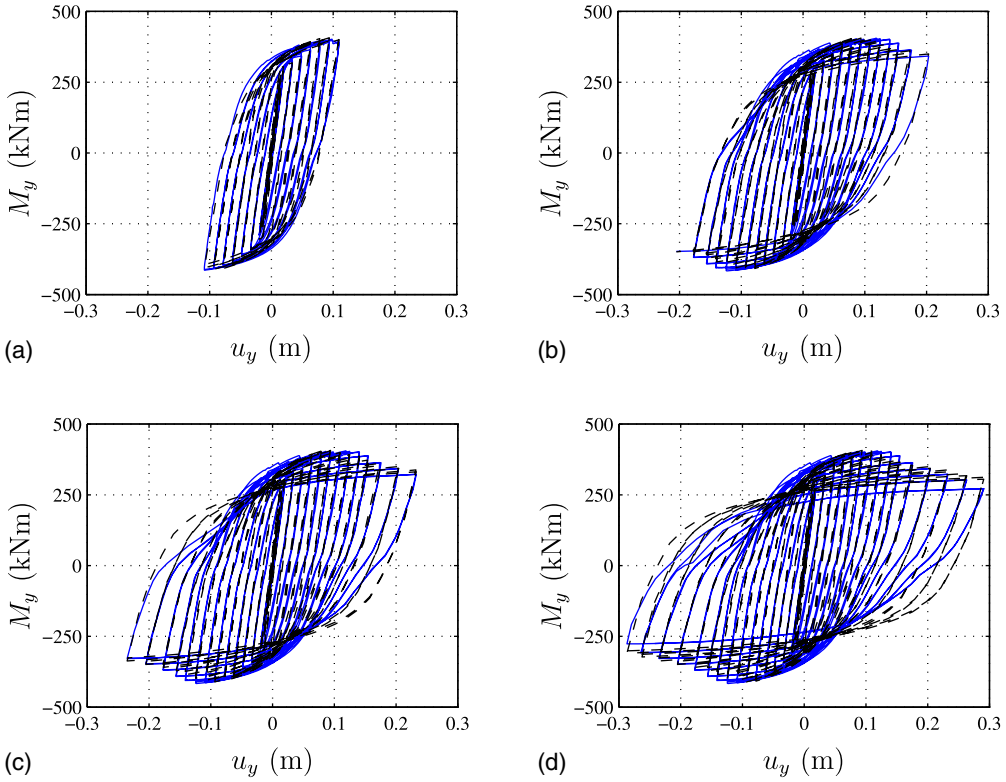

(—): Experiment, (D'Aniello et al. 2012). (– –): Present model.

Fig. 9. Cyclic bending of cantilevered HEB 240 beam: (a) first 38 cycles; (b) first 47 cycles; (c) first 50 cycles; (d) all 54 cycles

between the experimental and modeled response as in the case of the IPE 300 profile.

Tubular Offshore Frame

The plastic hinge model was implemented as an extension of the computer code *RONJA* (Rambøll Offshore Nonlinear Jacket Analysis) using a finite displacement corotational beam-column formulation (Krenk et al. 1999). This implementation was used to model cyclic loading on a plane offshore frame structure (Fig. 10) tested by Zayas et al. (1980). This structure is geometrically similar to that analyzed in Krenk et al. (1999) for monotonic loading by a linear hardening plasticity model, but representation of the response to cyclic loading is a considerably more challenging task. The jacket structure was a 1:6 scale model representative of offshore jacket structures located in the Gulf of Mexico. The jacket had equal bay heights, a width of 3.05 m, and was simply supported at the bottom of the legs and loaded by an in-plane horizontal compression force P at the top right corner. Each part of the bracing was modeled by two beam-column elements. Plastic hinges developed in the lower left brace of the upper bay, and following (Krenk et al. 1999) the column effect was represented by the introduction of a suitable imperfection in this brace by a center node offset in the transverse direction of 56 mm, corresponding to 2.6%. This value was determined by calibration via the experimental results and is somewhat larger than 0.45 and 0.30%, reproducing the Perry-Robertson imperfection-based column curves from the Danish and Norwegian structural codes, respectively, when using linear hardening. D'Aniello et al. (2013, 2015) treated the representation and effect of member imperfections on the deformation and collapse properties of steel frames in connection with earthquakes.

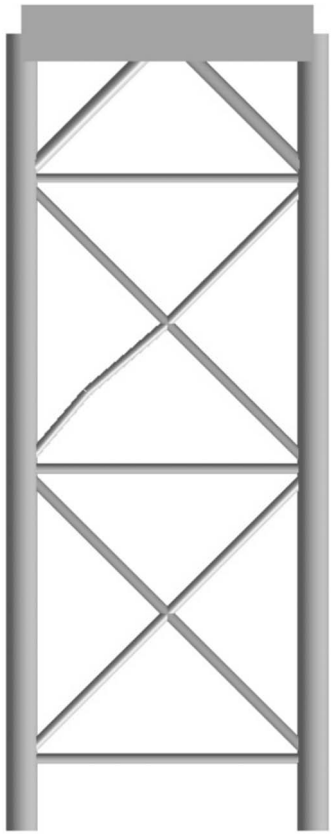

Fig. 10. Plane offshore frame structure geometry

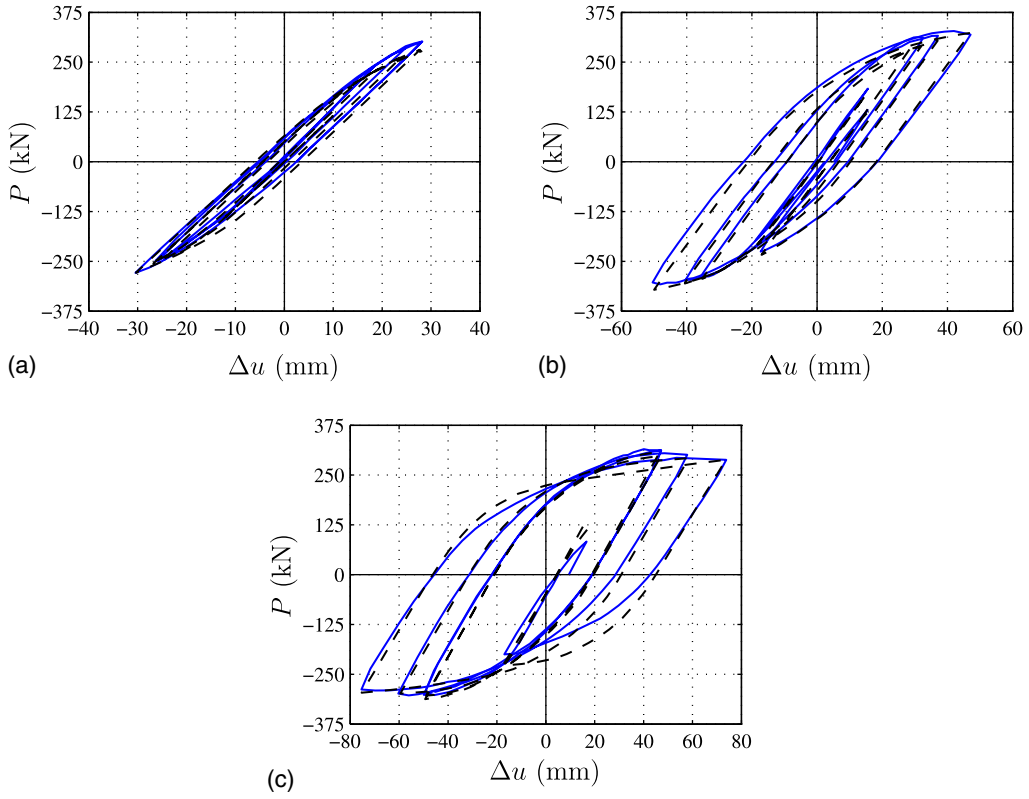

Fig. 11. Plane offshore frame: (a) Cycles 1–5; (b) Cycles 6–10; (c) Cycles 11–15

The remaining members did not buckle and were initially straight. The legs of the jacket had an outer diameter of 324 mm and a thickness of 9.53 mm, and all horizontal bracing and the upper bay bracing had outer diameter of 102 mm and thickness of 3.05 mm. The lower bay bracing had outer diameter of 114 mm and thickness of 4.78 mm, and the top half bracing had outer diameter of 152 mm and thickness of 4.60 mm.

The steel in the bracing had yield stress 180 MPa and the legs had yield stress 300 MPa. All members were modeled with $\beta_N = \beta_{M_y} = \beta_{M_z} = 0.700$ and $\alpha_N = \alpha_{M_y} = \alpha_{M_z} = 0.90$. The relative internal stiffness of the bracing was $(EA)_{\mathrm{i}}/(EA)_{\mathrm{e}} = 0.6$ and $(EI)_{\mathrm{i}}/(EI)_{\mathrm{e}} = 2.0$. The legs had sufficient strength to avoid the formation of plastic hinges. Because the D/t ratio of all members was relatively low, local buckling was not expected and degradation effects were not included in the model. Figs. 11(a–c) show the horizontal load-displacement ($P - \Delta u$) curves of the loaded top right corner, with each subfigure showing five cycles for clarity.

The figure shows good agreement between the experiment and the results of the model, and the characteristic load levels and shapes of the hysteresis curves of the model replicate the experimental results fairly well. A degradation of the ultimate capacity of the structure was caused by the permanent deformation of the geometry of the structure originating from elastoplastic deformation and column buckling.

Conclusions

A model of cyclic plastic hinges based on generalized stresses in the form of section forces was presented. The model has the ability to degrade stiffness and strength to account for the effects of local buckling, fracture, and so on in frame structures. The model is based on a yield surface and a plastic flow potential which have the same gradient with respect to the section forces. For beams, typical analytical yield surfaces have corners which are numerically difficult to handle and a generic, smooth, and convex yield surface representation is suggested. The present yield surface is formulated in terms of normalized generalized stresses and is homogeneous of degree one, which in combination with the plastic flow potential ensures the desired plastic behavior.

The plastic hinge model is described by five parameters for each generalized stress component: the elastic and elastoplastic stiffnesses, the yield and ultimate capacities, and a parameter controlling the shape of the hysteresis curve between yield and ultimate capacity. The plastic hinge model was implemented in an elastoplastic beam element formulated via an equilibrium format whereby the stiffness format can be inverted to the flexibility format, which is additive. A return algorithm was formulated for the beam element via the flexibility format, whereby the consistent algorithmic tangent stiffness matrix was derived. The algorithmic tangent stiffness matrix accounts for change in stiffness during yielding as well as change of stiffness and capacity parameters, leading to an efficient return algorithm.

The element was used to model cyclic bending of cantilevered steel beams utilizing very simple damage functions. In the final stages of the experiment, degradation included local instability effects, the representation of which will need further refinement of the specific damage model. The computed results compared well with the experimental results. The model also was used to model and calculate the response of a tubular offshore frame subjected to cyclic loading. In this case, too, the model captured the response well and clearly represented the experimentally observed increased displacements in continued cycling.

Acknowledgments

This paper is part of a project sponsored jointly by the Danish Agency for Science, Technology and Innovation, Maersk Oil A/S, and the Technical University of Denmark. The authors gratefully acknowledge access to the digital data of D'Aniello et al. (2012) provided by Prof. Raffaele Landolfo.

Notation

The following symbols are used in this paper:

$\mathbf{A}_k$ = positive definite, symmetric matrix;
$\mathbb{B}_y$ = yield capacity matrix;
$\mathbb{B}_\beta$ = relative additional capacity matrix;
$\mathbb{D}_\mathrm{e}$ = elastic stiffness;
$\mathbb{D}_\mathrm{i}$ = internal stiffness;
$\mathbb{D}_\mathrm{ed}$ = combined elastic and damage evolution matrix;
$\mathbb{D}_\mathrm{eid}$ = combined elastic, internal, and damage evolution matrix;
$\mathbb{D}_\mathrm{eid}^\mathrm{ep}$ = combined elastic, internal, and damage-like elastoplastic stiffness;
$\dot{\mathcal{D}}$ = dissipation rate;
$d\boldsymbol{\lambda}$ = plastic multiplier vector;
F = Yield function;
$\mathbf{f}_y = [F_1, F_2]^T$ = yield function vector;
G = plastic flow potential;
G_d = plastic flow potential solely dependent on generalized damage-like stresses;
$\mathbf{g} = [G_1, G_2]^T$ = plastic flow potential vector;
$\mathbf{K}_\mathrm{e}$ = elastic stiffness matrix of equilibrium format beam element;
$\mathbf{K}_\mathrm{i}$ = internal stiffness matrix of equilibrium format beam element;
$\mathbf{K}_\mathrm{ed} = \mathbb{D}_\mathrm{ed}$ for equilibrium format beam element;
$\mathbf{K}_\mathrm{eid} = \mathbb{D}_\mathrm{eid}$ for equilibrium format beam element;
$\mathbf{K}_\mathrm{ep}$ = elastoplastic tangent stiffness matrix of equilibrium format beam element;
$\mathbf{K}_\mathrm{eid}^A$ = algorithmic stiffness matrix;
$\mathbf{K}_\mathrm{r}$ = tangent stiffness matrix for rotation and length change effects;
$\mathbf{q}$ = element force vector of full format beam element;
$\tilde{\mathbf{q}}_\mathrm{e}$ = equilibrium force vector of beam element;
$\tilde{\mathbf{q}}_\mathrm{i}$ = internal equilibrium forces of beam element;
$\tilde{\mathbf{q}}_\mathrm{d}$ = damage-like equilibrium force vector of beam element;
$\tilde{\mathbf{q}} = [\tilde{\mathbf{q}}_\mathrm{e}^T, \tilde{\mathbf{q}}_\mathrm{i}^T, \tilde{\mathbf{q}}_\mathrm{d}^T]^T$ = common equilibrium, internal and damage-like force vector;
$\mathbf{r}_{\tilde{\mathbf{u}}}$ = displacement residual in return algorithm;
$\mathbf{T}$ = transformation matrix, transformation between equilibrium and full format;
$\mathbf{u}$ = displacement vector of full format beam element;
$\tilde{\mathbf{u}}_\mathrm{t} = \tilde{\mathbf{u}}_\mathrm{e} + \tilde{\mathbf{u}}_\mathrm{p}$ = deformations in beam element, sum of elastic and plastic deformations;
$\tilde{\mathbf{u}}_\mathrm{i}$ = internal deformation vector of beam element;
$\tilde{\mathbf{u}}_\mathrm{d}$ = damage-like deformation vector of beam element;
$\tilde{u}_{\mathrm{d},0}^{k,j}$ = reciprocal of saturation speed for material parameter k at node j;
$\tilde{\mathbf{u}} = [\tilde{\mathbf{u}}_\mathrm{e}^T, \tilde{\mathbf{u}}_\mathrm{i}^T, \tilde{\mathbf{u}}_\mathrm{d}^T]^T$ = common elastic, internal, and damage-like deformation vector;
α_j = hysteresis shape parameter for generalized stress j;
$\boldsymbol{\gamma} = \boldsymbol{\gamma}_\mathrm{e} + \boldsymbol{\gamma}_\mathrm{p}$ = generalized strains, sum of elastic and plastic generalized strains;
$\boldsymbol{\gamma}_\mathrm{i}$ = generalized internal strains;
$\Delta\tilde{\mathbf{u}}_\mathrm{t}$ = increment of $\tilde{\mathbf{u}}_\mathrm{t}$;
$\Delta\tilde{\mathbf{u}}$ = increment of $\tilde{\mathbf{u}}$;
$\Delta\boldsymbol{\lambda}$ = finite increment plastic multiplier vector;
$\boldsymbol{\partial} F$ = gradient of yield function;
$\delta\mathbf{r}_{\tilde{\mathbf{u}}}$ = increment of displacement residual;
$\delta\tilde{\mathbf{u}}$ = subincrement of $\tilde{\mathbf{u}}$;
$\delta\tilde{\mathbf{q}}$ = subincrement of $\tilde{\mathbf{q}}$;
$\delta\boldsymbol{\lambda}$ = increment of $\Delta\boldsymbol{\lambda}$;
$\boldsymbol{\eta}$ = generalized damage-like stresses;
$\eta_{k,j}$ = relative saturation level of material parameter k at node j;
$\dot{\lambda}$ = plastic multiplier;
$\boldsymbol{\xi}$ = generalized damage-like strains.
$\boldsymbol{\tau}$ = generalized stresses;
$\boldsymbol{\tau}_\mathrm{i}$ = generalized internal stresses;
$\tilde{\boldsymbol{\tau}}$ = normalized generalized stresses;
$\tilde{\boldsymbol{\tau}}_\mathrm{i}$ = normalized generalized internal stresses;
$\hat{\boldsymbol{\tau}}_k$ = offset of yield surface in normalized stress space;
Φ = internal energy of beam element;
Φ_d = internal energy of beam element solely dependent on damage-like deformations;
φ = internal energy;
φ_d = internal energy solely dependent on generalized damage-like strains;
$\partial_{\tilde{\mathbf{q}}}^T \mathbf{f}_y$ = gradients of yield function vector;
$\boldsymbol{\partial} G$ = gradient of plastic flow potential; and
$\partial_{\tilde{\mathbf{q}}}^T \mathbf{g}$ = gradients of plastic flow potential vector.

References

Attalla, M. R., Deierlein, G. G., and McGuire, W. (1994). "Spread of plasticity: Quasi-plastic-hinge approach." *J. Struct. Eng.*, 10.1061/(ASCE)0733-9445(1994)120:8(2451), 2451–2473.

Baber, T. T., and Wen, Y.-K. (1981). "Random vibration of hysteretic, degrading systems." *J. Eng. Mech. Div.*, 107(6), 1069–1087.

Bleyer, J., and de Buhan, P. (2013a). "A greedy algorithm for yield surface approximation." *Comptes Rendus Mecanique*, 341(8), 605–615.

Bleyer, J., and de Buhan, P. (2013b). "Yield surface approximation for lower and upper bound yield design of 3D composite frame structures." *Comput. Struct.*, 129, 86–98.

Chen, W.-F., and Atsuta, T. (2008). *Theory of beam-columns*, J. Ross Publishing, Fort Lauderdale, FL.

Cipollina, A., López-Inojosa, A., and Flórez-López, J. (1995). "A simplified damage mechanics approach to nonlinear analysis of frames." *Comput. Struct.*, 54(6), 1113–1126.

Coombs, W. M., Petit, O. A., and Motlagh, Y. G. (2016). "NURBS plasticity: Yield surface representation and implicit stress integration for isotropic inelasticity." *Comput. Methods Appl. Mech. Eng.*, 304, 342–358.

D'Aniello, M., La Manna Ambrosino, G., Portioli, F., and Landolfo, R. (2013). "Modelling aspects of the seismic response of steel concentric braced frames." *Steel Compos. Struct. Int. J.*, 15(5), 539–566.

D'Aniello, M., La Manna Ambrosino, G., Portioli, F., and Landolfo, R. (2015). "The influence of out-of-straightness imperfection in physical-theory models of bracing members on seismic performance assessment

of concentric braced structures." *Struct. Des. Tall Spec. Build.*, 24(3), 176–197.
D'Aniello, M., Landolfo, R., Piluso, V., and Rizzano, G. (2012). "Ultimate behavior of steel beams under non-uniform bending." *J. Construct. Steel Res.*, 78, 144–158.
Elchalakani, M. (2007). "Plastic mechanism analyses of circular tubular members under cyclic loading." *Thin-Walled Struct.*, 45(12), 1044–1057.
Elchalakani, M., Zhao, X. L., and Grzbieta, R. (2003). "Tests of cold-formed circular tubular braces under cyclic axial loading." *J. Struct. Eng.*, 10.1061/(ASCE)0733-9445(2003)129:4(507), 507–514.
Folino, P., Etse, G., and Will, A. (2009). "Performance dependent failure criterion for normal- and high-strength concretes." *J. Eng. Mech.*, 10.1061/(ASCE)EM.1943-7889.0000048, 1393–1409.
Ibarra, L. F., Medina, R. A., and Krawinkler, H. (2005). "Hysteretic models that incorporate strength and stiffness deterioration." *Earthquake Eng. Struct. Dyn.*, 34(12), 1489–1511.
Inglessis, P., Gómez, G., Quintero, G., and Flórez-López, J. (1999). "Model of damage for steel frame members." *Eng. Struct.*, 21(10), 954–964.
Iu, C. K., and Chan, S. L. (2004). "A simulation-based large deflection and inelastic analysis of steel frames under fire." *J. Constr. Steel Res.*, 60(10), 1495–1524.
Jiang, X.-M., Chen, H., and Liew, J. Y. R. (2002). "Spread-of-plasticity analysis of three-dimensional steel frames." *J. Constr. Steel Res.*, 58(2), 193–212.
Kaewkulchai, G., and Williamson, E. B. (2004). "Beam element formulation and solution procedure for dynamic progressive collapse analysis." *Comput. Struct.*, 82(7–8), 639–651.
Kamaris, G. S., Hatzigeorgiou, G. D., and Beskos, D. E. (2013). "A new damage index for plane steel frames exhibiting strength and stiffness degradation under seismic motion." *Eng. Struct.*, 46, 727–736.
Kitipornchai, S., Zhu, K., Xiang, Y., and Al-Bermani, F. G. A. (1991). "Single-equation yield surfaces for monosymmetric and asymmetric sections." *Eng. Struct.*, 13(4), 366–370.
Krenk, S. (2009). *Non-linear modeling and analysis of solids and structures*, Cambridge University Press, Cambridge, U.K.
Krenk, S., and Tidemann, L. (2017). "A compact cyclic plasticity model with parameter evolution." *Mech. Mater.*, 113, 57–68.
Krenk, S., Vissing, S., and Vissing-Jørgensen, C. (1993). "A finite step updating method for elastoplastic analysis of frames." *J. Eng. Mech.*, 10.1061/(ASCE)0733-9399(1993)119:12(2478), 2478–2495.
Krenk, S., Vissing-Jørgensen, C., and Thesbjerg, L. (1999). "Efficient collapse analysis techniques for framed structures." *Comput. Struct.*, 72(4–5), 481–496.
Liew, J. Y. R., Chen, H., Shanmugam, N. E., and Chen, W. F. (2000). "Improved nonlinear plastic hinge analysis of space frame structures." *Eng. Struct.*, 22(10), 1324–1338.
Liew, J. Y. R., White, D. W., and Chen, W. F. (1993). "Second-order refined plastic-hinge analysis for frame design. Part I." *J. Struct. Eng.*, 10.1061/(ASCE)0733-9445(1993)119:11(3196), 3196–3216.
Lignos, D. G., and Krawinkler, H. (2011). "Deterioration modeling of steel components in support of collapse prediction of steel moment frames under earthquake loading." *J. Struct. Eng.*, 10.1061/(ASCE)ST.1943-541X.0000376, 1291–1302.
Liu, Y., Xu, L., and Grierson, D. E. (2009). "Combined MVP failure criterion for steel cross-sections." *J. Constr. Steel Res.*, 65(1), 116–124.
Lu, Y., Vintzileou, E., Zhang, G.-F., and Tassios, T. P. (1999). "Reinforced concrete scaled columns under cyclic actions." *Soil Dyn. Earthquake Eng.*, 18(2), 151–167.
Mamaghani, I. H. P., and Kajikawa, Y. (1998). "Cyclic inelastic behavior of compact steel tubular columns." *Proc., 8th Int. Symp. on Tubular Structures*, Singapore, 381–389.
Masi, A., Santarsiero, G., Lignola, G. P., and Verderame, G. M. (2013). "Study of the seismic behavior of external RC beam-column joints through experimental tests and numerical simulations." *Eng. Struct.*, 52, 207–219.
MATLAB version 8.20 [Computer software]. MathWorks, Natick, MA.
Oran, C. (1973). "Tangent stiffness in space frames." *J. Struct. Div.*, 99(6), 987–1001.
Orbison, J. G., McGuire, W., and Abel, J. F. (1982). "Yield surface applications in nonlinear steel frame analysis." *Comput. Methods Appl. Mech. Eng.*, 33(1–3), 557–573.
Popov, E. P., Mahin, S. A., and Zayas, V. A. (1980). "Inelastic cyclic behavior of tubular braced frames." *J. Struct. Div.*, 106(12), 2375–2390.
Powell, G. H., and Chen, P. F.-S. (1986). "3D beam-column element with generalized plastic hinges." *J. Eng. Mech.*, 10.1061/(ASCE)0733-9399(1986)112:7(627), 627–641.
RONJA version 5.0 [Computer software]. Rambøll, Copenhagen, Denmark.
Skordeli, M.-A. A., and Bisbos, C. D. (2010). "Limit and shakedown analysis of 3D steel frames via approximate ellipsoidal yield surfaces." *Eng. Struct.*, 32(6), 1556–1567.
Ueda, Y., Akamatsu, T., and Ohmi, Y. (1969). "Elastic-plastic analysis of framed structures using the matrix method." *J. Soc. Nav. Archit. Japan*, 126, 253–262 (in Japanese).
Ueda, Y., Matsuishi, M., Yamakawa, T., and Akamatsu, Y. (1968). "Elastic-plastic analysis of framed structures using the matrix method." *J. Soc. Nav. Archit. Japan*, 124, 183–191 (in Japanese).
Ueda, Y., and Yao, T. (1982). "The plastic node method: A new method of plastic analysis." *Comput. Methods Appl. Mech. Eng.*, 34(1–3), 1089–1104.
Willam, K. J., and Warnke, E. P. (1974). "Constitutive model for the triaxial behaviour of concrete." *Proc., Int. Association for Bridge and Structural Engineering*, Zurich, Switzerland, 19, 1–30.
Zayas, V. A., Mahin, S. A., and Popov, E. P. (1980). "Cyclic inelastic behavior of steel offshore structures." *Rep. No. UCB/EERC-80/27*, Earthquake Engineering Research Center, Berkeley, CA.

P3

A robust frame element with cyclic plasticity and local joint effects

L. Tidemann & S. Krenk

Engineering Structures,
Vol. **168**:191–204, 2018.

Engineering Structures 168 (2018) 191–204

Contents lists available at ScienceDirect

Engineering Structures

journal homepage: www.elsevier.com/locate/engstruct

A robust frame element with cyclic plasticity and local joint effects

Lasse Tidemann[a,b,*], Steen Krenk[a]

[a] Department of Mechanical Engineering, Technical University of Denmark, DK-2800 Kongens Lyngby, Denmark
[b] Maersk Oil, DK-6700 Esbjerg, Denmark

ARTICLE INFO

Keywords:
Frame structures
Local joint flexibility
Plastic hinges
Cyclic plasticity
Return algorithm

ABSTRACT

A robust elasto-plastic element is developed for analysis of frame structures. The element consists of a beam member with end joints with properties permitting representation of the effect of section forces in adjoining members, like axial forces. By use of the equilibrium formulation the deformations of beam member, plastic hinges and joints become additive and can be expressed in explicit form. The plastic deformations of the beam and the joints are represented by separate plastic mechanisms, described by the same generic cyclic plasticity format. This format is defined by an energy function, a yield surface, and a plastic flow potential for each plastic mechanism. In the cyclic plasticity model each component is characterized by the elastic stiffness, the yield capacity, the additional flexibility at initial yield, the ultimate capacity and a shape parameter describing the curvature of the hysteresis curve. The yield surface is represented by a recently developed generic format, combining the section forces into a homogeneous function of degree one and permitting smooth transition between regions with large and more moderate curvature. A robust return algorithm of approximately second order is developed, using a mid-step state to obtain representative information about the return path. The element is implemented in a co-rotational large-deformation computer program for frame structures. The formulation is illustrated by application to a couple of typical offshore frame structures, and comparison of different representations of the plastic effects illustrates the importance of a robust element with realistic representation of the cyclic plastic mechanisms.

1. Introduction

In the design and analysis of frame structures, e.g. offshore tubular structures and steel frame buildings exposed to earthquakes, a large number of load cases are analysed to ensure the structure can withstand the external loading. Some important load cases involve substantial deformation of members in the elasto-plastic regime, followed by subsequent unloading introducing a need for an accurate representation of the cyclic plastic behaviour of beam members. The cyclic elasto-plastic response of a single beam member has been experimentally investigated in e.g. [1–5] for both uni-axial tension/compression and uni-axial bending, and elasto-plastic cyclic column-buckling of tubular steel columns was investigated and characterised by [6]. While cyclic plastic bending is dominated by the non-linearity in the material behaviour, cyclic column-buckling is characterised by the non-linearity in the material behaviour and in the geometry. Common to both cases is that the plastic deformation is local in the form of plastic hinges, suggesting that it is possible to separate geometric and material non-linearity by proper modelling. The localized plastic deformation in the form of plastic hinges is also observed in full structures [7–9], where cyclic loading of the local members comes naturally via global unloading or load-shedding caused by buckling or plasticity in other members. In full structures the plastic hinges may be caused by a plastic mechanism in the local member itself or by a plastic mechanism at the local joint connecting the structural member to the rest of the structure. It is necessary to distinguish the two types of mechanisms from each other and to acknowledge that they may both be present at the same time at the same location. Experimental investigation of capacities of local joints in tubular structures has been carried out in [10] and extensively characterized in [11].

In addition to plastic mechanisms, in practice the local joints between members introduce additional flexibility in the structure compared to completely rigid connections. The difference in the response of a structure modelled with and without local joint flexibility is clear in both traditional analysis of frames [12] and in bifurcation and stability analysis of frames [13]. Multiple experimental programs have investigated and characterized local joint flexibility [14–16], essentially describing the additional flexibility of the local joint by parametric equations depending on the local joint geometry. Recently detailed finite element models have been used to develop such parametric

* Corresponding author at: Department of Mechanical Engineering, Technical University of Denmark, DK-2800 Kongens Lyngby, Denmark.
E-mail address: lastid@mek.dtu.dk (L. Tidemann).

https://doi.org/10.1016/j.engstruct.2018.04.041
Received 7 November 2017; Received in revised form 17 March 2018; Accepted 12 April 2018

equations after validation with experimental data [17–19]. The inclusion of local joint flexibility in analyses has primarily been modelled by separate elastic joint elements [20–22], introducing a need for a transformation between flexibility and stiffness and most often introducing infinite stiffness terms for displacement directions with zero joint flexibility. Separate joint elements including both elastic and plastic flexibility have been introduced [23], introducing this infinite stiffness problem. In some finite element codes e.g. RONJA developed by Rambøll, the local joint flexibility has been introduced in the member elements by static condensation, a method that does not resolve the problem with infinite stiffness.

In most frame structures the imperfections of the individual members need to be modelled to account for the effect of the normal force. Imperfection effects were introduced by [24,25] in an element with negligible shear flexibility based on parabolic and a sine imperfection shape respectively. An explicit elastic element including shear flexibility and a parabolic imperfection shape was introduced in [26] and was extended to include plastic mechanisms in the form of concentrated plastic hinges at the ends of the elastic beam giving an explicit elasto-plastic beam element with initial imperfections.

The differences between beam elements with concentrated plastic hinges and beams modelled with spread of plasticity using fibre elements was investigated in [27], finding the relative magnitude of the generalized plastic strain components to be similar for the two types of models. Several element formulations with concentrated plastic hinges have been proposed, some having three possible plastic hinges [28–30] with one hinge located at mid-span to account for column buckling effects. The degrees of freedom associated with the mid-point plastic hinge are typically removed by static condensation. Other elements, primarily used for column problems, have been suggested [31] with only a hinge at mid-span, and a proposal for softening hinges with location dependent on the section force distribution in [32]. The difference between displacement, flexibility and mixed formulations of beams was investigated in [33] finding the flexibility format quite accurate taking into account its low-order modelling compared to higher-order modelling typically used in displacement and mixed formulations. Flexibility formulations via a 6×6 equilibrium format was proposed in [34,35] for monotonic and cyclic plasticity models as well as in [26] including local imperfections. In order to model cyclic plasticity in frame structures more accurately [36] introduced a generalized formulation of the cyclic plasticity model from [37]. The model is based on non-linear kinematic hardening rules and evolution of the model parameters and was subsequently extended to include local joint plastic mechanisms [38]. Common to all of the element formulations is that they are based on a set of yield functions bounding the elastic domain and a set of plastic flow potentials to describe the development of plastic deformation.

The yield surface of the individual plastic mechanisms may be determined either by approximate analytical methods [39] or numerical estimates [40] and subsequently modelled in various ways. A standard approach that ensures convexity of the yield surface is the use of multi-linear yield surfaces. However, the checks of multiple surfaces and determination of gradients at vertices may be difficult, see e.g [41]. To overcome the difficulty with multiple checks, single-equation formulations of yield surfaces have been proposed, e.g. higher-order polynomial approximations [42,43], NURBS-based formulations [44] or use of Fourier principles [45]. All these have the disadvantage that the coefficients in the equations or locations of the control points may be difficult to determine while simultaneously ensuring convexity of the yield surface. The convexity was ensured in a surface format proposed by [46,47] using a Minkowski sum of ellipsoids, and the use of the convexity of the ellipsoids was utilized by [36] to form a generic convex single-equation yield function without the need to form the actual Minkowski sum. For some cyclic plastic deformation histories the shape of the yield surface has been found to change, and a weighted average of different yield surfaces has been applied with success [48,49].

Independent of the choice of the yield surface formulation it is desirable to be able to make large load/deformation increments in order to have efficient computations. The analysis procedure typically determines the displacement increments via a global analysis and subsequently determining the element deformations and forces, ensuring that the yield condition is not violated in the individual elements. Satisfaction of the yield condition is typically attained by a return algorithm where combinations of the deformation evolution equations and the yield conditions determine the correct increment in element forces. For continuum elements [50] proposed a return algorithm for plane stress elasto-plasticity including the algorithmic tangent stiffness needed to ensure second order convergence of the global solution. While the plane-stress elasto-plasticity return algorithm was developed for a fairly simple yield surface, a more advanced algorithm was developed for structural concrete with a more complicated yield surface [51] making use of sub-stepping techniques as well as line search to ensure a proper return to the yield surface. In geotechnics the yield surface is typically divided into multiple domains and several return algorithms have been developed to overcome the problems with finding the correct domain to return to [52–54]. Where [52] modified the individual domains, [53] used bisection in a transformed space and a combination of returning to an unhardened state and subsequently returning to the hardened state, and [54] made use of a relaxation technique to obtain a more robust algorithm. The efficiency of the return algorithm may in some cases be increased by transforming to an invariant space [55] combined with multi-linear yield surfaces and defining separate rules for return to vertices [56]. Separate algorithms have also been developed for coupled problems including damage [57]. Common to all return algorithms is that they need to be quite robust to allow for large increments of deformation in any direction, and for plastic hinges it is paramount to ensure the robustness of the algorithm independently of the given yield surface.

This paper develops an elasto-plastic frame element, and introduces plastic beam hinges and elasto-plastic joints via the concept of additive flexibilities. The element is defined in an equilibrium-based co-rotational formulation and is sufficiently general to encompass elastic element formulations ranging from standard cubic shape functions to normal force dependent stiffness functions including initial member imperfections, see e.g. [26,58], as well as plastic mechanisms ranging from ideal plasticity to models coupling elasto-plasticity and damage. The cyclic plasticity formulation proposed in [37] is generalized and extended to ensure invariance for doubly-symmetric beam cross sections. The yield function is of the type proposed by [36] and determination of parameters as well as gradual change of shape and inclusion of shear effects are discussed. A novel two-step return algorithm that includes the effects of distributed loads is introduced and shown to increase the robustness of traditional single-step return algorithms considerably. Finally, examples of realistic tubular offshore structures are used to illustrate the effect of the plasticity formulation as well as the robustness of the equilibrium element formulation and the modified return algorithm. The examples highlight the differences between standard element and plasticity formulations and the present integrated formulation, illustrating the necessity of having an accurate representation of cyclic plasticity and local joint mechanisms.

2. Elasto-plastic frame element

The frame element is defined in an equilibrium format with six deformation modes with energy conjugate section forces as illustrated in Fig. 1. Details of the equilibrium formulation may be found in [26,58]. The deformations and the section forces are arranged in the vectors

$$\widetilde{\mathbf{u}}_{\mathrm{t}} = [u,\varphi_x,\varphi_{z1},\varphi_{z2},\varphi_{y1},\varphi_{y2}]^T_{\mathrm{t}}, \tag{1}$$

$$\widetilde{\mathbf{q}}_{\mathrm{e}} = [\widetilde{N},\widetilde{T},\widetilde{M}_{z1},\widetilde{M}_{z2},\widetilde{M}_{y1},\widetilde{M}_{y2}]^T, \tag{2}$$

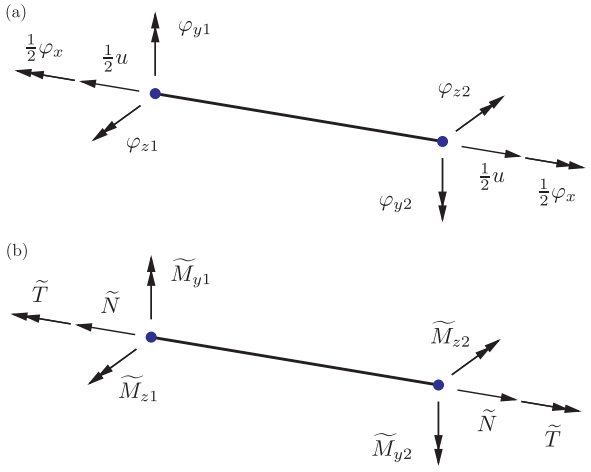

Fig. 1. Equilibrium format of beam element. (a) Element deformations, (b) section forces.

where the tilde indicates the relation to the equilibrium format and the subscript 't' indicates that it is the total deformation of the element, while the subscript 'e' indicates that sections forces are energy conjugate to the elastic deformations.

In frame structures with cyclic plasticity and local joint effects there are four primary mechanisms that must be represented; elastic deformation of the beam member $\tilde{\mathbf{u}}_{\mathrm{e}}^{\mathrm{M}}$, plastic deformation in the form of yield hinges at the beam member ends $\tilde{\mathbf{u}}_{\mathrm{p}}^{\mathrm{M}}$, elastic deformation at the local joints $\tilde{\mathbf{u}}_{\mathrm{e}}^{\mathrm{J}}$ and plastic deformation of the local joints $\tilde{\mathbf{u}}_{\mathrm{p}}^{\mathrm{J}}$. The three latter effects are concentrated at the beam ends and are assumed to be local mechanisms, whereby the section forces of all four mechanisms are the same as indicated in Fig. 2.

Assuming small deformations, the total deformation $\tilde{\mathbf{u}}_{\mathrm{t}}$ at each end is the sum of the mechanism deformations, and the flexibilities are thereby additive and the element may be described by a single deformation measure, $\tilde{\mathbf{u}}_{\mathrm{t}}$. In the case of a negligible mechanism effect the flexibility of the mechanism is zero and thus the format degenerates to a simple elastic frame element when the other mechanisms are negligible. Alternatively, in a stiffness format a negligible mechanism effect corresponds to an infinite stiffness making it difficult to have a simple algorithm where negligible mechanisms lead to a degenerate element because of numerical evaluations of infinite stiffness.

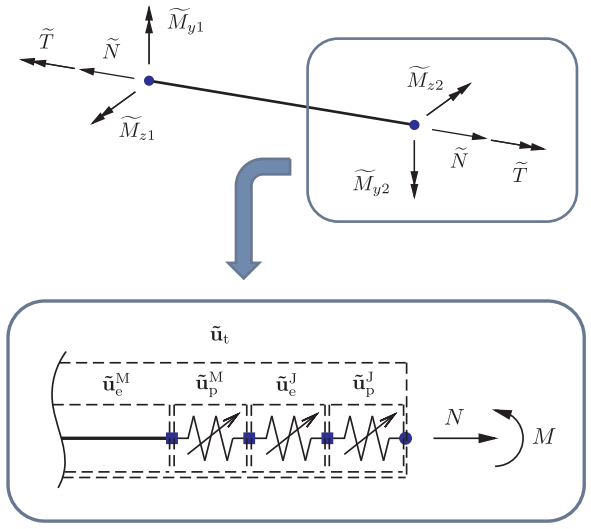

Fig. 2. Equilibrium frame element with non-linear elastic and plastic mechanisms.

2.1. Energy definition

The cyclic plasticity model is based on [37,36] and is defined via an energy potential, a yield function and a plastic flow potential. The energy defines the constitutive relations between deformations and sections forces, while the yield function set equal to zero defines the yield surface, and the gradient of the plastic flow potential defines the plastic deformation evolution. The energy potential is given by

$$\varphi = \varphi_{\mathrm{e}}(\tilde{\mathbf{u}}_{\mathrm{e}},\tilde{\mathbf{u}}_{\mathrm{d}}) + \varphi_{\mathrm{i}}(\tilde{\mathbf{u}}_{\mathrm{i}},\tilde{\mathbf{u}}_{\mathrm{d}}) + \varphi_{\mathrm{d}}(\tilde{\mathbf{u}}_{\mathrm{d}}) \tag{3}$$

where $\tilde{\mathbf{u}}_{\mathrm{e}}$ are elastic deformations, including both elastic member and elastic local joint deformation, $\tilde{\mathbf{u}}_{\mathrm{i}}$ are internal deformation measures and $\tilde{\mathbf{u}}_{\mathrm{d}}$ are damage-like deformation measures used to control model parameter evolution, see [37]. The elastic energy φ_{e} is unspecified, leaving room for geometric non-linearity/bowing and other non-linear elastic effects, but in the simplest case is a quadratic form of the elastic deformations. The internal energy φ_{i} may also take a general form; however a standard quadratic form may be preferable as non-linearity may be included via the gradient of the plastic flow potential. The dependence on $\tilde{\mathbf{u}}_{\mathrm{d}}$ in the elastic and internal energy terms φ_{e} and φ_{i} is introduced to allow for an evolution of the stiffness for the energy conjugate section forces. The damage-like energy term φ_{d} is unspecified to allow for any type of parameter evolution format desired.

The section forces energy conjugate to the elastic, the internal and the damage-like deformations, respectively, follow from the energy function as

$$\tilde{\mathbf{q}}_{\mathrm{e}} = \frac{\partial\varphi}{\partial\tilde{\mathbf{u}}_{\mathrm{e}}^T} = \frac{\partial\varphi_{\mathrm{e}}}{\partial\tilde{\mathbf{u}}_{\mathrm{e}}^T} \tag{4}$$

$$\tilde{\mathbf{q}}_{\mathrm{i}} = \frac{\partial\varphi}{\partial\tilde{\mathbf{u}}_{\mathrm{i}}^T} = \frac{\partial\varphi_{\mathrm{i}}}{\partial\tilde{\mathbf{u}}_{\mathrm{i}}^T} \tag{5}$$

$$\tilde{\mathbf{q}}_{\mathrm{d}} = \frac{\partial\varphi}{\partial\tilde{\mathbf{u}}_{\mathrm{d}}^T} = \frac{\partial\varphi_{\mathrm{e}}}{\partial\tilde{\mathbf{u}}_{\mathrm{d}}^T} + \frac{\partial\varphi_{\mathrm{i}}}{\partial\tilde{\mathbf{u}}_{\mathrm{d}}^T} + \frac{\partial\varphi_{\mathrm{d}}}{\partial\tilde{\mathbf{u}}_{\mathrm{d}}^T}. \tag{6}$$

The section forces $\tilde{\mathbf{q}}_{\mathrm{e}}$ are the equilibrium forces of the beam element, while the internal section forces $\tilde{\mathbf{q}}_{\mathrm{i}}$ are used to describe the centres of the yield surfaces for the different plastic mechanisms. Thus, the dimension of $\tilde{\mathbf{q}}_{\mathrm{e}}$ is smaller than the dimension of $\tilde{\mathbf{q}}_{\mathrm{i}}$. The damage-like deformations $\tilde{\mathbf{u}}_{\mathrm{d}}$ are used to model evolution of the elastic stiffness $\partial^T_{\tilde{\mathbf{u}}_{\mathrm{e}}}\tilde{\mathbf{q}}_{\mathrm{e}}$ and the internal stiffness $\partial^T_{\tilde{\mathbf{u}}_{\mathrm{i}}}\tilde{\mathbf{q}}_{\mathrm{i}}$, while the damage-like section forces $\tilde{\mathbf{q}}_{\mathrm{d}}$ are used to model isotropic hardening and evolution of other model parameters. The incremental relations for the elastic, internal and damage-like section forces are expressed via the 'chain rule' as

$$\dot{\tilde{\mathbf{q}}} = \begin{bmatrix} \dot{\tilde{\mathbf{q}}}_{\mathrm{e}} \\ \dot{\tilde{\mathbf{q}}}_{\mathrm{i}} \\ \dot{\tilde{\mathbf{q}}}_{\mathrm{d}} \end{bmatrix} = \begin{bmatrix} \partial^T_{\tilde{\mathbf{u}}_{\mathrm{e}}}\tilde{\mathbf{q}}_{\mathrm{e}} & \mathbf{0} & \partial^T_{\tilde{\mathbf{u}}_{\mathrm{d}}}\tilde{\mathbf{q}}_{\mathrm{e}} \\ \mathbf{0} & \partial^T_{\tilde{\mathbf{u}}_{\mathrm{i}}}\tilde{\mathbf{q}}_{\mathrm{i}} & \partial^T_{\tilde{\mathbf{u}}_{\mathrm{d}}}\tilde{\mathbf{q}}_{\mathrm{i}} \\ (\partial^T_{\tilde{\mathbf{u}}_{\mathrm{d}}}\tilde{\mathbf{q}}_{\mathrm{e}})^T & (\partial^T_{\tilde{\mathbf{u}}_{\mathrm{d}}}\tilde{\mathbf{q}}_{\mathrm{i}})^T & \partial^T_{\tilde{\mathbf{u}}_{\mathrm{d}}}\tilde{\mathbf{q}}_{\mathrm{d}} \end{bmatrix} \begin{bmatrix} \dot{\tilde{\mathbf{u}}}_{\mathrm{e}} \\ \dot{\tilde{\mathbf{u}}}_{\mathrm{i}} \\ \dot{\tilde{\mathbf{u}}}_{\mathrm{d}} \end{bmatrix} = \mathbf{K}_{\mathrm{eid}}\dot{\tilde{\mathbf{u}}}, \tag{7}$$

where $\mathbf{K}_{\mathrm{eid}}$ is the tangent stiffness matrix containing the double derivatives of the energy. The stiffness matrix $\partial^T_{\tilde{\mathbf{u}}_{\mathrm{e}}}\tilde{\mathbf{q}}_{\mathrm{e}}$ is the elastic tangent stiffness matrix containing the contributions from both the member elasticity and the local joint elasticity.

2.2. Plastic mechanisms

There are two plastic mechanisms at each end of the beam and hence a total of four plastic mechanisms. The plastic flow potentials and yield functions for these four mechanisms are arranged in the vectors

$$\mathbf{g} = [G_1(\tilde{\mathbf{q}}),...,G_4(\tilde{\mathbf{q}})]^T, \quad \mathbf{f}_y = [F_1(\tilde{\mathbf{q}}),...,F_4(\tilde{\mathbf{q}})]^T. \tag{8}$$

The part of the damage-like section forces $\tilde{\mathbf{q}}_{\mathrm{d}}$ used to model evolution of the yield function parameters must be independent from the part of the damage-like deformations $\tilde{\mathbf{u}}_{\mathrm{d}}$ used to model evolution of the elastic stiffness matrix given via (3) to ensure the yield surface only changes during plastic deformation, see e.g. a discussion of the decoupling in

[58].

The evolution of the elastic, plastic, internal and damage-like deformations is given by maximization of the dissipation rate under the assumption of the material being described by the flow potentials, giving

$$\dot{\tilde{\mathbf{u}}} = \begin{bmatrix} \dot{\tilde{\mathbf{u}}}_t \\ \mathbf{0} \\ \mathbf{0} \end{bmatrix} - \sum_j \partial_{\tilde{\mathbf{q}}} G_j \dot{\lambda}_j = \begin{bmatrix} \dot{\tilde{\mathbf{u}}}_t \\ \mathbf{0} \\ \mathbf{0} \end{bmatrix} - (\partial_{\tilde{\mathbf{q}}}^T \mathbf{g})^T \dot{\boldsymbol{\lambda}}, \quad \dot{\boldsymbol{\lambda}} = [\dot{\lambda}_1, \ldots, \dot{\lambda}_4]^T, \tag{9}$$

where $\dot{\lambda}_j \geqslant 0$, see e.g. [37,36] for a detailed derivation. During plastic deformation the various yield conditions should be fulfilled at all times imposing the consistency condition that during plastic deformation

$$\dot{\mathbf{f}}_y = (\partial_{\tilde{\mathbf{q}}}^T \mathbf{f}_y)\dot{\tilde{\mathbf{q}}} = \mathbf{0}. \tag{10}$$

Combining the evolution Eq. (9) with the incremental constitutive relation (7) and the consistency condition (10) gives the plastic multipliers

$$\dot{\boldsymbol{\lambda}} = [(\partial_{\tilde{\mathbf{q}}}^T \mathbf{f}_y)\mathbf{K}_{\text{eid}} \left(\partial_{\tilde{\mathbf{q}}}^T \mathbf{g}\right)^T]^{-1} (\partial_{\tilde{\mathbf{q}}}^T \mathbf{f}_y)\mathbf{K}_{\text{ed}} \dot{\tilde{\mathbf{u}}}_t = \mathbf{H}^{-1} (\partial_{\tilde{\mathbf{q}}}^T \mathbf{f}_y)\mathbf{K}_{\text{ed}} \dot{\tilde{\mathbf{u}}}_t. \tag{11}$$

Here, $\mathbf{K}_{\text{ed}}$ is the first block column of $\mathbf{K}_{\text{eid}}$ as defined in (7), corresponding to the increment $\dot{\tilde{\mathbf{q}}}$ when only $\dot{\tilde{\mathbf{u}}}_e$ is non-zero. The hardening matrix $\mathbf{H}$ to be inverted is of size $n \times n$ when n plastic mechanisms are active. Thus the maximum is 4×4 and $\mathbf{H}$ is most often easily inverted analytically. Combining the plastic multipliers (11) with the deformation evolution Eqs. (9) and the incremental constitutive relation (7) gives the elasto-plastic incremental constitutive relation

$$\dot{\tilde{\mathbf{q}}} = [\mathbf{K}_{\text{ed}} - \mathbf{K}_{\text{eid}} \left(\partial_{\tilde{\mathbf{q}}}^T \mathbf{g}\right)^T \mathbf{H}^{-1} (\partial_{\tilde{\mathbf{q}}}^T \mathbf{f}_y)\mathbf{K}_{\text{ed}}]\dot{\tilde{\mathbf{u}}}_t. \tag{12}$$

The elasto-plastic stiffness matrix $\mathbf{K}_{\text{ep}}$, relating the section force increment $\dot{\tilde{\mathbf{q}}}_e$ and the total displacement increment $\dot{\tilde{\mathbf{u}}}_t$, is used in equilibrium iterations and is identified from the top block of (12) as

$$\mathbf{K}_{\text{ep}} = \partial_{\tilde{\mathbf{u}}_e}^T \tilde{\mathbf{q}}_e - \mathbf{K}_{\text{ed}}^T \left(\partial_{\tilde{\mathbf{q}}}^T \mathbf{g}\right)^T \mathbf{H}^{-1} (\partial_{\tilde{\mathbf{q}}}^T \mathbf{f}_y)\mathbf{K}_{\text{ed}}. \tag{13}$$

It is noted that $\mathbf{K}_{\text{ep}}$ is symmetric whenever the elastic stiffness is independent of $\tilde{\mathbf{u}}_d$.

2.3. Elastic and internal stiffness

The section forces $\tilde{\mathbf{q}}_e$ may be a non-linear function of the energy conjugate elastic deformations $\tilde{\mathbf{u}}_e$ as indicated in (4). In the case of beam-column elements with bowing effects the non-linearity originates from the effect of the normal force, see e.g. [26]. When an elastic local joint mechanism is present the process of determining the section forces may be iterative and involve determination of how much of the elastic deformation $\tilde{\mathbf{u}}_e$ is elastic member deformation $\tilde{\mathbf{u}}_e^M$ and how much is elastic local joint deformation $\tilde{\mathbf{u}}_e^J$. The process of determining the section forces is based on additive elastic deformations

$$\tilde{\mathbf{u}}_e = \tilde{\mathbf{u}}_e^M + \tilde{\mathbf{u}}_e^J \tag{14}$$

and as the equation in general will not be satisfied automatically for non-linear elastic models the residual

$$\mathbf{r}_{\tilde{\mathbf{u}}_e} = \tilde{\mathbf{u}}_e - (\tilde{\mathbf{u}}_e^M + \tilde{\mathbf{u}}_e^J) \tag{15}$$

is formed. The deformations $\tilde{\mathbf{u}}_e^M$ and $\tilde{\mathbf{u}}_e^J$ are initially found by the constitutive relations for the individual mechanisms for an estimated set of section forces. It is typically advantageous to form an initial estimate of the section forces from the member constitutive equations, assuming $\tilde{\mathbf{u}}_e^M = \tilde{\mathbf{u}}_e$. Subsequently the deformations $\tilde{\mathbf{u}}_e^M$ and $\tilde{\mathbf{u}}_e^J$ corresponding to the section forces may be found. To ensure a correct deformation distribution a first order approximation of the residual (15) is made, where the first order variation of the residual is

$$\delta\mathbf{r}_{\tilde{\mathbf{u}}_e} = -(\delta\tilde{\mathbf{u}}_e^M + \delta\tilde{\mathbf{u}}_e^J) = -((\mathbf{K}_e^M)^{-1} + (\mathbf{K}_e^J)^{-1})\delta\tilde{\mathbf{q}}_e. \tag{16}$$

Here $(\mathbf{K}_e^M)^{-1}$ and $(\mathbf{K}_e^J)^{-1}$ are the elastic tangent flexibilities of the member and the local joint, respectively. Note, that the tangent flexibility of the member may include initial imperfections, see e.g. [26], while the tangent flexibility of the local joint may depend on the section forces in adjacent members. The correction in the section force estimate $\delta\tilde{\mathbf{q}}_e$ is found by setting the residual (15) equal to zero giving

$$\delta\tilde{\mathbf{q}}_e = ((\mathbf{K}_e^M)^{-1} + (\mathbf{K}_e^J)^{-1})^{-1}\mathbf{r}_{\tilde{\mathbf{u}}_e} = \mathbf{K}_e\mathbf{r}_{\tilde{\mathbf{u}}_e}. \tag{17}$$

This identifies the elastic tangent stiffness matrix $\partial_{\tilde{\mathbf{u}}_e}^T \tilde{\mathbf{q}}_e = \mathbf{K}_e = ((\mathbf{K}_e^M)^{-1} + (\mathbf{K}_e^J)^{-1})^{-1}$ to be used in (7). It is clear that the additive flexibility format is the key to determining the correct tangent stiffness, and it is seen that the standard tangent stiffness without local joint effects is simply a special case where the local joint flexibility is zero. The process of determining the section forces and the distribution of the elastic deformations is summarised in Table 1.

Table 1
Elastic deformation distribution.

1. Assume $\tilde{\mathbf{u}}_e^M = \tilde{\mathbf{u}}_e$ and determine $\tilde{\mathbf{q}}_e$ as with no joint flexibility.
2. Determine $\tilde{\mathbf{u}}_e^M$ and $\tilde{\mathbf{u}}_e^J$ based on $\tilde{\mathbf{q}}_e$ and constitutive relations.
3. Determine tangent flexibility matrices $(\mathbf{K}_e^M)^{-1}$, $(\mathbf{K}_e^J)^{-1}$ and residual $\mathbf{r}_{\tilde{\mathbf{u}}_e}$.
4. Determine increment $\delta\tilde{\mathbf{q}}_e = \mathbf{K}_e\mathbf{r}_{\tilde{\mathbf{u}}_e}$.
5. Update $\tilde{\mathbf{q}}_e = \tilde{\mathbf{q}}_e + \delta\tilde{\mathbf{q}}_e$. Go to 2 and repeat until convergence.

While the elastic tangent stiffness is found by the inverse of the sum of two flexibilities the internal tangent stiffness $\partial_{\tilde{\mathbf{u}}_i}^T \tilde{\mathbf{q}}_i$ is found directly by the double derivative of the internal energy φ_i. As the evolution of the internal deformations $\dot{\tilde{\mathbf{u}}}_i$ is controlled by the gradients of the flow potentials according to (9) it is of interest to have a constant internal stiffness to isolate the origin of non-linear behaviour of the internal section forces. Therefore the internal energy is here defined as

$$\varphi_i(\tilde{\mathbf{u}}_i, \tilde{\mathbf{u}}_d) = \frac{1}{2}\tilde{\mathbf{u}}_i^T \mathbf{K}_i(\tilde{\mathbf{u}}_d)\tilde{\mathbf{u}}_i \tag{18}$$

whereby the internal stiffness is $\partial_{\tilde{\mathbf{u}}_i}^T \tilde{\mathbf{q}}_i = \mathbf{K}_i(\tilde{\mathbf{u}}_d)$. The internal stiffness matrix is a diagonal matrix to ensure any coupling between the internal section forces controlling the centres of the yield surfaces is controlled by the plastic flow potentials.

2.4. Full component format

In order to use the beam element in a global analysis the formulation must be expanded to 6 components at each node and a rigid-body motion superimposed on the local element displacements, see e.g. [26,58] for details of the formulation used here. The full format three-dimensional beam element including rigid body motion is illustrated in Fig. 3. The element displacements and forces are arranged in the vectors

$$\mathbf{u}^T = [\mathbf{u}_1^T, \mathbf{u}_2^T], \quad \mathbf{u}_j = [u_x, u_y, u_z, \theta_x, \theta_y, \theta_z]_j^T, \tag{19}$$

$$\mathbf{q}^T = [\mathbf{q}_1^T, \mathbf{q}_2^T], \quad \mathbf{q}_j = [Q_x, Q_y, Q_z, M_x, M_y, M_z]_j^T, \tag{20}$$

and the link between the total element deformations $\tilde{\mathbf{u}}_t$ and the element displacements $\mathbf{u}$ and between the equilibrium format section forces $\tilde{\mathbf{q}}_e$ and the element forces $\mathbf{q}$ is provided by the equilibrium conditions. Axial, torsional, transverse and rotational equilibrium enables the relation

$$\mathbf{q} = \begin{bmatrix} \mathbf{q}_1 \\ \mathbf{q}_2 \end{bmatrix} = \begin{bmatrix} \mathbf{S}_1 \\ \mathbf{S}_2 \end{bmatrix} \tilde{\mathbf{q}}_e = \mathbf{S}\tilde{\mathbf{q}}_e, \tag{21}$$

where the transformation matrix $\mathbf{S}$ may take into account the effects of axial shortening, bowing etc. see e.g. [26]. The virtual work of the full format and the equilibrium format must be the same in order to have a consistent element, [26], whereby the deformation increment may be expressed in terms of the displacement increment

$$d\tilde{\mathbf{u}}_t = \mathbf{S}^T d\mathbf{u}. \tag{22}$$

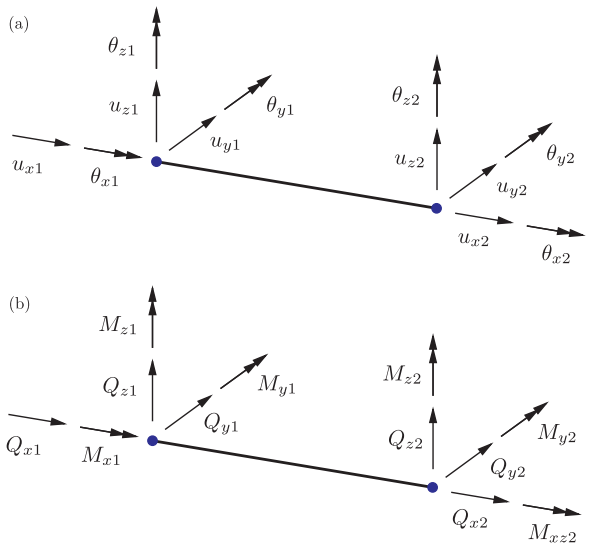

Fig. 3. Full format of beam element. (a) Element displacements and rotations, (b) element forces and moments.

Note, that this transformation between displacements and deformations removes the rigid body motion in a small-deformation format. The increment in the element forces is found by differentiation of (21),

$$d\mathbf{q} = \mathbf{S}\, d\tilde{\mathbf{q}}_{\mathrm{e}} + d\mathbf{S}\,\tilde{\mathbf{q}}_{\mathrm{e}}. \tag{23}$$

The first term is expressed in terms of $d\mathbf{u}$ by use of the constitutive relation (13) and the incremental deformation relation (22). The second term represents the contributions from rigid-body motion and element elongation. When extracting the displacement increment components this term can be expressed as $\mathbf{K}_{\mathrm{g}}\, d\mathbf{u}$, where the matrix $\mathbf{K}_{\mathrm{g}}$ represents the effects of the effects just mentioned. The full increment in the element forces $d\mathbf{q}$ then relates to the displacement increment $d\mathbf{u}$ by

$$d\mathbf{q} = (\mathbf{S}\mathbf{K}_{\mathrm{ep}}\mathbf{S}^T + \mathbf{K}_{\mathrm{g}})\, d\mathbf{u}, \tag{24}$$

where the local elasto-plastic stiffness matrix $\mathbf{K}_{\mathrm{ep}}$ is replaced by the local elastic tangent stiffness matrix $\mathbf{K}_{\mathrm{e}}$ in the absence of active plastic mechanisms. When used in a global analysis the components in (24) are transformed into a global coordinate system. The combination of including the global motion in the local stiffness relation and transforming the resulting stiffness relation into global components constitutes a co-rotational formulation, enabling realistic cyclic collapse analyses of offshore structures.

3. Plastic potentials

Each of the four plastic mechanisms are described by a yield surface and a corresponding plastic flow potential and the total model is obtained by arranging these in the two arrays $\mathbf{f}_y$ and $\mathbf{g}$ as shown in (8). In order to avoid an overly heavy notation each of the mechanisms will be described by its yield function $F(\tilde{\mathbf{q}})$ and flow potential $G(\tilde{\mathbf{q}})$ without explicitly introducing the subscript j identifying the particular mechanism. Similarly, the arrays $\tilde{\mathbf{q}}_{\mathrm{e}}$ and $\tilde{\mathbf{q}}_{\mathrm{i}}$ will be used to denote the components relating to this particular mechanism, and thus these vectors will have the same dimension in the present context. Also vectors like $\tilde{\mathbf{q}}_{\mathrm{d}}$ denoting damage parameters as well as other model parameters will be limited to those relevant for the particular mechanism.

The present cyclic plasticity model is based on non-linear kinematic hardening, with the centers of the individual yield surfaces represented by the internal section forces $\tilde{\mathbf{q}}_{\mathrm{i}}$ and the non-linearity of the hardening introduced via the gradient of the plastic flow potential. The yield function is defined in terms of normalized section forces as an iso-surface of the kinematic hardening yield function

$$F(\tilde{\mathbf{q}}) = \|\overline{\mathbf{q}}_{\mathrm{e}} - \overline{\mathbf{q}}_{\mathrm{i}}\| - 1, \quad \overline{\mathbf{q}}_{\mathrm{e}} = \mathbb{B}_y^{-1}\tilde{\mathbf{q}}_{\mathrm{e}},\ \overline{\mathbf{q}}_{\mathrm{i}} = \mathbb{B}_y^{-1}\tilde{\mathbf{q}}_{\mathrm{i}}, \tag{25}$$

where $\mathbb{B}_y = \mathbb{B}_y(\tilde{\mathbf{q}}_{\mathrm{d}})$ is a diagonal matrix with the current yield capacities in the diagonal, and the yield surface is defined by setting the yield function equal to zero. The normalization effectively defines the yield surface in terms of the relative sections force components, e.g. the relative normal force $n = N/N^y$. The capacity matrix $\mathbb{B}_y = \mathbb{B}_y(\tilde{\mathbf{q}}_{\mathrm{d}})$ as well as the norm $\|\,\|$ may be different for the different plastic mechanisms.

The norm has the general format

$$\|\overline{\mathbf{q}}_{\mathrm{e}} - \overline{\mathbf{q}}_{\mathrm{i}}\| = \sqrt{(\overline{\mathbf{q}}_{\mathrm{e}} - \overline{\mathbf{q}}_{\mathrm{i}})^T\mathbf{A}_1(\overline{\mathbf{q}}_{\mathrm{e}} - \overline{\mathbf{q}}_{\mathrm{i}})} + \sqrt{(\overline{\mathbf{q}}_{\mathrm{e}} - \overline{\mathbf{q}}_{\mathrm{i}})^T\mathbf{A}_2(\overline{\mathbf{q}}_{\mathrm{e}} - \overline{\mathbf{q}}_{\mathrm{i}})} + \cdots, \tag{26}$$

where $\mathbf{A}_1$, $\mathbf{A}_2$,... are all symmetric, positive definite matrices. This format gives homogeneous yield surfaces of degree one. For a homogeneous norm the exterior equipotential surfaces are scaled versions of the original yield surface, a valuable property in connection with development of an efficient return algorithm. The first and second order derivatives of the norm exist everywhere except in $\overline{\mathbf{q}}_{\mathrm{e}} - \overline{\mathbf{q}}_{\mathrm{i}} = \mathbf{0}$ where yielding is not present and the derivatives are not needed.

The plastic flow potential is a generalization of the multi-dimensional flow potential proposed in [37]. The relative capacity in addition to the yield capacity is given by a parameter β that may be different for the different section force components. Similarly the shape parameter α controlling the roundedness of the hysteresis curve may vary with the section force component. The possible directional-dependency of the parameters is accounted for by introduction of equivalent values in the flow potential

$$G(\tilde{\mathbf{q}}) = F(\tilde{\mathbf{q}}) + \frac{\|\hat{\boldsymbol{\beta}}\|}{\|\hat{\boldsymbol{\alpha}}\|}\left\{\|\hat{\mathbf{q}}_{\mathrm{i}}\| - 1 - \frac{1-\|\hat{\boldsymbol{\alpha}}\|}{\|\hat{\boldsymbol{\alpha}}\|}\ln(1 + \|\hat{\boldsymbol{\alpha}}\|(\|\hat{\mathbf{q}}_{\mathrm{i}}\| - 1))\right\} + G_{\mathrm{d}}(\tilde{\mathbf{q}}_{\mathrm{d}}), \tag{27}$$

where the norms $\|\hat{\mathbf{q}}_{\mathrm{i}}\|$,$\|\hat{\boldsymbol{\beta}}\|$ and $\|\hat{\boldsymbol{\alpha}}\|$ are defined by

$$\|\hat{\mathbf{q}}_{\mathrm{i}}\| = \left\| \frac{\overline{\mathbf{q}}_{\mathrm{i}}}{\|\hat{\boldsymbol{\beta}}\|} \right\|, \quad \|\hat{\boldsymbol{\beta}}\| = \hat{\beta}\,\|\mathbb{B}_\beta\mathbf{n}\|, \quad \|\hat{\boldsymbol{\alpha}}\| = \hat{\alpha}\,\|\mathbb{B}_\alpha\mathbf{n}\|. \tag{28}$$

The matrices $\mathbb{B}_\beta$ and $\mathbb{B}_\alpha$ are positive definite diagonal matrices that relate the individual β- and α-values to the reference values $\hat{\beta}$ and $\hat{\alpha}$. It is noted that all the resulting α-values have the same sign as $\hat{\alpha}$ and hence all the shape parameters are either positive or negative. The vector $\mathbf{n}$ is a unit vector with $\|\mathbf{n}\| = 1$ and is defined as a step-wise function that is always proportional to the current value of $\overline{\mathbf{q}}_{\mathrm{i}}$, unless $\overline{\mathbf{q}}_{\mathrm{i}} = \mathbf{0}$ in which case $\mathbf{n}$ is proportional to $\overline{\mathbf{q}}_{\mathrm{e}}$. The direction vector $\mathbf{n}$ is proportional to $\overline{\mathbf{q}}_{\mathrm{i}}$ because the parameters α and β interact solely with $\overline{\mathbf{q}}_{\mathrm{i}}$ via the plastic flow potential.

The gradients of the yield surface and the plastic flow potential are fairly simple

$$\partial^T_{\tilde{\mathbf{q}}_{\mathrm{e}}}F = -\partial^T_{\tilde{\mathbf{q}}_{\mathrm{i}}}F = \partial^T_{\tilde{\mathbf{q}}_{\mathrm{e}}}G = \frac{\partial\|\overline{\mathbf{q}}_{\mathrm{e}} - \overline{\mathbf{q}}_{\mathrm{i}}\|}{\partial(\overline{\mathbf{q}}_{\mathrm{e}} - \overline{\mathbf{q}}_{\mathrm{i}})}\frac{(\partial\overline{\mathbf{q}}_{\mathrm{e}} - \overline{\mathbf{q}}_{\mathrm{i}})}{\partial\overline{\mathbf{q}}_{\mathrm{e}}}\frac{\partial\overline{\mathbf{q}}_{\mathrm{e}}}{\partial\tilde{\mathbf{q}}_{\mathrm{e}}} = \frac{\partial\|\overline{\mathbf{q}}_{\mathrm{e}} - \overline{\mathbf{q}}_{\mathrm{i}}\|}{\partial(\overline{\mathbf{q}}_{\mathrm{e}} - \overline{\mathbf{q}}_{\mathrm{i}})}\mathbb{B}_y^{-1}, \tag{29}$$

where the gradient of the norm is easily determined. Similarly the gradient of the flow potential with respect to $\tilde{\mathbf{q}}_{\mathrm{i}}$ is given as

$$\partial^T_{\tilde{\mathbf{q}}_{\mathrm{i}}}G = \partial^T_{\tilde{\mathbf{q}}_{\mathrm{i}}}F + \frac{\|\hat{\mathbf{q}}_{\mathrm{i}}\|}{(1-\|\hat{\boldsymbol{\alpha}}\|) + \|\hat{\boldsymbol{\alpha}}\|\|\hat{\mathbf{q}}_{\mathrm{i}}\|}\frac{\partial\|\hat{\mathbf{q}}_{\mathrm{i}}\|}{\partial\hat{\mathbf{q}}_{\mathrm{i}}}\mathbb{B}_y^{-1}, \tag{30}$$

because $\mathbf{n}$ is a stepwise function. When neglecting parameter evolution the increment in $\tilde{\mathbf{u}}_{\mathrm{i}}$ and hence $\tilde{\mathbf{q}}_{\mathrm{i}}$ is proportional to $\partial^T_{\tilde{\mathbf{q}}_{\mathrm{i}}}G$ as seen from (9) and when $\partial^T_{\tilde{\mathbf{q}}_{\mathrm{i}}}G = \mathbf{0}$ the hardening stops and the ultimate capacity is reached. When $\|\hat{\mathbf{q}}_{\mathrm{i}}\|$ equals one the factor in (30) equals one and the second term will cancel the first term when $\hat{\mathbf{q}}_{\mathrm{i}} = \overline{\mathbf{q}}_{\mathrm{e}} - \overline{\mathbf{q}}_{\mathrm{i}}$ corresponding to an ultimate capacity of $\overline{\mathbf{q}}_{\mathrm{e}} = (1 + \|\hat{\boldsymbol{\beta}}\|)(\overline{\mathbf{q}}_{\mathrm{e}} - \overline{\mathbf{q}}_{\mathrm{i}})$. When the norm is homogeneous $\hat{\mathbf{q}}_{\mathrm{i}}$ can be replaced by $\overline{\mathbf{q}}_{\mathrm{i}}$ in (30) if $(1-\|\hat{\boldsymbol{\alpha}}\|)$ is replaced by $(1-\|\hat{\boldsymbol{\alpha}}\|)\|\hat{\boldsymbol{\beta}}\|$. As most plastic mechanisms of members and joints may be represented via a norm of the type (26) that is homogeneous such a rewritten format may be advantageous for program implementation. The format above ensures that the ultimate capacity of a tube in pure

bending is invariant with respect to the angle between the axis of bending and the defined main axes of the element for all values of $\|\hat{\boldsymbol{\alpha}}\|$ in contrast to the model originally proposed in [36].

The effects of the different model parameters for a plastic mechanism defined by an energy potential, a yield function of the type (25) and a plastic flow potential of the type (27) are illustrated in Fig. 4.

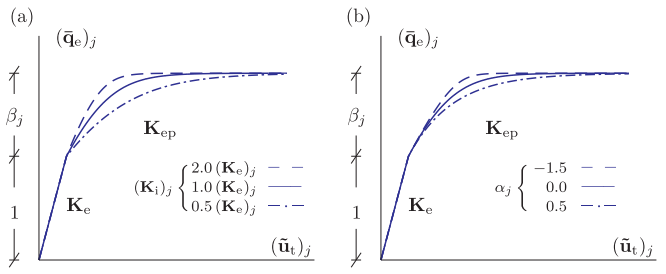

Fig. 4. Effect of model parameters.

Fig. 4 illustrates a uniaxial deformation in the direction of the j'th component of $\tilde{\mathbf{u}}_t$. While $\mathbf{K}_e$ characterises the initial elastic stiffness, the internal stiffness $\mathbf{K}_i$ characterizes the kink at plasticity, which occurs when the section force normalized by the current yield capacity is one. The plastic mechanism has a relative capacity of β_j in addition to the yield capacity. Finally the roundedness of the hysteresis curve is controlled by the α_j parameter. Note, that for a multi-axial loading $\bar{\mathbf{q}}_e$ will be replaced by $\|\bar{\mathbf{q}}_e\|$, β_j will be replaced by $\|\hat{\boldsymbol{\beta}}\|$ and α_j will be replaced by $\|\hat{\boldsymbol{\alpha}}\|$ in Fig. 4.

3.1. Representative norms

The concept of determining the relevant parameters of the matrices in the definition of the norm (26) in a simple way was discussed by [36]. It was found that yield surfaces for typical double-symmetric beams can be represented by two terms with diagonal matrices. Similarly, it was shown in [38] that the yield surface format is suitable for representing yield surfaces for tubular steel joints. Although it is possible to represent analytical yield surfaces with corners quite accurately, it can be advantageous to round the yield surface slightly in such regions, thereby enhancing the algorithmic properties of the surface. The most accurate representation of the yield surface overall is achieved by rounding on the inside of the surface because of the convexity of the surface. Whereas a rounding on the outside may give the option of having a yield surface predicting the correct uni-axial yield capacities, it will lead to over-prediction of capacity in generalized multi-axial stress states, e.g. bending and axial tension.

The solution to finding a proper roundedness for a specific problem without the need for a full library of different yield surfaces with different roundedness in a finite element program is interpolation between surfaces. Because the norm (26) is a convex function a sum of different norms will also be convex and ensure that an iso-surface like the yield surface will be convex. Thus, a weighted sum of different norms will be guaranteed to represent a convex yield surface when the weights are positive. Thereby it is only necessary to have two different yield surfaces in the library; one with the maximum acceptable rounding, typically represented by approximately a 5% reduction of the capacity in the region with large curvature in question, and the exact representation of the yield surface. Any other rounding between those states can be achieved by simply weighting the two norms with a factor between zero and one where the sum of the weight factors must equal one. The concept is illustrated by contour lines of the yield surface of a tubular steel beam in Fig. 5.

The exact yield surface representation is modelled using two terms with diagonal matrices $\mathbf{A}_1$ and $\mathbf{A}_2$ where $A^1_{1,1} = 1{-}2{\cdot}10^{-5}$, $A^1_{2,2} = A^1_{3,3} = 0.16$, $A^2_{1,1} = 1{\cdot}10^{-10}$ and $A^2_{2,2} = A^2_{3,3} = 0.36$.

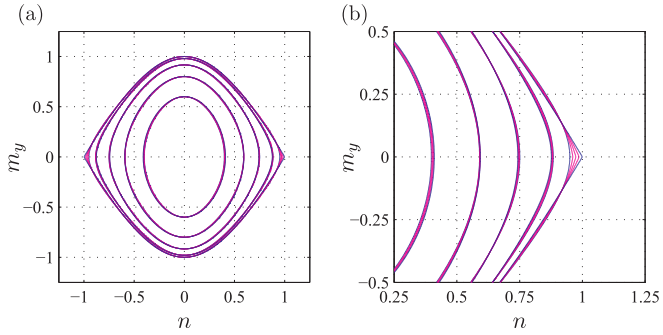

Fig. 5. Contour lines of rounded yield surface by weighting of two yield surfaces.

The rounded surface is represented using two diagonal matrices $\mathbf{A}_1$ and $\mathbf{A}_2$ with $A^1_{1,1} = 0.865$, $A^1_{2,2} = A^1_{3,3} = 0.0961$, $A^2_{1,1} = 0.0150$ and $A^2_{2,2} = A^2_{3,3} = 0.476$. Fig. 5 indicates that the interpolation between the exact and rounded representation of the yield surface only changes a very small region of the yield surface, where the curvature is large. The remaining part of the yield surface is indifferent to the rounding and the interpolation makes it very simple to create any rounding of the yield surface with just one weighting parameter, a constraint and the two yield surface representations to be interpolated.

Determining a representative yield surface may also be eased using an interpolation between multiple yield surfaces. By selecting representative points on the analytical yield surface that should be accurately represented a total error of a given yield surface representation can be determined by simply adding the values of the square of the given yield function at the selected points. With the error defined for multiple yield surface representations it is simple to set up a total error function being the weighted sum of the individual errors for the different yield surface representations. From that point on it is a simple linear optimization problem with inequalities as constraints as well as the constraint that the sum of the weights must equal one. This is a fairly standard optimization problem that is fast to solve however it may introduce the need for a large amount of different norms. In contrast a non-linear optimization routine minimizing the error with respect to the coefficients in the individual matrices need only one norm with fewer terms than the total amount of terms in a weighted sum, however the optimization may be more difficult to program.

3.2. Gradual change of yield surface

Besides enabling a simple representation of a rounded yield surface the interpolation enables the possibility of gradually changing the yield surface during plastic loading, described by e.g. [48,49] for anisotropic materials. A gradual shape change can be introduced by dedicating a properly defined damage-like section force of $\tilde{\mathbf{q}}_d$ to describe the weighting parameter of a norm. The damage-like section force of $\tilde{\mathbf{q}}_d$ is introduced via $\tilde{\mathbf{u}}_d$ in $\varphi_d(\tilde{\mathbf{u}}_d)$ in (3). Such a shape change enables initially using a first fibre yield surface and gradually changing to the full plastification yield surface without using a two-surface model. This is illustrated in Fig. 6.

If multiple surfaces are used in the interpolation to introduce e.g. dependency on loading type or similar effects multiple parameters are simply introduced in φ_d. With such a formulation it will be possible to use the exact representation of the yield surface for initial estimation of the yield capacity and subsequently gradually change the yield surface representation to a more rounded version to benefit the algorithmic properties.

Note, that because of the form of the norm (26) it is possible to introduce rotation of the yield surface simply by multiplying the matrices $\mathbf{A}_1, \mathbf{A}_2, \ldots$with rotation matrices symmetrically from each side. If it is found that the yield surface rotates during plastic loading such an

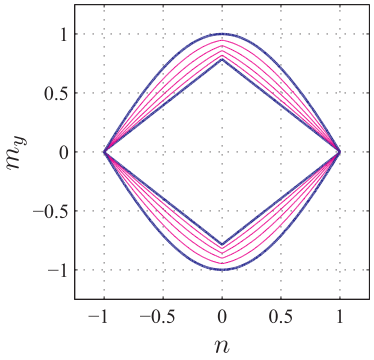

Fig. 6. Contour lines of gradual change from first fibre yield to full plastification.

effect may be introduced by letting the rotation matrix depend on a parameter of $\tilde{\mathbf{q}}_{\mathrm{d}}$. With the use of weighting of different norms, rotation matrices, the kinematic hardening and the dependency of the current yield values on $\tilde{\mathbf{q}}_{\mathrm{d}}$, it is possible to have expansion/contraction, distortion, translation, rotation and affine deformation of the yield surface in very simple and identifiable ways, similar to what is proposed for cubic polynomial representations of yield surfaces in [43].

3.3. Inclusion of shear effects and local joint coordinates

Yield surfaces for local joint plastic mechanisms are defined in terms of the local forces, typically defined in the local joint coordinate system rather than the section forces in the element coordinate system. Similarly the effect of shear forces may be important for some beams, primarily in the form of plastic mechanisms in the member ends. An example of a yield surface for a tubular steel joint from the MSL report [59] is shown in Fig. 7 in terms of normalized section forces, along with a representation using the proposed yield surface format.

Both effects are included without violating the equilibrium format introduced in the previous section. The shear force effect is most easily included by describing the yield surface in terms of the element forces $\mathbf{q}$, and when doing so the plastic mechanisms at each end should only be described by the element forces $\mathbf{q}_j$ at beam end j as defined in (20). Similarly, the local joint plastic mechanisms are defined in terms of the element nodal forces in the local joint coordinate system at the current end given by

$$\mathbf{q}_j^{\mathrm{J}} = \mathbf{T}_j^{\mathrm{J}}\mathbf{q}_j, \tag{31}$$

where $\mathbf{T}_j^{\mathrm{J}}$ is a transformation matrix, that transforms from the element coordinate system to the local joint coordinate system. The gradient of the yield function F with respect to the section forces is given by the transformation

$$\frac{\partial F}{\partial \tilde{\mathbf{q}}_{\mathrm{e}}} = \sum_{j=1,2} \frac{\partial F}{\partial \mathbf{q}_j^{\mathrm{J}}}\frac{\partial \mathbf{q}_j^{\mathrm{J}}}{\partial \mathbf{q}_j}\frac{\partial \mathbf{q}_j}{\partial \tilde{\mathbf{q}}_{\mathrm{e}}} = \sum_{j=1,2} \frac{\partial F}{\partial \mathbf{q}_j^{\mathrm{J}}}\mathbf{T}_j^{\mathrm{J}}\mathbf{S}_j. \tag{32}$$

In the case of a plastic mechanism in the member the joint coordinate system transformation matrix $\mathbf{T}_j^{\mathrm{J}}$ is the identity matrix and for a plastic mechanism F located at node 1, the derivative $\partial F/\partial \mathbf{q}_2^{\mathrm{J}}$ equals zero. The gradient of the plastic flow potentials are carried out in the same way.

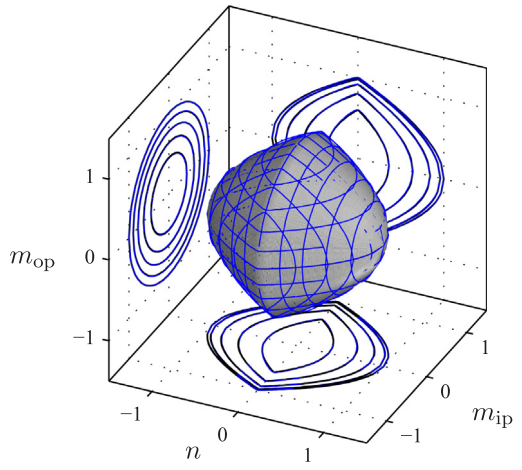

Fig. 7. Theoretical yield surface for tubular joint (MSL surface) and representation, (—). Contour lines are plotted in selected planes.

4. Robust return algorithm including distributed loads

The deformation evolution Eq. (9) is valid for infinitesimal increments of deformations, a format not suitable for actual finite element calculations where the increments are finite. To obtain a robust algorithm capable of handling finite increments of deformation, the deformation evolution Eq. (9) is replaced by its equivalent finite increment form

$$\Delta\tilde{\mathbf{u}} = \begin{bmatrix}\Delta\tilde{\mathbf{u}}_{\mathrm{t}}\\ \mathbf{0}\\ \mathbf{0}\end{bmatrix} - \sum_j \partial_{\tilde{\mathbf{q}}} G_j \Delta\lambda_j = \begin{bmatrix}\Delta\tilde{\mathbf{u}}_{\mathrm{t}}\\ \mathbf{0}\\ \mathbf{0}\end{bmatrix} - (\partial_{\tilde{\mathbf{q}}}^T\mathbf{g})^T\Delta\boldsymbol{\lambda}. \tag{33}$$

Here $\Delta\tilde{\mathbf{u}}_{\mathrm{t}}$ includes both the global deformations $\Delta\tilde{\mathbf{u}}_{\mathrm{g}}$ and the local deformations from the distributed load $\Delta\tilde{\mathbf{u}}_{\mathrm{l}}$. The local deformations are determined via the elastic flexibility matrix and the equivalent nodal forces

$$\Delta\tilde{\mathbf{u}}_{\mathrm{l}} = \mathbf{K}_{\mathrm{e}}^{-1}\Delta\mathbf{f}_{\mathrm{l}}. \tag{34}$$

The distributed load vector $\mathbf{f}_{\mathrm{l}}$ contains only the loads that can be represented by deformations and loads corresponding to rigid body motions must be added subsequently, i.e. non-homogeneous shear forces from the distributed load must be added to the element nodal forces separately.

It is assumed that the finite increment formulation (33) is satisfied in the final state, and to ensure that a residual is formed

$$\mathbf{r}_{\tilde{\mathbf{u}}} = \begin{bmatrix}\Delta\tilde{\mathbf{u}}_{\mathrm{t}}\\ \mathbf{0}\\ \mathbf{0}\end{bmatrix} - \Delta\tilde{\mathbf{u}} - (\partial_{\tilde{\mathbf{q}}}^T\mathbf{g})^T\Delta\boldsymbol{\lambda}. \tag{35}$$

The residual is generally not zero initially for yield surfaces representing plastic mechanisms in frame elements. The increment of the residual is found by variation about the final state

$$\delta\mathbf{r}_{\tilde{\mathbf{u}}} = -\delta\tilde{\mathbf{u}} - \left(\sum_j \frac{\partial^2 G_j}{\partial\tilde{\mathbf{q}}^T\partial\tilde{\mathbf{q}}}\Delta\lambda_j\right)\delta\tilde{\mathbf{q}} - (\partial_{\tilde{\mathbf{q}}}^T\mathbf{g})^T\delta\boldsymbol{\lambda}, \tag{36}$$

where the increments $\delta\tilde{\mathbf{u}}$, $\delta\tilde{\mathbf{q}}$ and $\delta\boldsymbol{\lambda}$ are all increments of the final state parameters. The increment $\delta\tilde{\mathbf{u}}$ is related to the increment $\delta\tilde{\mathbf{q}}$ via the constitutive relation (7) and the first order approximation of the residual can be expressed entirely in terms of $\delta\tilde{\mathbf{q}}$ and $\delta\boldsymbol{\lambda}$. The additional equations necessary to determine both $\delta\tilde{\mathbf{q}}$ and $\delta\boldsymbol{\lambda}$ come from the consistency condition that the final stress state must be located on the yield surface. That is ensured by a first order approximation

$$\mathbf{f}_y + (\partial_{\tilde{\mathbf{q}}}^T\mathbf{f}_y)\delta\tilde{\mathbf{q}} = \mathbf{0}. \tag{37}$$

Using the first order approximation of the residual via (35) and (36) and setting it equal to zero in combination with the consistency condition (37) gives the equation system

$$\begin{bmatrix}(\mathbf{K}_{\mathrm{eid}}^A)^{-1} & (\partial_{\tilde{\mathbf{q}}}^T\mathbf{g})^T\\ \partial_{\tilde{\mathbf{q}}}^T\mathbf{f}_y & \mathbf{0}\end{bmatrix}\begin{bmatrix}\delta\tilde{\mathbf{q}}\\ \delta\boldsymbol{\lambda}\end{bmatrix} = \begin{bmatrix}\mathbf{r}_{\tilde{\mathbf{u}}}\\ -\mathbf{f}_y\end{bmatrix}, \tag{38}$$

where the algorithmic stiffness matrix $\mathbf{K}_{\mathrm{eid}}^A$ is identified by its inverse

$$(\mathbf{K}^A_{\text{eid}})^{-1} = \mathbf{K}^{-1}_{\text{eid}} + \sum_j \frac{\partial^2 G_j}{\partial \widetilde{\mathbf{q}}^T \partial \widetilde{\mathbf{q}}} \Delta\lambda_j. \tag{39}$$

The equation system is solved explicitly by isolating $\delta\widetilde{\mathbf{q}}$ in the first row in (38), substituting it in the second row and solving for $\delta\lambda$ giving the increments

$$\delta\lambda = [(\partial^T_{\widetilde{\mathbf{q}}}\mathbf{f}_y)\mathbf{K}^A_{\text{eid}}\left(\partial^T_{\widetilde{\mathbf{q}}}\mathbf{g}\right)^T]^{-1}(\mathbf{f}_y + (\partial^T_{\widetilde{\mathbf{q}}}\mathbf{f}_y)\mathbf{K}^A_{\text{eid}}\mathbf{r}_{\widetilde{\mathbf{u}}}), \tag{40}$$

$$\delta\widetilde{\mathbf{q}} = \mathbf{K}^A_{\text{eid}}(\mathbf{r}_{\widetilde{\mathbf{u}}} - \left(\partial^T_{\widetilde{\mathbf{q}}}\mathbf{g}\right)^T\delta\lambda). \tag{41}$$

It is noted that the increments in the plastic multipliers $\delta\lambda$ must take values ensuring that $\Delta\lambda$ remains positive or zero.

4.1. Increased robustness

The increments (40) and (41) are essentially linear representations. In regions where the curvature of the yield surface is large or when the hardening is highly non-linear over the deformation increment a linear representation may not provide a sufficiently robust algorithm. The residual (35) is dependent on the direction of the return via the gradient of the flow potential and dependent on the magnitude of return via the plastic multipliers. A good estimate of the return is more dependent on the estimate of the direction than on the estimate of the magnitude. In order to increase the robustness of the return algorithm better estimates of the algorithmic stiffness and the gradients of the yield function and the flow potential are sought in order to get better estimates of the direction of the return.

The estimate of the gradients and algorithmic stiffness are determined by a procedure similar to the two-step procedure for explicit stress integration proposed in [60]. A second order Taylor expansion of $\delta\widetilde{\mathbf{q}}$ from the initial point $\delta\widetilde{\mathbf{q}}_0 = \mathbf{0}$ to the point $\delta\widetilde{\mathbf{q}}(\xi\mathbf{r}_{\widetilde{\mathbf{u}}}, \xi\mathbf{f}_y)$ is given by

$$\delta\widetilde{\mathbf{q}}(\xi) = \xi\frac{\partial(\delta\widetilde{\mathbf{q}})}{\partial\xi}\bigg|_{\xi=0} + \frac{1}{2}\xi^2\frac{\partial^2(\delta\widetilde{\mathbf{q}})}{\partial\xi^2}\bigg|_{\xi=0}. \tag{42}$$

The first order derivative is found by combination of the incremental relations (40) and (41) expressing the linear representation of $\delta\widetilde{\mathbf{q}}$ directly in terms of $\mathbf{r}_{\widetilde{\mathbf{u}}}$ and $\mathbf{f}_y$ by the general format

$$\frac{\partial(\delta\widetilde{\mathbf{q}})}{\partial\xi} = \mathbf{K}_{\mathbf{r}}\mathbf{r}_{\widetilde{\mathbf{u}}} - \mathbf{K}_{\mathbf{f}}\mathbf{f}_y, \tag{43}$$

where the stiffness matrices $\mathbf{K}_{\mathbf{r}}$ and $\mathbf{K}_{\mathbf{f}}$ are

$$\mathbf{K}_{\mathbf{r}} = \mathbf{K}^A_{\text{eid}} - \mathbf{K}^A_{\text{eid}}\left(\partial^T_{\widetilde{\mathbf{q}}}\mathbf{g}\right)^T\mathbf{H}_A^{-1}(\partial^T_{\widetilde{\mathbf{q}}}\mathbf{f}_y)\mathbf{K}^A_{\text{eid}}, \quad \mathbf{K}_{\mathbf{f}} = \mathbf{K}^A_{\text{eid}}\left(\partial^T_{\widetilde{\mathbf{q}}}\mathbf{g}\right)^T\mathbf{H}_A^{-1}, \tag{44}$$

with the algorithmic hardening matrix

$$\mathbf{H}_A = (\partial^T_{\widetilde{\mathbf{q}}}\mathbf{f}_y)\mathbf{K}^A_{\text{eid}}\left(\partial^T_{\widetilde{\mathbf{q}}}\mathbf{g}\right)^T. \tag{45}$$

It is noted that $\mathbf{K}_{\mathbf{r}}$ corresponds to the consistent elasto-plastic tangent operator. The three matrices $\mathbf{K}_{\mathbf{r}}$, $\mathbf{K}_{\mathbf{f}}$ and $\mathbf{H}_A$ all vary with $\widetilde{\mathbf{q}} = \widetilde{\mathbf{q}}_0 + \delta\widetilde{\mathbf{q}}$ as they depend on gradients of the yield functions and flow potentials and on second order derivatives of the flow potentials. The second order derivative in (42) is found by differentiation of (43),

$$\frac{\partial^2(\delta\widetilde{\mathbf{q}})}{\partial^2\xi} = \frac{\partial}{\partial\xi}(\mathbf{K}_{\mathbf{r}}\mathbf{r}_{\widetilde{\mathbf{u}}} - \mathbf{K}_{\mathbf{f}}\mathbf{f}_y) \simeq \frac{\Delta\mathbf{K}_{\mathbf{r}}}{\Delta\xi}\mathbf{r}_{\widetilde{\mathbf{u}}} - \frac{\Delta\mathbf{K}_{\mathbf{f}}}{\Delta\xi}\mathbf{f}_y, \tag{46}$$

illustrating that a higher order method needs more information than what is available at the initial point. To obtain $\Delta\mathbf{K}_{\mathbf{r}}$ and $\Delta\mathbf{K}_{\mathbf{f}}$ half a return step is made, corresponding to finding the midpoint of a full step in the linear return algorithm (40) and (41). The half-step is given by

$$\delta\widetilde{\mathbf{q}}_{1/2} = \frac{1}{2}(\mathbf{K}^0_{\mathbf{r}}\mathbf{r}_{\widetilde{\mathbf{u}}} - \mathbf{K}^0_{\mathbf{f}}\mathbf{f}_y), \tag{47}$$

where the superscript 0 indicates that the initial values of the matrices are used. The midpoint is characterized by $\widetilde{\mathbf{q}}_{1/2} = \widetilde{\mathbf{q}}_0 + \delta\widetilde{\mathbf{q}}_{1/2}$ and $\widetilde{\mathbf{u}}_{1/2} = \widetilde{\mathbf{u}}_0 + \delta\widetilde{\mathbf{u}}_{1/2}$. At the midpoint the matrices $\mathbf{K}^{1/2}_{\mathbf{r}}$ and $\mathbf{K}^{1/2}_{\mathbf{f}}$ are determined and in combination with $\mathbf{K}^0_{\mathbf{r}}$ and $\mathbf{K}^0_{\mathbf{f}}$ they are used to form the second order derivative in (46) where $\Delta\xi = 1/2$. Inserting the derivatives (43) and (46) into the Taylor expansion (42) and setting $\xi = 1$ gives a second order estimate of the increment $\delta\widetilde{\mathbf{q}}$ as

$$\delta\widetilde{\mathbf{q}} = \mathbf{K}^{1/2}_{\mathbf{r}}\mathbf{r}_{\widetilde{\mathbf{u}}} - \mathbf{K}^{1/2}_{\mathbf{f}}\mathbf{f}_y, \tag{48}$$

a format very similar to the two-step explicit stress integration format proposed in [60]. In practice it is more desirable to use the formulas (40) and (41) where algorithmic stiffness and gradients of the yield functions and plastic flow potentials are determined at the mid-point. By making the two-step subincrementation using (40) and (41) it is easy to limit how negative the increment $\delta\lambda_j$ may be to still have positive $\Delta\lambda_j$ and subsequently obtaining the consistent increment $\delta\widetilde{\mathbf{q}}$. The return procedure is illustrated in Fig. 8.

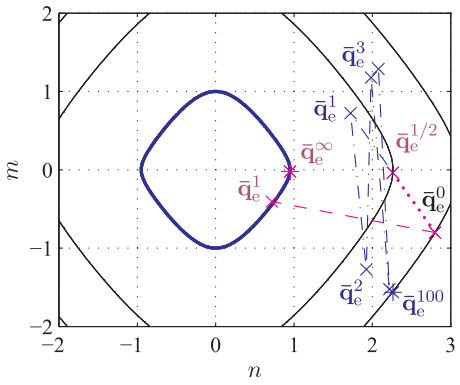

Fig. 8. Comparison between single step (blue) and the proposed two-step (magenta) return algorithm. (For interpretation of the references to colour in this figure legend, the reader is referred to the web version of this article.)

In Fig. 8 the return procedure is illustrated for a single active plastic mechanism. From the initial estimate of the final state $\bar{\mathbf{q}}^0_{\text{e}}$ half a return step is made to the position $\bar{\mathbf{q}}^{1/2}_{\text{e}}$ where the algorithmic stiffness and the gradients of the yield function and the flow potential are evaluated. With the information from $\bar{\mathbf{q}}^{1/2}_{\text{e}}$ a full step is taken from the initial position $\bar{\mathbf{q}}^0_{\text{e}}$ to the next estimate of the final state $\bar{\mathbf{q}}^1_{\text{e}}$. Note, that the estimate of the final state after the first return step $\bar{\mathbf{q}}^1_{\text{e}}$ is fairly close to the converged final state $\bar{\mathbf{q}}^{\infty}_{\text{e}}$. Marked in blue are the points of iterations when using a traditional single step return algorithm that will not converge in the present case.

The format above makes use of the algorithmic stiffness defined at the mid-point suggesting that $\Delta\lambda$ should also be updated at the mid-point as it is part of the algorithmic stiffness. However it is found that the algorithm is more robust when only the gradients of the yield functions and the plastic flow potentials as well as the double derivatives of the plastic flow potentials are updated at the mid-point, while the initial estimate of the plastic multiplier is retained. The difference in robustness is attributed to the fact that the estimate of the plastic multiplier is not systematically improved at the half-step position because it has not yet corrected the direction of the step.

4.2. Limitations on increments

In principle the algorithm above imposes no limits on the type of yield surface nor the flow potential as long as the incremental relation (7) holds and the second order derivatives of the plastic flow potentials exist. However, in the present theory it is necessary to impose limits on the increments of the internal section forces $\widetilde{\mathbf{q}}_{\text{i}}$ as the algorithm will be ill-behaved if $\|\hat{\mathbf{q}}_{\text{i}}\| > 1$, leading to an inconsistency in the flow potential gradient (30). To ensure a robust algorithm a limit is therefore put on the increment $\delta\widetilde{\mathbf{q}}_{\text{i}}$, similar to how a limit is imposed on the increment in the plastic multipliers $\delta\lambda$. The limitation is imposed by making a second order Taylor-expansion of the norm

$$\|\hat{\mathbf{q}}_i + \xi\delta\hat{\mathbf{q}}_i\| \simeq \|\hat{\mathbf{q}}_i\| + \xi\frac{\partial\|\hat{\mathbf{q}}_i\|}{\partial\hat{\mathbf{q}}_i}\delta\hat{\mathbf{q}}_i + \frac{1}{2}\xi^2\delta\hat{\mathbf{q}}_i^T\frac{\partial^2\|\hat{\mathbf{q}}_i\|}{\partial\hat{\mathbf{q}}_i^T\partial\hat{\mathbf{q}}_i}\delta\hat{\mathbf{q}}_i = 1. \tag{49}$$

Solving the second order equation with only the plus sign gives the solution of interest

$$\xi^* = \frac{-\frac{\partial\|\hat{\mathbf{q}}_i\|}{\partial\hat{\mathbf{q}}_i}\delta\hat{\mathbf{q}}_i + \sqrt{\left(\frac{\partial\|\hat{\mathbf{q}}_i\|}{\partial\hat{\mathbf{q}}_i}\delta\hat{\mathbf{q}}_i\right)^2 - 2(\|\hat{\mathbf{q}}_i\|-1)\left(\delta\hat{\mathbf{q}}_i^T\frac{\partial^2\|\hat{\mathbf{q}}_i\|}{\partial\hat{\mathbf{q}}_i^T\partial\hat{\mathbf{q}}_i}\delta\hat{\mathbf{q}}_i\right)}}{\delta\hat{\mathbf{q}}_i^T\frac{\partial^2\|\hat{\mathbf{q}}_i\|}{\partial\hat{\mathbf{q}}_i^T\partial\hat{\mathbf{q}}_i}\delta\hat{\mathbf{q}}_i}. \tag{50}$$

The second derivative is not defined when $\|\hat{\mathbf{q}}_i\| = \mathbf{0}$, and in this case it is used that the norm is most commonly homogeneous or close to homogeneous for eccentric surfaces, and ξ^* is found as

$$\xi^* = \frac{1}{\|\delta\hat{\mathbf{q}}_i\|}. \tag{51}$$

In practice (50) and (51) may not result in a solution where $\|\hat{\mathbf{q}}_i + \xi^*\delta\hat{\mathbf{q}}_i\| = 1$ and in that case a new value of ξ^* is calculated via (50) where $\hat{\mathbf{q}}_i = \hat{\mathbf{q}}_i + \xi^*\delta\hat{\mathbf{q}}_i$ is the starting point of the approximation. The resulting ξ^* is added to the previous value of ξ^* and that process is repeated until $\|\hat{\mathbf{q}}_i + \xi^*\delta\hat{\mathbf{q}}_i\| = 1$. With such an approach the basis of the model is not violated, making the return algorithm more robust. The final return algorithm is shown in Algorithm 1.

Algorithm 1. Return algorithm.

1. Calculate deformation increment from distributed load $\Delta\tilde{\mathbf{u}}_l = \mathbf{K}_e^{-1}\Delta\mathbf{f}_l$.
2. Update total deformation increment $\Delta\tilde{\mathbf{u}}_t = \Delta\tilde{\mathbf{u}}_g + \Delta\tilde{\mathbf{u}}_l$.
3. Calculate elastic increment in forces, $\Delta\tilde{\mathbf{q}}^0 = \mathbf{K}_{ed}\Delta\tilde{\mathbf{u}}_t$.
4. Calculate value of yield functions, $\mathbf{f}_y(\tilde{\mathbf{q}} + \Delta\tilde{\mathbf{q}}^k)$. If $F_j^0 \leqslant 0$, accept $\tilde{\mathbf{q}} = \tilde{\mathbf{q}}^0 + \Delta\tilde{\mathbf{q}}^0$ and exit.
5. Determine $\partial_{\tilde{\mathbf{q}}}^T\mathbf{g}$, $\partial_{\tilde{\mathbf{q}}}^T\mathbf{f}_y$ and $\mathbf{K}_{eid}^A$. If $k = 0$ determine $\Delta\boldsymbol{\lambda}$ as well.
6. Calculate $\mathbf{r}_{\tilde{\mathbf{u}}}$. If $\|\mathbf{r}_{\tilde{\mathbf{u}}}\| < \epsilon_{tol}\|\Delta\tilde{\mathbf{u}}_t\|$ and $F_j^k \leqslant 0$, accept $\tilde{\mathbf{q}} = \tilde{\mathbf{q}}^0 + \Delta\tilde{\mathbf{q}}^k$ and exit.
7. Determine $\delta\lambda_{1/2}^k$ and $\delta\tilde{\mathbf{q}}_{1/2}^k$ using (40) and (41) with $\frac{1}{2}\mathbf{r}_{\tilde{\mathbf{u}}}$ and $\frac{1}{2}\mathbf{f}_y$. Check magnitudes of $\delta\lambda_{1/2}^k$.
8. Determine $(\partial_{\tilde{\mathbf{q}}}^T\mathbf{g})_{1/2}$, $(\partial_{\tilde{\mathbf{q}}}^T\mathbf{f}_y)_{1/2}$ and $(\mathbf{K}_{eid}^A)_{1/2}$ at $\tilde{\mathbf{q}}_{1/2}^k = \tilde{\mathbf{q}}^0 + \Delta\tilde{\mathbf{q}}^k + \delta\tilde{\mathbf{q}}_{1/2}^k$.
9. Determine $\delta\lambda^k$ and $\delta\tilde{\mathbf{q}}^k$ using (40) and (41) with $(\partial_{\tilde{\mathbf{q}}}^T\mathbf{g})_{1/2}$, $(\partial_{\tilde{\mathbf{q}}}^T\mathbf{f}_y)_{1/2}$, $(\mathbf{K}_{eid}^A)_{1/2}$, $\mathbf{r}_{\tilde{\mathbf{u}}}$ and $\mathbf{f}_y$. Check magnitudes of $\delta\lambda^k$ and $\delta\tilde{\mathbf{q}}_i^k$.
10. Update $\Delta\tilde{\mathbf{u}}^{k+1} = \Delta\tilde{\mathbf{u}}^k + \mathbf{K}_{eid}^{-1}\delta\tilde{\mathbf{q}}^k$,$\Delta\tilde{\mathbf{q}}^{k+1} = \Delta\tilde{\mathbf{q}}^k + \delta\tilde{\mathbf{q}}^k$ and $\Delta\lambda^{k+1} = \Delta\lambda^k + \delta\lambda^k$ and go to 4 using $k = k + 1$.

The return algorithm shown in Algorithm 1 is based on a known deformation increment from the global analysis $\Delta\tilde{\mathbf{u}}_g$ and the local deformation increment $\Delta\tilde{\mathbf{u}}_l$ combined to a total deformation increment $\Delta\tilde{\mathbf{u}}_t$. While $\Delta\tilde{\mathbf{u}}_g$ is initially known, $\Delta\tilde{\mathbf{u}}_l$ is calculated via the increment in the local distributed load. Once $\Delta\tilde{\mathbf{u}}_t$ is found an elastic prediction step is made and it is checked whether the predicted state violates any of the yield conditions or not; if not, the predicted state is accepted and otherwise the plastic return is started. After the values of the yield functions are determined the gradients of the flow potentials and the yield functions are found along with the algorithmic stiffness, all in the predicted final state. In the first iteration an estimate of $\Delta\lambda$ is calculated as well via (11) where $\ddot{\tilde{\mathbf{u}}}_t$ is replaced by $\Delta\tilde{\mathbf{u}}_t$. Subsequently the residual is calculated via (35) and if the residual is sufficiently small and none of the yield conditions are violated, the predicted state is accepted. If the residual is not sufficiently small a midpoint state is determined by making half a step using (40) and (41) with $\mathbf{r}_{\tilde{\mathbf{u}}}/2$ and $\mathbf{f}_y/2$. The gradients of the flow potentials and the yield functions are determined at the midpoint along with the algorithmic stiffness at the midpoint and these are used in (40) and (41) to make a full step from the initially predicted state. It is found by several numerical tests that the highest degree of robustness is obtained when $\delta\lambda_{1/2}^k$ is not added to $\Delta\lambda^k$ in the determination of the algorithmic stiffness at midpoint. Similarly the algorithm is more robust when $(\delta\tilde{\mathbf{q}}_i)_{1/2}^k$ is not limited via the procedure described above, and in cases where $\|\hat{\mathbf{q}}_i\|_{1/2} > 1$ simply setting $\|\hat{\mathbf{q}}_i\|_{1/2} = 1$ in the calculation of the derivatives of the plastic flow potentials increases the robustness. The increased robustness by using the full increment $(\delta\tilde{\mathbf{q}}_i)_{1/2}^k$ is attributed to the increased prediction accuracy of the direction of the return step given by the full increment $(\delta\tilde{\mathbf{q}}_i)_{1/2}^k$ in comparison to using a limited version of it. In the prediction of the increments $\delta\lambda^k$ and $\delta\tilde{\mathbf{q}}^k$ limits are put on the increment in the plastic multipliers $\delta\lambda_j^k$ so $\Delta\lambda_j^{k+1} \geqslant 0$ and on the increment in the internal section forces $\delta\tilde{\mathbf{q}}_i^k$ so that $\|\hat{\mathbf{q}}_i\|^{k+1} \leqslant 1$. The final state is updated by the predicted states and the iteration is repeated again by determining the yield values in the new predicted final state and following the above steps.

5. Examples

The beam element and return algorithm described above have been implemented in the computer code RONJA (Rambøll Offshore Nonlinear Jacket Analysis) where the member elastic stiffness including imperfections derived in [26] is implemented. The original plastic hinge model implemented in RONJA is based on a constant linear hardening with a rounding introduced by taking into account the approximate length of the plastic zone. However, typically a very small hardening is used to ensure that section forces in members and joints will not exceed realistic capacities even for severe plastic deformation. In the original RONJA code local joint flexibility is introduced by an additional node and static condensation rather than additive flexibilities used in the present formulation.

Two examples are presented to illustrate the effects of the more realistic hardening behaviour compared to a linear hardening model and the effect of the more robust return algorithm and present integrated element formulation. Both examples are realistic models of offshore tubular structures located in the North Sea; one is a monopile structure and the other is a jacket structure. The models include the stiffness of the soil modelled by springs as well as initial member imperfections. The structures are vertically loaded by their own weight, weight of topsides (not illustrated) and attached bridges (not illustrated) and buoyancy corresponding to water depths of 47.9 meters and 45.0 meters, respectively. After the application of the vertical load, a horizontal load series is applied. The first part of the horizontal load series is wind with a recurrence period of 100 years and a wave with a recurrence period of 10.000 years and wave height 27.7 m. Such a loading is current standard for determining the push-over capacity of offshore structures [61]. Subsequently the horizontal load is reduced to zero and load from a wave with a 100 year recurrence period and wave height 21.9 m is applied in the opposite direction of the load from the wave with a 10.000 year recurrence period followed by a similar wave in the original horizontal loading direction. Local joint flexibilities are modelled using the flexibilities proposed by [16] and local joint plastic mechanisms are modelled with the MSL surface illustrated in Fig. 7 using the capacities predicted by the ISO 19902 standard, [62]. The MSL surface is rounded at the line corresponding to $n = 0$ in Fig. 7 to a capacity of $m_{ip} = m_{op} = 0.98$. The yield surface of tubular member plastic mechanisms correspond to the most rounded surface shown in Fig. 5. Parameter evolution is neglected in these examples, corresponding to removing the third block column and row of $\mathbf{K}_{eid}$ and the third block row of $\mathbf{K}_{ed}$. The effect of softening due to section changes from local buckling can be included and has been illustrated in [36].

5.1. Monopile structure

The geometry of the monopile structure is illustrated in Fig. 9 and it

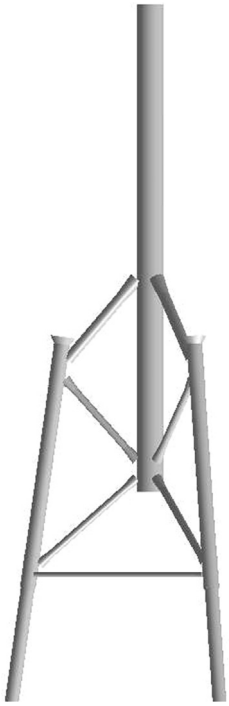

Fig. 9. Geometry of monopile structure.

is observed that very few tubular joints are present and the structure has very little redundancy. Failure mechanisms are expected to be plasticity at the intersection of the monopile and the supporting braces in the form of plastic deformation in the braces followed by plastification of the main column.

The response history is shown in Fig. 10 where the dashed black line indicates the response with the original linear hardening model, and the solid blue line indicates the response using the new beam formulation and plasticity model. The horizontal load is normalized with the horizontal load $P_{10.000y} = 14.5\,\text{MN}$ of the wave with a 10.000 year recurrence period.

It is observed that the elastic part of the response is the same for the two models and that the major difference occurs once the first plastic mechanisms become active. With both modelling types the first plastic mechanism that activates is a joint mechanism located in the tension brace at the connection with the main column. Subsequently the local joint plastic mechanism activates in the compression braces at the connection with the main column. The present model is capable of substantial hardening permitting a considerable load increase, whereas the original linear hardening model does not allow for much additional load, and once a plastic hinge forms in the main column a structural mechanism is created and the main column is essentially free to rotate. At that point a plastic hinge is created in the middle brace on the tension side reducing the rotational stiffness in the main column even further. The ultimate capacity is reached once all three braces have plastic mechanisms, the main column develops a plastic hinge and the lower part of the main column loses rotational stiffness due to a plastic mechanism in the brace on the tension side. If the load is reversed at this load level, there is hardly any plastic deformation predicted by the present model as illustrated in Fig. 10(a). In order to have a similar deformation level the load on the structure with the present plasticity model must be substantially increased as illustrated in Fig. 10(b). It is noted that while elastic load reversal is present for the monopile structure modelled by the linear hardening model that is not the case when the load is reversed with displacement control of the present model. In that case the structure unloads plastically, as the joint plastic hinges of the braces will still deform plastically. The local joint plastic mechanisms are active because the bending moment in the main column is so large that the bending capacity of the joint plastic mechanism in the braces is virtually zero. Once the loading on the main column is sufficiently low, the local joint plastic mechanisms become inactive and the structure unloads elastically. In Fig. 10(b) is it observed that for similar maximum deformation levels the present model predicts a plastic deformation at zero load that is roughly half the plastic deformation predicted by the linear hardening model.

The deformed monopile structure at three different load levels is illustrated in Fig. 11 with displacements scaled by a factor of 5. The columns show the three types of analysis: load control with linear hardening, and present model with either load or displacement control, and the rows correspond to the load stages identified in Fig. 10.

The deformed structure at the maximum load (×) is shown in the top row of Fig. 11. In Fig. 11(a) the five critical plastic mechanisms are observed; the plastic mechanisms in the upper joint where the braces deform plastically, the plastic mechanism in the main column and the plastic mechanism in the middle brace on the tension side. In Fig. 11(b) and (c) it is observed that the load must be increased in order to have similar deformation with the present non-linear hardening model and in that case, the plasticity is more wide-spread over the main column. In the second row (∘) the unloaded structure is shown and for the linear hardening case in (d) the plastic mechanism in the main column is clearly observed as a permanent deformation. With the proposed hardening model in Fig. 11(e) the permanent deformation is seen to be almost negligible corresponding to hardly any plastic deformation, whereas the more loaded structure in Fig. 11(f) has a deformation pattern more similar to the structure modelled with linear hardening. In the bottom row (∗) the deformed structure is shown when the load is maximum in the opposite direction and it is observed that the location most heavily loaded is the compression brace (originally the tension brace) that almost becomes plastic. It is noted that the 10.000 year wave load is scaled with a factor of 1.08 and the subsequent 100 year wave load is scaled by a factor of 1.1 to investigate if slightly larger loads than the original design loads can be sustained and if elastic shakedown would still be experienced. In the present case (without dynamic effects) that is found to be the case.

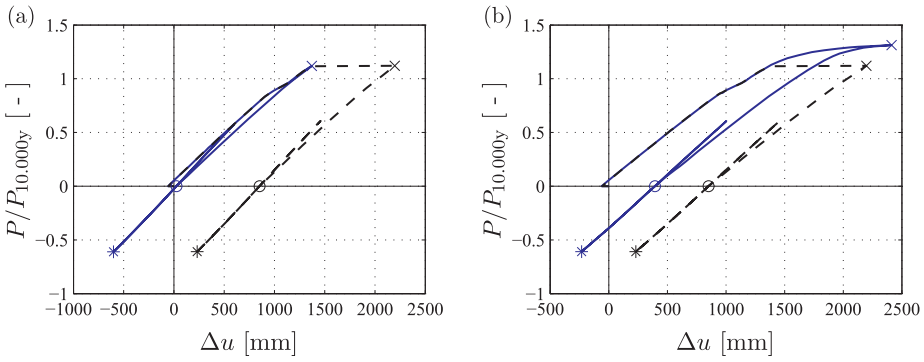

Fig. 10. Extreme response of monopile structure. Total horizontal load vs. top displacement. (a) Load control. (b) Displacement control. Linear hardening (– –), present hardening (——).

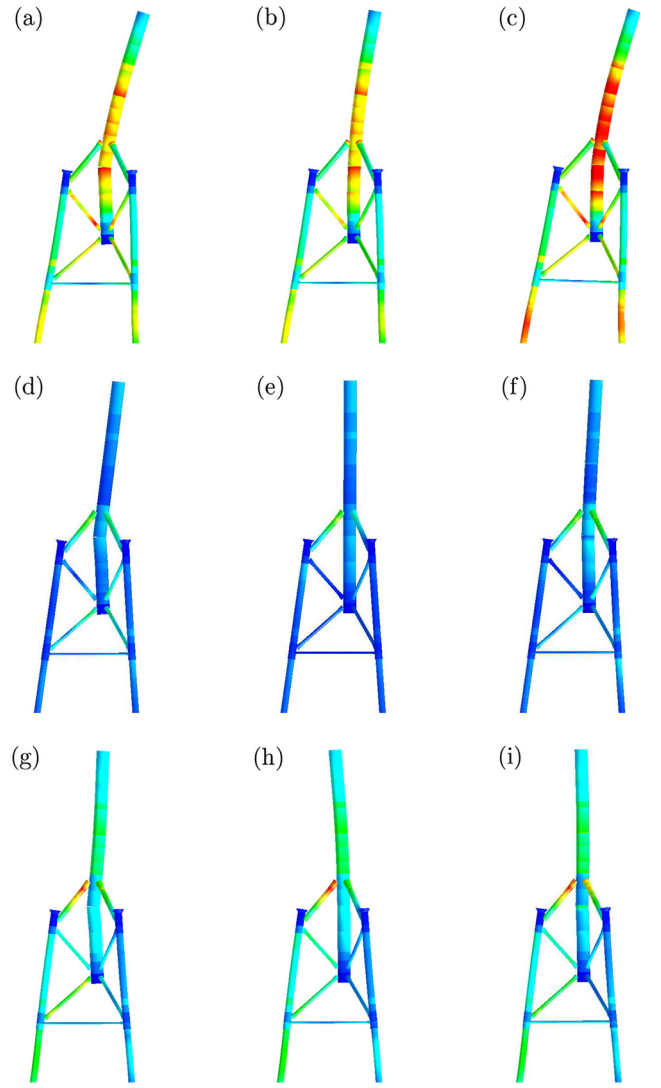

Fig. 11. Deformation of monopile structure. Left: Linear hardening model. Middle: Present model with load control. Right: Present model with displacement control. Top: State ×. Center: State ∘. Bottom: State ∗.

5.2. Jacket structure

The geometry of the jacket structure is illustrated in Fig. 12 and it is observed that in contrast to the monopile it is dominated by braces with tubular joints at the main legs and at brace-brace joints. Failure mechanisms are expected to be elasto-plastic buckling of bracing and most likely first failure will be buckling of the compression braces in the top X-brace, as this is a typical failure mechanism, see e.g. [26].

The response history is shown in Fig. 13 where the dashed line represents the response with the original linear hardening model and the solid blue line represents the response with the present beam formulation and plasticity model. The horizontal load is normalized with the horizontal load $P_{10.000y} = 36.1\,\mathrm{MN}$ of the wave with a 10.000 year recurrence period.

Similar to the monopile structure the elastic responses shown in Fig. 13 are identical for the original linear hardening RONJA implementation and the present beam model. During deformation elasto-plastic buckling of the compression braces in the top X-brace softens the response. In the linear hardening model the buckling of the brace leads

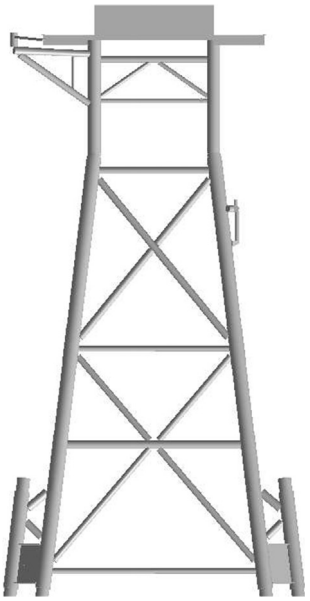

Fig. 12. Geometry of jacket structure.

to a redistribution of the load in the braces and they become loaded primarily in bending, while the present model hardens more and the braces are still loaded mostly in axial compression. The stiffness of the braces loaded in bending is significantly less than the stiffness of the braces loaded in axial compression as identified by Fig. 13(a). It is noted that with load control, there is some plastic deformation in the structure modelled by the present model in contrast to the monopile structure. If the jacket structure is loaded to similar deformation levels as shown in Fig. 13(b) rather than similar load levels as shown in Fig. 13(a) it is noted that the plastic deformation differs by less than a factor of two in contrast to the monopile structure where the difference is roughly a factor of two. It is noted that in both the load and the displacement controlled case both models experience plastic unloading. At unloading some elements will unload elastically, which is the reason for the difference between the loading and unloading tangent stiffness. However, some elements will experience a continued state of plastic deformation because of the stiffness redistribution in the structure. It is noted that at a relative load of approximately 2 the response of the structure is again fully elastic. The plastic deformation at reversed loading is also the reason why the top displacement increases slightly at load reversal with displacement control of the present model.

The deformed jacket structure is illustrated in Fig. 14 for three different load levels modelled with columns showing results from the linear hardening model and for the present model with load and displacement control, respectively, and the rows correspond to the load stages identified in Fig. 13. The displacements are scaled by a factor of 5.

The linear hardening model is shown in the left column of Fig. 14, while the middle and right column illustrate the present model with load and displacement control, respectively. The top row corresponds to maximum deformation (×), while the middle row corresponds to zero horizontal load (∘) and the bottom row corresponds to maximum load in the opposite direction (∗). Comparing Fig. 14(a)–(c) it is evident that the different hardening representations give rise to different load redistributions. While the linear hardening model in Fig. 14(a) illustrates an elasto-plastic buckling of the compression braces in the top X-brace so severe that the load is redistributed to bending, the remaining parts of the load are distributed to partly the tension braces in the top X-

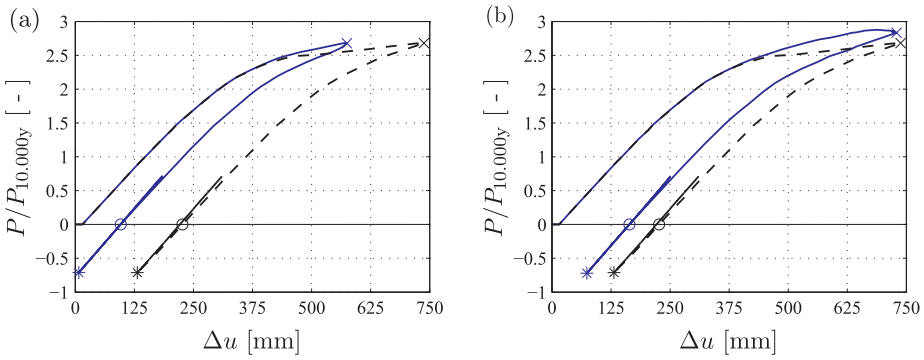

Fig. 13. Extreme response of jacket structure. Total horizontal load vs. top displacement. (a) Load control. (b) Displacement control. Linear hardening (– –), present hardening (——).

brace, partly the top braces of the lower X-brace and partly the legs at the buckled braces and the legs close to the topside. For the present model in Fig. 14(b) and (c) the braces do not buckle sufficiently to redistribute the loading to bending, and as a consequence the remaining part of the load is primarily redistributed to the lower tension braces in the top X-brace as well as to the top braces of the lower X-brace. Comparing the different models for similar deformations Fig. 14(a) and (c) it is evident that the redistribution of load differs significantly between the two models, where the present model predicts far less loading in the jacket legs and the top tension braces of the top X-brace. At zero horizontal load illustrated in Fig. 14(d)–(f) the permanent deformation is similar for the three models; the most visible permanent deformation is present in the buckled compression braces and the permanent buckle is much larger for the linear hardening model. The structure with maximum load in the opposite direction is illustrated in Fig. 14(g)–(i). The deformed compression braces are being stretched with slightly plastic deformation leading to a more symmetric structure with bracing acting in tension rather than bending, ultimately slightly stiffening the response. This effect is evident in Fig. 13 where it is noted that the response at reloading in the original direction is slightly stiffer than the initial unloading stiffness. Note, that for the present model the load of the wave with a 10.000 year recurrence period is scaled by a factor of 2.25 and the subsequent 100 year wave load is scaled by a factor of 1.1. Even with these increased loads (where dynamic effects are neglected) it is found that elastic shakedown would be expected.

In addition to the difference in the loading redistribution due to plasticity a notable difference between the original linear hardening RONJA code and the present cyclic plasticity beam model is the robustness and stability. In the original code local joint flexibility is introduced via internal nodes and static condensation instead of the additive flexibility format applied here. Furthermore the original code makes use of a standard return algorithm in contrast to the present more robust two-step algorithm. The main effect of the additive flexibility format and the return algorithm with increased robustness is that larger load increments are possible. When using the original code a smaller load step had to be taken 46 times in the jacket analysis, because of lack of convergence in either the condensation of the local joint flexibility or in the return algorithm. With the present non-linear hardening beam element formulation and return algorithm there was no need for a load step reduction. In addition, the present hardening model clearly enhances the RONJA code in comparison to the benchmarking study [63], where RONJA was found to be among the best offshore structure analysis codes. RONJA was found to predict the correct failure mechanisms, e.g. elasto-plastic buckling of an X-brace, and the sequence of these, however the main improvement point was found to be the response after activation of a plastic mechanism exhibiting too little hardening. The hardening was set low on purpose to avoid over-predicting the strength of plastic members with the linear hardening model, a problem that is solved by the form of the present plasticity model, where a natural ultimate capacity limit is represented in the model. This suggests that the present beam element with non-linear hardening not only increases the robustness and stability of the code, but also increases the accuracy of the code to make the correspondence between model and reality closer.

6. Conclusions

A robust frame element with cyclic plasticity and local joint effects has been presented. The element is based on additive flexibilities and includes plastic mechanisms in the member, plastic mechanisms in the local joints and elastic flexibilities at the local joints. The elastic stiffness of the element may include non-linear dependence on the normal force, bowing effects, initial imperfections etc. and it is found by the inverse of the total elastic flexibility including the local joint flexibility. The plastic mechanisms are described by a plasticity model capable of representing realistic cyclic plasticity phenomena including degradation effects via parameter evolution.

The cyclic plasticity model makes use of plastic potentials defined using a homogeneous norm of degree one. The norm consists of a sum of square roots of quadratic terms and is shown to be able to represent multiple different yield surfaces for both member and joint mechanisms. Furthermore, parameter estimation is discussed along with the possibility of a gradually changing yield surface, enabling a single-surface representation of first-fibre-yield and full plastification criteria. The yield surface format is shown to be able to incorporate effects of shear and local joint coordinate systems by simple transformation.

The robustness of the element comes partly from the additive flexibility format and partly from the robust return algorithm developed. The return algorithm includes the effects of distributed load and is a two-step algorithm where a half-step is made to obtain information and subsequently a full step is made using this information, making the algorithm approximately second order accurate. The algorithm is far more robust than traditional single-step algorithms and is sufficiently general to handle different types of yield surfaces and plastic flow potentials.

Finally, the developed element was used to model two realistic offshore structures and to investigate the numerical as well as qualitative differences between a linear hardening beam element, currently used in analysis of offshore structures, and the present element with non-linear hardening and integrated joint properties. It was found that the present element highly increased the robustness of the computation, eliminating otherwise necessary restarts of load steps due to lack of convergence. With a more realistic plasticity model the present element accounts for larger capacity of the structures caused by a more realistic hardening behaviour leading to somewhat different load shedding once plasticity and elasto-plastic buckling occurs. The examples highlight the usefulness of a robust frame element, capable of accounting for cyclic plasticity and local joint effects in a realistic manner, to ensure a realistic prediction of the behaviour of frame structures subjected to large loads.

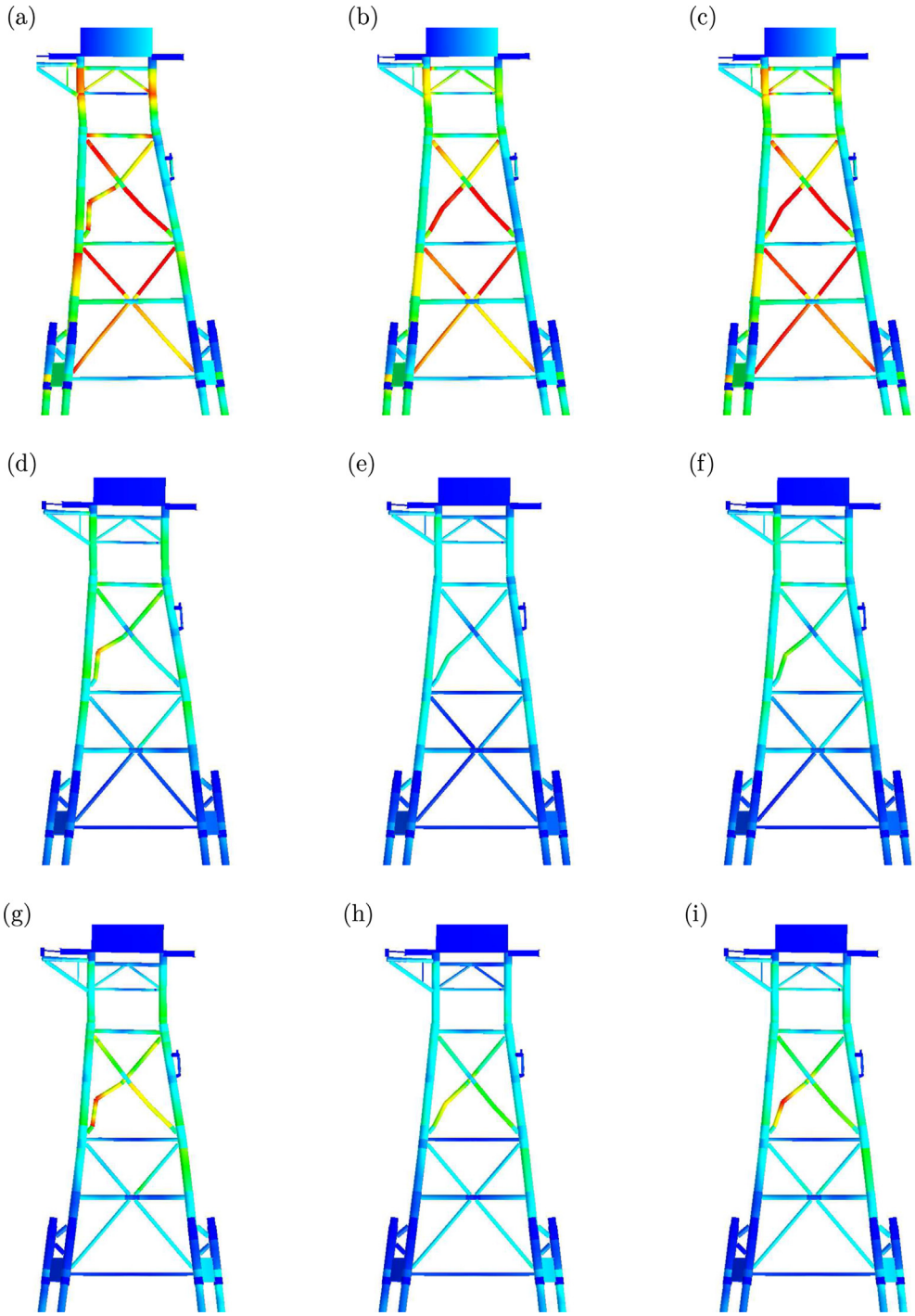

Fig. 14. Deformation of jacket structure. Left: Linear hardening model. Middle: Present model with load control. Right: Present model with displacement control. Top: State ×. Center: State ◦. Bottom: State ∗.

Acknowledgements

This paper is part of a project sponsored jointly by Innovation Fund Denmark, Maersk Oil A/S and the Technical University of Denmark.

References

[1] Elchalakani M, Zhao XL, Grzbieta R. Tests of cold-formed circular tubular braces under cyclic axial loading. J Struct Eng 2003;129:507–14.
[2] Elchalakani M, Zhao XL, Grzbieta R. Concrete-filled steel circular tubes subjected to constant amplitude cyclic pure bending. Eng Struct 2004;26:2125–35.
[3] Elchalakani M, Zhao XL, Grzbeita R. Variable amplitude cyclic pure bending tests to determine fully ductile section slenderness limits for cold-formed CHS. Eng Struct 2006;28:1223–35.
[4] Elchalakani M. Plastic mechanism analyses of circular tubular members under cyclic loading. Thin-Walled Struct 2007;45:1044–57.
[5] Elchalakani M, Zhao XL. Concrete-filled cold-formed circular steel tubes subjected to variable amplitude cyclic pure bending. Eng Struct 2008;30:287–99.
[6] Popov EP, Zayas VA, Mahin SA. Cyclic inelastic buckling of thin tubular columns. J Struct Div ASCE 1979;105:2261–77.
[7] Popov EP, Mahin SA, Zayas VA. Inelastic cyclic behavior of tubular braced frames. J Struct Div ASCE 1980;106:2375–90.
[8] Popov EP, Mahin SA, Clough RW. Inelastic response of tubular steel offshore towers. J Struct Eng 1985;111:2240–58.
[9] Zayas VA, Mahin SA, Popov EP. Cyclic inelastic behavior of steel offshore structures. Technical report report UCB/EERC-80/27. EERC, Berkeley, CA: Earthquake Engineering Research Center; 1980.
[10] Paul JC, Makino Y, Kurobane Y. Ultimate resistance of unstiffened multiplanar

tubular TT- and KK-joints. J Struct Eng 1994;120:2853–70.
[11] Kurobane Y. Static behaviour and earthquake resistant design of welded tubular structures. Jármai K, Farkas J, editors. Mechanics and design of tubular structures. International centre for mechanical sciences (courses and lectures), vol. 394. Vienna: Springer; 1998. p. 53–116.
[12] Chen W-F, Lui EM. Effects of joint flexibility on the behavior of steel frames. Comput Struct 1987;26:719–32.
[13] Ho WMG, Chan S-L. Semibifurcation and bifurcation analysis of flexibly connected steel frames. J Struct Eng 1995;117:939–45.
[14] Fessler H, Mockford PB, Webster JJ. Parametric equations for the flexibility matrices of multi-brace tubular joints in offshore structures. Proc Inst Civ Eng 1986;81:675–96.
[15] Chen B, Hu Y, Tan M. Local joint flexibility of tubular joints of offshore structures. Marine Struct 1990;3:177–97.
[16] Buitrago J, Healy BE, Chang TY. Local joint flexibility of tubular joints. In: Chakrabarti SK, editor. Proceedings of the 12th international conference on offshore mechanics and arctic engineering. Glasgow, Scotland: The American Society of Mechanical Engineers, Offshore Mechanics and Arctic Engineering Division; June 20–24, 1993.
[17] Gao F, Hu B, Zhu HP. Parametric equations to predict LJF of completely overlapped tubular joints under lap brace axial loading. J Constr Steel Res 2013;89:284–92.
[18] Gao F, Hu B, Zhu HP. Local joint flexibility of completely overlapped tubular joints under in-plane bending. J Constr Steel Res 2014;99:1–9.
[19] Gao F, Hu B. Local joint flexibility of completely overlapped tubular joints under out-of-plane bending. J Constr Steel Res 2015;115:121–30.
[20] Hu Y, Chen B, Ma J. An equivalent element representing local flexibility of tubular joints in structural analysis of offshore platforms. Comput Struct 1993;47:957–69.
[21] Golafshani AA, Kia M, Alanjari P. Local joint flexibility element for offshore plateforms structures. Marine Struct 2013;33:56–70.
[22] Asgarian B, Alanjari P, Aghaeidoost V. Three-dimensional joint flexibility element for modeling of tubular offshore connections. J Mar Sci Technol 2015;20:629–39.
[23] Ueda Y, Rashed SMH, Nakacho K. An improved joint model and equations for flexibility of tubular joints. J Offshore Mech Arct Eng 1990;112:157–68.
[24] Chan S-L, Zhou ZH. Second-order elastic analysis of frames using single imperfect element per member. J Struct Eng 1995;121:939–45.
[25] Chan S-L, Gu J-X. Exact tangent stiffness for imperfect beam-column members. J Struct Eng 2000;126:1094–102.
[26] Krenk S, Vissing-Jørgensen C, Thesbjerg L. Efficient collapse analysis techniques for framed structures. Comput Struct 1999;72:481–96.
[27] El-Tawil S, Deierlein GG. Stress-resultant plasticity for frame structures. J Eng Mech 1998;124:1360–70.
[28] Søreide T, Amdahl J, Granli T, Astrud OC. Collapse analysis of framed offshore structures. In: Proceedings of the 18th offshore technology conference, Houston, Texas, May 5–8, 1986. p. 95–102.
[29] Liew JYR, Tang LK. Advanced plastic hinge analysis for the design of tubular space frames. Eng Struct 2000;22:769–83.
[30] Rodrigues PFN, Jacob BP. Collapse analysis of steel jacket structures for offshore oil exploitation. J Constr Steel Res 2005;61:1147–71.
[31] Davaran A, Far NE. An inelastic model for low cycle fatigue prediction in steel braces. J Constr Steel Res 2009;65:523–30.
[32] Armero F, Ehrlich D. Numerical modeling of softening hinges in thin Euler-Bernoulli beams. Comput Struct 2006;84:641–56.
[33] Alemdar BN, White DW. Displacement, flexibility, and mixed beam-column finite element formulations for distributed plasticity analysis. J Struct Eng 2005;131:1812–9.
[34] Ueda Y, Matsuishi M, Yamakawa T, Akamatsu Y. Elastic-plastic analysis of framed structures using the matrix method (in japanese). J Soc Naval Architects Jpn 1968;124:183–91.
[35] Ueda Y, Akamatsu T, Ohmi Y. Elastic-plastic analysis of framed structures using the matrix method (in japanese). J Soc Naval Architects Jpn 1969;126:253–62.
[36] Tidemann L, Krenk S. Cyclic plastic hinges with degradation effects for frame structures. J Eng Mech 2017;143.
[37] Krenk S, Tidemann L. A compact cyclic plasticity model with parameter evolution. Mech Mater 2017;113:57–68.
[38] Tidemann L, Krenk S. Beam element including local member and joint plasticity effects. In: Chung J, editor. The proceedings of the 27th (2017) international ocean and polar engineering conference. San Francisco, California: International Society of Offshore and Polar Engineering, ISOPE; 2017.
[39] Chen W-F, Atsuta T. Theory of beam-columns. Fort Lauderdale, USA: J. Ross Publishing; 2008.
[40] Liu Y, Xu L, Grierson DE. Combined MVP failure criterion for steel cross-sections. J Constr Steel Res 2009;65:116–24.
[41] Krenk S, Vissing S, Vissing-Jørgensen C. A finite step updating method for elasto-plastic analysis of frames. J Eng Mech 1993;119:2478–95.
[42] Kitipornchai S, Zhu K, Xiang Y, Al-Bermani FGA. Single-equation yield surfaces for monosymmetric and asymmetric sections. Eng Struct 1991;13:366–70.
[43] Liu L-W, Hong H-K. A description of three-dimensional yield surfaces by cubic polynomials. J Eng Mech 2017;143.
[44] Coombs WM, Petit OA, Motlagh YG. NURBS plasticity: yield surface representation and implicit stress integration for isotropic inelasticity. Comput Methods Appl Mech Eng 2016.
[45] Soare SC, Benzerga AA. On the modeling of asymmetric yield functions. Int J Solids Struct 2016;80:486–500.
[46] Bleyer J, de Buhan P. A greedy algorithm for yield surface approximation. C R Mec 2013;341:605–15.
[47] Bleyer J, de Buhan P. Yield surface approximation for lower and upper bound yield design of 3D composite frame structures. Comput Struct 2013;129:86–98.
[48] Bron F, Besson J. A yield function for anisotropic materials: Application to aluminum alloys. Int J Plast 2004;20:937–63.
[49] Martinez M, Pépin, A, Sicsic P. Ovality prediction of reeled seamless and seam welded pipes. In: Chung J, editor. The proceedings of the 27th (2017) international ocean and polar engineering conference. San Francisco, California: International Society of Offshore and Polar Engineering, ISOPE; 2017.
[50] Simo JC, Taylor RL. A return mapping algorithm for plane stress elastoplasticity. Int J Numer Meth Eng 1986;22:649–70.
[51] Li T, Crouch R. A C_2 plasticity model for structural concrete. Comput Struct 2010;88:1322–32.
[52] Brannon RM, Leelavanichkul S. A multi-stage return algorithm for solving the classical damage component of constitutive models for rocks, ceramics and other rock-like media. Int J Fract 2010;163:133–49.
[53] Homel MA, Guilkey JE, Brannon RM. Numerical solution for plasticity models using consistency bisection and a transformed-space closest-point return: a nongradient solution method. Comput Mech 2015;56:565–84.
[54] Homel MA, Brannon RM. Relaxing the multi-stage nested return algorithm for curved yield surfaces and nonlinear hardening laws. Int J Fract 2015;194:51–7.
[55] Peng Q, Chen MX. An efficient return mapping algorithm for general isotropic elastoplasticity in principal space. Comput Struct 2012;92–93:173–84.
[56] Clausen J, Damkilde L, Andersen L. An efficient return algorithm for non-associated plasticity with linear yield criteria in principal stress space. Comput Struct 2007;85:1795–807.
[57] Heinze T, Galvan B. Novel numerical strategy for solving strongly coupled elasto-plastic damage models with explicit return algorithms: Applications to geomaterials. Int J Solids Struct 2016;80:64–72.
[58] Krenk S. Non-linear modeling and analysis of solids and structures. Cambridge, UK: Cambridge University Press; 2009.
[59] Dier AF, Lalani M. JIP – Assessment criteria, reliability and reserve strength of tubular joints (Phase II), Technical Report DOC REF C20400R014 Rev 0, MSL Engineering Limited, MSL House, 5–7 High Street, Sunninghill, Ascot, Berkshire SL5 9NQ, UK; 2000.
[60] Zienkiewicz OC, Taylor RL, Zhu JZ. The finite element method. 6 ed. Oxford: Elsevier Butterworth–Heinemann; 2005.
[61] DNV, SINTEF, BOMEL, Ultiguide – Best practice guidelines for use of non-linear analysis methods in documentation of ultimate limit states of jacket type offshore structures, Det Norske Veritas, Høvik, Norway; 1999.
[62] CEN, EN ISO 19902 – Petroleum and natural gas industries – Fixed steel offshore structures, European Committee for Standardization, Brussels, Belgium; 2007.
[63] Bolt HM. Joint industry tubular frames project – Phase III, Benchmark conclusions. Technical Report C636\32\084R, BOMEL Engineering Consultants, Berkshire, UK; 1999.

C1

Beam element including local member and joint plasticity effects

L. Tidemann & S. Krenk

Proceedings of the 27th (2017) International Ocean and Polar Engineering Conference, ISOPE, pp. 249–256.

San Francisco, California, June 25–30, 2017.

Proceedings of the Twenty-seventh (2017) International Ocean and Polar Engineering Conference **www.isope.org**
San Francisco, CA, USA, June 25-30, 2017

ISBN 978-1-880653-97-5; ISSN 1098-6189

Beam Element Including Local Member and Joint Plasticity Effects

Lasse Tidemann[†,‡] *and Steen Krenk*[†]

[†)] Department of Mechanical Engineering,
Technical University of Denmark,
Kongens Lyngby, Denmark.

[‡)] Facilities & Projects Discipline Area,
Maersk Oil,
Esbjerg, Denmark.

ABSTRACT

In the present paper a cyclic plasticity model accounting for multiple plastic mechanisms is developed. A flexible yield surface representation is proposed and used to implement the cyclic plasticity model in an equilibrium-based beam element accounting for local member and joint plasticity effects. The yield surface representation is sufficiently flexible to represent analytical yield surfaces for both tubular steel beams and tubular steel joints. The accuracy of the beam element is illustrated by comparison with experimental data of cyclic in-plane bending of a T-joint and cyclic out-of-plane bending of an X-joint.

KEY WORDS: Cyclic plasticity; Cyclic yield hinge; Combined plasticity mechanisms; Plastic frame analysis.

INTRODUCTION

Plasticity in idealised frame structures where joint effects are negligible is often represented by yield hinges in the beams where plasticity cause local elongation and angle discontinuities, e.g. (Krenk et al. 1999). In more realistic representations multiple plastic mechanisms may be present at approximately the same location, e.g. at joints between two or more beams where the plastic capacities are governed by physical properties different from the properties in the beam members forming the joint, and plastic deformation may occur both in the joint and in the local member. Within the geometrical accuracy of a beam model the two different types of plastic mechanism will be located the same place whereby the section forces in the two different plastic mechanisms will be the same. The section forces typically controlling the behaviour at yield hinges in beams are the normal force and the two bending moments, but the format proposed in this paper is sufficiently general to account for the effect of shear forces and torsion as well.

With multiple plastic mechanisms present it is necessary to refine standard single mechanism plasticity theory as done by e.g. (Ibrahimbegovic et al. 2008) where a continuum formulation coupling plasticity and damage is developed. The continuum formulation is achieved by having two separate mechanisms, a plastic and a damage mechanism, each having a criterion for activation corresponding to a traditional yield surface. For reinforced concrete beams (Bui et al. 2014) proposed a model with two plastic mechanisms; one accounting for cracking in the concrete and one accounting for yield in reinforcement bars, both depending on the bending moment. Additionally (Bui et al. 2014) introduced a separate plastic mechanism for the shear forces, completely decoupled from the other two as it only relates to the shear strains whereas the first two only relate to the bending curvature.

A central theme for all plasticity models is the yield surface and the gradients of this. The yield surface must be convex to abide with assumptions of elasticity and the gradients are a key part of the elasto-plastic stiffness, whereby a uniquely defined gradient is needed everywhere. Analytically determined yield surfaces for beam members and joints typically include corners or lines where the gradients are undefined suggesting that alternative representation of the yield surface has to be made. One option is to make local modifications to the yield surface (Krenk et al. 1999) resulting in a need to check multiple yield surfaces for a single plastic mechanism. Formulating a single-equation yield function that ensures convexity and still holds sufficient flexibility to be applied to different types of yield surfaces is difficult and proposed formulations include e.g. sums of higher-order terms (Orbison et al. 1982), use of a single ellipsoid (Skordeli and Bisbos 2010), and Minkowski sum of ellipsoids (Bleyer and de Buhan 2013a; Bleyer and de Buhan 2013b). The first type exhibits problems with ensuring convexity, while the second type ensures convexity but has rather limited flexibility, and in the third case the actual formation of the Minkowski sum may be difficult. To overcome these problems (Tidemann and Krenk 2017) proposed a single-equation, first order homogeneous yield function defined as a sum of terms consisting of the square-root of a quadratic form, ensuring convexity and flexibility, and examples have illustrated the potential of the formulation.

In the present paper a general cyclic plasticity model with multiple plastic mechanisms is presented. The paper presents a plastic flow potential suitable for cyclic plasticity and formulates the general elasto-plastic stiffness matrix with multiple plastic mechanisms via a flexibility format. A flexible yield surface representation is introduced and is shown to be sufficiently accurate to represent the yield surface of both tubular steel beams and tubu-

lar steel joints. The cyclic plasticity model is implemented in an equilibrium based beam element in a form including local member and joint plasticity without adding extra nodes. The accuracy of the beam element is illustrated by comparison with experimental data for in-plane bending of a T-joint and out-of-plane bending of an X-joint.

CYCLIC PLASTICITY MODEL

In the following the cyclic plasticity model developed in (Krenk and Tidemann 2017; Tidemann and Krenk 2017) is extended to include several mechanisms e.g. representing yield at the end section of a beam and deformation and yield at the connection joint. It is convenient to formulate hardening and cyclic plasticity by a formalism that makes use of external and internal kinematic variables. The internal energy is then given in the form

$$\Phi \,=\, \tfrac{1}{2}\mathbf{v}_{\rm e}^T\mathbf{K}_{\rm e}\mathbf{v}_{\rm e} + \tfrac{1}{2}\mathbf{v}_{\rm i}^T\mathbf{K}_{\rm i}\mathbf{v}_{\rm i}\,, \tag{1}$$

where the first quadratic term is the elastic energy with $\mathbf{v}_{\rm e}$ representing the the elastic deformations – for beams typically the elongation and the angle of rotation. The second quadratic term is an analogous internal energy with $\mathbf{v}_{\rm i}$ representing a set of internal and unobservable deformations, introduced into the energy to enable modeling of hardening. $\mathbf{K}_{\rm e}$ and $\mathbf{K}_{\rm i}$ are the elastic and internal stiffness matrices, respectively. These define the conjugate forces by differentiation of the energy

$$\mathbf{p} \,=\, \partial_{\mathbf{v}_{\rm e}}\Phi \,=\, \mathbf{K}_{\rm e}\mathbf{v}_{\rm e}\,, \quad \mathbf{p}_{\rm i} \,=\, \partial_{\mathbf{v}_{\rm i}}\Phi \,=\, \mathbf{K}_{\rm i}\mathbf{v}_{\rm i}\,. \tag{2}$$

Thus, both the observable section forces $\mathbf{p}$ and the internal forces $\mathbf{p}_{\rm i}$ have a Hooke's law type relation to the elastic and internal deformation measures $\mathbf{v}_{\rm e}$ and $\mathbf{v}_{\rm i}$, respectively. The observable section forces $\mathbf{p}$ will typically be the normal force and two bending moments as discussed in the above, while $\mathbf{p}_{\rm i}$ will be analogous internal forces acting as kinematic hardening parameters when introduced in the yield function. Note, that in the case of multiple plastic mechanisms with the same location, the dimension of the internal force array $\mathbf{p}_{\rm i}$ may be larger than the dimension of the section force array $\mathbf{p}$.

Yield Functions and Flow Potentials

As there are multiple plastic mechanisms the internal force vector $\mathbf{p}_{\rm i}$ is divided into multiple parts, each relating to a separate plastic mechanism

$$\mathbf{p}_{\rm i} \,=\, [\,\mathbf{p}_{\rm i1}^T, \mathbf{p}_{\rm i2}^T, \cdots]^T\,, \tag{3}$$

where the subscript 1 identifies the part of $\mathbf{p}_{\rm i}$ that relates to plastic mechanism 1 and similarly subscript 2 identifies the part of $\mathbf{p}_{\rm i}$ that relates to plastic mechanism 2 etc. When the normal force and the two bending moments are used to describe the yield surface it is desirable to use normalized variables. In the present context is convenient to normalize both the observable section forces $\mathbf{p}$ and the internal forces $\mathbf{p}_{\rm i}$ with the yield capacities for the individual section force components at each plastic mechanism

$$\bar{\mathbf{p}}_j \,=\, \mathbb{B}_{yj}^{-1}\mathbf{p}\,, \quad \bar{\mathbf{p}}_{{\rm i}j} \,=\, \mathbb{B}_{yj}^{-1}\mathbf{p}_{{\rm i}j}\,, \quad \mathbb{B}_{yj} \,=\, \begin{bmatrix} N^y & & \\ & \ddots & \\ & & \end{bmatrix}_j\,, \tag{4}$$

where N^y is the normal force that activates the plastic mechanism when no bending moments are present and the subscript j indicates that the parameters relate to plastic mechanism j. In terms of the normalized section forces and internal forces, the yield surface for the plastic mechanism j is of the form

$$F_j(\mathbf{p}, \mathbf{p}_{\rm i}) \,=\, \|\bar{\mathbf{p}}_j - \bar{\mathbf{p}}_{{\rm i}j}\| - 1 \le 0\,, \tag{5}$$

where the norm $\|\,\|$ is a suitable first order homogeneous function that is discussed in further detail in the following section. The normalized internal forces $\bar{\mathbf{p}}_{{\rm i}j}$ are used to represent the center of the yield surface in Eq. (5) equivalent to kinematic hardening of the yield surface. A kinematic hardening yield surface is chosen in order to capture the characteristics of cyclic plasticity.

The characteristics of the hysteresis curve for plastic mechanisms in the local beam members are discussed by (Tidemann and Krenk, 2017) and the characteristics of plastic mechanisms in joints are approximately the same. The hysteresis curve is characterised by an initially linear-elastic part followed by a (relatively small) kink in the force-deformation curve once the plastic mechanism is activated, and subsequently the stiffness decreases continuously with increased deformation until the ultimate capacity of the force is reached, where the hysteresis curve show ideal-plasticity behaviour. The linear-elastic relation is represented by $\mathbf{K}_{\rm e}$, and the kink in the curve at initial plasticity is represented by $\mathbf{K}_{\rm i}$, while the elasticity limit is represented by $\mathbb{B}_{yj}$. To represent the ultimate capacity a set of non-dimensional parameters $\boldsymbol{\beta}_j = [\beta_N^j, \cdots]^T$ defining the non-dimensional additional capacity beyond the initial yield is introduced for each plastic mechanism j. Hereby the relative ultimate capacities become $1+\beta$. Finally, each plastic mechanism j has set of parameters $\boldsymbol{\alpha}_j = [\alpha_N^j, \cdots]^T$ controlling the gradual development of plastic deformation after first yield. With these parameters the normalized plastic flow potential used in the present model for mechanism j is similar to that presented by (Tidemann and Krenk 2017),

$$G_j(\mathbf{p}, \mathbf{p}_{\rm i}) \,=\, F_j(\mathbf{p}, \mathbf{p}_{\rm i}) + \sum_k \Big(\frac{\beta_k^j}{\alpha_k^j}\Big\{\frac{|\bar{p}_k^{{\rm i}j}|}{\beta_k^j} - \frac{1-\alpha_k^j}{\alpha_k^j}\ln\Big(1 + \frac{\alpha_k^j}{1-\alpha_k^j}\frac{|\bar{p}_k^{{\rm i}j}|}{\beta_k^j}\Big)\Big\}\Big). \tag{6}$$

It is noted that the flow potential G_j only depends on $\mathbf{p}$ via the yield function F_j making it an associated plasticity theory, an assumption often found to be accurate for plastic mechanisms in steel beam members.

Elasto-Plastic Stiffness

The elasto-plastic stiffness matrix is derived by maximising the plastic dissipation rate under the assumption, that the material can be described by the plastic flow potentials for each plastic mechanism j, while enforcing the consistency condition that during plastic loading the forces $\mathbf{p}$ must always be located on the yield surfaces of the active plastic mechanisms, see e.g. (Krenk and Tidemann 2017) for a more detailed derivation. The deformations associated with the beam end and the attachment to the joint are assumed to be local and are concentrated at a single node, following the equilibrium based element formulation in (Krenk et al. 1999). In this formulation the local plastic deformations are simply added in the beam flexibility. Thus, the total deformation is

$$\mathbf{v} \,=\, \mathbf{v}_{\rm e} + \mathbf{v}_{\rm p}^1 + \mathbf{v}_{\rm p}^2 + \cdots\,, \tag{7}$$

where $\mathbf{v}_{\rm e}$ is the elastic deformation used in Eq. (1), and $\mathbf{v}_{\rm p}^j$ is the plastic deformation of the plastic mechanism j. The total

deformation is illustrated in Fig. 1, showing additive deformation and common section forces.

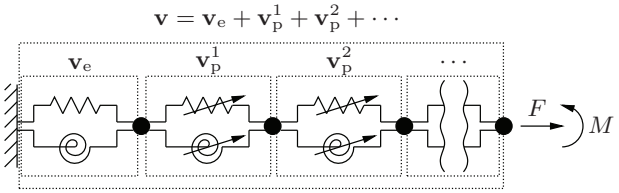

Figure 1: Deformation concept with multiple plastic mechanisms.

Each of the plastic mechanisms shown in Fig. 1 has a yield surface of the type described in Eq. (5) and a flow potential of the type described in Eq. (6) and they are organised in the two vectors

$$\mathbf{f}_y \;=\; [\,F_1(\mathbf{p},\mathbf{p}_\mathrm{i}), F_2(\mathbf{p},\mathbf{p}_\mathrm{i}), \cdots]^T\,, \tag{8}$$

$$\mathbf{g} \;=\; [\,G_1(\mathbf{p},\mathbf{p}_\mathrm{i}), G_2(\mathbf{p},\mathbf{p}_\mathrm{i}), \cdots]^T\,, \tag{9}$$

to simplify the derivation of the elasto-plastic stiffness matrix.

Based on the maximization of the dissipation rate and the enforcement of the consistency condition, the elasto-plastic stiffness matrix is expressed as

$$\mathbf{K}_\mathrm{e}^\mathrm{ep} \;=\; \mathbf{K}_\mathrm{e} - \mathbf{K}_\mathrm{e}(\partial_\mathbf{p}^T\mathbf{g})^T\,\mathbf{H}^{-1}\,(\partial_\mathbf{p}^T\mathbf{f}_y)\mathbf{K}_\mathrm{e}\,, \tag{10}$$

where

$$\mathbf{H} \;=\; (\partial_\mathbf{p}^T\mathbf{f}_y)^T\,\mathbf{K}_\mathrm{e}\,(\partial_\mathbf{p}^T\mathbf{g}) + (\partial_{\mathbf{p}_\mathrm{i}}^T\mathbf{f}_y)^T\,\mathbf{K}_\mathrm{i}\,(\partial_{\mathbf{p}_\mathrm{i}}^T\mathbf{g})\,, \tag{11}$$

is a $n \times n$ block matrix, where n is the number of plastic mechanisms. The matrix $\mathbf{H}$ contains the effect of hardening, represented by the second term. The constitutive behaviour in the case of a single plastic mechanism is shown in Fig. 2 along with a clear identification of the different model parameters.

Figure 2 illustrates the force-deformation characteristics of a single plastic mechanism and the role the model parameters. The elastic stiffness is clearly identified as $\mathbf{K}_\mathrm{e}$, and the yield capacity is identified by p_j^y with the parameter β_j defining the relative additional capacity. Figure 2(a) shows that the magnitude of $\mathbf{K}_\mathrm{i}$ relative to $\mathbf{K}_\mathrm{e}$ controls the magnitude of the kink at yield, while Fig. 2(b) illustrates how the value of α_j controls the shape of the curve between initial yield and the ultimate capacity. With these clear relations between physical characteristics and the model parameters it is rather easy to calibrate the model for a single plastic mechanism.

YIELD SURFACE REPRESENTATION

A simple and versatile yield surface format can be obtained by using a sum of square roots of quadratic forms as introduced in (Tidemann and Krenk 2017). It turns out that two terms in the sum is typically sufficient to get an accurate representation of common yield surfaces and thus the yield surface Eq. (5) is represented by

$$\begin{aligned} F_j(\mathbf{p},\mathbf{p}_\mathrm{i}) \;=& \sqrt{(\bar{\mathbf{p}}-\bar{\mathbf{p}}_\mathrm{i})^T\mathbf{A}_1(\bar{\mathbf{p}}-\bar{\mathbf{p}}_\mathrm{i})}_j + \\ & \sqrt{(\bar{\mathbf{p}}-\bar{\mathbf{p}}_\mathrm{i})^T\mathbf{A}_2(\bar{\mathbf{p}}-\bar{\mathbf{p}}_\mathrm{i})}_j - 1\,, \end{aligned} \tag{12}$$

where the subscript j indicates that the parameters for the plastic mechanism j are used. The matrices $\mathbf{A}_1$ and $\mathbf{A}_2$ need to be positive definite in order to ensure convexity.

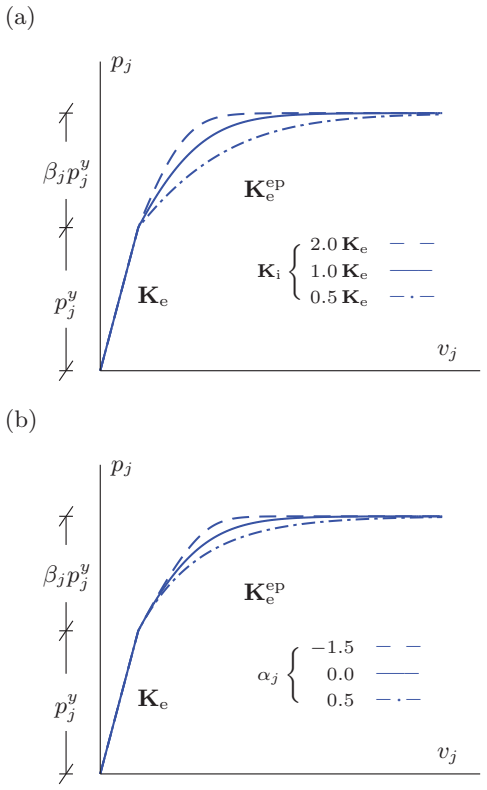

Figure 2: Influence of parameters on stress-strain relation: (a) relative internal stiffness $\mathbf{K}_\mathrm{i} = (-)\mathbf{K}_\mathrm{e}$, (b) modification of flow potential G via the shape parameter α_j.

The only formal restriction on $\mathbf{A}_1$ and $\mathbf{A}_2$ is that they need to be positive definite the coefficients of the matrices can be chosen in various ways giving the format the desired flexibility. Choosing the coefficients in the matrices properly in order to accurately represent analytically determined yield surfaces is typically based on the shape of the yield surface in the planes of the section forces as outlined in the following.

Yield Surface Parameters

As the yield surface representation Eq. (12) is first order homogeneous the value of the yield function at any point is a good estimate of the distance from the point to the yield surface. If the points on the analytical yield surface is known, it is easily determined what the "error" of the yield surface representation Eq. (12) is measured by the distance from the point of the analytical yield surface to the corresponding point on the yield surface representation, as the distance will correspond to the value of the yield function Eq. (12). When a point is known on the analytical yield surface the quality of the representation by Eq. (12) follows by substitution. In the ideal case that the representation equals the analytical yield surface the measure of error would be zero and in other cases it can be minimized in various ways. In such an 'optimization procedure' it is possible to select what parts of the analytical yield surface that are accurately represented and hence it is possible to neglect points on the yield surface where the curvature is large allowing a reduced curvature in these ar-

eas without changing the optimization procedure. When only a single yield surface needs to be represented it may be sufficient to do a simple 'trial and error' optimization procedure instead of programming a gradient based optimization algorithm.

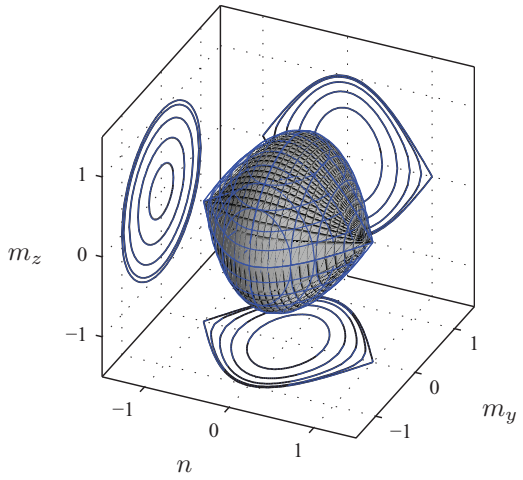

Figure 3: Theoretical yield surface for tubular steel beam and representation, (—). Contour lines are plotted in various planes.

To illustrate the flexibility and accuracy of the yield surface format Eq. (12) two different yield surfaces are represented. The classic analytical yield surface for a tubular steel beam,

$$F(n, m_y, m_z) = \sqrt{m_y^2 + m_z^2} - \cos\left(\frac{\pi}{2} n\right) \tag{13}$$

is represented by diagonal matrices $\mathbf{A}_1$ and $\mathbf{A}_2$ where $A^1_{1,1} = 1 - 2 \cdot 10^{-5}$, $A^1_{2,2} = A^1_{3,3} = 0.16$, $A^2_{1,1} = 1 \cdot 10^{-10}$ and $A^2_{2,2} = A^2_{3,3} = 0.36$ and the analytical yield surface is shown along with the yield surface representation in Fig. 3.

It is observed from Fig. 3 that the representation is highly accurate and the differences in the contour lines are indistinguishable. There are small differences as the analytical yield surface has undefined gradients at $(n, m_y, m_z) = (\pm 1, 0, 0)$ while the representation has an actual gradient in these points. The curvature in the area around these points is high for both the analytical yield surface and the yield surface representation.

In Fig. 4 the yield surface for a tubular steel joint (MSL surface) is shown along with the representation with diagonal matrices $\mathbf{A}_1$ and $\mathbf{A}_2$ where $A^1_{1,1} = 0.21$, $A^1_{2,2} = A^1_{3,3} = 0.97$, $A^2_{1,1} = 0.29$ and $A^2_{2,2} = A^2_{3,3} = 2.3 \cdot 10^{-4}$. The yield surface shown in Fig. 4 is described in terms of the normalized normal force n, in-plane bending moment m_{ip} and out-of-plane bending moment m_{op}. Fig. 4 illustrates that by changing the coefficients in the matrices $\mathbf{A}_1$ and $\mathbf{A}_2$ a rather different yield surface is represented quite well. The analytical yield surface and the representation are very similar as depicted both from the 3D figure and the contour lines. It is noted that where the yield surface of the tubular steel beam only has two points with undefined gradients, the tubular joint yield surface has a whole line with undefined gradients as the gradient is undefined for $|n| = 0$. The yield surface representation Eq. (12) is sufficiently flexible to be able to model such a surface as well.

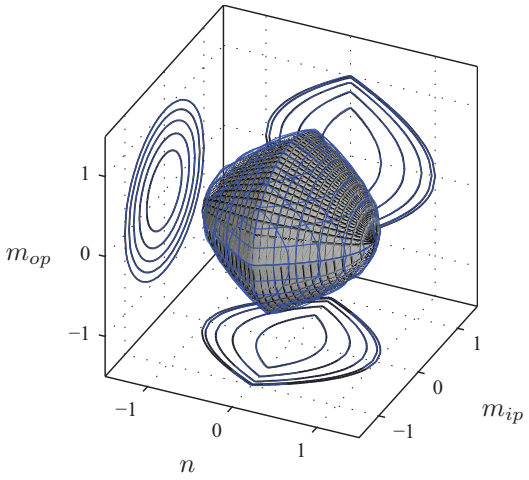

Figure 4: Theoretical yield surface for tubular joint (MSL surface) and approximation, (—). Contour lines are plotted in various planes.

Exterior Equipotential Surfaces

Aside from the possibility of local rounding of the yield surface, while still using a single-equation yield surface that is guaranteed convex, another positive feature of the yield surface format Eq. (12) is that it is homogeneous of degree one, whereby exterior equipotential surfaces are scaled versions of the yield surfaces. This ensures that if the curvature of the yield surface is relatively small, the curvature of the exterior surfaces used for return to the yield surface will also be relatively small. The analytical yield surface of a tubular steel beam Eq. (13) does not hold this property and special measures have to be taken to ensure convergence in a return algorithm because of the harmonic term in the yield function. Due to the harmonic term the gradient of the yield function may be directed away from the yield surface potentially causing divergence in the return algorithm. In Fig. 5 contour lines of the exterior surfaces of the tubular joint yield surface for $m_z = 0$ are shown along with the contour lines of the exterior surfaces of the present homogeneous yield surface representation Eq. (12).

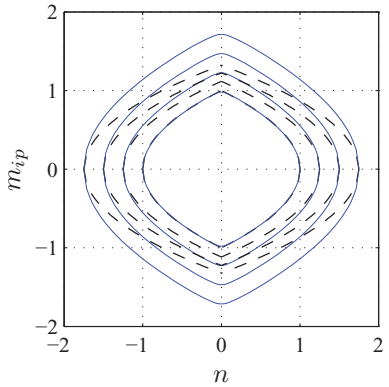

Figure 5: Yield surface with exterior equipotential curves for tubular joint (– –) and yield surface representation, (—).

It is observed in Fig. 5 that while the exterior surfaces of the homogeneous representation are simply an enlarged version of the actual yield surface, the exterior equipotential surfaces of the analytical yield surface change shape, reducing the curvature around $n = 0$ and increasing the curvature in the area where $m_{ip} \simeq 0$.

FRAME ELEMENT IMPLEMENTATION

As discussed in connection with Fig. 1 in a beam element the plastic deformation at the nodes is additive, while the section forces at the nodes are common for the beam and the plastic deformation mechanisms. This suggests the use of an equilibrium based formulation of the beam element flexibility, see e.g. (Krenk et al. 1999).

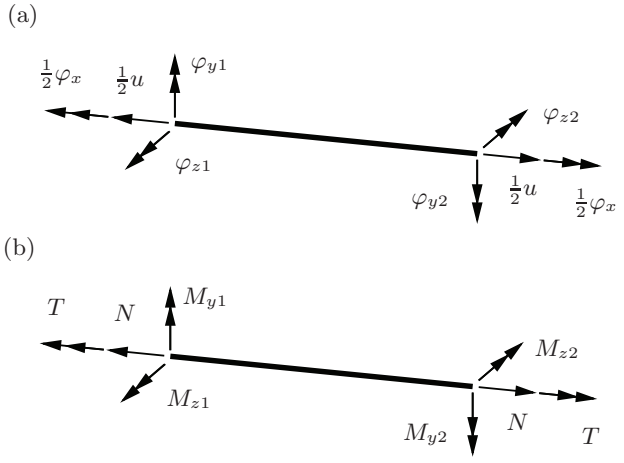

Figure 6: Deformation format of beam element. (a) Element deformations, (b) section forces.

Figure 6 shows the beam element with the axial force N and the moment components together with the corresponding total nodal deformations. The deformations are arranged in the vector

$$\mathbf{v} = [\,u, \varphi_x, \varphi_{z1}, \varphi_{z2}, \varphi_{y1}, \varphi_{y2}\,]^T = \mathbf{v}_\mathrm{e} + \mathbf{v}_\mathrm{p}^\mathrm{M} + \mathbf{v}_\mathrm{p}^\mathrm{J}\,, \tag{14}$$

fitting the energy format Eq. (1). The deformations are split into three parts; an elastic part $\mathbf{v}_\mathrm{e}$ and two plastic parts $\mathbf{v}_\mathrm{p}^\mathrm{M}$ and $\mathbf{v}_\mathrm{p}^\mathrm{J}$, where $\mathbf{v}_\mathrm{p}^\mathrm{M}$ represents plastic deformations in the local member at each end and $\mathbf{v}_\mathrm{p}^\mathrm{J}$ represents plastic deformations at the joints in each end. With this formulation there is a total of four plastic mechanisms with a local member plastic mechanism and a joint plastic mechanism at each end respectively. The section forces conjugate to the elastic deformation $\mathbf{v}_\mathrm{e}$ are

$$\mathbf{p} = [\,N, T, M_{z1}, M_{z2}, M_{y1}, M_{y2}\,]^T\,, \tag{15}$$

corresponding to the standard section forces in a beam as illustrated in Fig. 6. The displacements and element forces are arranged as for standard beam elements with displacement vector

$$\mathbf{u}^T = [\mathbf{u}_1^T, \mathbf{u}_2^T]\,, \quad \mathbf{u}_j = [u_x, u_y, u_z, \theta_x, \theta_y, \theta_z]_j^T\,, \tag{16}$$

where u_x, u_y, u_z and θ_x, θ_y, θ_z are the displacements and rotations about the x- y- and z-axis, respectively. The corresponding element force vector is

$$\mathbf{q}^T = [\mathbf{q}_1^T, \mathbf{q}_2^T]\,, \quad \mathbf{q}_j = [Q_x, Q_y, Q_z, M_x, M_y, M_z]_j^T\,, \tag{17}$$

where Q_x, Q_y, Q_z and M_x, M_y, M_z are the moments about the x-, y- and z-axis respectively.

Via the six equilibrium conditions of the beam it is possible to express the element forces $\mathbf{q}$ in terms of the equilibrium forces $\mathbf{p}$,

$$\mathbf{q} = \begin{bmatrix} \mathbf{q}_1 \\ \mathbf{q}_2 \end{bmatrix} = \begin{bmatrix} \mathbf{T}_1 \\ \mathbf{T}_2 \end{bmatrix} \mathbf{p} = \mathbf{T}\,\mathbf{p}\,, \tag{18}$$

where $\mathbf{T}$ is the transformation matrix and can be found in e.g. (Krenk et al. 1999). As virtual work must be the same in the deformation format and the displacement format the deformation increment $d\mathbf{v}$ has a relationship to the displacement increment $d\mathbf{u}$ similar to the relationship between element forces $\mathbf{q}$ and section forces $\mathbf{p}$ as

$$d\mathbf{v} = \mathbf{T}^T\, d\mathbf{u}\,. \tag{19}$$

The stiffness matrix Eq. (10) is then transformed from the deformation format to the displacement format by use of Eqs. (18) and (19).

The internal deformation variables $\mathbf{v}_\mathrm{i}$ and internal forces $\mathbf{p}_\mathrm{i}$ are arranged in vectors as shown in Eq. (3), and when the plastic mechanisms each depend on the normal force and the two bending moments there is a total of 12 internal variables. The size of $\mathbf{v}$ and $\mathbf{v}_\mathrm{e}$ is different from the size of $\mathbf{v}_\mathrm{i}$ as the former only have six variables. In addition the structure of $\mathbf{K}_\mathrm{i}$ is different from the structure of $\mathbf{K}_\mathrm{e}$ as the latter includes coupling terms between the two ends, the internal stiffness matrix $\mathbf{K}_\mathrm{i}$ is taken to be a diagonal matrix such that the different internal variables do not couple. The internal variables should not be coupled through the stiffness matrix as a uniaxial loading should not cause movement of the yield-surface in other directions unless the shape of the yield surface dictates it, and in that case the coupling will come through the gradient of the yield surface. With the choice of having four plastic mechanisms the size of the matrix $\mathbf{H}$ in Eq. (11) will be 4×4 when all four plastic mechanisms are active and smaller for fewer active plastic mechanisms making the computational cost of inverting the $\mathbf{H}$ matrix inconsiderable. The internal stiffness matrix $\mathbf{K}_\mathrm{i}$ will be a 12×12 diagonal matrix so any associated multiplication is rather straightforward. In total the formulation of the beam element stiffness matrix in the deformation format via Eq. (10) is very efficient computationally as is the transformation to the displacement format.

For joints between elements the yield surface is most often given in terms of the in-plane and out-of-plane bending moments rather than the bending moments about the y– and z–axis of the beam element as shown in Fig. 4. The gradient of the yield function and the flow potential must be with respect to the bending moments about the y– and z–axis of the beam element and it is necessary to transform between the formats. The transformation between the two is a geometric rotation of vectors and the gradient with respect to the bending moments about the y– and z–axis of the beam element is easily found by standard rotation of a vector using a rotation matrix.

EXAMPLES

The theory described above has been implemented in the finite element code RONJA (Rambøll Offshore Nonlinear Jacket Analysis) where automatic calculation of tubular joint capacities is implemented according to several design codes including the MSL code. The accuracy of the plastic mechanism model is illustrated

by two cases of in-plane cyclic bending of a T-joint with different compression in the chord in the two cases. The accuracy of the model with combined multiple plastic mechanisms is illustrated by out-of-plane bending of a X-joint with simultaneous active plastic mechanisms in the joint and in the brace ends at the joint.

In-Plane Bending of T-Joint

The T-joint illustrated in Fig. 7 was experimentally tested by (Kim et al. 2012) to determine the behaviour of T-joints in cyclic in-plane bending and the effect of compression in the chord. The T-joint has a chord diameter of $D_c = 450\,\text{mm}$ and chord length $L_c = 2000\,\text{mm}$. The characteristics of the tubular joint are $\gamma = D_c/2t_c = 18.75$, $\beta = D_b/D_c = 0.778$ and $\tau = t_b/t_c = 1.00$. The length of the brace is $L_b = 1775\,\text{mm}$ measured from the centerline of the chord to the brace end.

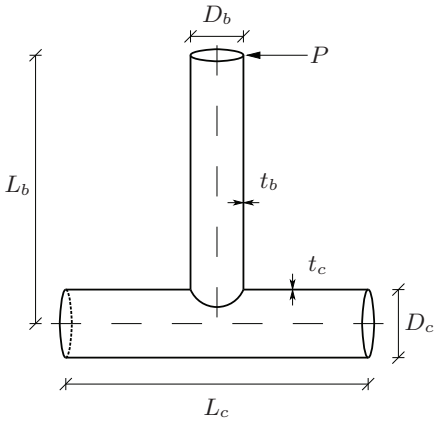

Figure 7: Geometry of T-joint.

The chord ends have hinged connections and the left chord end is fixed against all in-plane motion whereas the right chord end may move in the axial direction to allow for zero chord compression. The brace end is loaded by an in-plane transverse force and otherwise free. Coupon tests were made by (Kim et al. 2012) identifying a yield stress of $\sigma_y = 584\,\text{MPa}$ and an ultimate stress of $\sigma_u = 670\,\text{MPa}$ for both brace and chord steel.

The chord compression is achieved by initial compression of the chord via force control to the desired level and subsequently holding the chord compression constant throughout the experiment. The in-plane bending is achieved by displacement control of the brace end consisting of 18 cycles of 5.63 mm, 7.5 mm and 11.25 mm peak displacement with six cycles of each. Subsequently, four cycles of 15 mm displacement are carried out, followed by six times two cycles with displacements of 22.5 mm, 30 mm, 45 mm, 60 mm, 75 mm and 90 mm, respectively. The displacements account for rotation of the brace, rotation of the chord as well as elastic deformation in the brace and plastic deformation at the tubular joint.

The experiment is modelled using three beam elements of the type described above; one for each half of the chord and one for the brace. The yield stress of 584 MPa has been used to calculate all the brace and chord yield capacities and the ultimate stress levels have all been set by the parameter $\beta^{\text{M}} = \sigma_u/\sigma_y - 1 = 0.147$. The yield capacities at the joint have all been calculated using the MSL norm and the β^{J} values have been set to 2.06 to get an accurate representation of the experimental results. It is noted that the values of β^{J} are much larger than β^{M} because the plastic mechanism at the joint is not governed by the yield and ultimate stress in the same way as the plastic mechanisms in the members. The shape parameters α are set to 0.80. The results of the experiment and the numerical analysis with no chord compression and with chord compression $N/N^y = 0.2$ are shown in Fig. 8 where Δu is the brace end displacement and P is the applied transverse force. In Fig. 8 the numerical results obtained by (Kim et al. 2012) using a detailed thick-shell model including transverse shear effects are also shown.

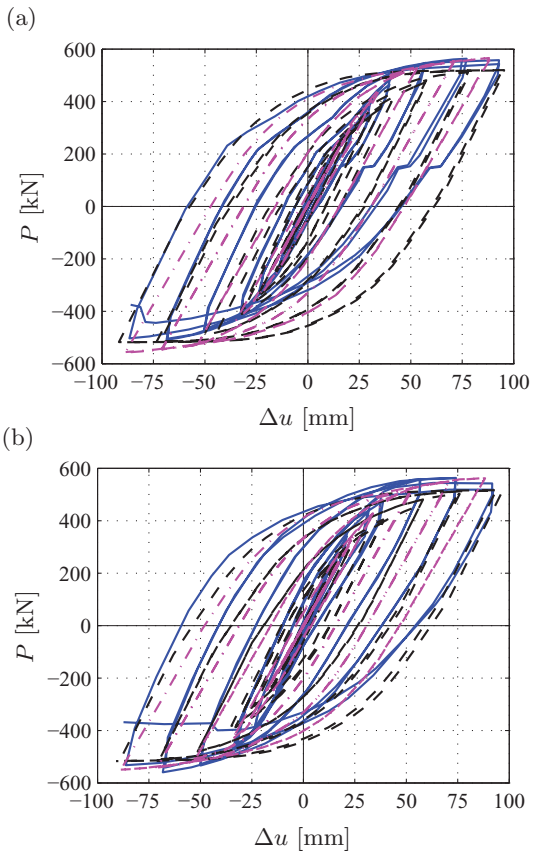

Figure 8: T-joint: experiment (Kim et al. 2012) (—), FE shell model (– · –). Present model (– –). (a) No chord compression, (b) Chord compression $N/N^y = 0.2$.

It is observed in Fig. 8 that the present section-force based model represents the hysteresis curve quite well with load levels and shape of each of the hysteresis loops well represented. There is a discrepancy between the experimental hysteresis loop and the numerical model when the load becomes increasingly negative and the model is not as accurate as when the load becomes increasingly positive. The discrepancy is largest in the case without chord compression and is to a large extent caused by the horizontal shift in the experimental hysteresis curve at a load level of $P \simeq 180\,\text{kN}$. However, there is no evident explanation of the cause of this plateau and it is noted that the highly detailed shell-model provided by (Kim et al. 2012) does not replicate this behaviour either. It is observed that in the case of chord compression the shifts on the unloading path disappear and the model reproduces the hysteresis curve better. In both cases the hysteresis curve is modelled with about equal accuracy by the present

section-force based model as with a quite detailed shell element model. Neither of the models reproduce the drop in capacity in the last half cycle, as this is caused by cracking at the joint and neither of the models account for cracking.

Out-of-Plane Bending of X-Joint

The X-joint shown in Fig. 9 was experimentally tested in out-of-place bending by (Wang et al. 2010) to determine the hysteretic behaviour of moment transferring joints in tubular structures. The X-joint has a chord diameter of $D_c = 273\,\text{mm}$ and chord length $L_c = 1700\,\text{mm}$ and the characteristics of the tubular joint are $\gamma = D_c/2t_c = 8.53$, $\beta = D_b/D_c = 0.90$ and $\tau = t_b/t_c = 0.75$ and each brace has a length of 845 mm measured from the centerline of the chord.

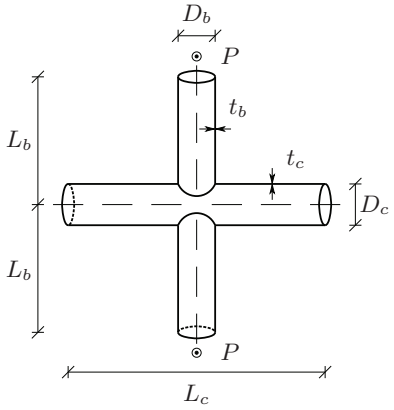

Figure 9: Geometry of X-joint.

The test setup is made in such a way that the out-of-plane boundary conditions of the chord ends are pinned allowing rotation about the in-plane transverse axis of the chord. As the test setup is symmetric torsion of the chord is restrained at the ends. The yield strength of the brace is reported by (Wang et al. 2010) to be $\sigma_y = 368\,\text{MPa}$ for the chord and $\sigma_y = 385\,\text{MPa}$ for the braces and the ultimate strength is reported to be $\sigma_u = 520\,\text{MPa}$ for the chord and $\sigma_u = 551\,\text{MPa}$ for the braces. These values are used to model the member capacities while a yield stress of $\sigma_y = 250\,\text{MPa}$ is used to model the joint capacities. The special choice of the joint capacity yield strength is based on the elastic range of the hysteresis curve and it is assumed that the welding process is what may have changed the apparent yield stress at the joint. All joint capacities are determined based on the MSL standard and it was found suitable to use a value of $\beta^{\text{J}} = 1.8$ and $\alpha^{\text{J}} = 0.85$, while $\alpha^{\text{M}} = 0.80$; all values that are fairly similar to the values used to model the T-joint.

The test is made by displacement control where the brace ends are cycled in the out-of-plane direction with increasing magnitude for each cycle and the displacement is the same for both brace ends and the experimental results as well as the numerical results are shown in Fig. 10 where Δu is the displacement of a brace end and P is the load on each brace end.

It is observed in Fig. 10 that the accuracy of the model is quite high with the characteristic load levels reproduced well and the shape of the individual hysteresis curves reproduced with reasonable accuracy. The results in Fig. 10 reveal that both joint and local member plastic mechanisms are active at the same time,

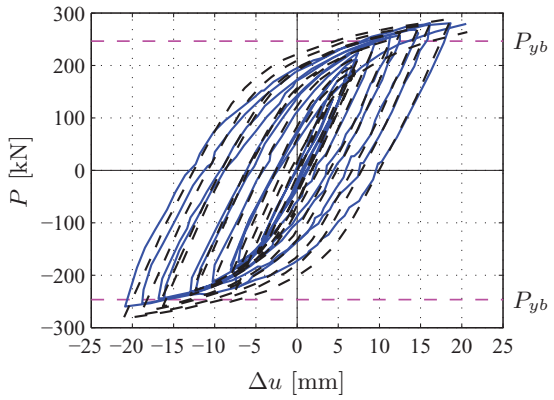

Figure 10: X-joint: experiment (Wang et al. 2010) (—). Present model (– –).

stressing the need for multiple plastic mechanisms at each end. The joint properties are fairly similar for the T-joint and the X-joint, suggesting that only small variation in the model parameters is needed to get a good overall representation of actual joint behaviour even for different joint types.

CONCLUSIONS

A cyclic plasticity model based on section-forces has been developed for analysis of offshore structures. The basic plasticity model makes use of a kinematically hardening yield surface and a flow potential in which the yield function is augmented by terms containing internal variables controlling the development of plastic strains. The yield function is in the form of a sum of square roots of quadratic forms of the section-forces. This particular format is very flexible with respect to representation of the characteristics of tubular joints, and furthermore generates self-similar exterior surfaces convenient in the formulation of return type algorithms for the elasto-plastic increments. The model contains a series representation of yield mechanisms, enabling e.g. the simultaneous action of a member yield hinge and the yield mechanism of the associated joint. The cyclic plasticity model is implemented in an equilibrium-based beam element in such a way that no additional global degrees of freedom are added to the beam model.

The performance of the model is illustrated by application to published experimental results for the development of elasto-plastic deformation of a T- and an X-joint. The hysteresis cycles and their general shape are represented quite well although the model only contains five parameters for each yield mechanism. The basic parameters of the model – representing initial yield, ultimate capacity, and a single shape parameter describing the gradual development of plasticity – are similar for the two cases analyzed, and indeed seem to be representative values for typical offshore joints.

ACKNOWLEDGEMENTS

This paper is part of a project sponsored jointly by the Danish Agency for Science, Technology and Innovation, Maersk Oil A/S and the Technical University of Denmark.

REFERENCES

Bleyer, J, and de Buhan, P (2013a).“A Greedy Algorithm for Yield Surface Approximation,” *Comptes Rendus Mecanique*, 341, 605–615.

Bleyer, J, and de Buhan, P (2013b). “Yield Surface Approximation for Lower and Upper Bound Yield Design of 3D Composite Frame Structures,” *Computers & Structures*, 129, 86–98.

Bui, NN, Ngo, M, Nikolic, M, Brancherie, D, and Ibrahimbegovic, A (2014). “Enriched Timoshenko Beam Finite Element for Modeling Bending and Shear Failure of Reinforced Concrete Frames,” *Computers and Structures*, 143, 9–18.

Ibrahimbegovic, A, Jehel, P, and Davenne, L (2008). “Coupled Damage-Plasticity Constitutive Model and Direct Stress Interpolation,” *Computational Mechanics*, 42, 1–11.

Kim, JW, Kim, SS, Lee, MJ, and Yang, JG (2012). “Vierendeel Joints in the Circular Hollow Sections of High Strength Steel Subjected to Brace Moment and Chord Compressive Loadings,” *International Journal of Steel Structures*, 12, 579–587.

Krenk, S, and Tidemann, L (2017). “A Compact Cyclic Plasticity Model with Parameter Evolution.” (Submitted for publication, sk@mek.dtu.dk).

Krenk, S, Vissing-Jørgensen, C, and Thesbjerg, L (1999). “Efficient Collapse Analysis Techniques for Framed Structures,” *Computers and Structures*, 72, 481–296.

Orbison, JG, McGuire, W, and Abel, JF (1982). “Yield Surface Applications in Non-linear Steel Frame Analysis,” *Computer Methods in Applied Mechanics and Engineering*, 33, 557–573.

Skordeli, MAA, and Bisbos, CD (2010). “Limit and Shakedown Analysis of 3D Steel Frames via Approximate Ellipsoidal Yield Surfaces,” *Engineering Structures*, 32, 1556–1567.

Tidemann, L, and Krenk, S (2017). “Cyclic Plastic Hinges with Degradation Effects for Frame Structures.” (Submitted for publication, lastid@mek.dtu.dk).

Wang, W, Chen, Y, Meng, X, and Leon, RT (2010). “Behavior of Thick-Walled CHS X-Joints Under Cyclic Out-of-Plane Bending,” *Journal of Constructional Steel Research*, 66, 826–834.

C2

Robust return algorithm for anisotropic plasticity models

L. Tidemann & S. Krenk

Proceedings of the 30th Nordic Seminar on Computational Mechanics, pp. 197–200.

Kongens Lyngby, Denmark, October 25–27, 2017.

30th Nordic Seminar on Computational Mechanics
NSCM-30
J. Høgsberg. N.L. Pedersen (Eds.)
2017

ROBUST RETURN ALGORITHM FOR ANISOTROPIC PLASTICITY MODELS

L. TIDEMANN*† AND S. KRENK*

*Department of Mechanical Engineering, Technical University of Denmark
DK-2800 Kongens Lyngby, Denmark

†Mærsk Olie & Gas
DK-6700 Esbjerg, Denmark
e-mail: lastid@mek.dtu.dk

Key words: Return algorithms, Computational methods, Cyclic plasticity.

1 INTRODUCTION

Plasticity models can be defined by an energy potential, a plastic flow potential and a yield surface. The energy potential defines the relation between the observable elastic strains $\boldsymbol{\gamma}_\mathrm{e}$ and the energy conjugate stresses $\boldsymbol{\tau}_\mathrm{e}$ and between the non-observable internal strains $\boldsymbol{\gamma}_\mathrm{i}$ and the energy conjugate internal stresses $\boldsymbol{\tau}_\mathrm{i}$, where the internal stresses control the various hardening mechanisms. Plasticity models may be defined either in terms of traditional stresses and strains $\boldsymbol{\tau} = [\sigma_{11}, \sigma_{22}, \cdots]^T$ and $\boldsymbol{\gamma} = [\varepsilon_{11}, \varepsilon_{22}, \cdots]^T$ or generalized stresses and strains, e.g. $\boldsymbol{\tau} = [N, M_y, \cdots]^T$ and $\boldsymbol{\gamma} = [\varepsilon, \kappa_y, \cdots]^T$, the latter typically used in plastic analysis of frame structures. To have a compact notation in the following $\boldsymbol{\tau}_\mathrm{e}$ and $\boldsymbol{\tau}_\mathrm{i}$ are arranged in a common vector $\tilde{\boldsymbol{\tau}}^T = [\boldsymbol{\tau}_\mathrm{e}^T, \boldsymbol{\tau}_\mathrm{i}^T]$ and correspondingly $\boldsymbol{\gamma}_\mathrm{e}$ and $\boldsymbol{\gamma}_\mathrm{i}$ are arranged in the common vector $\tilde{\boldsymbol{\gamma}}^T = [\boldsymbol{\gamma}_\mathrm{e}^T, \boldsymbol{\gamma}_\mathrm{i}^T]$.

In traditional stress-based analyses the stress is evaluated at a material point, where a single plastic mechanism may be active, whereas in the case of frame structures each beam may have two active plastic mechanisms, in the form of a yield hinge in each end as illustrated in Fig. 1. In general multiple plastic mechanisms may be active for different types of elements. Each plastic mechanism has a yield surface described by a yield function F_j and a flow potential G_j describing the plastic flow evolution by its gradient and these potentials are conveniently collected in the vectors $\mathbf{f}_y = [F_1(\tilde{\boldsymbol{\tau}}), \dots, F_n(\tilde{\boldsymbol{\tau}})]^T$ and $\mathbf{g} = [G_1(\tilde{\boldsymbol{\tau}}), \dots, G_n(\tilde{\boldsymbol{\tau}})]^T$ respectively.

The key to developing a general and robust return algorithm for anisotropic plasticity models is the strain evolution equation. The strain evolution equation is obtained from maximizing the dissipation rate under the assumption that the material is described by the flow potential[1,2]

$$\dot{\tilde{\gamma}} = \begin{bmatrix} \dot{\boldsymbol{\gamma}}_\mathrm{t} \\ \mathbf{0} \end{bmatrix} - \sum_j \partial_{\tilde{\boldsymbol{\tau}}} G_j \, \dot{\lambda}_j = \begin{bmatrix} \dot{\boldsymbol{\gamma}}_\mathrm{t} \\ \mathbf{0} \end{bmatrix} - \left(\partial_{\tilde{\boldsymbol{\tau}}}^T \mathbf{g}\right)^T \dot{\boldsymbol{\lambda}} \,, \tag{1}$$

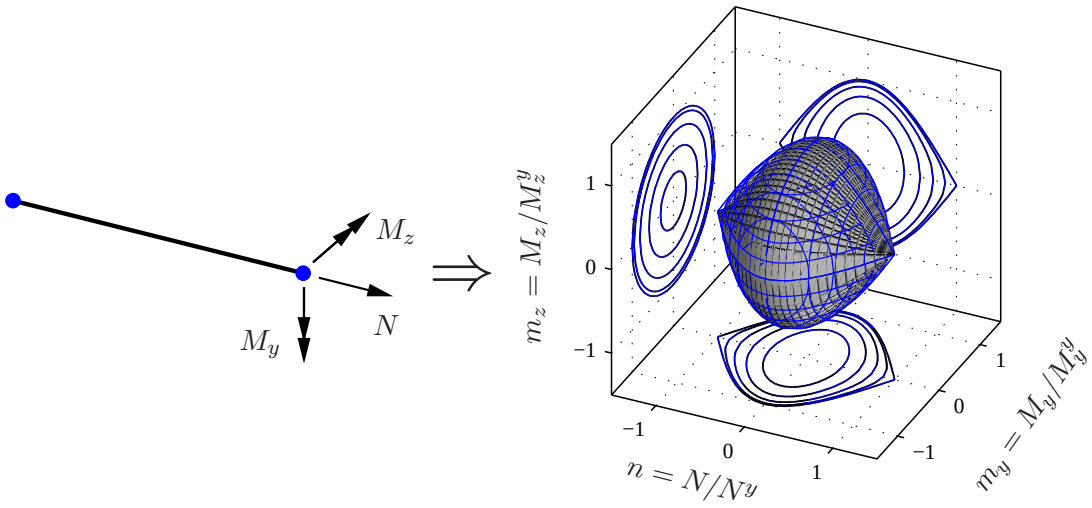

Figure 1: Beam with plastic hinges and corresponding yield surface.

where $\dot{\boldsymbol{\gamma}}_{\mathrm{t}}$ is the total increment in the observable strains. The plastic multipliers $\dot{\boldsymbol{\lambda}}$ are determined by the consistency condition that during plastic loading, the stress state $\boldsymbol{\tau}_{\mathrm{e}}$ must stay on the yield surfaces defined in $\mathbf{f}_y$.

2 RETURN ALGORITHM

The strain evolution equation (1) is reformulated to finite increments and is assumed to be satisfied in the final generalized stress state[3]. For non-trivial yield surfaces the strain evolution equation will not initially be satisfied and a residual is formed

$$\mathbf{r}_{\tilde{\gamma}} \;=\; \begin{bmatrix} \Delta\boldsymbol{\gamma}_{\mathrm{t}} \\ \mathbf{0} \end{bmatrix} - \Delta\tilde{\boldsymbol{\gamma}} - \left(\partial_{\tilde{\boldsymbol{\tau}}}^T \mathbf{g}\right)^T \Delta\boldsymbol{\lambda}\,. \tag{2}$$

The final state where $\mathbf{r}_{\tilde{\gamma}} = \mathbf{0}$ is obtained by a first order variation of the residual (2) combined with the consistency condition that the final stress state must be on the yield surface. The first order variation is formulated entirely in terms of $\delta\tilde{\boldsymbol{\tau}}$ and $\delta\boldsymbol{\lambda}$ with use of the constitutive relation

$$\delta\tilde{\boldsymbol{\tau}} \;=\; \tilde{\mathbf{K}}\,\delta\tilde{\boldsymbol{\gamma}}\,, \tag{3}$$

where the tangent stiffness matrix $\tilde{\mathbf{K}}$ contains the double derivatives of the energy potential. The resulting equation system to solve is

$$\begin{bmatrix} \tilde{\mathbf{K}}_A^{-1} & \left(\partial_{\tilde{\boldsymbol{\tau}}}^T \mathbf{g}\right)^T \\ \partial_{\tilde{\boldsymbol{\tau}}}^T \mathbf{f}_y & \mathbf{0} \end{bmatrix} \begin{bmatrix} \delta\tilde{\boldsymbol{\tau}} \\ \delta\boldsymbol{\lambda} \end{bmatrix} \;=\; \begin{bmatrix} \mathbf{r}_{\tilde{\gamma}} \\ -\mathbf{f}_y \end{bmatrix}\,, \quad \tilde{\mathbf{K}}_A^{-1} \;=\; \tilde{\mathbf{K}}^{-1} + \sum_j \frac{\partial^2 G_j}{\partial\tilde{\boldsymbol{\tau}}^T \partial\tilde{\boldsymbol{\tau}}} \Delta\lambda_j\,, \tag{4}$$

where $\tilde{\mathbf{K}}_A$ is the consistent algorithmic stiffness matrix. Instead of solving (4) directly it is solved sequentially by eliminating $\delta\tilde{\boldsymbol{\tau}}$ in the first equation and determining $\delta\boldsymbol{\lambda}$ from the second equation and back-substituting the result into the first equation. Anisotropic

plasticity models may have yield surfaces with regions with large curvature, Fig. 1, leading to large changes in the direction of the gradient of the yield surface and the plastic flow potential. Though $\delta\tilde{\boldsymbol{\tau}}$ is a linear function of the residual $\mathbf{r}_{\tilde{\gamma}}$ and the value of the yield function $\mathbf{f}_y$ according to (4) the function is non-linear as $\tilde{\mathbf{K}}_A^{-1}$, $\partial_{\tilde{\boldsymbol{\tau}}}^T\mathbf{g}$ and $\partial_{\tilde{\boldsymbol{\tau}}}^T\mathbf{f}_y$ in general are non-linear. The increment $\delta\tilde{\boldsymbol{\tau}} = \delta\tilde{\boldsymbol{\tau}}(\xi\mathbf{r}_{\tilde{\gamma}}, \xi\mathbf{f}_y)$ is therefore represented by a second order approximation

$$\delta\tilde{\boldsymbol{\tau}}(\xi) \;=\; \xi\,\frac{\partial(\delta\tilde{\boldsymbol{\tau}})}{\partial\xi}\bigg|_{\xi=0} + \tfrac{1}{2}\xi^2\frac{\partial^2(\delta\tilde{\boldsymbol{\tau}})}{\partial\xi^2}\bigg|_{\xi=0}, \tag{5}$$

where the constant term is zero for $\xi = 0$ and the two derivatives are given by

$$\frac{\partial(\delta\tilde{\boldsymbol{\tau}})}{\partial\xi} \;=\; \mathbf{K}_\mathbf{r}\mathbf{r}_{\tilde{\gamma}} - \mathbf{K}_\mathbf{f}\mathbf{f}_y\,, \quad \frac{\partial^2(\delta\tilde{\boldsymbol{\tau}})}{\partial^2\xi} \;=\; \frac{\partial}{\partial\xi}\Big(\mathbf{K}_\mathbf{r}\mathbf{r}_{\tilde{\gamma}} - \mathbf{K}_\mathbf{f}\mathbf{f}_y\Big) \;\simeq\; \frac{\Delta\mathbf{K}_\mathbf{r}}{\Delta\xi}\mathbf{r}_{\tilde{\gamma}} - \frac{\Delta\mathbf{K}_\mathbf{f}}{\Delta\xi}\mathbf{f}_y\,. \tag{6}$$

The differences $\Delta\mathbf{K}_\mathbf{r}$ and $\Delta\mathbf{K}_\mathbf{f}$ are determined by making half a step, i.e. setting $\xi = 1/2$ and determining the matrices in the updated state by the gradients $\partial_{\tilde{\boldsymbol{\tau}}}^T\mathbf{g}$ and $\partial_{\tilde{\boldsymbol{\tau}}}^T\mathbf{f}_y$ as well as the second order derivatives $\partial^2 G_j/(\partial\tilde{\boldsymbol{\tau}}^T\partial\tilde{\boldsymbol{\tau}})$. These are combined with the solution of the equation system (4) to form $\mathbf{K}_\mathbf{r}^{1/2}$ and $\mathbf{K}_\mathbf{f}^{1/2}$. Inserting the results into (6) and (5) with $\Delta\xi = 1/2$ and setting $\xi = 1$ gives the relation

$$\delta\tilde{\boldsymbol{\tau}} \;=\; \mathbf{K}_\mathbf{r}^{1/2}\mathbf{r}_{\tilde{\gamma}} - \mathbf{K}_\mathbf{f}^{1/2}\mathbf{f}_y\,. \tag{7}$$

This is analogous to a method used in explicit stress integration[3] where a midpoint is found and the elasto-plastic stiffness at the midpoint is used for a full step.

3 NUMERICAL EXAMPLES

The robustness of the return algorithm is illustrated by deformation of a beam with plastic hinges, Fig. 1, described by a cyclic plasticity model[1] in terms of the normalized section forces[2] $n = N/M^y$ and $m = M/M^y$. The yield surface is slightly rounded in comparison to the one shown in Fig. 1. The energy potential consists of two quadratic terms uncoupling $\boldsymbol{\tau}_\mathrm{e}$ and $\boldsymbol{\tau}_\mathrm{i}$ whereby $\tilde{\mathbf{K}}$ becomes a block diagonal matrix with $\mathbf{K}_\mathrm{e}$ and $\mathbf{K}_\mathrm{i}$ in the diagonals. The yield surface is kinematic hardening and is tailored for cyclic plasticity models with general hardening behaviour[1]. The beam is modelled with parameters representing ideal-plastic behaviour, Fig. 2(a) and (b), and parameters representing non-linear hardening plastic hinges, Fig. 2(c) and (d). Both beams are subjected to a large strain increment with an equivalent estimated elastic stress state with $n = 14$ and $m_y = 4$ at one hinge and $n = 14$ and $m_y = 0$ at the other hinge.

The estimated elastic stress state is located far away from the yield surface in a region with relatively large curvature of the yield surface and two plastic mechanisms. Nevertheless the algorithm returns the stress state to the yield surfaces in just 10 iterations in the ideal plasticity case as illustrated in Fig. 2(a) and (b). About half the number of iterations is used to get to the neighbourhood of the final state and the remaining half is

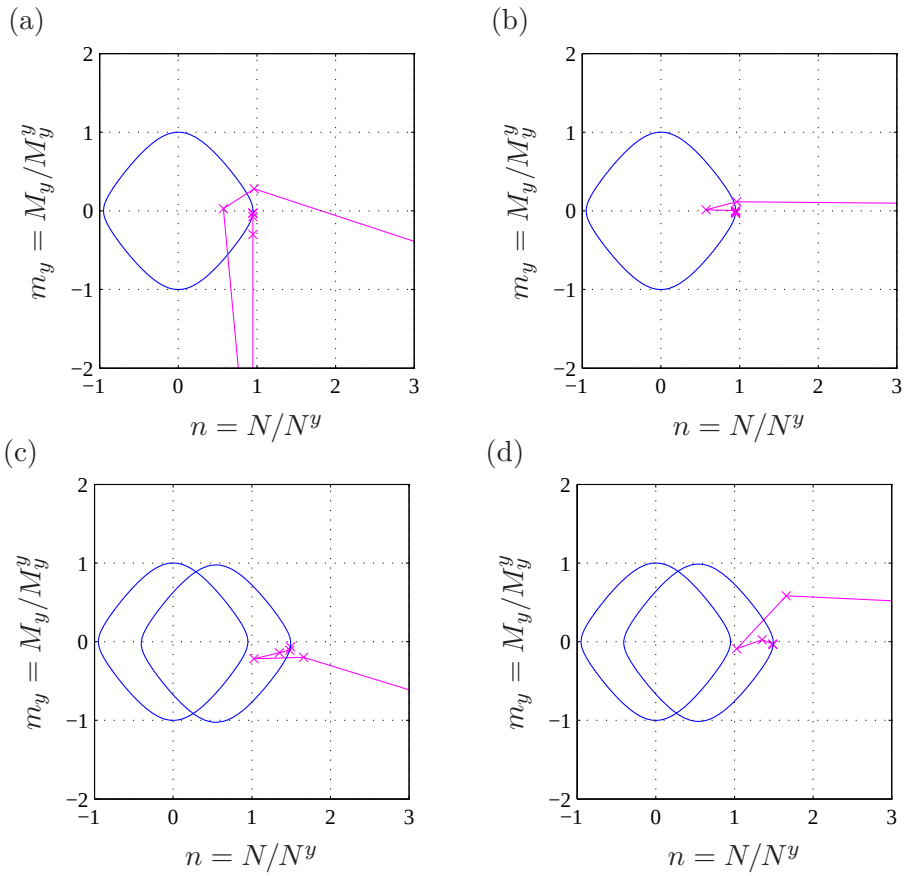

Figure 2: Return with ideal plasticity parameters (top) and hardening plasticity parameters (bottom). Left: Yield surface 1. Right: Yield surface 2.

to ensure $\mathbf{r}_{\tilde{\gamma}} = \mathbf{0}$. Hardening typically eases return and as shown in Fig. 2(c) and (d) it does in the present case as well, as the return is made in only 7 steps. It is noted that a traditional single-step return algorithm fails to converge for the predicted stress states shown in Fig. 2. In general the method presented here is more robust, e.g. if half the deformation increment used above is applied a traditional single-step return algorithm will converge in the ideal-plastic case but not in the hardening case.

REFERENCES

[1] Krenk, S. & Tidemann, L. A compact cyclic plasticity model with parameter evolution. *Mechanics of Materials* **113**, 57–68 (2017).

[2] Tidemann, L. & Krenk, S. Cyclic plastic hinges with degradation effects for frame structures. *Journal of Engineering Mechanics* (accepted for publication) (2017).

[3] Zienkiewicz, O. C., Taylor, R. L. & Zhu, J. Z. *The Finite Element Method* (Elsevier Butterworth–Heinemann, Oxford, 2005), 6 edn.

DTU Mechanical Engineering
Section of Solid Mechanics
Technical University of Denmark

Nils Koppels Allé, Bld. 404
DK-2800 Kgs. Lyngby
Denmark
Phone (+45) 4525 4250
Fax (+45) 4593 1475
www.mek.dtu.dk
ISBN: 978-87-7475-516-6

DCAMM
Danish Center for Applied Mathematics and Mechanics

Nils Koppels Allé, Bld. 404
DK-2800 Kgs. Lyngby
Denmark
Phone (+45) 4525 4250
Fax (+45) 4593 1475
www.dcamm.dk
ISSN: 0903-1685